

A boundary element analysis of symmetric laminate composite shallow shells

E. L. Albuquerque¹ and M. H. Aliabadi²

¹ Faculty of Mechanical Engineering, State University of Campinas
Campinas, Brazil, ederlima@fem.unicamp.br
Currently at Imperial College London as an academic visitor.

¹ Department of Aeronautics, Imperial College London
London, UK, m.h.aliabadi@imperial.ac.uk

Keywords: Laminated composites, shallow shells, radial integration method.

Abstract. This paper presents a boundary element formulation for the analysis of symmetric laminate composite shallow shells where only the boundary is discretized. Classical plate bending and plane elasticity formulations are coupled and effects of curvature are treated as body forces. Body forces are written as a sum of approximation functions multiplied by coefficients. Domain integrals which arise in the formulation are transformed into boundary integrals by the radial integration method. The accuracy of the proposed formulation is assessed by comparison with results from literature.

Introduction

Nowadays, the demand for construction of advanced aerospace, automotive, and marine structures has increased the interest in composite laminated shells. Some requirements, as for example high strength-to-weight ratio, good resistance to corrosion, as well as long fatigue life, cannot be obtained with the use of metallic or any other engineering materials except composites. Other requirements, as aerodynamic profile and good stealth characteristics demand curved structures or shell like structures. Although the large majority of papers about the numerical analysis of composite shells are related to the finite element method, there are few works in literature that present boundary element formulations applied to orthotropic or even anisotropic shells [1, 2, 3]. However, all these works involve complicated fundamental solutions that need to be computed numerically. An alternative approach to the these previous formulations is the coupling of plate bending and plane elasticity formulations, as proposed by Zhang and Atluri [4] who derived a formulation for static and dynamic analysis of isotropic classical shallow shells. Domain integrals were computed by the domain discretization into cells. Dirgantara and Aliabadi [5] extended this approach to the analysis of shear deformable isotropic shallow shells. For the best of authors knowledge, there is no paper in the literature for anisotropic shells using the coupling of plate bending and plane elasticity formulations.

In this paper, a boundary element formulation for anisotropic shallow shells with no domain discretization is presented. Classical plate bending and plane elasticity formulations are coupled and effects of curvature are treated as body forces. The domain integrals due to body forces are transformed into boundary integrals using the radial integration method. Numerical results are presented to assess the accuracy of the method. Displacements computed using the proposed formulation are in good agreement with results available in literature.

Boundary integral equations

Consider a shallow shell of an anisotropic elastic material with the mid-surface being described by $z = z(x_1, x_2)$. The base-plane of the shell is defined in a domain Ω in the plane x_1, x_2 whose boundary is given by Γ .

Using the equilibrium equation of shallow shells, the reciprocity relation, and the Green theorem, it is possible to derive integral equations that can be divided in terms of plane elasticity and plate bending formulations as shown by Zhang and Atluri [4] for isotropic shallow shells. These equations

are coupled by the domain integrals that arise in both of them. Integral equations for the plane elasticity formulation are given by:

$$c_{ij}u_j + \int_{\Gamma} t_{ik}^*(Q, P)u_k(P)d\Gamma(P) = \int_{\Gamma} u_{ik}^*(Q, P)t_k(P)d\Gamma(P) + \int_{\Omega} C\kappa_{kj}u_3u_{ik,j}^*(Q, P)d\Omega, \quad (1)$$

where $i, j, k = 1, 2$; u_k is the displacement in directions x_1 and x_2 , $t_i = N_{ij}n_j$, N_{ij} are membrane forces applied in the shell; u_3 stands for the displacement in the normal direction of the shell surface; κ depends on the curvature radii R_{ij} of the shallow shell; k_{ij} are the inverse of curvature radii. P is the field point; Q is the source point; and asterisks denote fundamental solutions. The anisotropic plane elasticity fundamental solutions can be found, for example, in [6]. The constant c_{ij} is introduced in order to take into account the possibility that the point Q can be placed in the domain, on the boundary, or outside the domain.

The integral equation for the plate bending formulation is given by:

$$\begin{aligned} Ku_3(Q) + \int_{\Gamma} \left[V_n^*(Q, P)w(P) - m_n^*(Q, P)\frac{\partial w(P)}{\partial n} \right] d\Gamma(P) + \sum_{i=1}^{N_c} R_{ci}^*(Q, P)u_{3ci}(P) \\ = \sum_{i=1}^{N_c} R_{ci}(P)u_{3ci}^*(Q, P) + \int_{\Omega} q_3(P)u_3^*(Q, P)d\Omega \\ + \int_{\Gamma} \left[V_n(P)u_3^*(Q, P) - m_n(P)\frac{\partial u_3^*(Q, P)}{\partial n} \right] d\Gamma(P) \\ + \int_{\Gamma} C\kappa n_j u_i(P)u_3^*(Q, P)d\Gamma(P) + \int_{\Omega} C\frac{\kappa_{ij}}{\rho_{ij}}u_3^*(Q, P)u_3(P)d\Omega \\ + \int_{\Omega} [C\kappa_{ij}(P)u_3^*(Q, P)]_j u_i(P)d\Omega, \end{aligned} \quad (2)$$

where $\frac{\partial(\cdot)}{\partial n}$ is the derivative in the direction of the outward vector \mathbf{n} that is normal to the boundary Γ ; m_n and V_n are, respectively, the normal bending moment and the Kirchhoff equivalent shear force on the boundary Γ ; R_c is the thin-plate reaction of corners; u_{3ci}^* is the transverse displacement of corners; q_3 is the domain force in the x_3 direction; The constant K is introduced in order to take into account the possibility that the point Q can be placed in the domain, on the boundary, or outside the domain. As in the previous equation, an asterisk denotes a fundamental solution. Fundamental solutions for anisotropic thin plates can be found, for example, in [7].

As can be seen, domain integrals arise in the formulation owing to the curvature of the shell. In order to transform these integrals into boundary integrals, consider that a body force b is approximated over the domain Ω as a sum of M products between approximation functions f_m and unknown coefficients γ_m , that is:

$$b(P) = \sum_{m=1}^M \gamma_m f_m. \quad (3)$$

The approximation function used in this work is:

$$f_{m_1} = 1 + R, \quad (4)$$

Equation (3) can be written in a matrix form, considering all source points, as:

$$\mathbf{b} = \mathbf{F}\boldsymbol{\gamma} \quad (5)$$

Thus, γ can be computed as:

$$\gamma = \mathbf{F}^{-1}\mathbf{b} \quad (6)$$

Body forces of integral equations (1) and (2) depend on the displacements. So, using equation (6) and following the procedure presented by Albuquerque *et al.* [8], domain integrals that come from these body forces can be transformed into boundary integrals. Then, by discretization of these boundary integrals, a matrix equation can be obtained. Finally, after applying boundary conditions, this matrix equation is transformed in a linear system that can be solved to find the unknowns of the shell problem.

Numerical results

In order to assess the accuracy of the proposed formulation, consider a square spherical shallow shell, as shown in Figure 1. The geometry and material properties of the shell are as follow: length of the base edge of the shell $a = 0.254$ m, thickness $h = 0.0127$ m, curvature radii $R_1 = R_2 = R = 2.54$ m ($R_{12} = R_{21} = 0$), elastic moduli $E_2 = 6.895$ GPa and $E_1 = 2E_2$, Poisson ratio $\nu_{12} = 0.3$, and shear modulus $G_{12} = E_2/[2(1 - \nu_{12})]$. The shell is under a uniformly distributed load in the transversal direction (internal pressure) $q_3 = 2.07$ MPa ($q_1 = q_2 = 0$).

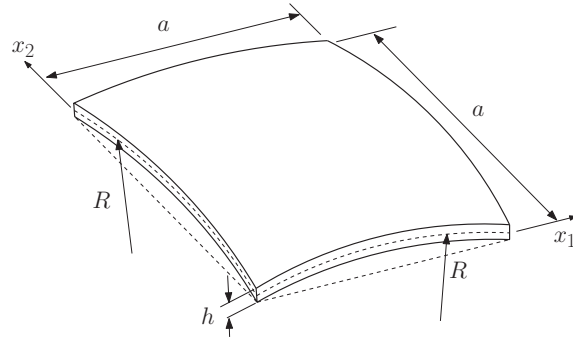


Figure 1: Square spherical shallow shell.

This problem was analysed considering two types of boundary conditions, i.e., clamped and simply-supported. Three meshes were used. Mesh 1 has 12 constant boundary elements and 9 internal points, mesh 2 has 20 constant boundary elements and 25 internal points, and mesh 3 has 28 constant boundary elements and 49 internal points. Mesh 3 is shown in Figure 2. All meshes have elements of equal length and uniformly distributed internal points.

Figures 3 and 4 show results for the clamped and simply-supported boundary conditions, respectively, together with meshless results obtained by Sladek *et al.* [9] for the same problems but considering the shell as shear deformable.

As it can be seen, the results for the clamped boundary conditions are in good agreement with the meshless results while for the simply-supported boundary conditions they are slightly lower.

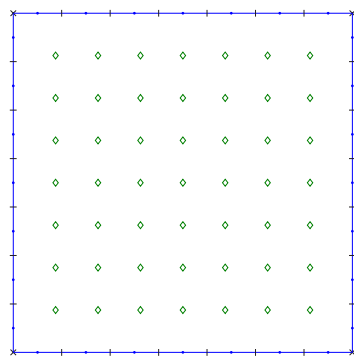


Figure 2: Mesh and internal points for the square shallow spherical shell.

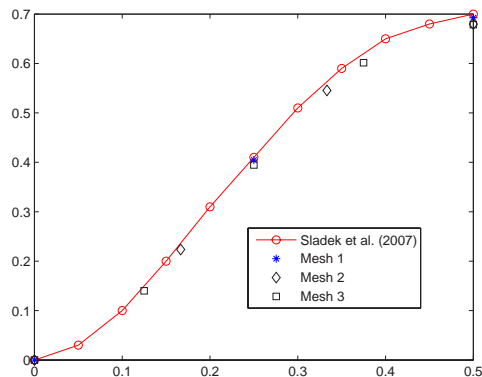


Figure 3: Transversal displacement for the spherical shell with clamped edge.

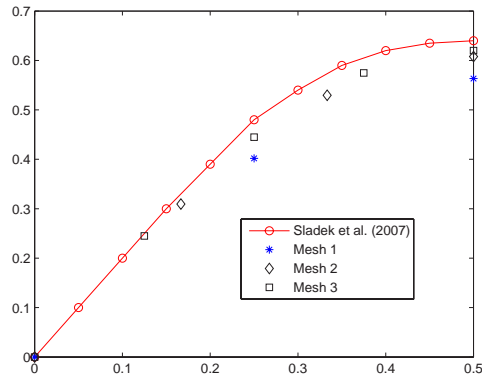


Figure 4: Transversal displacement for the spherical shell with simply-supported edge.

Conclusions

This paper presented a boundary element formulation for the analysis of symmetric laminated composite shallow shells where domain integrals are transformed into boundary integrals by the radial integration method. As the radial integration method doesn't demand particular solutions, it is easier to implement than the dual reciprocity boundary element method. Results obtained with the proposed formulation are in good agreement with results presented in literature.

Acknowledgment

The first author would like to thank the CNPq (The National Council for Scientific and Technological Development, Brazil), AFOSR (Air Force Office of Scientific Research, USA), and FAPESP (the State of São Paulo Research Foundation, Brazil) for financial support for this work.

References

- [1] W. Jianguo. The fundamental solutions of orthotropic shallow shells. *Acta Mechanica*, 94:113–121, 1992.
- [2] P. Lu and O. Mahrenholtz. The fundamental solution for the theory of orthotropic shallow shells involving shear deformation. *Int. J. of Solids and Structures*, 31:913–923, 1994.
- [3] J. Wang and K. Schweizerhof. The fundamental solution of moderately thick laminated anisotropic shallow shells. *Int. J. Engng. Sci.*, 33:995–1004, 1995.
- [4] J. D. Zhang and S. N. Atluri. A boundary/interior element method for quasi-static and transient response analysis of shallow shells. *Computers and Structures*, 24:213–223, 1986.
- [5] T. Dirgantara and M. H. Aliabadi. A new boundary element formulation for shear deformable shells analysis. *Int. J. for Numerical Methods in Engn.*, 45:1257–1275, 1999.
- [6] P. Sollero and M. H. Aliabadi. Fracture mechanics analysis of anisotropic plates by the boundary element method. *Int. J. of Fracture*, 64:269–284, 1993.

- [7] E. L. Albuquerque, P. Sollero, W. Venturini, and M. H. Aliabadi. Boundary element analysis of anisotropic kirchhoff plates. *International Journal of Solids and Structures*, 43:4029–4046, 2006.
- [8] E. L. Albuquerque, P. Sollero, and W. P. Paiva. The radial integration method applied to dynamic problems of anisotropic plates. *Communications in Numerical Methods in Engineering*, 23:805–818, 2007.
- [9] J. Sladek, V. Sladek, J. Krivacek, and M. H. Aliabadi. Local boundary integral equations for orthotropic shallow shells. *International Journal of Solids and Structures*, 44:2285–2303, 2007.

A Simple Numerical Procedure to Improve the Accuracy of the Boundary Element Method

Loeffler, C.F.¹ and Wrobel, L.C.²

¹ Mechanical Engineering Department, Federal University of Espírito Santo
Av Fernando Ferrari, 514, Vitoria, ES – CEP 29075-910 – Brazil
carlosloeffler@bol.com.br

² School of Engineering and Design, Brunel University, Uxbridge UB8 3PH – UK
luiz.wrobel@brunel.ac.uk

Keywords: Boundary Element Method, recursive calculations, accuracy

Abstract. This paper presents a simple procedure to improve the accuracy of numerical calculations with the Boundary Element Method. In the BEM, values at internal points are usually determined through the application of an integral equation after all the boundary values are calculated. In this work, it is shown that the same idea can be used to improve the accuracy of the boundary results. The aim of this numerical procedure is to correct the boundary values by recalculating them through the use of a boundary integral equation, based on the boundary values calculated previously. The procedure is applied to the solution of the Laplace equation. Numerical results are compared with analytical ones to show the improvements obtained with the proposed technique.

Boundary Integral Equation

Let $u(x)$ be a scalar potential in a two-dimensional domain Ω . Considering mathematical fundamentals of the Theory of Integral Equations [1], an integral equation equivalent to the Laplace equation may be written as:

$$u(\xi) = \int_{\Gamma} u^*(\xi; X) q(X) d\Gamma - \int_{\Gamma} q^*(\xi; X) u(X) d\Gamma \quad (1)$$

in which $q(X)$ is the normal derivative of $u(X)$ and Γ defines the boundary. The two-dimensional fundamental solutions are of the form:

$$u^*(\xi; X) = (-1/2\pi) \ln r(\xi; X) \quad (2)$$

$$q^*(\xi; X) = (-1/2\pi r) r_i n_i \quad (3)$$

where $r(\xi; X)$ is the Euclidean distance between the source point ξ and the field point X , and n_i is the external unit normal vector at the field point. When the source point is positioned on the boundary, $u^*(\xi; X)$ and $q^*(\xi; X)$ present singularities. The mathematical procedure applied to solve this problem considers the domain Ω augmented by a circular sector of radius ε centered at ξ and then takes the limit as $\varepsilon \rightarrow 0$ [2]. Considering this extended boundary, the integral equation (1) may be rewritten as:

$$u(\xi) = \int_{\Gamma} u^*(\xi; X) q(X) d\Gamma - \lim_{\varepsilon \rightarrow 0} \left\{ \int_{\Gamma - \Gamma_\varepsilon} q^*(\xi; X) u(X) d\Gamma + \int_{\Gamma_\varepsilon} q^*(\xi; X) u(X) d\Gamma \right\} \quad (4)$$

The third integral in eq (4) must be studied considering an extra potential field $u(\xi)$, that is:

$$\lim_{\varepsilon \rightarrow 0} \int_{\Gamma_\varepsilon} q^*(\xi; X) u(X) d\Gamma = \lim_{\varepsilon \rightarrow 0} \left\{ \int_{\Gamma_\varepsilon} q^*(\xi; X) [u(X) - u(\xi)] d\Gamma + \int_{\Gamma_\varepsilon} q^*(\xi; X) u(\xi) d\Gamma \right\} \quad (5)$$

Provided $u(X)$ is a continuous function, a Taylor series expansion of first order may hold in the first term on the right-hand side of eq (5). Taking into consideration that, in a circular sector, $r=\varepsilon$ and $d\Gamma_\varepsilon = \varepsilon d\theta$, results in:

$$\lim_{\varepsilon \rightarrow 0} \left\{ \int_{\Gamma_\varepsilon} q^*(\xi; X) [u(X) - u(\xi)] d\Gamma \right\} = - \lim_{\varepsilon \rightarrow 0} \left\{ \int_{\Gamma_\varepsilon} \frac{1}{2\pi} \frac{[u_i(\xi) \Delta x_i]}{\varepsilon} d\Gamma \right\} = - \lim_{\varepsilon \rightarrow 0} \left\{ \int_0^\pi \frac{1}{2\pi} u_i(\xi) n_i \varepsilon d\theta \right\} = 0 \quad (6)$$

If $u(x)$ satisfies the Holder condition, the second integral on the right-hand side of eq (4) exists in the Cauchy Principal Value (CPV) sense [2]. The second term on the right-hand side of eq (5) can be easily integrated, but it is left here in general form because of its dependence on the internal angle between adjacent elements [2]. Thus, the integral equation for source points located on the boundary is given by:

$$u(\xi) [1 - \lim_{\varepsilon \rightarrow 0} \int_{\Gamma_\varepsilon} q^*(\xi; X) d\Gamma] = c(\xi) u(\xi) = \int_{\Gamma} u^*(\xi; X) q(X) d\Gamma - \int_{\Gamma} q^*(\xi; X) u(X) d\Gamma \quad (7)$$

Following standard BEM discretisation and integration procedures [2], eq (7) is collocated at a number N of source points, generating the system of equations:

$$\mathbf{H} \mathbf{U} - \mathbf{G} \mathbf{Q} = \mathbf{0} \quad (8)$$

Recursive Boundary Element Procedure

The solution of the BEM system (8) provides the missing potential or its normal derivative at all N boundary nodes. Regarding internal unknowns, it is possible to determine their values by directly using the integral eq (1) for source points inside the domain. The accuracy for the internal variables is usually better than for the boundary ones.

The discrete form of eq (1), for a boundary point and considering smooth boundaries, can be written as:

$$(0.5)u(\xi^i) = \sum_{e=1}^N Q_k^e \int_{\Gamma_e} \phi_k u^*(\xi^i; X) d\Gamma - \sum_{e=1}^N U_k^e \int_{\Gamma_e} \phi_k q^*(\xi^i; X) d\Gamma \quad (9)$$

where ϕ_k are the interpolation functions and Q_k^e and U_k^e are the nodal values at the boundary. The potential values and their spatial derivatives in the x_j direction (or normal and tangential directions) can be also calculated. However, the integral equations for the spatial derivatives are hyper-singular [3-5]. Taking the Cartesian derivatives of eq (1) and using the Leibniz rule gives:

$$u_{,i}(\xi) = q_i(\xi) = \int_{\Gamma} q_i^*(\xi; X) u(X) d\Gamma - \int_{\Gamma} u_{,i}^*(\xi; X) q(X) d\Gamma \quad (10)$$

where:

$$u_{,i}^*(\xi; X) = q_i^* = -(1/2\pi r) r_i \quad (11)$$

$$q_i^*(\xi; X) = p_i^* = -(1/2\pi r^2) [2r_{,i} r_j n_j - r_{j,i} n_j] \quad (12)$$

Considering, as previously, an augmented sector of radius ε and applying a constant potential field $u(\xi)$ in the complete domain for convenience, eq (10) can be rewritten as:

$$\begin{aligned} q_i(\xi) &= \lim_{\varepsilon \rightarrow 0} \left\{ \int_{\Gamma - \Gamma_\varepsilon} p_i^*(\xi; X) [u(X) - u(\xi)] d\Gamma + \int_{\tilde{\Gamma}_\varepsilon} p_i^*(\xi; X) [u(X) - u(\xi)] d\Gamma + \right. \\ &\quad \left. - \int_{\Gamma - \Gamma_\varepsilon} q_i^*(\xi; X) q(X) d\Gamma - \int_{\tilde{\Gamma}_\varepsilon} q_i^*(\xi; X) q(X) d\Gamma \right\} \end{aligned} \quad (13)$$

On the augmented boundary Γ_ε the expression of $p_i^*(\xi; X)$ can be simplified as:

$$p_i^*(\xi; X) = -(1/2\pi\varepsilon^2) n_i \quad (14)$$

in which $r=\varepsilon$ and $r_{,i} = r/\varepsilon$. Taking into consideration the last equation and a first-order Taylor expansion, the second integral on the right-hand side of eq (13) results in:

$$\lim_{\varepsilon \rightarrow 0} \left\{ \int_{\tilde{\Gamma}_\varepsilon} p_i^*(\xi; X) [u(X) - u(\xi)] d\Gamma \right\} = \lim_{\varepsilon \rightarrow 0} \left\{ \int_{0_\varepsilon} (1/2\pi\varepsilon^2) n_i [u_{,j} \Delta x_j] \varepsilon d\theta \right\} = \lim_{\varepsilon \rightarrow 0} \left\{ \int_{0_\varepsilon} (1/2\pi\varepsilon) n_i [u_{,j} n_j] \varepsilon d\theta \right\} \quad (15)$$

Except for the negative sign, the same result can be found by analysing the last integral on the right-hand side of eq (13). The complete expression is dependent on the internal angle between neighboring element [3-5], represented here simply as $s(\xi)$. Considering smooth boundaries, especially when constant boundary elements are used, the result of eq (15) is $0.5q_i$. For the remaining integrals, the two limits exist when considered together in a CPV sense [5]. Thus, taking into consideration the former procedures, eq (13) can finally be written as:

$$s(\xi) q_i(\xi) = CPV \left\{ \int_{\Gamma} p_i^*(\xi; X) [u(X) - u(\xi)] d\Gamma - \int_{\Gamma} q_i^*(\xi; X) q(X) d\Gamma \right\} \quad (16)$$

Once the boundary values are calculated, eq (16) can be discretised and applied to points ξ^i on the boundary:

$$s(\xi^j) q_i(\xi^j) = CPV \left\{ \sum_{e=1}^N Q_k^e \int_{\Gamma_e} \phi_k q_i^*(\xi^j; X) d\Gamma - \sum_{e=1}^N U_k^e \int_{\Gamma_e} \phi_k p_i^*(\xi^j; X) d\Gamma \right\} \quad (17)$$

Numerical Simulations

All the following numerical simulations consider a semi-circular domain, with zero normal flux along the curved boundary and a prescribed temperature along the horizontal boundary. The temperature values are discontinuous at $r=0$, according to Fig.1. The BEM discretisation has 22

constant elements. The geometric nodes (extreme points) of the boundary elements along the circular boundary were taken as new points for the application of the recursive BEM (RBI).

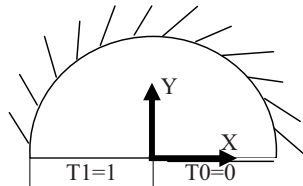


Fig. 1: Semi-circular domain subjected to a discontinuous temperature field

Table 1 presents analytical and numerical results for the temperature at nodal points. Although a small number of boundary elements is used the numerical results display very good accuracy, with the largest errors appearing near the corners.

ϕ (°)	X	Y	NUMERICAL	ANALYTICAL	ERROR (%)
10	.38794E+01	.68405E+00	.5175E-01	.5555E-01	6.85
30	.34115E+01	.19696E+01	.1644E+00	.1667E+00	1.38
50	.25321E+01	.30176E+01	.2764E+00	.2778E+00	0.50
70	.13473E+01	.37016E+01	.3880E+00	.3889E+00	0.23
85	.34730E+00	.39696E+01	.4719E+00	.4722E+00	0.06
95	-.34730E+00	.39696E+01	.5281E+00	.5277E+00	0.08
110	-.13473E+01	.37016E+01	.6120E+00	.6111E+00	0.15
130	-.25321E+01	.30176E+01	.7236E+00	.7222E+00	0.19
150	-.34112E+01	.19696E+01	.8355E+00	.8333E+00	0.26
170	-.38791E+01	.68405E+00	.9483E+00	.9444E+00	0.41

Table 1 - Temperatures at nodal points calculated directly on the circular boundary

Table 2 shows normal derivatives on the horizontal boundary. Results have the same value but opposite sign for negative values of the coordinate x. Comparing with the temperature results, it can be seen that there is a decrease in numerical accuracy.

X	Y	NUMÉRICAL	ANALYTICAL	ERROR (%)
.350E+01	.000E+00	.9631E-01	.9095E-01	5.89
.250E+01	.000E+00	.1251E+00	.1273E+00	1.73
.175E+01	.000E+00	.1819E+00	.1819E+00	0.00
.125E+01	.000E+00	.2502E+00	.2546E+00	1.73
.750E+00	.000E+00	.3592E+00	.4244E+00	15.36
.250E+00	.000E+00	.1557E+01	.1273E+01	22.31

Table 2 - Normal fluxes at nodal points calculated directly on the horizontal boundary

Table 3 contains temperature results on the circular boundary obtained with the recursive use of the BEM. The comparison of results in this table with results presented in Table 1 shows a similar level of accuracy for both cases. In principle, the RBI does not appear to improve significantly the accuracy of the original temperature results in this case. It must be noted that the points selected for the RBI procedure connect two straight boundary elements, being necessary to determine the correct angle between them to determine $s(\xi)$.

X	Y	NUMERICAL	ANALYTICAL	ERROR (%)
.37588E+01	.13681E+01	.1081E+00	.1111E+00	2.70
.30642E+01	.25711E+01	.2204E+00	.2222E+00	0.81
.20000E+01	.34641E+01	.3323E+00	.3333E+00	0.30
.69460E+00	.39392E+01	.4437E+00	.4444E+00	0.16
.00000E+00	.40000E+01	.5002E+00	.5000E+00	0.00
-.69460E+00	.39392E+01	.5545E+00	.5555E+00	0.18
-.20000E+01	.34641E+01	.6676E+00	.6667E+00	0.14
-.30642E+01	.25712E+01	.7794E+00	.7778E+00	0.20
-.37582E+01	.13681E+01	.8922E+00	.8889E+00	0.37

Table 3 - Temperatures at nodal points calculated recursively on the circular boundary

Table 4 presents the numerical results for the normal flux at points located at the horizontal boundary, calculated recursively by the RBI procedure. In this case, the performance of the RBI procedure was more effective, significantly increasing the accuracy of the results in comparison to Table 2.

X	Y	NUMERICAL	ANALYTICAL	ERROR (%)
.300E+01	.000E+00	.1056E+00	.1061E+00	0.47
.200E+01	.000E+00	.1587E+00	.1591E+00	0.25
.150E+01	.000E+00	.2119E+00	.2122E+00	0.14
.100E+01	.000E+00	.3181E+00	.3183E+00	0.06

Table 4 - Normal fluxes at nodal points calculated recursively on the horizontal boundary

Table 5 shows a further comparison of the results obtained directly with 25 linear boundary elements [6] and recursively with the previous discretisation of 22 constant elements. Again, the RBI procedure significantly improves the accuracy of the normal fluxes, particularly at points located close to the singularity.

X	Y	NUMERICAL RECURSIVE	NUMERICAL LINEAR BEM	ANALYTICAL SOLUTION
.800E+00	.000E+00	.3977E+00	.3689E+00	.3979E+00
.450E+00	.000E+00	.7072E+00	.6732E+00	.7073E+00
.170E+00	.000E+00	.1872E+01	.1472E+01	.1819E+01
.090E+00	.000E+00	.3537E+01	.5975E+01	.3537E+01

Table 5 – Comparison of normal fluxes calculated directly with linear boundary elements and recursively using constant elements

Conclusions

It is known that the use of a boundary integral equation to determine internal values produces numerical results with better accuracy than at boundary points. This behaviour is justified by the error minimization imposed by the discretisation procedure. However, the use of this strategy to recalculate boundary values has not been previously discussed in the BEM literature. Following preliminary tests, the recursive procedure has been shown to improve the solution especially for potential derivatives. In the example presented, the RBI displayed a superior performance to a standard BEM calculation, particularly close to discontinuities and singularities.

The computational cost is not high because no new system of equations needs to be solved. The singularities in the flux calculations can be removed analytically or numerically, e.g. by using Kutt quadrature points [7].

References

- [1] F.B. Hildebrand, *Methods of Applied Mathematics*, Dover, New York (1992).
- [2] C.A. Brebbia, J.C.F. Telles and L.C. Wrobel, *Boundary Element Techniques*, Springer-Verlag, Berlin (1984).
- [3] J.C.F. Telles, A.A. Prado, *Hyper-singular Formulation for 2-D Potential Problems*, Advanced Formulations in Boundary Element Methods, Vol. 6, Elsevier, London (1993).
- [4] W.J. Mansur, P. Fleury Jr, J.P.S. Azevedo, *A Vector Approach to the Hyper-singular BEM Formulation for Laplace's Equation in 2D*, International Journal of BEM Communication 8, pp 239-250 (1997).
- [5] L.C. Wrobel and M.H. Aliabadi, *The Boundary Element Method*, Wiley, Chichester (2002).
- [6] A.L. Halbritter, J.C.F. Telles, W.J. Mansur, *Boundary Element Application to Field Problems*, Conference on Analysis, Design and Construction of Structures of Nuclear Central Stations (in Portuguese), Porto Alegre, Brazil, pp 707-724 (1978).
- [7] H.R. Kutt, *On the Numerical Evaluation of Finite Part Integrals Involving an Algebraic Singularity*, Special Report WISK 179, National Research Institute for Mathematical Sciences, Pretoria (1975).

A Boundary Element Formulation for 3D Wear Simulation in Rolling-Contact problems

L. Rodríguez-Tembleque^{1*}, R. Abascal², M.H. Aliabadi³

^{1,2} Departamento de Mecánica de los Medios Continuos, Escuela Técnica Superior de Ingenieros, Camino de los descubrimientos s/n, 41092 Sevilla, SPAIN

¹ luisroteso@us.es, ² abascal@us.es

³Department of Aeronautics, Faculty of Engineering, Imperial College, South kensington Campus, London SW7 2AZ, UK

m.h.aliabadi@imperial.ac.uk

Keywords: Boundary Element Method, Rolling-Contact Mechanics, Wear Simulation.

Abstract. The present work shows a new methodology for wear simulation in rolling-contact 3D problems. The formulation is based on the Boundary Element Method (BEM) for computing the elastic influence coefficients, and on projection functions over the augmented Lagrangian of tractions for rolling-contact restrictions fulfilment. The loss of material on the bodies' surface is modeled using the Archard's linear wear law. The methodology is applied to simulate a disc-on-disc dry wear test. Results will show the solids profiles evolution in a disc-on-disc rolling-contact problem when the wear is taking place.

Introduction

Wear phenomenon is presented in the mechanical surface interaction between solids in rolling-contact. From an engineering point of view, wear estimation is a very interesting mechanical topic because allow to predict the life of a mechanical component, to select proper materials, and to have an optimum design for durability. Wear prediction also allow to plan maintenance operations more precisely, which reduces costs as a result of engine or machine immobilization.

In spite of the importance of this phenomenon, there are no many works in the literature related with the numerical simulation of wear in rolling contact problems. Among these works should be mentioned Olofsson and Andersson [1], who simulate mild wear in boundary lubricated rollers thrust bearings using Archard's wear law, and Jendel's work [2], where computes train wheel profiles wear compared with field measurements. In both cases the wear depth is computed neglecting the elastic slip. Telliskivi *et al.* [3]-[4] simulates wear in rolling problems using a semi-winkler model.

This work presents a new methodology for wear simulation in rolling-contact 3D problems. The formulation is based on the Boundary Element method (BEM) for computing the elastic influence coefficients, and on projection functions over the augmented Lagrangian of tractions for rolling-contact restrictions fulfilment. The material loss of the bodies is modelled using the Archard's [5] linear wear law which is one of the most used models for engineering applications.

Boundary element method equations

The elastic equations for the domains Ω and $\bar{\Omega}$ using the BEM, could be written respectively, as:

$$\mathbf{H}\mathbf{u} - \mathbf{G}\mathbf{p} = \mathbf{b} \quad ; \quad \bar{\mathbf{H}}\bar{\mathbf{u}} - \bar{\mathbf{G}}\bar{\mathbf{p}} = \bar{\mathbf{b}} \quad (1)$$

where the vector \mathbf{u} ($\bar{\mathbf{u}}$) represents the nodal displacements, and \mathbf{b} ($\bar{\mathbf{b}}$) contains the applied boundary conditions. This equations are well known and can be found in books like [6] or [7].

The Equations (1) have to be regrouped to study a rolling contact problem as

$$\mathbf{A}_q\mathbf{x}_q + \mathbf{A}_u\mathbf{u}_c - \mathbf{A}_p\mathbf{p}_c = \mathbf{b} \quad ; \quad \bar{\mathbf{A}}_q\bar{\mathbf{x}}_q + \bar{\mathbf{A}}_u\bar{\mathbf{u}}_c - \bar{\mathbf{A}}_p\bar{\mathbf{p}}_c = \bar{\mathbf{b}} \quad (2)$$

where $\mathbf{u}_c = [\mathbf{u}_n^T \ \mathbf{u}_t^T]^T$ ($\bar{\mathbf{u}}_c$) are the nodal displacements on the potential contact zone (A_c), $\mathbf{p}_c = [\mathbf{p}_n^T \ \mathbf{p}_t^T]^T$ ($\bar{\mathbf{p}}_c$) are the nodal contact tractions, \mathbf{x}_q ($\bar{\mathbf{x}}_q$) are the unknown nodal displacements or tractions outside A_c , and \mathbf{A}_q ($\bar{\mathbf{A}}_q$) are the columns of \mathbf{H} ($\bar{\mathbf{H}}$) and \mathbf{G} ($\bar{\mathbf{G}}$) matrices, depending on the outside A_c boundary conditions.

The discrete equilibrium equation (proposed by Signorini) for the contact tractions of each body, could be expressed in the following way:

$$\mathbf{p}_c = -\mathbf{T}\bar{\mathbf{p}}_c \quad (3)$$

where \mathbf{T} is a Boolean matrix which establishes the relations between the tractions nodes components of each domain. The couple of nodes which are going to be in contact have the same but opposite tractions.

The normal separation for each pair in contact, and the tangential difference: $(\bar{\mathbf{u}}_t - \mathbf{u}_t)$, can be written as follows:

$$\mathbf{k}_c = \mathbf{T}\bar{\mathbf{u}}_c - \mathbf{u}_c + \mathbf{k}_{og} \quad (4)$$

In the expressions above, $\mathbf{k}_c = [\mathbf{k}_n^T \ \mathbf{k}_t^T]^T$ represents the contact pair separation, and $\mathbf{k}_{og} = [\mathbf{k}_{ng}^T \ \mathbf{0}^T]^T$; ($\mathbf{k}_{ng} = \bar{\mathbf{X}}_n - \mathbf{X}_n$) is the geometric normal contact pair separation.

Equations (2)-(4), can be rewritten in the following way:

$$\mathbf{R}_q \begin{bmatrix} \mathbf{x}_q \\ \bar{\mathbf{x}}_q \end{bmatrix} + \mathbf{R}_u \mathbf{u}_c + \mathbf{R}_p \mathbf{p}_c + \mathbf{R}_k \mathbf{k}_c = \mathbf{F} \quad (5)$$

where the matrices \mathbf{R}_q , \mathbf{R}_u , \mathbf{R}_p and \mathbf{R}_k are defined as:

$$\begin{aligned} \mathbf{R}_q &= \begin{bmatrix} \mathbf{A}_q & \mathbf{0} \\ \mathbf{0} & \bar{\mathbf{A}}_q \end{bmatrix} ; \quad \mathbf{R}_u = \begin{bmatrix} \mathbf{A}_u \\ \bar{\mathbf{A}}_u \mathbf{T}^T \end{bmatrix} ; \quad \mathbf{R}_p = \begin{bmatrix} -\mathbf{A}_p \\ \bar{\mathbf{A}}_p \bar{\mathbf{T}}^T \end{bmatrix} \\ \mathbf{R}_k &= \begin{bmatrix} \mathbf{0} \\ \bar{\mathbf{A}}_u \bar{\mathbf{T}}^T \end{bmatrix} ; \quad \mathbf{F} = \begin{bmatrix} \mathbf{b} \\ \tilde{\mathbf{b}} \end{bmatrix} \end{aligned} \quad (6)$$

and $\tilde{\mathbf{b}} = \bar{\mathbf{b}} + \bar{\mathbf{A}}_u \mathbf{T}^T \mathbf{k}_{og}$

Rolling-Contact equations

The rolling contact restrictions for every contact pair I are summarized in: the *Non-penetration condition*, the *Coulomb friction law* and the *Principle of maximum energy dissipation*. The mathematical expressions for these contact restrictions, can be classified into two groups: normal and tangential.

- *Normal direction*: The unilateral contact conditions can be written, in the form of a complementarity relation, as:

$$(\mathbf{k}_n)_I \geq 0 \quad ; \quad (\mathbf{p}_n)_I \leq 0 \quad ; \quad (\mathbf{p}_n)_I (\mathbf{k}_n)_I = 0 \quad (7)$$

- *Tangential direction*: For tangential direction, the fulfilment of friction law and the principle of maximum dissipation is guaranteed by:

$$\|(\mathbf{p}_t)_I\| \leq \mu |(\mathbf{p}_n)_I| \quad ; \quad (\mathbf{s}_t)_I = -\lambda(\mathbf{p}_t)_I \quad ; \quad \lambda \geq 0 \quad ; \quad (\mathbf{s}_t)_I (\|(\mathbf{p}_t)_I\| - \mu |(\mathbf{p}_n)_I|) = \mathbf{0} \quad (8)$$

In the expression above, \mathbf{s}_t stores the tangential slip velocities of every contact pair I , $(\mathbf{s}_t)_I$, which can be written as [8]

$$(\mathbf{s}_t)_I = (\bar{\mathbf{c}})_I + \hat{\mathbf{D}} (\mathbf{k}_t)_I \approx (\bar{\mathbf{c}})_I + \text{row } I \left(\hat{\mathbf{D}} \right) \mathbf{k}_t \quad (9)$$

where

$$\hat{\mathbf{D}} = \begin{bmatrix} v_{t,1} \frac{\partial}{\partial X_{t1}} + v_{t,2} \frac{\partial}{\partial X_{t2}} & 0 \\ 0 & v_{t,1} \frac{\partial}{\partial X_{t1}} + v_{t,2} \frac{\partial}{\partial X_{t2}} \end{bmatrix} \quad (10)$$

So, considering all the nodes in the contact surface, the tangential slip velocity expression is

$$\mathbf{s}_t = \bar{\mathbf{c}} + \mathbf{D} \mathbf{k}_t \quad (11)$$

being \mathbf{k}_t and \mathbf{s}_t the tangential slip, and the slip velocities vectors, respectively, and \mathbf{D} an algebraic matrix operator, as [8].

Using the projection defined in [8, 9], over the augmented tractions, the rolling contact restrictions (7-8) can be written as

$$\begin{aligned} (\mathbf{p}_n)_I &= \mathbb{P}_n [(\mathbf{p}_n)_I + r_n(\mathbf{k}_n)_I] \\ (\mathbf{p}_t)_I &= \mathbb{P}_t [(\mathbf{p}_t)_I - r_t(\mathbf{s}_t)_I] \end{aligned} \quad (12)$$

Wear modelling

One of the most used model for engineering applications is the linear wear equation, the Archard's wear law [5]. This law considers that the wear arises from the adhesive forces set up when atoms come into intimate contact. This kind of wear is known as a *Delamination Wear* and it occurs when the sliding speed remains at low levels, such as the surface heating can be neglected, and the applied load not exceed a limit where seizure takes place. The expression for the Archard's wear law could be written as:

$$W = \hat{\kappa} P d \quad (13)$$

and shows that the volumetric wear of one body is proportional to the product between the applied load and the sliding tangential distance (d). The constant $\hat{\kappa}$ is defined as: $\hat{\kappa} = \kappa/H_o$, where the constants κ and H_o are respectively, the non-dimensional wear coefficient and the hardness of the material in contact. For Archard [5], the constant κ represents the probability that a fragment will be formed at an adhesive joint resulting in a wear particle.

In order to simulate numerically the worm on contact surfaces, we can write (13) in a differential equation form, for every contact pair I , as

$$(\dot{\mathbf{h}}_w)_I = \hat{\kappa} (\mathbf{p}_n)_I \|(\mathbf{s}_t)_I\| \quad (14)$$

using the nodal wear depth vector \mathbf{h}_w , the nodal normal pressure vector \mathbf{p}_n and the nodal tangential slip vector \mathbf{s}_t .

From the solid particle point of view which is travelling with velocity V through the contact zone, the wear depth after the rotation ($k+1$) can be approximated as

$$(\Delta \mathbf{h}_w^{(k+1)})_I = \sum_{\substack{I \\ \{I: I \in A_c \text{ and} \\ \mathbf{X}(I) \text{ is parallel to } V \text{ direction}\}}}^{N_I} \Delta t \left(\hat{\kappa} (\mathbf{p}_n^{(k+1)})_I \|(\mathbf{s}_t^{(k+1)})_I\| \right) \quad (15)$$

where the super-index ($k+1$) express the rotation which is taking place, N_I is the number of contact pairs that are located in the same direction (parallel to V), $\Delta t = \tau/N_I$, and τ is the solid particle time of residence in A_c travelling with V velocity. The same scheme was used by Jendel in [2], but in this work, we consider the elastic slip velocity.

Solution algorithm

The quasi-static wear problem presented in equations (5,12,15) is solved as follows. Considering that all the problem variables, $\mathbf{z}^T = [\mathbf{x}_q^T \ \bar{\mathbf{x}}_q^T \ \mathbf{u}_c^T \ \mathbf{k}_c^T \ \mathbf{s}_t^T \ \mathbf{h}_w^T]$ are known for the rotation (k), their values at ($k+1$) rotation are computed using a Uzawa scheme with index (n):

- (I) Apply the rigid body rapprochement increment: $\Delta \mathbf{k}_o^{(n)}$

(II) Initialize all the contact pair tractions and their wear depth:

$$(\mathbf{p}_c^{(n)})_I = (\mathbf{p}_c^{(k)})_I, \quad (\mathbf{h}_w^{(n)})_I = (\mathbf{h}_w^{(k)})_I, \quad (\Delta\mathbf{h}_w^{(n)})_I = 0 \quad (16)$$

(III) Solve the linear equations set:

$$\begin{bmatrix} \mathbf{R}_q & \mathbf{R}_u & \mathbf{R}_k \end{bmatrix} \begin{bmatrix} \mathbf{x}_q \\ \bar{\mathbf{x}}_q \\ \mathbf{u}_c \\ \mathbf{k}_c \end{bmatrix}^{(n+1)} = \mathbf{F}^{(k)} + \begin{bmatrix} \mathbf{0} \\ \bar{\mathbf{A}}_u \mathbf{T}^T (\Delta\mathbf{h}_w^{(n)} + \Delta\mathbf{k}_o^{(n)}) \end{bmatrix} + \mathbf{R}_p \mathbf{p}_c^{(n)} \quad (17)$$

(IV) Compute the contact tractions: $\mathbf{p}_c^{(n+1)}$, the tangential slip velocity: $\mathbf{s}_t^{(n+1)}$, and the wear depth increment: $\Delta\mathbf{h}_w^{(n+1)}$ for each pair I :

$$(\mathbf{s}_t^{(n+1)})_I = (\bar{\mathbf{c}})_I + \text{row } I \left(\hat{\mathbf{D}} \right) \mathbf{k}_t^{(n+1)} \quad (18)$$

$$(\mathbf{p}_n^{(n+1)})_I = \mathbb{P}_n \left[(\mathbf{p}_n^{(n)})_I + r_n (\mathbf{k}_n^{(n+1)})_I \right] \quad (19)$$

$$(\mathbf{p}_t^{(n+1)})_I = \mathbb{P}_t \left[(\mathbf{p}_t^{(n)})_I - r_t (\mathbf{s}_t^{(n+1)})_I \right] \quad (20)$$

$$(\Delta\mathbf{h}_w^{(n+1)})_I = \sum_{\substack{I \\ \{I: I \in A_c \text{ and} \\ \mathbf{X}(I) \text{ is parallel to } V \text{ direction}\}}}^{N_I} \Delta t \left(\hat{\kappa} (\mathbf{p}_n^{(k+1)})_I \|(\mathbf{s}_t^{(k+1)})_I\| \right) \quad (21)$$

(V) Compute the error function:

$$\Psi(\mathbf{p}_c^{(n+1)}) = \left\| \mathbf{p}_c^{(n+1)} - \mathbf{p}_c^{(n)} \right\| \quad (22)$$

(a) If $\Psi(\mathbf{p}_c^{(n+1)}) \leq \varepsilon$, the solution for the rotation $(k+1)$ is reached: $\mathbf{z}^{(k+1)} = \mathbf{z}^{(n+1)}$.

In case the applied boundary condition is the external load i -component ($(\mathbf{Q}^{(k+1)})_i$), before reaching the solution at rotation $(k+1)$, the resultant loads applied on the contact zone (Γ_c) have to be computed: $(\mathbf{Q}^{(n+1)})_i = \int_{A_c} (\mathbf{p}_c^{(n+1)})_i dA$

(a.1) If $|(\mathbf{Q}^{(n+1)})_i| > |(\mathbf{Q}^{(k+1)})_i| + \varepsilon_{load}$, modify $\Delta\mathbf{k}_o^{(n)}$ and return to (II).

(a.2) Otherwise, the solution for the rotation $(k+1)$ is reached: $\mathbf{z}^{(k+1)} = \mathbf{z}^{(n+1)}$.

(b) Otherwise, return to (III) doing $\mathbf{p}_c^{(n)} = \mathbf{p}_c^{(n+1)}$ and $\Delta\mathbf{h}_w^{(n)} = \Delta\mathbf{h}_w^{(n+1)}$, and iterate until convergence is reached.

After the solution at rotation $(k+1)$ is reached ($\mathbf{z}^{(k+1)}$), the solution for the next rotation is achieved evaluating: $\mathbf{z}^{(k)} = \mathbf{z}^{(k+1)}$ and returning to (I).

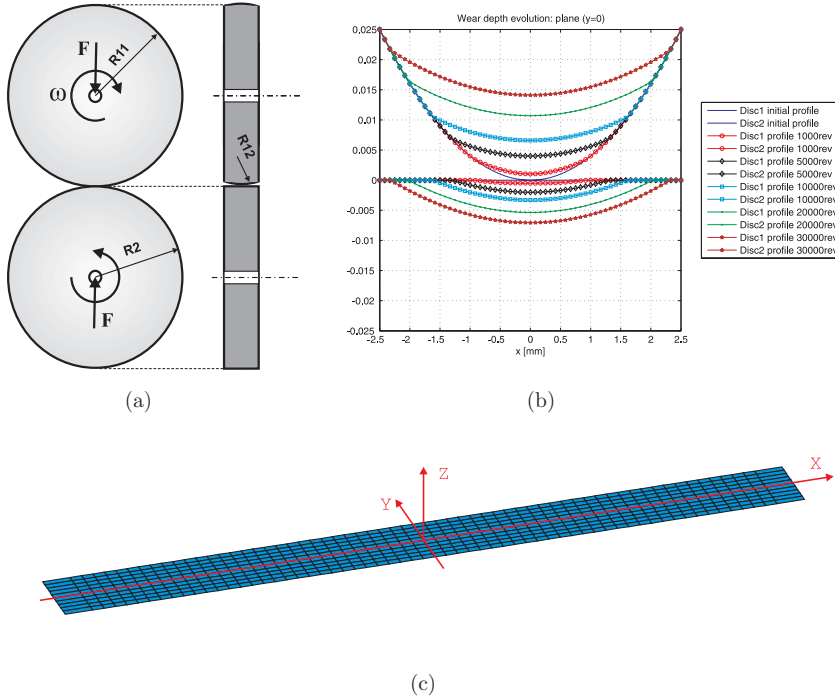


Figure 1: Disc-on-disc scheme (a), solids wear profiles evolution(b) and elastic half-space boundary elements mesh (c).

Results

The proposed methodology was applied to solve a disc-on-disc rolling contact simulation (see Figure 1a), considering wear, in 30000 cycles. The applied force was $F = 300N$, the discs geometric parameters were: $R_{11} = 32.5mm$, $R_1 = 125mm$ and $R_2 = 32.3mm$, constant rotational speed: $\omega = 300rev/min$, the Creep = 0.5%, the materials properties: $G = 8 \cdot 10^{10}Pa$ (modulus of rigidity) and $\nu = 0.25$ (Poisson's ratio), and the wear parameters: $H = 2.5 \cdot 10^9Pa$ (hardness) $k = 5 \cdot 10^{-3}$ (coefficient of wear) $kw = k/H = 2 \cdot 10^{-6}mm^2/N$.

Figure 1b shows the discs profiles evolution during the wear process, and in Figure 1c we can see the elastic-halfspace boundary elements mesh used. Another wear simulation has been done increasing only the creep value (Creep = 1.5%). The resulting discs profiles after 30000 rotations in both cases (Creep = 0.5% and Creep = 1.5%), are showed in Figure 2a together with the experimental results (Figure 2b) showed by Telliskivi in [3]. The results reveal a good enough agreement with the experimental results.

Summary and conclusions

This work presents new methodology for wear simulation in rolling-contact 3D problems using the BEM for computing the elastic influence coefficients, and the projection functions for rolling-contact restrictions fulfilment. The material loss of the bodies is modelled using the Archard's linear wear law. The methodology is applied to simulate a disc-on-disc profile wear. The comparison with the

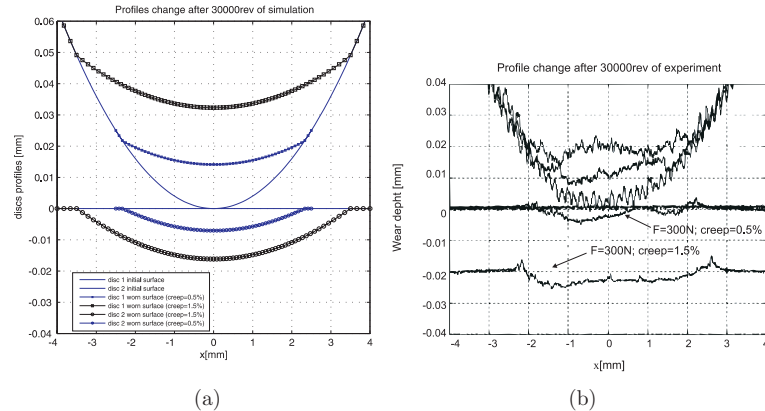


Figure 2: Wear depth evolution in two different creep cases: numerical results (left) and experimental results (right).

experimental results has a good enough agreement, so the proposed methodology seems to be a powerful numerical tool for wear computing in 3D rolling contact problems.

Acknowledgments

This work was funded by the *Conserjería de Innovación Ciencia y Empresa de la Junta de Andalucía*, Spain, research project P05-TEP-00882, and by the *Ministerio de Educación y Ciencia*, Spain, research project DPI2006-04598.

References

- [1] U. Olofsson, S. Andersson, and S. Björklund. Simulation of mild wear in boundary lubricated spherical roller thrust bearings. *Wear*, 241(2):180–185, 2008.
- [2] T. Jendel. Prediction of wheel profile wear - comparisons with field measurements. *Wear*, 253(1-2):89–99, 2002.
- [3] T. Telliskivi. Simulation of wear in a rolling-sliding contact by a semi-winkler model and the archard's wear law. *Wear*, 256(7-8):817–831, 2004.
- [4] T. Telliskivi and U. Olofsson. Wheel-rail wear simulation. *Wear*, 257(11):1145–1153, 2004.
- [5] J.F. Archard. Contact and rubbing of flat surfaces. *J. Appl. Phys.*, 24:981–988, 2006.
- [6] C.A. Brebbia and J. Domínguez. *Boundary Elements: An Introductory Course (second edition)*. Computational Mechanics Publications, 1992.
- [7] M.H. Aliabadi. *The Boundary Element Method Vol 2: Application in Solids and Structures*. Wiley, London, 2002.
- [8] R. Abascal and L. Rodríguez-Tembleque. Steady-state 3d rolling-contact using boundary elements. *Comm. Num. Meth. Eng.*, 23(10):905–920, 2007.
- [9] R. Abascal and L. Rodríguez-Tembleque. Fast 3d contact mechanics bem algorithm. In Selvadurai A.P.S., Tan C.L., and Aliabadi M.H., editors, *Advances in Boundary Elements Techniques VI*. EC, Ltd., UK, 2005.

A CQM based symmetric Galerkin Boundary Element Formulation for semi-infinite domains

Lars Kielhorn^{1,a}, Martin Schanz^{1,b}

¹Institute for Applied Mechanics, Technikerstraße 4/II, 8010 Graz, Austria

^al.kielhorn@tugraz.at , ^bm.schanz@tugraz.at ,

Keywords: Time domain SGBEM, CQM, 3-d elastodynamics, hypersingular kernels, semi-infinite domains

Abstract. The present work deals with the problem of modelling wave propagation phenomena within a 3-d elastodynamic halfspace. While there exist several Boundary Element formulations based on the more common collocation method, the development of Symmetric Galerkin Boundary Element Methods in this field is at the very beginning and rather challenging. On that score the present work should be understood as a first step.

Here, the time discretization of the underlying Boundary Integral Equations (BIEs) is done via the Convolution Quadrature Method (CQM) proposed by Lubich. After the time discretization, a variational formulation is established resulting in a Galerkin based method in space. Moreover, to obtain a symmetric Galerkin Boundary Element formulation the 2nd BIE is required. This BIE involves hypersingular kernel functions which must be treated carefully in the numerical implementation. Hence, a regularization based on integration by parts of the elastodynamic fundamental solution is presented which, finally, results in a Boundary Element formulation containing at least only weakly singular kernel functions.

In Boundary Element Methods semi-infinite domains are commonly approximated in space by considering just a sufficiently large enough region. Unfortunately, applying this procedure to the symmetric formulation implies the evaluation of additional terms on the truncated surface's boundary due to the regularization of the involved kernel functions.

Therefore, a methodology based on infinite elements intended to overcome this drawback will be presented. The numerical tests done so far show that this approach might be capable of treating semi-infinite domains also within a symmetric Galerkin scheme.

Initial boundary value problem for elastodynamics

By definition of the Lamé-Navier operator

$$\mathcal{L} := -(\lambda + \mu)\nabla\nabla \cdot -\mu\nabla \cdot \nabla \quad (1)$$

in terms of the Nabla operator ∇ and Lamé's constants λ, μ the initial boundary value problem for some linear elastic solid occupying the domain $\Omega \subset \mathbb{R}^3$ with its boundary $\Gamma = \partial\Omega$ reads as

$$\begin{aligned} (\mathcal{L}\mathbf{u})(\tilde{\mathbf{x}}; t) + \varrho \frac{\partial^2}{\partial t^2} \mathbf{u}(\tilde{\mathbf{x}}; t) &= \mathbf{b}(\tilde{\mathbf{x}}; t) & (\tilde{\mathbf{x}}; t) \in \Omega \times (0, \infty) \\ \mathbf{u}_\Gamma(\mathbf{y}; t) &= \mathbf{g}_D(\mathbf{y}; t) & (\mathbf{y}; t) \in \Gamma_D \times (0, \infty) \\ \mathbf{t}(\mathbf{y}; t) &= \mathbf{g}_N(\mathbf{y}; t) & (\mathbf{y}; t) \in \Gamma_N \times (0, \infty). \end{aligned} \quad (2)$$

In (2), the unknown displacement field $\mathbf{u}(\tilde{\mathbf{x}}; t)$ depends on the location $\tilde{\mathbf{x}} \in \Omega$ and the time $t \in (0, \infty)$. Furthermore, \mathbf{u}_Γ and \mathbf{t} are the boundary displacements and tractions for which the

Dirichlet data and Neumann data, \mathbf{g}_D and \mathbf{g}_N are prescribed on the boundary parts Γ_D and Γ_N , respectively. The body's mass density is denoted by ϱ and $\mathbf{b}(\tilde{\mathbf{x}}; t)$ is a given body force per unit volume. For simplicity this body force is assumed to be absent in the following. Finally, homogeneous initial conditions are considered, i.e., $\mathbf{u}(\tilde{\mathbf{x}}; 0) = \mathbf{0}$ and $\frac{\partial}{\partial t}\mathbf{u}(\tilde{\mathbf{x}}; 0) = \mathbf{0}$ for all $\tilde{\mathbf{x}} \in \Omega$.

Boundary integral equations. To obtain a boundary element formulation of the stated problem, first, an appropriate boundary integral representation of the given system (2) is introduced [1]

$$\begin{aligned} \mathbf{u}(\tilde{\mathbf{x}}; t) &= \int_0^t \int_{\Gamma} \mathbf{U}(\mathbf{y} - \tilde{\mathbf{x}}; t - \tau) \cdot (\mathcal{T}_{\mathbf{y}}\mathbf{u})(\mathbf{y}; \tau) \, d\mathbf{s}_{\mathbf{y}} \, d\tau \\ &\quad - \int_0^t \int_{\Gamma} [(\mathcal{T}_{\mathbf{y}}\mathbf{U})(\mathbf{y} - \tilde{\mathbf{x}}; t - \tau)]^{\top} \cdot \mathbf{u}(\mathbf{y}; \tau) \, d\mathbf{s}_{\mathbf{y}} \, d\tau \quad \forall \tilde{\mathbf{x}} \in \Omega, \mathbf{y} \in \Gamma, t \in (0, T) \end{aligned} \quad (3)$$

containing the fundamental solution $\mathbf{U}(\mathbf{y} - \tilde{\mathbf{x}}; t - \tau)$. In (3), $\mathcal{T}_{\mathbf{y}} = \mathcal{T}(\partial_{\mathbf{y}}, \mathbf{n}(\mathbf{y}))$ denotes the stress operator based on Hooke's law

$$(\mathcal{T}_{\mathbf{y}}\mathbf{u})(\mathbf{y}; t) = \mathbf{t}(\mathbf{y}; t) = \boldsymbol{\sigma}(\mathbf{y}; t) \cdot \mathbf{n}(\mathbf{y}) \quad (4)$$

where $\boldsymbol{\sigma}(\mathbf{y}; t)$ is the Cauchy stress tensor and $\mathbf{n}(\mathbf{y})$ is the outward normal vector. The first boundary integral equation is obtained by applying a limiting process $\Omega \ni \tilde{\mathbf{x}} \rightarrow \mathbf{x} \in \Gamma$ onto the representation formula (3). Using operator notation, this boundary integral equation reads for a sufficiently smooth boundary Γ

$$(\mathcal{V} * \mathbf{t})(\mathbf{x}; t) = ((\frac{1}{2}\mathcal{I} + \mathcal{K}) * \mathbf{u})(\mathbf{x}; t) \quad \forall \mathbf{x} \in \Gamma. \quad (5)$$

The introduced operators are the single layer operator \mathcal{V} , the identity operator \mathcal{I} , and the double layer operator \mathcal{K} which are defined by

$$(\mathcal{V} * \mathbf{t})(\mathbf{x}, t) = \int_0^t \int_{\Gamma} \mathbf{U}(\mathbf{y} - \mathbf{x}, t - \tau) \cdot \mathbf{t}(\mathbf{y}, \tau) \, d\mathbf{s}_{\mathbf{y}} \, d\tau \quad (6a)$$

$$(\mathcal{I} * \mathbf{u})(\mathbf{x}, t) = \int_0^t \int_{\Gamma} \delta(\mathbf{y} - \mathbf{x}; t - \tau) \mathbf{I} \cdot \mathbf{u}(\mathbf{y}; \tau) \, d\mathbf{s}_{\mathbf{y}} \, d\tau \quad (6b)$$

$$(\mathcal{K} * \mathbf{u})(\mathbf{x}, t) = \lim_{\varepsilon \rightarrow 0} \int_0^t \int_{\Gamma \setminus B_{\varepsilon}(\mathbf{x})} (\mathcal{T}_{\mathbf{y}}\mathbf{U})^{\top}(\mathbf{y} - \mathbf{x}, t - \tau) \cdot \mathbf{u}(\mathbf{y}, \tau) \, d\mathbf{s}_{\mathbf{y}} \, d\tau. \quad (6c)$$

In these expressions, $B_{\varepsilon}(\mathbf{x})$ denotes a ball of radius ε centered at the point \mathbf{x} . Note that the single layer operator (6a) involves a weakly singular integral and that the integration of the double layer operator (6c) has to be understood in the sense of a Cauchy principal value. Moreover, in the definition (6b) \mathbf{I} denotes the identity matrix, and δ is the Delta-distribution. To obtain a symmetric formulation, additionally the second boundary integral formula is needed. The application of the traction operator $\mathcal{T}_{\mathbf{x}}$ to the dynamic representation formula (3) with a subsequent limit $\Omega \ni \tilde{\mathbf{x}} \rightarrow \mathbf{x} \in \Gamma$ yields

$$(\mathcal{D} * \mathbf{u})(\mathbf{x}, t) = ((\frac{1}{2}\mathcal{I} - \mathcal{K}') * \mathbf{t})(\mathbf{x}, t) \quad \forall \mathbf{x} \in \Gamma. \quad (7)$$

The newly introduced operators are the hypersingular operator \mathcal{D} and the adjoint double layer operator \mathcal{K}'

$$(\mathcal{D} * \mathbf{u})(\mathbf{x}, t) = -\lim_{\varepsilon \rightarrow 0} \int_0^t \mathcal{T}_{\mathbf{x}} \int_{\Gamma \setminus B_{\varepsilon}(\mathbf{x})} (\mathcal{T}_{\mathbf{y}}\mathbf{U})^{\top}(\mathbf{y} - \mathbf{x}, t - \tau) \cdot \mathbf{u}(\mathbf{y}, \tau) \, d\mathbf{s}_{\mathbf{y}} \, d\tau \quad (8a)$$

$$(\mathcal{K}' * \mathbf{t})(\mathbf{x}, t) = \lim_{\varepsilon \rightarrow 0} \int_0^t \int_{\Gamma \setminus B_{\varepsilon}(\mathbf{x})} (\mathcal{T}_{\mathbf{x}}\mathbf{U})(\mathbf{y} - \mathbf{x}, t - \tau) \cdot \mathbf{t}(\mathbf{y}, \tau) \, d\mathbf{s}_{\mathbf{y}} \, d\tau. \quad (8b)$$

The application of the hypersingular operator has to be understood in the sense of a finite part.

Symmetric formulation. For the solution of the initial boundary value problem (2) the symmetric formulation as proposed in [3, 11] using both boundary integral equations (5) and (7) is considered. While the first integral equation (5) is used only on the Dirichlet part Γ_D of the boundary the second one (7) is evaluated on the Neumann part Γ_N

$$\begin{aligned} (\mathcal{V} * \mathbf{t})(\mathbf{x}; t) - (\mathcal{K} * \mathbf{u})(\mathbf{x}; t) &= (\frac{1}{2}\mathcal{I} * \mathbf{g}_D)(\mathbf{x}; t) & (\mathbf{x}, t) \in \Gamma_D \times (0, \infty) \\ (\mathcal{K}' * \mathbf{t})(\mathbf{x}; t) + (\mathcal{D} * \mathbf{u})(\mathbf{x}; t) &= (\frac{1}{2}\mathcal{I} * \mathbf{g}_N)(\mathbf{x}; t) & (\mathbf{x}, t) \in \Gamma_N \times (0, \infty). \end{aligned} \quad (9)$$

Further, the Cauchy data \mathbf{u}, \mathbf{t} are decomposed into

$$\mathbf{u} = \tilde{\mathbf{u}} + \tilde{\mathbf{g}}_D \quad \text{and} \quad \mathbf{t} = \tilde{\mathbf{t}} + \tilde{\mathbf{g}}_N. \quad (10)$$

In these decompositions, arbitrary but fixed extensions, $\tilde{\mathbf{g}}_D$ and $\tilde{\mathbf{g}}_N$, of the given Dirichlet and Neumann data, \mathbf{g}_D and \mathbf{g}_N , are introduced such that

$$\begin{aligned} \tilde{\mathbf{g}}_D(\mathbf{x}; t) &= \mathbf{g}_D(\mathbf{x}; t) & (\mathbf{x}, t) \in \Gamma_D \times (0, \infty) \\ \tilde{\mathbf{g}}_N(\mathbf{x}; t) &= \mathbf{g}_N(\mathbf{x}; t) & (\mathbf{x}, t) \in \Gamma_N \times (0, \infty) \end{aligned} \quad (11)$$

holds. Note that the extension $\tilde{\mathbf{g}}_D$ of the given Dirichlet datum has to be continuous due to regularity requirements [12].

Inserting the decompositions (10) into (9) leads to the symmetric formulation for the unknown Cauchy data $\tilde{\mathbf{u}}, \tilde{\mathbf{t}}$

$$\begin{aligned} \mathcal{V} * \tilde{\mathbf{t}} - \mathcal{K} * \tilde{\mathbf{u}} &= (\frac{1}{2}\mathcal{I} + \mathcal{K}) * \tilde{\mathbf{g}}_D - \mathcal{V} * \tilde{\mathbf{g}}_N & (\mathbf{x}, t) \in \Gamma_D \times (0, \infty) \\ \mathcal{K}' * \tilde{\mathbf{t}} + \mathcal{D} * \tilde{\mathbf{u}} &= (\frac{1}{2}\mathcal{I} - \mathcal{K}') * \tilde{\mathbf{g}}_N - \mathcal{D} * \tilde{\mathbf{g}}_D & (\mathbf{x}, t) \in \Gamma_N \times (0, \infty). \end{aligned} \quad (12)$$

Variational principles. Using the inner product $\langle f, g \rangle_\Gamma = \int_\Gamma f(\mathbf{x})g(\mathbf{x}) d\mathbf{s}_x$ a variational formulation is introduced to find $\tilde{\mathbf{u}}$ and $\tilde{\mathbf{t}}$ such that

$$\begin{aligned} \langle \mathcal{V} * \tilde{\mathbf{t}}, \mathbf{w} \rangle_{\Gamma_D} - \langle \mathcal{K} * \tilde{\mathbf{u}}, \mathbf{w} \rangle_{\Gamma_D} &= \langle (\frac{1}{2}\mathcal{I} + \mathcal{K}) * \tilde{\mathbf{g}}_D - \mathcal{V} * \tilde{\mathbf{g}}_N, \mathbf{w} \rangle_{\Gamma_D} \\ \langle \mathcal{K}' * \tilde{\mathbf{t}}, \mathbf{v} \rangle_{\Gamma_N} + \langle \mathcal{D} * \tilde{\mathbf{u}}, \mathbf{v} \rangle_{\Gamma_N} &= \langle (\frac{1}{2}\mathcal{I} - \mathcal{K}') * \tilde{\mathbf{g}}_N - \mathcal{D} * \tilde{\mathbf{g}}_D, \mathbf{v} \rangle_{\Gamma_N} \end{aligned} \quad (13)$$

holds for all test functions $\mathbf{w}(\mathbf{x})$ and $\mathbf{v}(\mathbf{x})$. Note, as this Galerkin scheme is used only for the spatial integrations the test functions $\mathbf{w}(\mathbf{x})$ and $\mathbf{v}(\mathbf{x})$ exhibit no time dependency.

Temporal discretization. The time discretization of (13) can be done in several ways. Here, the Convolution Quadrature Method (CQM) developed by Lubich [8] is chosen. Thereby, the time convolution integrals of the form

$$y(t) = f * g = \int_0^t f(t - \tau)g(\tau) d\tau. \quad (14)$$

are approximated by a quadrature rule which forms a discrete convolution

$$y_m = y(m \Delta t) \approx \sum_{k=0}^m \omega_{m-k}(\hat{f}, \Delta t)g(k \Delta t). \quad (15)$$

In (15), the quadrature weights ω_{m-k} depend only on the time step size Δt and the Laplace transform \hat{f} of the function f . Confer to [10] for more details about the application of the CQM in boundary element methods.

Finally, applying this time stepping scheme to (13) yields a semi-discrete variational form

$$\sum_{k=0}^m \left[\langle \hat{\mathcal{V}}_{m-k} \tilde{\mathbf{t}}_k, \mathbf{w} \rangle_{\Gamma_D} - \langle \hat{\mathcal{K}}_{m-k} \tilde{\mathbf{u}}_k, \mathbf{w} \rangle_{\Gamma_D} \right] = \sum_{k=0}^m \left[\langle (\frac{1}{2}\hat{\mathcal{I}} + \hat{\mathcal{K}})_{m-k} \tilde{\mathbf{g}}_{D_k}, \mathbf{w} \rangle_{\Gamma_D} - \langle (\frac{1}{2}\hat{\mathcal{I}} - \hat{\mathcal{K}}')_{m-k} \tilde{\mathbf{g}}_{N_k}, \mathbf{w} \rangle_{\Gamma_N} \right] \quad (16)$$

where $(\cdot)_{m-k}$ denotes the weight $\omega_{m-k}(\cdot, \Delta t)$ depending on the respective Laplace transformed integral operator.

A Boundary Element formulation for semi-infinite domains

The typical problem statement for an elastodynamic halfspace where the domain $\Omega = \{\tilde{\mathbf{x}} \mid \tilde{\mathbf{x}} \in \mathbb{R}^3 \wedge \tilde{x}_3 < 0\}$ as well as the boundary $\Gamma = \{\mathbf{y} \mid \mathbf{y} \in \mathbb{R}^3 \wedge y_3 = 0\}$ are unbounded reads as

$$\begin{aligned} ((\mathcal{L} + \varrho \frac{\partial^2}{\partial t^2})\mathbf{u})(\tilde{\mathbf{x}}; t) &= \mathbf{0} & (\tilde{\mathbf{x}}, t) \in \Omega \times (0, \infty) \\ \mathbf{t}(\mathbf{y}; t) &= \mathbf{g}(\mathbf{y}; t) & (\mathbf{y}, t) \in \Gamma \times (0, \infty) \end{aligned} \quad (17)$$

with homogeneous initial conditions $\mathbf{u}(\tilde{\mathbf{x}}; 0) = \mathbf{0}$ and $\frac{\partial}{\partial t}\mathbf{u}(\tilde{\mathbf{x}}; 0) = \mathbf{0}$ ensuring that the solution of (17) fulfill the Sommerfeld radiation condition [5].

Since $\Gamma_D = \{\emptyset\}$ and $\Gamma_N = \Gamma$ the semi-discrete variational form (16) reduces to

$$\sum_{k=0}^m \langle \hat{\mathcal{D}}_{m-k} \tilde{\mathbf{u}}_k, \mathbf{v} \rangle_{\Gamma} = \sum_{k=0}^m \langle (\frac{1}{2}\hat{\mathcal{I}} - \hat{\mathcal{K}}')_{m-k} \mathbf{g}_k, \mathbf{v} \rangle_{\Gamma} \quad (18)$$

which is an appropriate Galerkin formulation of (17) in terms of boundary integral equations.

Regularization of the hypersingular operator. Concerning the numerical evaluation of the bilinear form in (18) the involved hypersingularity makes a direct evaluation rather impossible. Therefore, a regularization based on Stokes theorem is used to transfer the hypersingular bilinear form to a weak one. This regularization is given in detail in [7] and based itself mainly on the work of Han [6]. Additionally, the double layer potential is also transferred to a weak form using the same techniques as for the hypersingular bilinear form.

Within this work it is sufficient to mention that the regularization process demands either a closed boundary surface Γ or vanishing integral kernels at infinity. Since the involved kernels fulfill the Sommerfeld radiation condition the last constraint is satisfied and the regularization holds also for the elastodynamic halfspace.

Nevertheless, problems might occur on a discrete level. There, it is a common practice to model just a truncated part of the infinite geometry. Unfortunately, the emerging truncation's borderline represents the surface's boundary such that Γ is neither closed anymore nor that the integral kernels can be assumed to vanish. Therefore, it must be ensured that the discretized area is closed or modelling the infinite surface.

Spatial discretization. Figure 1(a) illustrates the discretization approach of an unbounded domain. Thereby, the boundary Γ is represented in the computation by an approximation Γ_h which is the union of two sets of different geometrical elements

$$\Gamma_h = \bigcup_{\ell=0}^{N_e^f} \tau_{\ell}^f \cup \bigcup_{m=0}^{N_e^i} \tau_m^i. \quad (19)$$

In (19), τ^f denotes standard linear finite elements, e.g., surface triangles, and N_e^f is their total number. Additionally, the boundary's far-field is represented by N_e^i infinite boundary elements τ^i whose configuration is depicted in Fig. 1(b). For the concept of infinite elements refer to [2] and the references cited there.

Further, the boundary functions $\tilde{\mathbf{u}}$ and \mathbf{g} are approximated by the separation of variables with trial functions φ_i and ψ_j , which are defined with respect to the geometry partitioning (19), and time dependent coefficients \mathbf{u}_i and \mathbf{g}_j

$$\tilde{\mathbf{u}}(\mathbf{x}) \approx \sum_{i=1}^N \mathbf{u}_i(t) \varphi_i(\mathbf{x}) \quad \text{and} \quad \mathbf{g}(\mathbf{x}) \approx \sum_{j=1}^M \mathbf{g}_j(t) \psi_j(\mathbf{x}). \quad (20)$$

In case of finite boundary elements the functions φ_i are chosen to be equivalent to those shape functions forming the geometry approximation.

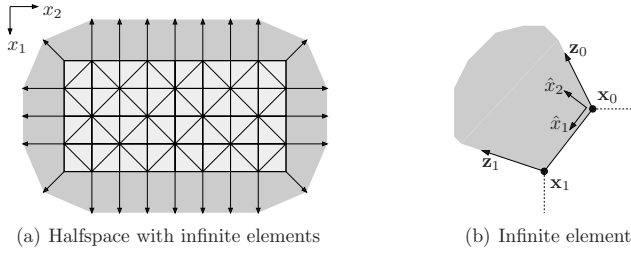


Figure 1: Discretized halfspace and infinite mapping

By introducing local coordinates $\hat{\mathbf{x}} = [\hat{x}_1, \hat{x}_2]^\top \in [0, 1] \times [0, 1]$ the mapping $\chi_\tau : \hat{\tau} \rightarrow \tau$ from the reference element $\hat{\tau}$ to an infinite element τ reads as

$$\mathbf{x} = \chi_\tau(\hat{\mathbf{x}}) = \langle \phi(\hat{x}_1), \begin{bmatrix} \mathbf{x}_0 \\ \mathbf{x}_1 \end{bmatrix} \rangle + \frac{\hat{x}_2}{1 - \hat{x}_2} \langle \phi(\hat{x}_1), \alpha \begin{bmatrix} \mathbf{z}_0 \\ \mathbf{z}_1 \end{bmatrix} \rangle \quad (21)$$

where \mathbf{x}_0 and \mathbf{x}_1 denote the two fixed vertex nodes, and \mathbf{z}_0 and \mathbf{z}_1 represent two direction vectors with the property $\langle \mathbf{z}_k, \mathbf{z}_k \rangle = 1$. The scalar value $\alpha > 0$ is a scaling factor. The function ϕ within the dot product $\langle \cdot, \cdot \rangle$ describes the approximation for the finite extent and is given by $\phi(\hat{x}_1) = [1 - \hat{x}_1, \hat{x}_1]^\top$.

Since the integral kernels depend mostly on the distance $r = |\mathbf{y} - \mathbf{x}|$ between two points \mathbf{y} and \mathbf{x} it is preferable to note that for infinite elements the asymptotic behavior of the distance is of order $\mathcal{O}((1 - \hat{x}_2)^{-1})$. Moreover, the transformation of the integral kernels to the reference element demands the computation of the Gram determinant which itself can be expressed via the Jacobi matrix

$$\mathbf{J}_{\tau^i}(\hat{\mathbf{x}}) = \begin{bmatrix} \frac{\partial \mathbf{x}}{\partial \hat{x}_1} & \frac{\partial \mathbf{x}}{\partial \hat{x}_2} \end{bmatrix} =: [\mathbf{J}_1 \quad \mathbf{J}_2] = [\mathcal{O}(r) \quad \mathcal{O}(r^2)] \quad (22)$$

and reads as

$$g_{\tau^i}(\hat{\mathbf{x}}) = \sqrt{\det(\mathbf{J}_{\tau^i}^\top \mathbf{J}_{\tau^i})} = \sqrt{\langle \mathbf{J}_1, \mathbf{J}_1 \rangle \langle \mathbf{J}_2, \mathbf{J}_2 \rangle - \langle \mathbf{J}_1, \mathbf{J}_2 \rangle^2} = \mathcal{O}(r^3). \quad (23)$$

For some kernel function $k(\mathbf{x}(\hat{\mathbf{x}}), \mathbf{y}(\hat{\mathbf{y}})) = \mathcal{O}(r^{-1})$ the integrand in a Galerkin scheme takes the form

$$I[\ell, m] = \int_{\tau_\ell} \int_{\tau_m} g_{\tau_\ell}(\hat{\mathbf{x}}) g_{\tau_m}(\hat{\mathbf{y}}) k(\mathbf{x}(\hat{\mathbf{x}}), \mathbf{y}(\hat{\mathbf{y}})) \hat{\varphi}_\ell(\hat{\mathbf{x}}) \hat{\varphi}_m(\hat{\mathbf{y}}) d\hat{\mathbf{x}} d\hat{\mathbf{y}}. \quad (24)$$

From (24), it is obvious that the trial function for an infinite element has to be of order $\mathcal{O}(r^{-3})$ to guarantee that the integral is finite. Therefore, the trial and test functions φ_i of an infinite element are chosen as

$$\varphi_i(\mathbf{x}) \circ \hat{\varphi}(\hat{\mathbf{x}}) = \phi(\hat{x}_1)(1 - \hat{x}_2)^3 \quad (25)$$

where $\phi(\hat{x}_1)$ is identical to the function used for the geometry approximation (21).

Finally, a comment concerning the singular integrals must be made. All integral operators used in the present work are weakly singular. They are treated completely numerical based on quadrature rules developed by Sauter and Erichsen [4].

Numerical examples

Now, numerical results for the present Boundary Element formulation are given. The material data represents soil with Lamé's constants $\lambda = \mu = 1.3627 \cdot 10^8 \text{ N/m}^2$, and mass density $\rho = 1884 \text{ kg/m}^3$. The discretization of the infinite domain consists of 800 regular linear triangles and 80 infinite elements with a scaling factor of $\alpha = 1$. The triangles occupy a total area of $20\text{m} \times 20\text{m}$. Moreover, at the mesh's center an area of $A = 2\text{m}^2$ is excited by a traction jump $\mathbf{g} = [0, 0, -1]^\top H(t) \text{ N/m}^2$ according to the unit step function $H(t)$. The remaining surface is traction free.

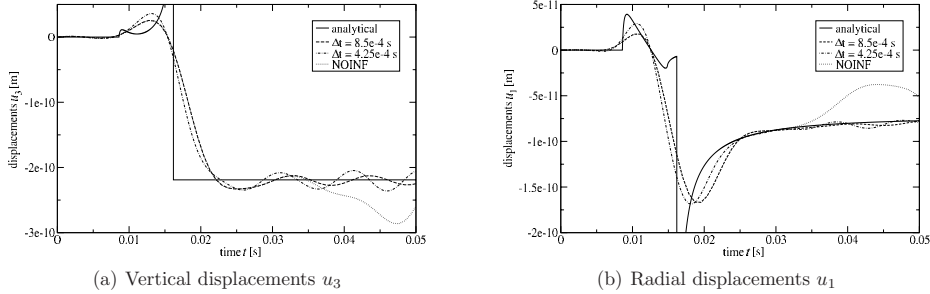


Figure 2: Vertical and radial displacements at the observation point \mathbf{x}^*

Figure 2 depicts the solution for an observation point \mathbf{x}^* on the surface in 4m distance to the center of the loading. The first and the second numerical solution vary in the chosen time step size but reveal in general the same behavior. Compared to the analytical solution [9] both displacement solutions exhibit oscillations for larger times which are due to artificial reflections at the crossing of finite and infinite boundary elements. But beside these effects, both numerical solutions show approximately the characteristics of the analytical solution. Contrary, a computation without infinite elements titled as 'NOINF' but with the same time step size as the first depicted numerical solution namely $\Delta t = 8.5 \cdot 10^{-4} \text{ s}$ yields a defective result for times larger than 0.034s. This is exactly the time the compression wave with the velocity $c_1 = \sqrt{\lambda+2\mu/\rho} = 465.8 \text{ m/s}$ has to travel from the center of loading to the truncated boundary and back to the observation point \mathbf{x}^* . From this it can be stated that the infinite element approach for the treatment of semi-infinite domains by symmetric Boundary Element Methods is expedient but requires further research.

Conclusions

A boundary element method for elastodynamics based on a Galerkin discretization in space and on the Convolution Quadrature Method in time was presented. To obtain a symmetric formulation, also the usage of the second boundary integral equation is required which demands the computation of hypersingular kernel functions. Therefore, a regularization of the elastodynamic hypersingular integral operator is used leading to a weakly singular bilinear form. Since the regularization is based on integration by parts it is not suitable for treating problems where the mesh of a halfspace is truncated.

To overcome this drawback the concept of infinite elements was used and adopted to the present boundary element formulation. Unfortunately, the numerical results obtained so far are not completely satisfactory since they feature oscillations for larger times. To reduce these oscillations or, better, to eliminate them further investigations are essential. Nevertheless, the infinite element approach is advantageous compared to computations without any infinite elements as it reaches the static limit for larger times.

References

- [1] J.D. Achenbach. *Wave propagation in elastic solids*. North-Holland, 2005.
- [2] P. Betti. *Infinite Elements*. Penshaw Press, 1992.
- [3] M. Costabel and E. P. Stephan. Integral equations for transmission problems in linear elasticity. *Journal of Integral Equations and Applications*, 2:211–223, 1990.
- [4] S. Erichsen and S. A. Sauter. Efficient automatic quadrature in 3-d Galerkin BEM. *Computer Methods in Applied Mechanics and Engineering*, 157:215–224, 1998.
- [5] D. Givoli. *Numerical Methods for Problems in Infinite Domains*, volume 33 of *Studies in applied mechanics*. Elsevier, 1992.
- [6] H. Han. The boundary integro-differential equations of three-dimensional Neumann problem in linear elasticity. *Numerische Mathematik*, 68:269–281, 1994.
- [7] L. Kielhorn and M. Schanz. Convolution Quadrature Method based symmetric Galerkin Boundary Element Method for 3-d elastodynamics. *International Journal for Numerical Methods in Engineering*, 2008. (accepted).
- [8] C. Lubich. Convolution quadrature and discretized operational calculus I & II. *Numerische Mathematik*, 52:129–145 & 413–425, 1988.
- [9] C. L. Pekeris. The seismic surface pulse. *Proceedings of the National Academy of Sciences of the United States of America*, 41:469–480, 1955.
- [10] M. Schanz. *Wave Propagation in Viscoelastic and Poroelastic Continua: A Boundary Element Approach*, volume 2 of *Lecture Notes in Applied Mechanics*. Springer-Verlag Berlin Heidelberg, 2001.
- [11] S. Sirtori. General stress analysis method by means of integral equations and boundary elements. *Meccanica*, 14:210–218, 1979.
- [12] O. Steinbach. *Numerical Approximation Methods for Elliptic Boundary Value Problems*. Springer, 2008.

An efficient method for boundary element analysis of thermoelastic problems without domain discretization

R. Fazeli^{1,a} and M. R. Hematiyan^{1,b}

¹Department of Mechanical Engineering, Shiraz University, Shiraz, Iran

^ae-mail: fazelirazieh@gmail.com, ^be-mail: mhemat@shirazu.ac.ir

Keywords: boundary element method, thermoelasticity, temperature rise, boundary integrals.

Abstract. In thermoelastic problems with a non-uniform temperature rise, a domain integral appears in the boundary element formulation of the problem. To save the main advantage of boundary element method as a boundary-only technique, a method is presented to solve thermoelastic problems without domain discretization.

Temperature rise function is approximated by a function with an arbitrary distribution in a Cartesian direction and a piecewise quadratic variation in the other Cartesian direction. The domain integrals in 2D displacement and stress integral equations of thermoelasticity are then exactly transformed into boundary by Cartesian transformation method. Two 2D thermoelastic examples are presented to show the efficiency of the proposed method.

Introduction

To solve engineering problems by boundary element method (BEM), it is sufficient to discretize only the boundary of the problem. This is the main attractiveness of BEM in comparison with finite element method (FEM). High accuracy of BEM as a semi-analytic method is another characteristic of the method. On the other hand, presence of body forces in elastic problems or temperature rise in thermoelastic problems produce some domain integrals in the displacement and stress integral equations. Evaluating the mentioned domain integrals by boundary-only discretization is an important task in BEM. Various techniques have been developed for this purpose. Danson presented an approach for gravitational, centrifugal and thermoelastic forces based on the Galerkin vector and Gauss-Green theorem [1]. A different approach was presented by Henry and Banerjee based on using a particular-integral approach [2]. A simple and effective technique, called Radial Integration Method (RIM), was developed by Gao [3, 4]. This method is based on mathematical operations. It can evaluate any domain integral with boundary-only discretization.

Recently, a method for exact transformation of a wide variety of BEM domain integrals into boundary has been presented by Hematiyan [5, 6]. In this method, domain integrals are transformed into boundary integrals simply by Green's theorem in Cartesian coordinates system. It has been successfully employed for potential and elastostatic problems [5] and also for thermoelastic problems [6]. For very complicated cases where, the domain integral cannot be exactly transformed into the boundary, the integral can be evaluated by a meshless adaptive method [7]. The general form of the methods presented in [5-7] is called Cartesian Transformation Method [8].

In this paper, the displacement integral equation of thermoelasticity is employed to develop a new form of stress integral equation of thermoelasticity. The temperature rise function is approximated by a function with an arbitrary variation in one Cartesian direction and Piecewise-quadratic variation in the other direction. By this form of temperature rise function, it is possible to transform exactly all domain integrals into boundary integrals in both displacement and stress integral equations. The mentioned approximation for temperature rise function is accurate enough and unlike approximation methods with radial basis functions, it can be carried out with no need of system solving and therefore it is faster.

Integral equations of thermoelasticity

Temperature distribution over an isotropic material can cause a volumetric expansion. The relationship between the total strain ε_{ij} and the stress σ_{ij} in thermoelasticity can be expressed as

$$\varepsilon_{ij} = \frac{1}{2G} \{ \sigma_{ij} - \frac{\nu}{1+\nu} \delta_{ij} \sigma_{kk} \} + \delta_{ij} \alpha \theta \quad (1)$$

where, G is shear modulus, ν is Poisson's ratio, θ is temperature rise function and α is coefficient of linear thermal expansion. The first term in the right hand side of Eq. 1 represents the strain produced by actual stress, while the second term represents the thermal expansion effect. The stress-strain relation can be expressed as

$$\sigma_{ij} = 2G \{ \varepsilon_{ij} + \frac{\nu}{1-2\nu} \delta_{ij} \varepsilon_{kk} \} - \frac{2G(1+\nu)}{1-2\nu} \alpha \delta_{ij} \theta \quad (2)$$

The displacement integral equation of thermoelasticity for an isotropic material can be expressed as [9]

$$C_{ij}(\mathbf{x}) u_j(\mathbf{x}) + \int_S T_{ij}(\mathbf{x}, \mathbf{y}) u_j(\mathbf{y}) dS = \int_S U_{ij}(\mathbf{x}, \mathbf{y}) t_j(\mathbf{y}) dS + \tilde{k} \int_V U_{ik,k}(\mathbf{x}, \mathbf{z}) \theta(\mathbf{x}) dV \quad (3)$$

where,

$$\tilde{k} = \frac{2G(1+\nu)}{1-2\nu} \alpha \quad (4)$$

S and V in Eq. 3 represent the boundary and the domain of the problem respectively. $C_{ij} = 0.5\delta_{ij}$ for smooth boundaries and $C_{ij} = \delta_{ij}$ for internal points. \mathbf{x} , \mathbf{z} and \mathbf{y} are respectively source point, field point and boundary point. U_{ij} and T_{ij} are 2D fundamental solutions and are expressed as follow [9]:

$$U_{ij} = \frac{1+\nu}{8\pi G(1-\nu)} \{ -(3-4\nu) \delta_{ij} \ln r + r_i r_j \} \quad (5)$$

$$T_{ij} = \frac{-1}{4\pi(1-\nu)r} \left\{ \frac{\partial r}{\partial n} [(1-2\nu)\delta_{ij} + 2r_i r_j] + (1-2\nu)(n_i r_j - n_j r_i) \right\} \quad (6)$$

where $r_i = z_i - x_i$.

Differentiating Eq. 5 with respect to z_j yields

$$U_{ij,j} = \frac{-(1-2\nu)}{4\pi(1-\nu)G} \frac{r_j}{r} \quad (7)$$

The following relations are employed to derive Eq. 7:

$$\frac{\partial r}{\partial n} = r_j n_i, \quad r_j r_i = 1, \quad r_{jj} = \frac{1}{r} (\delta_{jj} - r_j r_{jj}), \quad \frac{\partial f(r)}{\partial x_j} = \frac{\partial f(r)}{\partial r} \frac{\partial r}{\partial x_j} = \frac{\partial f(r)}{\partial r} r_{jj}$$

Substituting Eq. 7 in Eq. 3, results in:

$$C_{ij}(\mathbf{x}) u_j(\mathbf{x}) = \int_S (U_{ij}(\mathbf{x}, \mathbf{y}) t_j(\mathbf{y}) - T_{ij}(\mathbf{x}, \mathbf{y}) u_j(\mathbf{y})) dS + \int_V \Psi_i \theta(\mathbf{x}) dV \quad (8)$$

where

$$\Psi_i = \frac{-(1+\nu)k}{2\pi(1-\nu)} \frac{r_i}{r} \quad (9)$$

Displacement for an internal point can be calculated by considering $C_{ij} = \delta_{ij}$ in Eq. 8. By using Eq. 2 and the relation between strain and displacement $\varepsilon_{ij} = (u_{i,j} + u_{j,i})/2$, the stress equation for an internal point p can be expressed as follows:

$$\sigma_{ij}(p) = \frac{2G\nu}{1-2\nu} \delta_{ij} \frac{\partial u_m}{\partial x_m^p} + G \left(\frac{\partial u_i}{\partial x_j^p} + \frac{\partial u_j}{\partial x_i^p} \right) - \frac{2G(1+\nu)\alpha}{1-2\nu} \delta_{ij} \theta(p) \quad (10)$$

As it can be seen, in order to establish stress integral equation, derivatives of Eq. 8 must be found. The derivatives of displacement component at an internal point can be expressed as follows:

$$\frac{\partial u_i}{\partial x_j^p} = \int_S \left(\frac{\partial U_{ik}}{\partial x_j^p} t_k - \frac{\partial T_{ik}}{\partial x_j^p} u_k \right) dS + \frac{\partial}{\partial x_j^p} \int_V \Psi_i \theta dV \quad (11)$$

In which V_δ is an infinitesimal circle with radius δ around the singular point. After some mathematical and geometrical manipulations, one can show:

$$\frac{\partial}{\partial x_j^p} \int_{V_\delta} \Psi_i \theta dV = \int_{V_\delta} \frac{\partial \Psi_i}{\partial x_j^p} \theta dV - \theta \int_{S_\delta} \Psi_i n_j dS \quad (12)$$

Substituting $r = \delta$, $n_j = -r_j$ and $\frac{\partial(\cdot)}{\partial x_i} = -\frac{\partial(\cdot)}{\partial z_i}$, the last boundary integral of Eq. 12 can be written as:

$$\int_{S_\delta} \Psi_i n_j dS = \frac{(1+\nu)\alpha}{2\pi(1-\nu)\varepsilon} \int_0^{2\pi} r_j r_j \varepsilon d\theta = \frac{(1+\nu)\alpha}{2(1-\nu)} \delta_{ij} \quad (13)$$

and Eq. 11 is written as follows:

$$\frac{\partial u_i}{\partial x_j^p} = \int_S \left(\frac{\partial U_{ik}}{\partial x_j^p} t_k - \frac{\partial T_{ik}}{\partial x_j^p} u_k \right) dS - \frac{(1+\nu)\alpha}{2\pi(1-\nu)} \int_{V_\delta} \frac{(\delta_{ij} - 2r_j r_{ij})}{r^2} \theta dV - \frac{(1+\nu)\alpha}{\beta(1-\nu)} \delta_{ij} \theta(p) \quad (14)$$

Finally, substituting Eq. 14 into Eq. 10, the internal stress integral equation is found as follows:

$$\sigma_{ij} = \int_S U_{ijk} t_k dS - \int_S T_{ijk} u_k dS - \frac{G(1+\nu)\alpha}{\pi(1-\nu)} \int_{V_\delta} \frac{(2r_j r_{ij} - \delta_{ij})}{r^2} \theta dV - \frac{G(1+\nu)\alpha}{(1-\nu)} \delta_{ij} \theta(p) \quad (15)$$

Transformation of domain integrals into boundary integrals by Cartesian transformation method

As it can be seen, two domain integrals appear in Eqs 8 and 15. The first one is weakly singular and the second one is strongly singular. Integrand of these integrals include the temperature rise function θ . At first, it is shown that if the temperature rise function can be expressed by a function with arbitrary variation in one Cartesian direction and quadratic variation in the other direction, one can exactly transform the domain integrals into boundary. Then, for exact transformation of a complicated temperature rise function, it is approximated by a function with arbitrary variation in one direction and piecewise quadratic in the other direction. This method of approximation is fast and accurate.

A temperature rise function with arbitrary variation in y -direction and quadratic variation in x -direction can be expressed as follows:

$$\theta = f_0(y) + f_1(y)x + f_2(y)x^2 \quad (16)$$

The domain integrals in (8) and (15) can be written in the general form of:

$$I = A \int_{V_\delta} (f_0(y) + f_1(y)x + f_2(y)x^2) h^*(\mathbf{x}) dV \quad (17)$$

in which A is a constant coefficient and $h^*(\mathbf{x})$ is a singular function. One can write:

$$I = I_0 + I_1 + I_2 \quad (18)$$

where

$$I_\alpha = \int_{V_\delta} [f_\alpha(y)x^\alpha] h^*(\mathbf{x}) dV \quad \alpha = 0, 1, 2 \quad (19)$$

The function $F_\alpha(x, y)$ is defined as follows:

$$F_\alpha(x, y) = \int [f_\alpha(y)x^\alpha] h^*(\mathbf{x}) dx = f_\alpha(y) \int x^\alpha h^*(\mathbf{x}) dx \quad (20)$$

Now, Eq. 19 can be expressed as:

$$I_\alpha = \int_{V_\delta} \frac{\partial F_\alpha(x, y)}{\partial x} dV \quad \alpha = 0, 1, 2$$

Using Green's theorem one can write:

$$I_\alpha = \int_S F_\alpha(x, y) dy - \int_{S_\delta} F_\alpha(x, y) dy \quad \alpha = 0, 1, 2 \quad (21)$$

where S is the main boundary of the problem and S_δ is boundary of an infinitesimal circular region around singular point. As seen, the domain integral in Eq. 19 was converted to two boundary

integrals in Eq. 21. Since the transformation was carried out in Cartesian coordinates system, the method is called Cartesian transformation method (CTM) [8].

The 1-D integral in Eq. 20 can be calculated analytically. The singular kernel in Eq. 8 is $h^*(\mathbf{x}) = \frac{r_i}{r^2}$.

The integral in Eq. 20 for this singular kernel and $i=1$ can be expressed as follow:

$$F_1 = \int \frac{r_i}{r^2} dx = \ln r \quad (22-a)$$

$$F_2 = \int x \frac{r_i}{r^2} dx = \xi_1 \ln r - r_2 \tan^{-1}\left(\frac{r_i}{r_2}\right) + x \quad (22-b)$$

$$F_3 = \int x^2 \frac{r_i}{r^2} dx = (\xi_1^2 - r_2^2) \ln r - 2\xi_1 r_2 \tan^{-1}\left(\frac{r_i}{r_2}\right) + \frac{1}{2} x^2 + \xi_1 x \quad (22-c)$$

and for $i=2$:

$$F_1 = \int \frac{r_2}{r^2} dx = \tan\left(\frac{r_i}{r_2}\right) \quad (23-a)$$

$$F_2 = \int x \frac{r_2}{r^2} dx = r_2 \ln r + \xi_1 \tan^{-1}\left(\frac{r_i}{r_2}\right) \quad (23-b)$$

$$F_3 = \int x^2 \frac{r_2}{r^2} dx = 2\xi_1 r_2 \ln r + (\xi_1^2 - r_2^2) \tan^{-1}\left(\frac{r_i}{r_2}\right) + r_2 x \quad (23-c)$$

where (ξ_1, ξ_2) represent coordinates of the source point.

The singular kernel in the domain integral of the stress integral equation in Eq. 15 is:

$$h^*(\mathbf{x}) = \frac{2r_i r_j - \delta_{ij}}{r^2}.$$

For $i=j=1$, one can write $h^*(\mathbf{x}) = \frac{r_1^2 - r_2^2}{r^4}$ and the corresponding integrals in Eq. 20 are expressed as follow:

$$F_1 = \int \frac{r_1^2 - r_2^2}{r^4} dx = -\frac{r_1}{r^2} \quad (24-a)$$

$$F_2 = \int x \frac{r_1^2 - r_2^2}{r^4} dx = \ln r + \frac{1}{r^2} (r_2^2 - \xi_1 r_1) \quad (24-b)$$

$$F_3 = \int x^2 \frac{r_1^2 - r_2^2}{r^4} dx = 2\xi_1 \ln r - 2r_2 \tan^{-1}\left(\frac{r_1}{r_2}\right) + \frac{1}{r^2} (2x r_2^2 + \xi_1 r_2^2 + x r_1^2 - \xi_1^2 r_1) \quad (24-c)$$

In the case of $i=j=2$, one can write $h^*(\mathbf{x}) = -\frac{r_1^2 - r_2^2}{r^4}$ and the integrals are same as Eqs 24 with a minus sign.

For $i=1, j=2$ or $i=2, j=1$, one can write $h^*(\mathbf{x}) = \frac{2r_i r_2}{r^2}$ and the integrals can be expressed as follow:

$$F_1 = \int \frac{2r_i r_2}{r^4} dx = -\frac{r_2}{r^2} \quad (25-a)$$

$$F_2 = \int x \frac{2r_i r_2}{r^4} dx = \tan^{-1}\left(\frac{r_1}{r_2}\right) - \frac{x r_2}{r^2} \quad (25-b)$$

$$F_3 = \int x^2 \frac{2r_i r_2}{r^4} dx = 2r_2 \ln r + 2\xi_1 \tan^{-1}\left(\frac{r_1}{r_2}\right) + \frac{1}{r^2} (2\xi_1 x r_2 + \xi_1^2 r_2 + r_2^3) \quad (25-c)$$

The second integral in Eq. 21 vanishes for the domain integral in the displacement integral equation.

Using Eqs 22 and 23, the Eq. 8 can be written as

$$C_{ij}(\mathbf{x}) u_j(\mathbf{x}) = \int_S U_{ij}(\mathbf{x}, \mathbf{y}) t_j(\mathbf{y}) dS - \int_S T_{ij}(\mathbf{x}, \mathbf{y}) u_j(\mathbf{y}) dS - \frac{(1+\nu)\alpha}{2\pi(1-\nu)} \int_S B_{ij}(\mathbf{x}, \mathbf{y}) dy \quad (26)$$

where

$$\begin{Bmatrix} B_1 \\ B_2 \end{Bmatrix} = \begin{cases} f_0(y) \ln r + f_1(y)(\xi_1 \ln r - r_2 \tan^{-1}(\frac{r_1}{r_2}) + x) + f_2(y)((\xi_1^2 - r_2^2) \ln r - 2\xi_1 r_2 \tan^{-1}(\frac{r_1}{r_2}) + \frac{1}{2}x^2 + \xi_1 x) \\ f_0(y) \tan(\frac{r_1}{r_2}) + f_1(y)(r_2 \ln r + \xi_1 \tan^{-1}(\frac{r_1}{r_2})) + f_2(y)(2\xi_1 r_2 \ln r + (\xi_1^2 - r_2^2) \tan^{-1}(\frac{r_1}{r_2}) + r_2 x) \end{cases} \quad (27)$$

The second integral in Eq. 21 does not vanish for the domain integral in the stress integral equation, but it can be evaluated analytically.

Using relations (24) and (25), Eq. 15 is expressed as

$$\sigma_{ij}(p) = \int_S U_{kij} t_k dS - \int_S T_{kij} u_k dS - \frac{E\alpha}{2\pi(1-\nu)} \int_S E_{ij} dy - \frac{E\alpha}{(1-\nu)} \theta(p) J_{ij} \quad (28)$$

Where

$$E_{11} = -f_0(y) \frac{r_1}{r^2} + f_1(y)(\ln r + \frac{1}{r^2}(r_2^2 - \xi_1 r_1)) + f_2(y)(2\xi_1 \ln r - 2r_2 \tan^{-1}(\frac{r_1}{r_2}) + \frac{1}{r^2}(2xr_2^2 + \xi_1 r_2^2 + xr_1^2 - \xi_1^2 r_1))$$

$$E_{22} = -E_{11}$$

$$E_{12} = E_{21} = -f_0(y) \frac{r_2}{r^2} + f_1(y)(\tan^{-1}(\frac{r_1}{r_2}) - \frac{xr_2}{r^2}) + f_2(y)(2r_2 \ln r + 2u \tan^{-1}(\frac{r_1}{r_2}) + \frac{1}{r^2}(-2uxr_2 + u^2 r_2 + r_2^3))$$

$$J_{ij} = \begin{bmatrix} 1 & 0 \\ 0 & 0 \end{bmatrix}$$

For more complicated temperature rise functions, where θ cannot be expressed in the form of Eq. 16, it is approximated by a function with an arbitrary variation in one Cartesian direction and Piecewise-quadratic function in the other direction. In this case, temperature rise function is expressed as follows:

$$\theta(\mathbf{x}) = \sum_{i=1}^m \theta^{(i)}(\mathbf{x}) \quad (29)$$

where

$$\theta^{(i)} = \begin{cases} f_0^{(i)}(y) + f_1^{(i)}(y)x + f_2^{(i)}(y)x^2 & a_{i-1} \leq x \leq a_i \\ 0 & \text{else} \end{cases}$$

and

$$f_0^{(i)}(y) = \theta(a_{i-1}, y) - a_{i-1} \frac{\theta(a_{i-1} + h_i, y) - \theta(a_{i-1}, y)}{h_i} + (a_{i-1})(a_i + h_i) \frac{\theta(a_i, y) - 2\theta(a_{i-1} + h_i, y) + \theta(a_{i-1}, y)}{2h_i^2}$$

$$f_1^{(i)}(y) = \frac{\theta(a_{i-1} + h_i, y) - \theta(a_{i-1}, y)}{h_i} - (2a_{i-1} + h_i) \frac{\theta(a_i, y) - 2\theta(a_{i-1} + h_i, y) + \theta(a_{i-1}, y)}{2h_i^2}$$

$$f_2^{(i)}(y) = \frac{\theta(a_i, y) - 2\theta(a_{i-1} + h_i, y) + \theta(a_{i-1}, y)}{2h_i^2}$$

In Eq. 29, temperature rise function is approximated by m sub-functions through the domain. This approximation is simple and fast because there is no need of system solving and considering internal points. By this approximation, all domain integrals appeared in the formulation are efficiently transformed into boundary. The geometrical description of m sub-functions is shown in Fig. 1.

The domain integral (17) can be written as follows

$$I = A \int_{V-V_\delta} (\sum_{i=1}^m \theta^{(i)}(\mathbf{x})) h^*(\mathbf{x}) dV$$

or

$$I = A \int_S (\int_{a_0}^{a_1} \theta^{(1)} h^*(\mathbf{x}) dx + \int_{a_1}^{a_2} \theta^{(2)} h^*(\mathbf{x}) dx + \dots + \int_{a_{m-1}}^{a_m} \theta^{(m)} h^*(\mathbf{x}) dx) dy - A \int_S (\int \theta h^*(\mathbf{x}) dx) dy \quad (30)$$

The inner 1-D integrals in the first integral in Eq. 30 (over S) can be evaluated analytically. The last integral in Eq. 30 (over S_δ) is zero when $h^*(\mathbf{x})$ is weakly singular (in displacement integral

equation) and it can be evaluated analytically for cases where $h^*(\mathbf{x})$ is strongly singular (in stress integral equation).

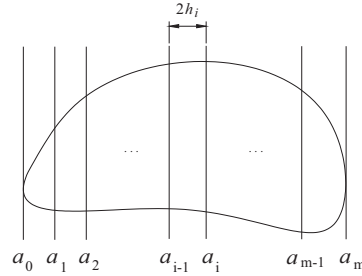


Figure 1: Approximating the temperature rise function with arbitrary variation in y direction and m quadratic function in x direction

Examples

Two examples are presented to demonstrate the validity and accuracy of the proposed method. In spite of using constant boundary elements to discretize boundary of problems, the results are very accurate. The results have been compared with the result of finite element method with fine mesh.

Example 1. A rectangular region with the boundary conditions shown in Fig. 2 is subjected to a temperature rise with the form of $\theta = (2 - x^2)(10 + 30\sin(2\pi y))$. It is analyzed under plane strain condition with $E = 210 \text{ GPa}$, $\nu = 0.3$ and $k = 11.7 \times 10^{-6} \text{ }^\circ\text{C}^{-1}$. Because of the symmetry of the geometry, boundary conditions and temperature rise function with respect to y axis, only one half of the problem is modeled. 128 constant boundary elements are used for discretization of the boundary. Since θ has a quadratic variation in x direction, the corresponding domain integrals can be exactly transformed into boundary. The obtained results along the line $x = 0.5$ are compared with results of accurate FEM. The results are shown in Fig. 3. As it can be seen, the obtained results are very good.

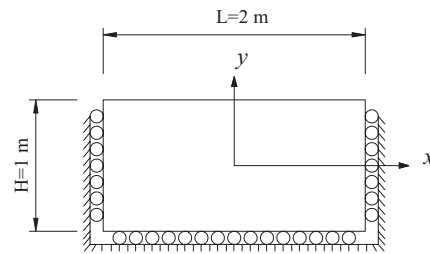


Figure 2: A rectangular domain subjected to a temperature rise (Example 1)

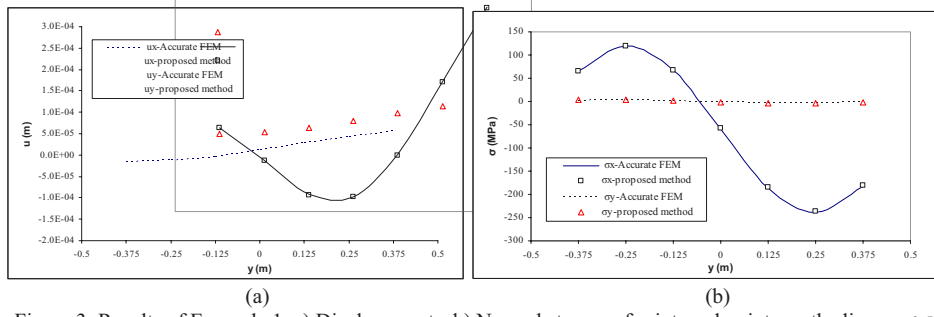


Figure 3: Results of Example 1, a) Displacements, b) Normal stresses, for internal points on the line $x = 0.5$

Example 2. A square plate with the boundary conditions shown in Fig. 4 is subjected to a temperature rise with the form of $\theta = 20\sin(100\exp(2\sqrt{(x+y)}))$. This problem is analyzed under plane stress condition with $E = 210 \text{ GPa}$, $\nu = 0.3$ and $k = 11.7 \times 10^{-6} \text{ }^{\circ}\text{C}$. Each side is divided into 16 constant boundary elements. The function θ is approximated with a number of sub-functions. Results are obtained for two different cases with 4 and 8 sub-functions. The results are shown in Tables 1 and 2 and Fig. 5. Results are more accurate when θ is approximated by 8 functions.

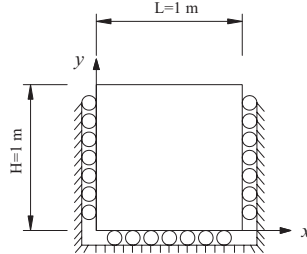


Figure 4: Geometry of a plate subjected to temperature rise (Example 2)

Table 1: Normal stress in x direction (MPa) on the line $x=0.5$

y	Accurate FEM solution	Present method 4 sub-functions		Present method 8 sub-functions	
		σ_x	σ_x	Error	σ_x
0.25	12.46	11.89	4.6 %	12.39	0.6 %
0.375	23.91	20.64	13.7 %	23.80	0.5 %
0.5	-7.63	-6.84	10.3 %	-7.61	0.3 %
0.625	-22.35	-16.92	24.3 %	-22.10	1.1 %
0.75	13.09	10.32	21.2 %	13.22	1.0 %

Table 2: Normal stress in y direction (MPa) on the line $x=0.5$

y	Accurate FEM solution	Present method 4 sub-functions		Present method 8 sub-functions	
		σ_y	σ_y	Error	σ_y
0.25	8.40	9.07	8.0 %	8.57	2.1 %
0.375	22.30	25.64	15.0 %	22.49	0.8 %
0.5	-8.60	-8.53	0.7 %	-8.53	0.7 %
0.625	-23.03	-28.51	23.8 %	-23.19	0.7 %
0.75	14.99	17.24	15.1 %	14.85	0.9 %

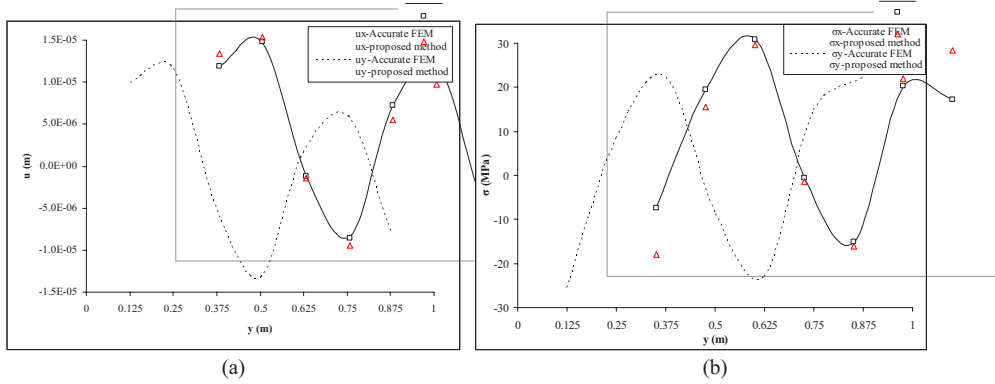


Figure 5: Results of Example 2, a) Displacement, b) Normal stresses, for internal points on the line $x=0.5$, θ is approximated by 8 sub-functions

Conclusions

An efficient boundary element formulation for analysis of thermoelastic problems with complicated temperature rise function was presented. The temperature rise function was approximated with a function with arbitrary variation in one Cartesian direction and piecewise quadratic variation in the other direction. There is no need for definition of any internal point and system solving for this approximation. After this approximation, weakly and strongly singular domain integrals in displacement and stress integral equations can be exactly transformed into boundary by Cartesian transformation method. By presenting two 2D thermoelastic examples with complicated temperature rise functions the accuracy and efficiency of the proposed method was highlighted.

References

- [1] D.J. Danson, in: Boundary Element Methods, edited by C.A. Brebbia, Springer, Berlin, 105-122 (1981).
- [2] D.P. Henry, D.A. Pape and P.K. Banerjee: Journal of the Engineering Mechanics Division (ASCE), 113, 671-688 (1987).
- [3] X.W. Gao: International Journal for Numerical Methods in Engineering, 57, 975-990 (2003).
- [4] X.W. Gao: Engineering Analysis with Boundary Elements, 26, 905-916 (2002).
- [5] M.R. Hematiyan: Communication in numerical methods in engineering, Early View (2008).
- [6] M.R. Hematiyan, in: Advances in Boundary Element Techniques VIII, edited by V. Minutolo and M.H. Aliabadi, EC, Ltd, UK, 263-268 (2007).
- [7] M.R. Hematiyan: Computational mechanics, 39 (4), 509-520 (2007).
- [8] M.R. Hematiyan: 9th International Conference on Boundary Element Techniques (BeTeq 2008).
- [9] M.H. Aliabadi: The boundary element method, Vol. 2: Applications in Solids and Structures, John Wiley & Sons (2002).
- [10] F. Paris and J. Canas: Boundary element method (fundamentals and applications), Oxford University Press Inc., New York (1997).

**Analysis of Piezoelectric active patches performances by
Boundary Element Techniques**

A. Alaimo¹, A.Milazzo², C. Orlando³

¹Dipartimento di Tecnologie ed Infrastrutture Aeronautiche, Università di Palermo, Viale delle Scienze, Edificio 8, 90128, Palermo, Italy, a.alaimo@unipa.it

² Dipartimento di Tecnologie ed Infrastrutture Aeronautiche, Università di Palermo, Viale delle Scienze, Edificio 8, 90128, Palermo, Italy, alberto.milazzo@unipa.it

³ Dipartimento di Tecnologie ed Infrastrutture Aeronautiche, Università di Palermo, Viale delle Scienze, Edificio 8, 90128, Palermo, Italy, c.orlando@unipa.it

Keywords: Active Repair, Piezoelectric Materials, Boundary Element Method, Imperfect Bonding.

Abstract. This paper presents the analysis of active piezoelectric patches for cracked structures by Boundary Element Method. A two dimensional boundary integral formulation based on the multidomain technique is used to model cracks and to assemble the multi-layered piezoelectric patches to the host damaged structures. The fracture mechanics behavior of the repaired structures is analyzed for both perfect and imperfect interface between patches and host beams. The imperfect interface, representing the adhesive between two different layers, is modeled by using a “Spring Model” that involves linear relationships between the interface tractions, in normal and tangential directions, and the respective discontinuity in displacements. Numerical analyses performed on a cracked cantilever beam repaired by single and multilayered patches are presented. It is pointed out that the adhesive deeply influences the performances of the repair as highlighted by an increasing of the SIF’s values with respect to perfect bonding case.

Introduction. The repair technology of cracked structures is a primary topic in the field of aerospace, mechanical and civil engineering [1-3]. In many practical cases the use of patch repairs, applied to damaged components, can extend the service lifetime of a structure. For this reason repair represents an efficient and cost saving alternative method to be applied in order to avoid immediate replacement of damaged components [4]. The most conventional repair methods involve metallic or composite passive patches applied to the damaged structure to reduce the stress intensity factors and consequently to increase the fatigue life. Although the aforementioned passive patches have proven to be quite effective, a new repair methodology, called “active repair”, is emerging. The development of active repair is deeply linked with advancement of smart materials such as piezoelectric composites [5]. Active repair technology is based on the converse piezoelectric effect according to which piezoelectric materials undergo deformation when an electric field is applied across them [6]. So when a piezoelectric patch is used to repair a damaged component, the strain induced by an applied electric field can help the structure to reduce the crack opening [7]. To exploit the potentiality of the active repair methodology a deeply understanding of the electromechanical behavior of piezoelectric materials is needed. Research on the piezoelectric

active repair was proposed by Wang et al [5]. They developed an analytical model for a cracked beam with a piezoelectric actuator layer with the aim to reduce the singularity at the crack tip by inducing a local moment. Two dimensional finite element analyses were performed by Liu [7] to study active repair for cracked structures by using multi-layered piezoelectric patches.

In this paper a multidomain boundary integral formulation [8] is developed to analyze the active patches performances for both perfect and imperfect interface condition. The characterization of the adhesive layer between the host structure and the piezoelectric patches is approached by using a spring model which involves shear and peel stiffness and is based on the assumption that the displacement jump at the interface is proportional to tractions [9-10]. Single patch and multilayered patches configuration are analyzed. The modeling of the adhesive evidences a decay of the actuation performances for both repair configurations considered. This trend is pointed out by the computation of the SIFs that characterize the fracture mechanics behavior of the repaired structures.

Basic equations and Boundary integral representation. The formulation is developed for two-dimensional electro-elastic domains Ω with boundary $\partial\Omega$ lying in the x_1x_2 plane. By assuming that both the mechanical and the electric responses do not vary along the x_3 direction [11], the problem is treated as a generalized plane strain elasticity and an in-plane electrostatic. Following the Barnett and Lothe's [13] formalism for piezoelectrics, the problem is formulated in terms of generalized displacements $\mathbf{U} = [u_1 \ u_2 \ u_3 \ \phi]^T$, that are mechanical displacements and electric potential, and generalized tractions $\mathbf{T} = [t_1 \ t_2 \ t_3 \ D_n]^T$, that are mechanical tractions and the normal component of the electric displacement.

By virtue of the analogy between elastic and electro-elastic governing equations, the Betti's reciprocal theorem is straightforward extended to the piezoelectric problem leading to the analogous of the classical Somigliana identity for the electro-mechanical problem and constitutes its boundary integral representation [14]. By using four independent fundamental solutions associated with the concentrated point load directed along the three axes and with a concentrated charge, the generalized displacements at the generic point P_0 can be expressed in terms of generalized displacements and generalized tractions on the boundary. In compact matrix notation, with the assumption of null body forces, it reads

$$\mathbf{c}^* \mathbf{U}(P_0) + \int_{\partial\Omega} (\mathbf{T}^* \mathbf{U} - \mathbf{U}^* \mathbf{T}) d\partial\Omega = \mathbf{0} \quad (1)$$

where the kernel \mathbf{U}^* and \mathbf{T}^* are the piezoelectricity fundamental solutions [8, 16] and the matrix \mathbf{c}^* is defined according to [15]. The boundary integral formulation is numerically implemented by using the boundary element method [17, 18], which provides a linear algebraic resolving system expressed in terms of generalized displacements and tractions nodal values $\boldsymbol{\delta}$ and \mathbf{P} , respectively

$$\mathbf{H}\boldsymbol{\delta} + \mathbf{G}\mathbf{P} = \mathbf{0} \quad (2)$$

Eqs. (2), coupled with the electromechanical boundary conditions, provide the solution of the problem for a single domain.

Imperfect Interface. To take into account the presence of cracks and to join the piezoelectric patches to the host structure the use of the Multidomain Technique is employed. The original domain is divided into a suitable number of homogenous sub-regions, each one governed by Eqs. (2). Thus, the following relationships can be written

$$\sum_{j=1}^M \mathbf{H}_{ij}^i \delta_{ij}^i = \sum_{j=1}^M \mathbf{G}_{ij}^i \mathbf{P}_{ij}^i \quad (i=1, 2, \dots, M) \quad (3)$$

where M is the number of subregions considered, the superscript i indicates the quantities associated with the i -th subdomain, while the subscript ij relates quantities to the nodes belonging to the interface between the i -th and j -th subdomains, provided that for $i=j$ the nodes belong to the external boundary of the i -th subdomain. In the Eqs. (3) \mathbf{H}_{ij}^i and \mathbf{G}_{ij}^i denote the matrices of influence coefficients pertaining to the quantities δ_{ij}^i and \mathbf{P}_{ij}^i , respectively. To restore the integrity of the original domain, generalized continuity and equilibrium conditions are imposed at sub-regions' interfaces. In particular, perfect bonding case is modeled by imposing the following conditions at the interface

$$\delta_{ij}^i = \delta_{ij}^j \quad \text{and} \quad \mathbf{P}_{ij}^i = -\mathbf{P}_{ij}^j \quad i=1 \dots M-1; \quad j=i+1, \dots, M \quad (4)$$

while to model the interface bonding as imperfect, since the generalized displacement continuity condition is no longer valid, a generalized displacement gap $\Delta\delta^{ij}$ along the conjugated interfaces is taken into account and the imperfect bonding compatibility conditions can be written as

$$\delta_{ji}^j = \delta_{ij}^i + \Delta\delta^{ij} \quad i=1, \dots, M-1; \quad j=i+1, \dots, M. \quad (5)$$

In the present work, the effect of the adhesive between the patch and the host structure is considered by using an interface Spring Model. It follows that the generalized displacement gap $\Delta\delta^{ij}$ is written as functions of the generalized tractions at the interfaces as

$$\Delta\delta^{ij} = \mathbf{K}_{ij} \mathbf{P}_{ij}^i \quad i=1, \dots, M-1; \quad j=i+1, \dots, M. \quad (6)$$

In Eqs. (6) \mathbf{K}_{ij} is the matrix containing the interface compliance coefficients defined as in [10]. It is worth noting that the present imperfect interface model does not require auxiliary interface elements since the compliance constants, characterizing the elastic behavior of the adhesive between different layers, directly enter the definition of matrices \mathbf{H} and \mathbf{G} .

Numerical results.

Single Layered patch. In this section the analysis of a single-layer active piezoelectric patch applied on a cracked cantilever isotropic beam is presented. The crack is located at $x_i=L/2$ and the patch is attached on the opposite side with respect to the damage as shown in figure 1. The patch is actuated with the aim to reduce the crack opening caused by the force F . Using a single patch the aim at issue is obtained by the elongation of the repair in x_1 -direction. Such a piezoelectric strain induces a bending moment in the host beam allowing the reduction of COD. The geometry, the load and the material properties of the host beam and of the piezoelectric patches are taken from Liu [7] and are summarized in table 1 and 2.

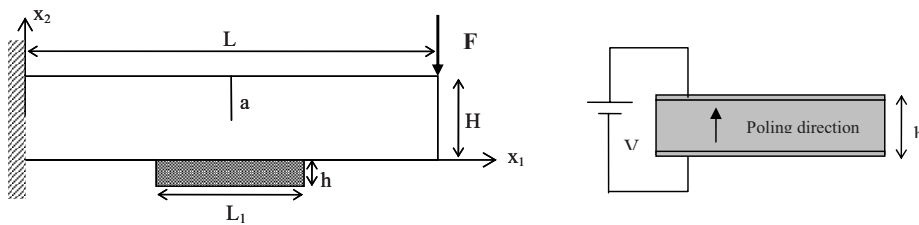


Fig. 1: Single-layered active patch configuration.

Table 1: Geometry and load.

Geometry and Load	L	H	h	L ₁	a	F
	0.08 m	0.02 m	0.25 H	H/0.75	0.5 H	100 N/m

Table 2: Material properties.

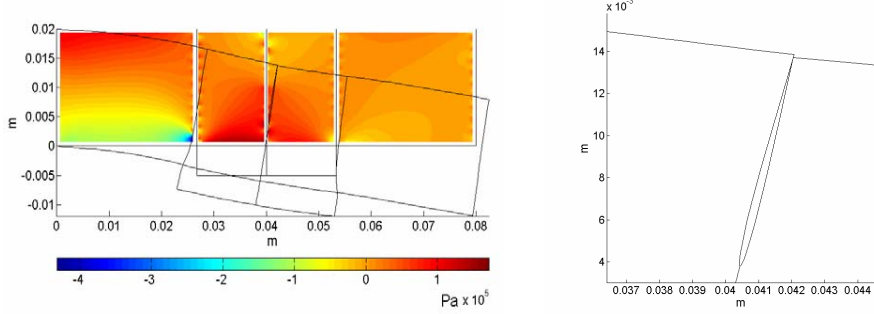
PZT-4		PMMA		Adhesive	
Elastic constants (GPa)	Piezoelectric const. (C/m ²)	Dielectric const. (pC/Vm)	Young Modulus (GPa)	Poisson ratio	Young Modulus (GPa) Poisson ratio
$C_{11}=139$					
$C_{22}=115$	$e_{21}=-5.2$				
$C_{12}=74.3$	$e_{22}=15.1$	$\epsilon_{11}=6447$	$E=3.3$	$v=0.35$	$E=3$
$C_{13}=77.8$	$e_{14}=12.7$	$\epsilon_{22}=5617$			$v=0.4$
$C_{44}=25.6$					

The analyses are carried out to highlight the differences occurring between passive and active repair with respect to the damaged beam. Moreover the influence of the adhesive on the repair performances, expressed in terms of the reference voltage and of the SIFs increment, is investigated. In the case of active patch the “reference voltage” is that able to close the crack surfaces. Considering that for this particular load case mode I is predominant, the fracture behavior can be simply characterized by the K_I values. The K_I computed for the cracked beam without repair is $9004.2 \text{ Pa}\cdot\text{m}^{1/2}$ as in Liu [7]. In table 3 the K_I and the reference voltages obtained for both perfect and imperfect bonding condition are shown.

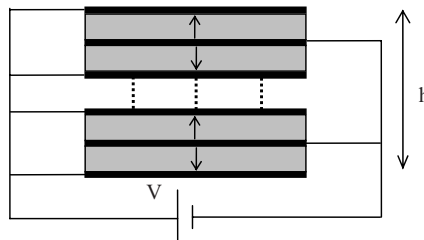
Table 3: SIFs and reference voltages for single layer patch.

	Perfect bonding		Imperfect bonding		
	K_I Pa·m ^{1/2}	Ref. Voltage V_p (Volt)	K_I	K_I at V_p	Ref. Voltage V_{IMP} (Volt)
Passive patch	3569.3		3845.6		
Active patch	1524.4	1290	1529.3 (at V_{IMP})	2137.3	1740

Figure 2 shows the crack opening displacement in the case of perfect bonding when the relative reference voltage is applied across the patch. It's worth noting that at this voltage only the crack mouth is closed and the reduction of K_I passing from passive to active repair is about 57%. On the other hand, in the case of imperfect interface, the same reduction of SIF is obtained by increasing the reference voltage of about 35%.

**Fig. 2:** σ_{11} stress distribution-Crack Opening Displacement.

Multi-Layered patch. The multi-layered piezoelectric patch repair is obtained by stacking 5 piezoelectric bimorphs in series configuration as shown in figure 3. The overall geometry of the multi-layered patch is the same as the previous case, thus the passive repair effect is almost the same. However the actuated multi-layered configuration is more effective from an electric point of view than the single layer patch since less actuating energy is needed to close the crack mouth. The reference voltage is about one tenth of single-layer patch due to the fact that the actuated stacked bimorphs directly undergo bending deformation.

**Fig. 3:** Multi-layered active patch configuration.

The effect of the adhesive deeply affect the multilayered patch passive behavior. The SIF value is in fact about 39% higher than the perfect bonding one, while in the single-layer case the percentage difference between perfect and imperfect bonding condition is about 8%. The active repair

performances are also influenced by the presence of the adhesive. The reference voltage must be increased of about 42% to obtain a similar fracture mechanics behavior.

Table 4: SIFs and reference voltages for multi-layered patch.

	Perfect bonding		Imperfect bonding		
	K_I Pa·m ^{1/2}	Ref. Voltage V_p (Volt)	K_I	K_I at V_p	Ref. Voltage V_{IMP} (Volt)
Passive patch	3557.5		4959.3		
Active patch	1408.2	123	1321.2 (at V_{IMP})	2417.6	175

Conclusions. The performances of active patch repair bonded on a damaged cantilever beam have been investigated by using a multidomain boundary element approach. The adhesive has been modeled by using a spring interface model. Single and multi-layered repair configurations have been studied for both perfect or imperfect interfaces between contiguous plies. In all cases, numerical results have shown better performances of the actuated multi-layered patch.

References.

- [1] Baker A. A., Jones R., "Bonded Repair of Aircraft Structures", *Martinus Nijhoff Publishers, Dordrecht, The Netherlands*, 1988.
- [2] Baker A. A., Callinan R. J., Davis M. J., Jones R., Williams J. F., "Repair of Mirage III aircraft using BFRP crack patching technique", *Theor. Appl. Fract. Mech.*, Vol. 2, 1984, pp. 1-16.
- [3] Heller H., Hill T. G., Williams J. F., Jones R., "Increasing the fatigue life of cracked fastener holes using bonded repair", *Theor. Appl. Fract. Mech.*, Vol. 11, 1989, pp. 1-8.
- [4] Wang Q., Quek S. T., "Repair of delaminated beams via piezoelectric patches", *Smart Materials and Structures*, Vol. 13, 2004, pp. 1222-1229.
- [5] Wang Q., Quek S. T., Liew K. M., "On the repair of a cracked beam with a piezoelectric patch", *Smart Materials and Structures*, Vol. 11, 2002, pp. 404-410.
- [6] Chopra I., "Review of State of Art of Smart Structures and Integrated Systems", *AIAA Journal*, Vol. 40, No. 11, 2002, pp.2145-2187.
- [7] Liu T. J. C., "Fracture mechanics and crack contact analyses of the active repair of multi-layered piezoelectric patches bonded on cracked structures", *Theor. Appl. Fract. Mech.*, Vol. 47, 2007, pp. 120-132.
- [8] Davi, G., Milazzo, A., "Multidomain boundary integral formulation for piezoelectric materials fracture mechanics", *International Journal of Solids and Structures*, Vol. 38, 2001, pp. 7065-7078.
- [9] Alaimo, A., Milazzo, A., Benedetti, I., "Analysis of composite laminates with imperfect bonding conditions", Accepted for the Proceedings of the VIII International Conference on Boundary Element Techniques (BeTeq 2007), July 2007, Naples, Italy.
- [10] Milazzo A., Alaimo A., Benedetti I., "Piezoelectric bimorph response with imperfect bonding conditions", Proceeding of ICICES-08, March 2008, Honolulu, Haway.
- [11] Pak, Y.E., "Linear electro-elastic fracture mechanics of piezoelectric materials", *International Journal of Fracture*, Vol. 54, No. 1, 1992, pp. 79-100.
- [12] Davi, G., Milazzo, A., "Boundary element solution for the free edge stresses in composite laminates", *Journal of Applied Mechanics*, Vol. 64, No. 3, 1997, pp. 877-884.
- [13] Barnett D.M., Lothe J., "Dislocations and line charges in anisotropic piezoelectric insulators", *Physics State Solid (b)*, 67 (1975), 105-111.
- [14] Lee, J. S., Jiang, L. Z., "A boundary integral formulation and 2D fundamental solution for piezoelectric media", *Mechanical Research Communications*, Vol. 21, No. 1, 1994, pp. 47-54.
- [15] Davi, G., "A general boundary integral formulation for the numerical solution of bending multilayer sandwich plates", In: Brebbia, C.A., Connor, J.J. (Eds.) *Advances in BoundaryElement. Proceeding of the 11th International Conference on Boundary Element Methods*. Computational Mechanics Publications, Southampton, 1989 pp.25-35.
- [16] Lekhnitskii, S. G., "Theory of Elasticity of an Anisotropic Body", Holden-Day, San Francisco, 1963.
- [17] Aliabadi, M. H., *The Boundary Element Method*, Vol.2, Wiley, (2002)
- [18] Banerjee, P. K., Butterfield, R., *Boundary Element Methods in Engineering Science*, McGraw-Hill, Maidenhead, 1981.

Analytical integrations in 3D BEM elastodynamics

Temponi, A., Salvadori, A., Bosco, E., Carini, A., and Alsalaet, J.
 CeSiA - International Center for Research on Applied Seismology and Structural Dynamics,
 DICATA - Dipartimento di Ingegneria Civile, Architettura, Territorio e Ambiente
 Università di Brescia, via Branze 43, 25123 Brescia, Italy
 E-mail: alessandro.temponi@ing.unibs.it, alberto.salvadori@ing.unibs.it, angelo.carini@ing.unibs.it

Abstract

Some results on the analytical integration of kernels in hyperbolic problems [1] (acoustics, elastodynamics) for 3D Boundary Element Methods are presented. Adopting polynomial shape functions of arbitrary degree (in space and time) on flat discretizations, integrations are performed both in space and time for Lebesgue integrals working in a local coordinate system. For singular integrals, both a limit to the boundary as well as the finite part of Hadamard [2, 3] approach have been pursued.

Keywords: Boundary elements, dynamics, analytical integrations, finite part of Hadamard.

1 Introduction

Modeling hyperbolic problems by means of boundary integral equations (BIEs) and approximating their solution through boundary element methods (BEM) is firmly established in the academic community as well as in industry. Several well known yet stimulating as well as modern applications and on going research topics can be effectively described via BIEs: to cite but a few, the analysis of ground motion due to moving surface loads induced by high-speed trains [4], the dynamic analysis of the interaction between structures and their surrounding soils, modeled as visco-elastic or porous media [5], the simulation of ultrasonic nondestructive evaluation [6] and of dynamic fracture mechanics in anisotropic media [7].

The present note aims at providing a closed form for analytical integrations involved in 3D BIEs, what seems to be of interest for computational and theoretical purposes. Educational advantages of analytical integrations can also be envisaged, as in [8]. In this note, reference will be made to linear elastodynamics as a prototype of a hyperbolic problem; the boundary integral formulation [9] of Navier's equations of motion stems from Graffi's [10] (see also Wheeler and Sternberg's proof [11]) generalization of Betti's theorem to elastodynamics. Under the hypothesis of vanishing initial conditions and no body forces, the boundary integral representation (BIR) of displacements in the interior of an open domain Ω at time t reads:

$$\mathbf{u}(\mathbf{x}, t) = \int_{\Gamma} \int_0^t \mathbf{G}_{uu}(\mathbf{r}, t - \tau) \mathbf{p}(\mathbf{y}, \tau) d\tau d\Gamma_y - \int_{\Gamma} \int_0^t \mathbf{G}_{up}(\mathbf{r}, \mathbf{l}(\mathbf{y}), t - \tau) \mathbf{u}(\mathbf{y}, \tau) d\tau d\Gamma_y, \quad \mathbf{x} \in \Omega \quad (1)$$

Here, $\mathbf{r} = \mathbf{x} - \mathbf{y}$ stands for the vector that joins point \mathbf{y} to \mathbf{x} . Identity (1) is based on Green's functions (also called kernels) which represent components u_i of the displacement vector \mathbf{u} in a point \mathbf{x} due to: i) a unit force concentrated in space (point \mathbf{y}) and time (instant τ) and acting on the unbounded elastic space Ω_{∞} in direction j (such functions are gathered in matrix \mathbf{G}_{uu}); ii) a unit relative displacement concentrated in time (instant τ) and space (at a point \mathbf{y}), crossing a surface with normal $\mathbf{l}(\mathbf{y})$, and acting on the unbounded elastic space Ω_{∞} (in direction j) (gathered in matrix \mathbf{G}_{up}).

To obtain an additional integral equation, required for the variational formulation of elastodynamics BIEs [12] as well as by nowadays standard numerical techniques [13], the traction operator can be applied to identity¹ (1), thus obtaining the BIR of tractions on a surface of normal $\mathbf{n}(\mathbf{x})$ in the interior of the domain, i.e. $\mathbf{x} \in \Omega$:

$$\mathbf{p}(\mathbf{x}, t) = \int_{\Gamma} \int_0^t \mathbf{G}_{pu}(\mathbf{r}, \mathbf{n}(\mathbf{x}), t - \tau) \mathbf{p}(\mathbf{y}, \tau) d\tau d\Gamma_y - \int_{\Gamma} \int_0^t \mathbf{G}_{pp}(\mathbf{r}, \mathbf{n}(\mathbf{x}), \mathbf{l}(\mathbf{y}), t - \tau) \mathbf{u}(\mathbf{y}, \tau) d\tau d\Gamma_y \quad (2)$$

Such a BIR involves Green's functions (collected in matrices \mathbf{G}_{pu} and \mathbf{G}_{pp}) which describe components (p_i) of the traction vector \mathbf{p} on a surface of normal $\mathbf{n}(\mathbf{x})$ due to: i) a unit force concentrated in space (point \mathbf{y}) and time (instant τ) and acting on the unbounded elastic space Ω_{∞} in direction j ; ii) a unit relative displacement concentrated in space (at a point \mathbf{y}), crossing a surface with normal $\mathbf{l}(\mathbf{y})$ and acting at instant τ on the unbounded elastic space Ω_{∞} (in direction j).

BIEs for the linear elastic problem can be derived from BIRs (1) (thus obtaining the so-called "displacement equation") and (2) (so that the "traction equation" comes out) by performing the space boundary limit² $\Omega \ni \mathbf{x} \rightarrow \mathbf{x} \in \Gamma$. In the limit process, after integration in time, singularities of Green's functions are triggered off: their singularity-orders show to be equivalent to the elastostatic case³. Assuming smooth boundaries, after imposing the fulfillment of the displacement equation on Dirichlet boundary Γ_u and of the traction equation on Neumann boundary Γ_p , the following linear boundary integral problem (omitting the arguments of Green's functions for paucity of space) comes out:

$$\int_{\Gamma_u} \int_0^t \mathbf{G}_{uu} \mathbf{p}(\mathbf{y}, \tau) d\tau d\Gamma_y - \int_{\Gamma_p} \int_0^t \mathbf{G}_{up} \mathbf{u}(\mathbf{y}, \tau) d\tau d\Gamma_y = \mathbf{f}^u(\mathbf{x}, t), \quad \mathbf{x} \in \Gamma_u \quad (3)$$

$$- \int_{\Gamma_u} \int_0^t \mathbf{G}_{pu} \mathbf{p}(\mathbf{y}, \tau) d\tau d\Gamma_y + \int_{\Gamma_p} \int_0^t \mathbf{G}_{pp} \mathbf{u}(\mathbf{y}, \tau) d\tau d\Gamma_y = \mathbf{f}^p(\mathbf{x}, t), \quad \mathbf{x} \in \Gamma_p \quad (4)$$

Vectors \mathbf{f}^i , $i = u, p$, that gather all data are the following:

$$\begin{aligned} \mathbf{f}^u(\mathbf{x}, t) &= \frac{1}{2} \bar{\mathbf{u}}(\mathbf{x}, t) - \int_{\Gamma_p} \int_0^t \mathbf{G}_{uu} \bar{\mathbf{p}}(\mathbf{y}, \tau) d\tau d\Gamma_y + \int_{\Gamma_u} \int_0^t \mathbf{G}_{up} \bar{\mathbf{u}}(\mathbf{y}, \tau) d\tau d\Gamma_y, \quad \mathbf{x} \in \Gamma_u \\ \mathbf{f}^p(\mathbf{x}, t) &= -\frac{1}{2} \bar{\mathbf{p}}(\mathbf{x}, t) + \int_{\Gamma_p} \int_0^t \mathbf{G}_{pu} \bar{\mathbf{p}}(\mathbf{y}, \tau) d\tau d\Gamma_y - \int_{\Gamma_u} \int_0^t \mathbf{G}_{pp} \bar{\mathbf{u}}(\mathbf{y}, \tau) d\tau d\Gamma_y, \quad \mathbf{x} \in \Gamma_p \end{aligned}$$

Integral problem (3-4) can be written in the compact form:

$$\mathcal{L}[y] = f \quad (5)$$

with all terms defined by comparison. Unknown vector y is made of tractions (Neumann data) \mathbf{p} on the Dirichlet boundary Γ_u and displacements (Dirichlet data) \mathbf{u} on the Neumann boundary Γ_p . Let $h > 0$ be a parameter and let $[\mathbf{p}_h(\mathbf{y}, \tau), \mathbf{u}_h(\mathbf{y}, \tau)]^T \stackrel{\text{def}}{=} y_h \in Y_{\mathcal{L}, h}$ be an approximation of the unknown vector field y , denoting with $Y_{\mathcal{L}, h}$ a family of finite dimensional subspaces of $Y_{\mathcal{L}}$ such that

$$\forall y \in Y_{\mathcal{L}}, \inf_{y_h \in Y_{\mathcal{L}, h}} \|y - y_h\| \rightarrow 0 \quad \text{as } h \rightarrow 0 \quad (6)$$

Discretization (6) allows to transform integral problem (5) into a set of algebraic equations. Several techniques have been developed to this aim: the collocation boundary element method (CBEM) [15],

¹The above introduced kernels are infinitely smooth in their domain, which is the whole space \mathbb{R}^3 with exception of the origin (that is $\mathbf{x} \neq \mathbf{y}$)

²In the traction equation (4) the boundary limit must be taken at a smooth point \mathbf{x} with a well defined normal vector $\mathbf{n}(\mathbf{x})$. Strong and hypersingular kernels generate free terms in the limit process such that $\chi_{\Gamma}^u(\mathbf{x}) = \chi_{\Gamma}^p(\mathbf{x}) = \frac{1}{2} \mathbf{1}$ for smooth boundaries, whereas special cares are required for the discrete problem [14].

³Kernel \mathbf{G}_{uu} shows an integrable singularity (named "weak"); kernels \mathbf{G}_{up} and \mathbf{G}_{pu} present a strong singularity $O(r^{-2})$; kernel \mathbf{G}_{pp} is usually named hypersingular, because it shows a singularity (of $O(r^{-3})$) greater than the dimension of the integral.

the hypersingular collocation approach (HBEM) [16], the Galerkin [17] method (GBEM), the dual BEM [13], the convolutive variational method [12], the variational formulation in extended sense [18]. All aforementioned method require the evaluation of “integrals” of the form:

$$\int_{\Gamma_s} \int_0^t \mathbf{G}_{rs}(\mathbf{x}, \mathbf{y}, t - \tau) \chi_h(\mathbf{y}, \tau) d\Gamma_y dt \quad r = u, s = u, p \quad (7)$$

denoting with $\chi_h(\mathbf{y}, \tau)$ scalar shape functions for modeling the components of approximation y_h of the unknown vector fields along $\partial\Omega \times [0, T]$. For CBEM and HBEM, point $\{\mathbf{x}, t\}$ in integral (7) belongs to a selected set of collocation points $\mathbf{x}_i^* \in \partial\Omega$, $t_j^* \in [0, T]$; for other techniques, point $\{\mathbf{x}, t\}$ takes different meanings.

2 Shape functions

The assumption of time-space variable separation is taken, namely:

$$\chi_h(\mathbf{y}, \tau) = \phi_n(\mathbf{y}) \omega_k(\tau) \quad (8)$$

where $\omega_k(\tau)$ is assumed to be a polynomial in τ .

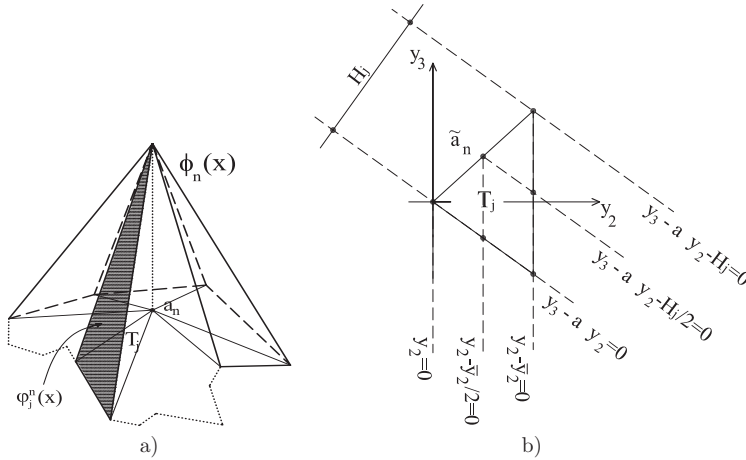


Figure 1: a) Local $\varphi_j^n(\mathbf{x})$ and global $\phi_n(\mathbf{x})$ shape functions. b) Local coordinate system L_Δ . The extension to quadrilateral or mixed triangular-quadrilateral tessellation is straightforward.

Let Γ_h be a triangulation of boundary Γ , $T_j \subset \Gamma_h$ its generic triangle and \mathbf{a}_n a generic node of Γ_h . Collect in set $\mathcal{T}_n := \{T_j \text{ s.t. } \mathbf{a}_n \in T_j\}$ all triangles of Γ_h sharing node \mathbf{a}_n (see figure 1-a). Choose over T_j a local (lagrangian) basis $\boldsymbol{\varphi} := \{\varphi_j^1, \varphi_j^2, \dots, \varphi_j^{M(j)}\}$ and denote with $\varphi_j^{n(j)}$ the unique element of $\boldsymbol{\varphi}$ such that $\varphi_j^{n(j)}(\mathbf{a}_n) = 1$. Define shape function $\phi_n(\mathbf{x})$ (see figure 1-a) as a piecewise continuous function over Γ_h whose value is zero outside \mathcal{T}_n , as follows:

$$\phi_n \in C^0(\Gamma_h) \quad \text{supp}(\phi_n) = \mathcal{T}_n \quad \phi_n|_{T_j} = \varphi_j^{n(j)} \quad (9)$$

A suitable choice of an orthogonal cartesian coordinate system allows an effective representation for $\varphi_j^{n(j)}(\mathbf{y})$. Let $\mathcal{L}_\Delta \equiv \{y_1, y_2, y_3\}$ define a local coordinate system such that: i) a vertex of T_j is the

origin; ii) the plane $y_1 = 0$ contains T_j ; iii) the plane $y_3 = 0$ is orthogonal to the side of T_j opposite to the origin. In \mathcal{L}_Δ , T_j is defined by:

$$T_j := \{\mathbf{y} \in \mathbb{R}^3 \text{ s.t. } y_1 = 0; 0 \leq y_2 \leq \bar{y}_2; ay_2 - y_3 \leq 0; by_2 - y_3 \geq 0\}$$

where a and b denote the slopes of the two sides of T_j that cross the origin (see figure 1-b). Selecting arbitrarily one of these two sides, say $y_3 - ay_2 = 0$, denote with H_j the height of T_j , namely the segment orthogonal to a side emanating from the vertex opposite to it - see figure 1-b. Denoting with $\mathbf{d} = \mathbf{y} - \mathbf{x}$, $r = \|\mathbf{d}\|$, shape functions can be readily expressed in terms of H_j in the form:

$$\varphi_j^n(\mathbf{y}) = \mathbf{d}_3^\top \mathbf{T}_3^\top \Lambda_j^n \mathbf{T}_2 \mathbf{d}_2 \quad (10)$$

where $\mathbf{d}_2 = \{d_2^i\}_{i=0,1,\dots,m}$, $\mathbf{d}_3 = \{d_3^i\}_{i=0,1,\dots,m}$,

$$\{\mathbf{T}_k\}_{i,j} = \begin{pmatrix} i-1 \\ j-1 \end{pmatrix} x_k^{(i-j)} \quad k = 2, 3 \quad i, j = 1, 2, \dots$$

and matrix of constants Λ_j^n depends on node \mathbf{a}_n . For linear shape functions and with reference to the node at the origin,

$$\varphi_j^n(\mathbf{y}) = \begin{bmatrix} 1 & -\frac{1}{\bar{y}_2} \end{bmatrix} \begin{bmatrix} 1 & x_2 \\ 0 & 1 \end{bmatrix} \begin{bmatrix} 1 \\ d_2 \end{bmatrix} \quad (11)$$

Description (9) of shape functions extends straightforwardly to quadrilateral panels Q_j , and representation can be made effectively in a local coordinate system $\mathcal{L}_\square \equiv \{y_1, y_2, y_3\}$ such that: i) barycenter of Q_j is the origin; ii) the plane $y_1 = 0$ contains Q_j ; iii) planes $y_2 = 0$ and $y_3 = 0$ are orthogonal to the sides of Q_j . In \mathcal{L}_\square , Q_j is defined by:

$$Q_j := \{\mathbf{y} \in \mathbb{R}^3 \text{ t.c. } y_1 = 0; -a \leq y_2 \leq a; -b \leq y_3 \leq b\}$$

where a and b denote half the length of the two sides of Q_j . By the binomial expansion rule, it is straightforward to get:

$$\varphi_j^n(\mathbf{y}) = \mathbf{a}_h^\top \mathbf{Q}_2^\top \mathbf{d}_2 \mathbf{d}_3^\top \mathbf{Q}_3 \mathbf{a}_k \quad (12)$$

where $\mathbf{a}_h, \mathbf{a}_k$ are vector of constants and

$$\{\mathbf{Q}_k\}_{i,j} := \binom{j-1}{i-1} x_k^{j-i} \quad k = 2, 3 \quad i, j = 1, 2, \dots$$

3 Main result

3.1 Analytical integration in time

Focusing on discretization (12) and exploiting a well known convolution property, integral (7) can be recast in the form:

$$\sum_\alpha \omega_\alpha \mathbf{a}_h^\top \mathbf{Q}_2^\top \mathbb{K}_{rs}(\mathbf{x}, t) \mathbf{Q}_3 \mathbf{a}_k \quad r = u, s = u, p$$

where:

$$\mathbb{K}_{rs}(\mathbf{x}, t) = \int_{Q_j} \mathbf{d}_2 \int_0^t \mathbf{G}_{rs}(\mathbf{x}, \mathbf{y}, \tau) (t - \tau)^\alpha d\tau \mathbf{d}_3^\top d\Gamma_y = \widehat{\mathbb{K}}^{rs}(\mathbf{x}, d_2, d_3; t) \Big|_{\substack{d_3=b-x_3 \\ d_3=-b-x_3}} \Big|_{\substack{d_2=a-x_2 \\ d_2=-a-x_2}} \quad (13)$$

Integration in time, because of the nature of Green's functions, is given in terms of the following outcome of distributions theory:

$$\int_0^t (t - \tau)^\alpha \frac{\partial^k}{\partial \tau^k} H(\tau - \beta) d\tau = \prod_{j=\inf \Xi}^{\sup \Xi} (\alpha - j)^{\operatorname{sgn}(j)} (\tau - \beta)^{\alpha+1-k} H(t - \beta) \quad (14)$$

where: i) $H(\cdot)$ is the Heaviside distribution, $\delta(\cdot) = \dot{H}(\cdot)$ is the Dirac distribution; ii) $\beta > 0$ holds $\frac{r}{c_T}$ or $\frac{r}{c_F}$, with c_L (c_T) the dilatational (shear) wave speed; iii) $k \in \mathbb{Z}$ can be negative, in this case indicating a primitive of order $|k|$ of $H(\cdot)$; iv) $\Xi \subset \mathbb{Z}$ is the set of numbers between 0 and $k - 1$ including both of them: for instance, $k = 2 \Rightarrow \Xi = \{0, 1\}$, $k = 1 \Rightarrow \Xi = \{0\}$, $k = 0 \Rightarrow \Xi = \{-1, 0\}$, $k = -1 \Rightarrow \Xi = \{-2, -1, 0\}$; v) function $\text{sgn} : \mathbb{Z} \rightarrow -1, 0, 1$ is defined as:

$$\text{sgn}(j) = \begin{cases} -1 & \text{if } j < 0 \\ 0 & \text{if } j = 0 \\ 1 & \text{if } j > 0 \end{cases}$$

3.2 Analytical integration in space

In view of Green's functions contributions, terms of the following kind must be dealt with in order to evaluate $\mathbb{K}_{rs}(\mathbf{x}, t)$:

$$\int_{-a-x_2}^{a-x_2} \int_{-b-x_3}^{b-x_3} \frac{d_3^k}{r^{2m+1}} dd_3 \quad k, m \in \mathbb{N}_0$$

The identity:

$$\frac{x^{2k}}{\alpha^2 + x^2} = (-1)^k \frac{\alpha^{2k}}{\alpha^2 + x^2} + \sum_{j=1}^k \binom{k}{j} (-1)^{k-j} (\alpha^2 + x^2)^{j-1} (\alpha^2)^{k-j} \quad (15)$$

which comes out from the binomial expansion rule, permits to obtain the following recursive relationship, that seems to be useful for analytical integrations:

$$\frac{d_3^k}{r^{2m+1}} = (-\alpha^2)^{\hat{k}} \frac{d_3^{k[2]}}{r^{2m+1}} + \sum_{j=1}^{\hat{k}} \binom{\hat{k}}{j} (-1)^{\hat{k}-j} \sum_{h=0}^{j-1} \binom{j-1}{h} \alpha^{2(\hat{k}-1-h)} \frac{d_3^{2h+k[2]}}{r^{2m-1}} \quad k, m \in \mathbb{N}_0 \quad (16)$$

where $\alpha^2 = d_1^2 + d_2^2$ is the squared projection of the distance on the plane $d_3 = 0$. Here and in the rest of the paper $\hat{k} = k \div 2$ stands for the integer division, whereas $k_{[2]} = k - 2\hat{k}$ is its remainder. Making use of formula (16) and reference to [19] for details, $\widehat{\mathbb{K}}^{rs}(\mathbf{x}, d_2, d_3; t)$ can be reduced to the sum of a set of basic integrals and its final expression, reads:

$$\widehat{\mathbb{K}}^{rs} = \mathbb{L}_2^{rs} \log(d_2 + r) + \mathbb{L}_3^{rs} \log(d_3 + r) + \mathbb{A}^{rs} \operatorname{arctanh} \frac{d_3}{r} + \mathbb{I}_\square^{r^{-3}}() + \mathbb{R}^{rs} r + \mathbb{P}^{rs} + \mathbb{S}^{rs} \frac{1}{r} + \mathbb{H}^{rs} \frac{1}{r^3} \quad (17)$$

where: i) $\mathbb{I}_\square^{r^{-3}}(\mathbf{x}, d_2, d_3)$ is the Lebesgue integral of function $\frac{1}{r^3}$ over Q_j , discussed in details in [20]; ii) $\mathbb{L}_2^{rs}, \mathbb{L}_3^{rs}, \mathbb{A}^{rs}, \mathbb{I}^{rs}, \mathbb{R}^{rs}, \mathbb{P}^{rs}, \mathbb{S}^{rs}, \mathbb{H}^{rs}$ are polynomial matrices of the same order of \mathbb{K}^{rs} whose expression can be found in [19] for constant and linear shape functions in time and space.

4 Concluding Remarks

Analytical integrations have been performed for both the singular and the regular part of $\widehat{\mathbb{K}}^{rs}(\mathbf{x}, d_2, d_3; t)$: for paucity of space, discussion on singularity issues has been here omitted and the reader is referred to [19] for details. The proposed outcomes are exhaustive for the collocation approach as well as for the post-process reconstruction of primal and dual fields (temperature and flux, displacement and stress). It seems to be of interest for the dual, the Galerkin, and the variational technique as well, because it firmly distinguishes the weakly singular terms relevant to the outer integral and the singular terms in the outer integration process. Besides accuracy and computational efficiency, the availability of closed form (17) entails the possibility of analytical manipulations - see e.g. [21] - which are hardly possible with alternative approaches. Obtained results may have influence on extremely modern and stimulating applications, e.g. [22] but need to be extended in order to comply with very promising techniques for time marching schemes [23] to which hypothesis (8) does not apply.

References

- [1] M. Costabel. *Encyclopaedia of Computational Mechanics*, chapter Time-dependent problems with the boundary integral equations method. John Wiley and Sons, 2004.
- [2] J. Hadamard. *Lectures on Cauchy's problem in linear partial differential equations*. Yale Univ. Press, New Haven, Conn., USA, 1923.
- [3] A.H. Zemanian. *Distribution theory and transform analysis*. Dover, 1987.
- [4] P. Galvin and J. Dominguez. Analysis of ground motion due to moving surface loads induced by high-speed trains. *Engng. Anal. Boundary Elem.*, 31(931-941), 2007.
- [5] Jeng D.S. Lu, J.F. and S. Williams. A 2.5-d dynamic model for a saturated porous medium. part ii: Boundary element method. *International Journal of Solids and Structures*, 45:359–377, 2008.
- [6] H. Yoshikawa and N. Nishimura. An improved implementation of time domain elastodynamic biem in 3d for large scale problems and its application to ultrasonic nde. *Electronic Journal of Boundary Elements*, 1(2):201–217, 2003.
- [7] Sollero P. Albuquerque, E.L. and M.H. Aliabadi. Dual boundary element method for anisotropic dynamic fracture mechanics. *Int. J. Numer. Methods Eng.*, 59:11871205, 2004.
- [8] S. Rjasanow and O. Steinbach. *The Fast Solution of Boundary Integral Equations*. Springer, 2007.
- [9] J. Dominguez. *Boundary Elements in Dynamics*. Computational Mechanics Publication & Elsevier, 1997.
- [10] D. Graffi. Sul teorema di reciprocità nella dinamica dei corpi elastici. *Mem. Accad. Sci. Bologna*, 18:103–109, 1947.
- [11] L.T. Wheeler and E. Sternberg. Some theorems in classical elastodynamics. *Archive for Rational Mechanics and Analysis*, 31:51–90, 1968.
- [12] G. Maier, M. Diligenti, and Carini A. A variational approach to boundary element elastodynamic analysis and extension to multidomain problems. *Comp. Methods Appl. Mech. Eng.*, 92:193–213, 1991.
- [13] Aliabadi M.H. Wen, P.H. and A. Young. A time-dependent formulation of dual boundary element method for 3d dynamic crack problems. *Int. J. Numer. Methods Eng.*, 45:1887–1905, 1999.
- [14] A. Salvadori. Hypersingular boundary integral equations and the approximation of the stress tensor. *Int. J. Numer. Methods Eng.*, 72:722–743, 2007.
- [15] S. Kobayashi. *BEM in mechanics*, volume 3, chapter Elastodynamics, pages 191–254. 1987.
- [16] R. Gallego and J. Dominguez. Hypersingular bem for transient elastodynamics. *Int. J. Numer. Methods Eng.*, 39:1681–1705, 1996.
- [17] J.J. Perez-Gavilan and M.H. Aliabadi. A galerkin boundary element formulation with dual reciprocity for elastodynamics. *Int. J. Numer. Methods Eng.*, 48:1331–1344, 2000.
- [18] A. Carini and F. Genna. Saddle point principles and numerical integration methods for second order hyperbolic equations. *Comp. Meth. in Appl. Mech. and Engng.*, 190:1663–1678, 2000.
- [19] A. Temponi, A. Salvadori, E. Bosco, and A. Carini. Analytical integrations in 3d bem elastodynamics. Technical report, University of Brescia, In preparation.
- [20] A. Carini and A. Salvadori. Analytical integrations in 3D BEM: preliminaries. *Comp. Mech.*, 28(3-4):177–185, 2002.
- [21] A. Salvadori and L.J. Gray. Analytical integrations and SIFs computation in 2D fracture mechanics. *Int. J. Numer. Methods Eng.*, 70:445–495, 2007.
- [22] H. Bao, J. Bielak, O. Ghattas, L.F. Kallivokas, D.R. O'Hallaron, J.R. Shewchuk, and J. Xu. Large-scale simulation of elastic wave propagation in heterogeneous media on parallel computers. *Comput. Math. Appl. Mech. Eng.*, 152:85–102, 1998.
- [23] A. Lew, J.E. Marsden, M. Ortiz, and M. West. Variational time integrators. *Int. J. Numer. Methods Eng.*, 60:153212, 2004.

BEM analysis of an interface crack with friction

Enrique Graciani^{1,a}, Vladislav Mantič^{1,b} and Federico París^{1,c}

¹Grupo de Elasticidad y Resistencia de Materiales, Escuela Técnica Superior de Ingenieros,
Camino de los Descubrimientos s/n, 41092, Sevilla, Spain

^agraciani@esi.us.es, ^bmantic@esi.us.es, ^cparis@esi.us.es

Keywords: Interface crack, frictional contact, axial symmetry, weak contact conditions.

Abstract. In the present paper, a penny-shape interface crack at the interface of two dissimilar materials subjected to uniform far-field tensile loads is analysed, using an axi-symmetric formulation of the Boundary Element Method, considering the possibility of frictional contact between crack faces. A weak formulation is used to impose frictional contact conditions. In order to improve the accuracy of the results a three-step solution scheme has been employed, in which the mesh is successively refined in the vicinity of the extreme of the previously estimated contact zone. Numerical results are presented for the singularity order of the asymptotic solution, the contact length and the Stress Intensity Factor as a function of the friction coefficient and the bi-material elastic properties.

Introduction

A numerical study of the classical problem of a penny-shaped crack at the interface of two dissimilar isotropic materials, subjected to uniform far-field tensile loads, is presented here. The possibility of frictional contact between crack faces is considered using an axi-symmetric formulation of the Boundary Element Method (BEM) applied to frictional contact problems [1,2].

The problem under study is a classical Interfacial Fracture Mechanics, since it resembles the initiation of a small interface crack inside a bi-material interface. Interesting analytical or semi-analytical solutions of this problem can be found in the literature [2-4], either using the Williams' open model [5], which assumes traction free crack faces [2,3], or the Comninou's frictionless contact model [6], which assumes the existence of a near-tip frictionless contact zone [2,4]. The small-scale contact conditions [7] are not assumed *a priori* in the present study. Therefore, the possibility of contact between crack faces must be considered in the analysis. According to Comninou [8], the presence of friction in the near-tip contact zone changes the asymptotic behaviour of the near-tip elastic solution, decreasing the singularity order of the stresses. This decrease depends upon a bi-material elastic constant and the friction coefficient between crack faces.

The objective of this paper is to show that an excellent accuracy can be obtained with BEM in the solution of this receding frictional contact problem, and to elucidate the influence of the friction coefficient and the bi-material elastic constant over the asymptotic behaviour of near-tip displacements and stresses. In particular, the analysis has been focused on the numerical evaluation of the near-tip contact length, and the singularity order and the Stress Intensity Factor (S.I.F.) which characterize the near-tip elastic solution.

Overview of the BEM formulation

The employed BEM formulation for the frictional elastic contact between two axi-symmetric solids will be briefly described in this section. The radial sections of the contacting solids will be denoted as Ω^k , with $k = A, B$, and the corresponding radial sections of their boundaries will be denoted as Γ^k . The boundary of each solid will be considered as divided into two distinct zones: Γ_o^k , where

there is no possibility of contact, and Γ^k where contact is developed, i.e. the bi-material interface. In order to solve the collocation and contact equations described in the following by means of the BEM, boundaries Γ^k of the solids have been discretized by a set of continuous linear elements S_t^k , with $t=1,\dots,T^k$, in which displacements and tractions are assumed to have a linear evolution.

A symmetric Boundary Integral Equation (ABIE) for displacements components. Using the abovementioned elements, the discretized ABIE of the displacements in each of the solids takes the form (the superscript k denoting the solid has been removed for simplicity, and two different situations have to be considered depending on whether the collocation point lies outside the symmetry axis or not) [1,2]:

$$\begin{aligned} C_{\beta\alpha}^*(z)u_\alpha(z) &= \sum_{t=1}^T \sum_{i=1}^2 \left[B_{\beta\alpha}^{i,t}(z) O_{\alpha\gamma}^t t_\gamma^{i,t} - A_{\beta\alpha}^{i,t}(z) u_\alpha^{i,t} \right], \text{ with } z \in \Gamma, z_r > 0, \\ \hat{C}_{zz}^*(\hat{z})u_z(\hat{z}) &= \sum_{t=1}^T \sum_{i=1}^2 \left[\hat{B}_{z\alpha}^{i,t}(\hat{z}) O_{\alpha\gamma}^t t_\gamma^{i,t} - \hat{A}_{z\alpha}^{i,t}(\hat{z}) u_\alpha^{i,t} \right], \text{ with } \hat{z} \in \Gamma, \hat{z}_r = 0, \end{aligned} \quad (1)$$

where, $u_\alpha^{i,t}$ refer to radial and axial components of the displacements at both nodes of each element, with $\alpha, \beta = r, z$, and $t_\gamma^{i,t}$ refer to the normal and tangential components of the tractions, with $\gamma = n, s$. $O_{\alpha\gamma}^k = n_\alpha^k$ and $O_{\alpha\gamma}^s = s_\alpha^k$ are the components of the a rotation matrix from intrinsic to global co-ordinates. Closed form expressions of the free term components can be found in [2]. Integration constants are defined as:

$$\begin{aligned} A_{\beta\alpha}^{i,t}(z) &= fp \int_{S_t - S_t^\varepsilon(z)} T_{\beta\alpha}^*(z, y) N_t^i(y) dS_t, \quad \hat{A}_{z\alpha}^{i,t}(\hat{z}) = \int_{S_t} \hat{T}_{z\alpha}^*(\hat{z}, y) N_t^i(y) dS_t, \\ B_{\beta\alpha}^{i,t}(z) &= \lim_{\varepsilon \rightarrow 0} \int_{S_t - S_t^\varepsilon(z)} U_{\beta\alpha}^*(z, y) N_t^i(y) dS_t, \quad \hat{B}_{z\alpha}^{i,t}(\hat{z}) = \int_{S_t} \hat{U}_{z\alpha}^*(\hat{z}, y) N_t^i(y) dS_t, \end{aligned} \quad (2)$$

in which fp refer to the Hadamard's finite part of the strongly singular integrals [9]. $N_t^i(y)$, with $y \in S_t$, refer to the linear form functions ($i=1,2$ respectively denotes if the form function corresponds to the initial or the end node of element S_t). $U_{\beta\alpha}^*(z, y)$ and $T_{\beta\alpha}^*(z, y)$ are the components of the fundamental solutions of displacements and tractions for a unit ring load, which are expressed in terms of the complete elliptic integrals of the first and second kind [10]. Finally, $S_t^\varepsilon(z) = S_t \cap \mathcal{B}^\varepsilon(z)$ is the portion of the original element which lies inside an excluding circular vanishing zone $\mathcal{B}^\varepsilon(z)$ defined around the collocation point.

To carry out the numerical solution of this particular problem, a very strong near-tip refinement of the mesh has been carried out. Therefore, when the collocation point belongs to the integration element, an accurate integration scheme has to be employed for the evaluation of the integration constants defined in (2). As the components of the axi-symmetric fundamental solution kernels are highly complicated functions, written in terms of the complete elliptic integrals of the first and second kind, the analytical evaluation of the singular integration constants seems to be nearly impossible. Therefore, a semi-analytic integration scheme has been employed in these cases.

When the integration point tends to the collocation point, the singular terms of the axi-symmetric fundamental solution kernels have been identified [2], yielding the following behaviour:

$$\begin{aligned} U_{\beta\alpha}^*(z, y) &= U_{\beta\alpha}^W(z, y) + U_{\beta\alpha}^B(z, s) \eta \ln(\eta) + U_{\beta\alpha}^R(z, y), \quad \hat{U}_{z\alpha}^*(\hat{z}, y) = \hat{U}_{z\alpha}^R(\hat{z}, y) \\ T_{\beta\alpha}^*(z, y) &= T_{\beta\alpha}^S(s, n) \eta^{-1} + T_{\beta\alpha}^W(z, n) \ln(\eta) + T_{\beta\alpha}^B(z, s, n) \eta \ln(\eta) + T_{\beta\alpha}^R(z, y), \quad \hat{T}_{z\alpha}^*(\hat{z}, y) = \hat{T}_{z\alpha}^S(s, n) \eta^{-1}, \end{aligned} \quad (3)$$

where s and n are the unit vectors respectively tangent and normal to the integration element, $\eta = |y - z|$, and the functions $U_{\beta\alpha}^R(z, y)$, $\hat{U}_{z\alpha}^R(\hat{z}, y)$ and $T_{\beta\alpha}^R(z, y)$ have a regular behaviour in the vicinity of the collocation point.

Using this procedure the strongly singular terms $T_{\beta\alpha}^S(s, \mathbf{n})\eta^{-1}$ and $T_{\beta\alpha}^S(s, \mathbf{n})\eta^{-1}$ and the weakly singular terms $U_{\beta\alpha}^W \ln(\eta)$ and $T_{\beta\alpha}^W(z, \mathbf{n})\ln(\eta)$ are integrated analytically. The regular terms $U_{\beta\alpha}^R(z, \mathbf{y})$, $\hat{U}_{za}^R(\hat{z}, \mathbf{y})$ and $T_{\beta\alpha}^R(z, \mathbf{y})$ are integrated numerically, as they are highly complicated non-explicit functions. However, due to their regular behaviour, they can be numerically integrated with a high accuracy. Finally, terms $U_{\beta\alpha}^B(z, s)\eta \ln(\eta)$ and $T_{\beta\alpha}^B(z, s, \mathbf{n})\eta \ln(\eta)$ are bounded terms with infinite slope at the collocation point. Those terms could either be integrated analytically or numerically. It has been checked that the numerical integration of these terms yield low accuracy results if a strong refinement of the mesh is carried out. Therefore, they have been analytically integrated in the present BEM formulation. Closed form expression of the analytical integrals of all the non regular terms can be found in [2].

Weak formulation of contact conditions. The equilibrium and compatibility conditions along the contact zone between Ω^A and Ω^B have been imposed in a weak manner, derived from the Principle of Virtual Work [1,2,11].

In this way, interface stresses are defined as the tractions along Γ_I^A . Equilibrium at all points \mathbf{y} belonging to the opposite boundary, which means $\mathbf{t}^B(\mathbf{y}) + \mathbf{t}^A(\mathbf{y}) = 0$, is guaranteed by the fulfilment of the following integral equation extended to Γ_I^B (i.e. the interface boundary of Ω^B):

$$\int_{\Gamma_I^B} [\mathbf{t}_\gamma^B(\mathbf{y}) - \mathbf{t}_\gamma^A(\mathbf{y})] u_\gamma^{B\psi}(\mathbf{y}) y_r d\Gamma_I^B = 0, \text{ with } \gamma = n, s, \quad (4)$$

for any virtual field of compatible displacements $\mathbf{u}^{B\psi}(\mathbf{y})$.

Displacements along the interface are defined by the displacements at Γ_I^B . Compatibility at all points \mathbf{y} belonging to the opposite boundary: $\delta^A(\mathbf{y}) = \mathbf{u}^A(\mathbf{y}) - \mathbf{u}^B(\mathbf{y})$, with $\delta^A(\mathbf{y})$ being the relative displacements between opposite points of the interface, is guaranteed by the fulfilment of the following integral equation extended to Γ_I^A (i.e. the interface boundary of Ω^A):

$$\int_{\Gamma_I^A} \mathbf{t}_\gamma^{A\psi}(\mathbf{y}) [u_\gamma^A(\mathbf{y}) + u_\gamma^B(\mathbf{y}) - \delta_\gamma^A(\mathbf{y})] y_r d\Gamma_I^A = 0, \text{ with } \gamma = n, s, \quad (5)$$

for any virtual tractions field in equilibrium $\mathbf{t}^{A\psi}(\mathbf{y})$.

Using the same elements and linear form functions described in the previous section to discretize equations (4,5), and imposing the fulfilment of both equations for any discretized virtual fields, yields a system of equations which can be straightforwardly coupled with the collocation system of equations, since the same displacements and tractions unknowns are employed in both [2].

Description of the problem

A centred penny-shaped crack at the interface of two sufficiently large cylinders of different materials (denoted A and B) has been studied. Only the radial section of the problem, in cylindrical co-ordinates (r, z) , has been modelled, with the geometry and boundary conditions shown in Fig. 1, where $a = 1\text{mm}$ and $b = h = 100a$. A tensile load $\sigma_0 = 1\text{ MPa}$ has been applied at both ends.

Material properties of the upper cylinder are defined by the Young modulus $E_A = 1\text{ MPa}$ and the Poisson ratio $\nu_A = 0.3$, while material properties of the lower cylinder are varied according to: $E_B/E_A = \nu_B/\nu_A = k$, with $0 \leq k \leq 1$. Bi-material elastic properties will be characterized by the β mismatch parameter, the ε parameter and the harmonic mean of the Young moduli E^* :

$$\beta = \frac{\mu_A(\kappa_B - 1) - \mu_B(\kappa_A - 1)}{\mu_A(\kappa_B + 1) + \mu_B(\kappa_A + 1)}, \quad \varepsilon = \frac{1}{2\pi} \ln \frac{1-\beta}{1+\beta} \quad \text{and} \quad \frac{1}{E^*} = \frac{1+\kappa_A}{16\mu_A} + \frac{1+\kappa_B}{16\mu_B} \quad (6)$$

where $\mu_K = E_K/(2+2\nu_K)$ is the shear modulus of material $K = A, B$ and $\kappa_K = 3-4\nu_K$.

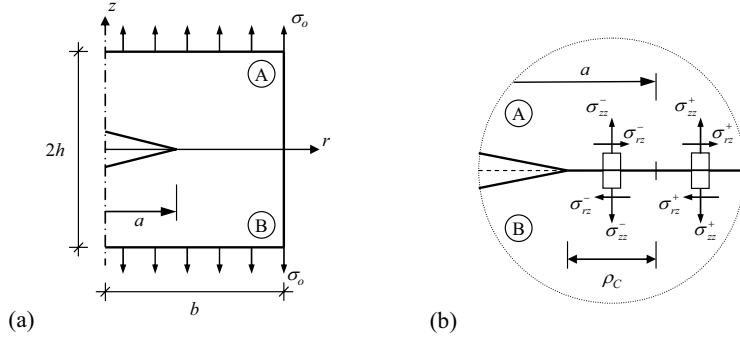


Figure 1: Definition of the problem: (a) geometry; (b) near-tip notation.

The initial BEM mesh was created employing the following set of rules: a maximum element length equal to $0.02a$ along the crack faces, a maximum element length equal to $2a$ along the interface and the external boundaries, equal lengths of every element adjacent to each corner, and a minimum element length equal to $10^{-12}a$ at both sides of the crack tip. Where a mesh refinement is required, a constant 13:10 ratio has been kept between the lengths of adjacent elements. Using this mesh, the bi-material elastic parameter and the friction coefficient were parametrically varied in the range $0 \leq \beta \leq 0.5$ and $0 \leq \mu \leq 1$. As the near-tip contact length, ρ_c , is dramatically reduced with β , accurate solution of the problem was only possible in the range $0.3 \leq \beta \leq 0.5$, which results in, $8.710^{-8} \leq \rho_c/a \leq 1.310^{-4}$. Results obtained with the initial mesh showed that the near-tip contact length increases slightly with friction coefficient. To obtain a higher accuracy a different mesh refinement was made for each of the β values employed, using 30 elements of constant length in the region where the extremes of contact zones were obtained for $0 \leq \mu \leq 1$. Finally, a third refinement was made, using a distinct mesh for each distinct values of β and μ , dividing by 10 the element length in the vicinity of the extreme of the corresponding contact zone.

Numerical results

According to the asymptotic solution presented by Comninou [8], when $\rho \rightarrow 0$, normal stresses $\sigma_{yy}(\rho)^+$ ahead of the crack tip are bounded, while shear stresses $\sigma_{xy}(\rho)^+$ ahead of the crack tip and contact stresses $\sigma_{yy}(\rho)^-$ and $\sigma_{xy}(\rho)^-$ are singular:

$$\sigma_{xy}(\rho)^+ = K_H(2\pi\rho)^{-\lambda}, \quad \sigma_{yy}(\rho)^- = -\beta \operatorname{sen}(\lambda\pi)K_H(2\pi\rho)^{-\lambda}, \quad \sigma_{xy}(\rho)^- = \cos(\lambda\pi)K_H(2\pi\rho)^{-\lambda}, \quad (7)$$

with K_H being the S.I.F. and the singularity order λ given by $\tan(\lambda\pi) = (\mu\beta)^{-1}$.

Relative opening $\Delta u_y(\rho)^-$ is null for $\rho \leq \rho_c$, and near-tip relative sliding $\Delta u_x(\rho)^-$ is given by

$$\Delta u_x(\rho)^- = \frac{1-\beta^2}{E^*} \frac{\operatorname{sen}(\lambda\pi)}{2\pi(1-\lambda)} K_H(2\pi\rho)^{(1-\lambda)}. \quad (8)$$

Near-tip contact length. The extent of the near-tip contact zone given by the BEM solution is located within the element containing the last node in contact and the first separated node. As shown in Fig. 2(a), a finer mesh in that zone increases the precision in the results.

BEM results obtained for the near-tip contact length are shown in Fig. 2 (a) as a function of μ , for $\beta = 0.5$, and in Fig. 2(b) as a function of β , for several μ values. As can be seen, the near-tip contact length slightly increases with μ in an almost linear way.

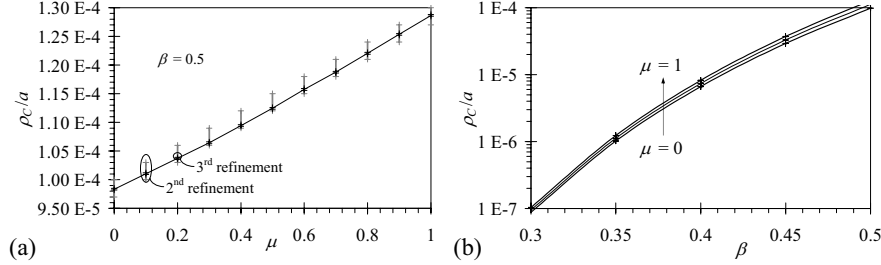


Figure 2: Near-tip contact length: (a) as a function of μ ; (b) as a function of β .

Accuracy in the evaluation of the singularity order. The singularity order λ can be obtained from the near-tip BEM solution of any of the magnitudes defined in (7) and (8). As λ is the only value which has been analytically determined for this problem, it has been evaluated numerically to show the excellent accuracy that can be obtained with the BEM formulation employed. Obviously, a BEM evaluation of λ from the contact stresses $\sigma_{yy}(\rho)^-$ and $\sigma_{xy}(\rho)^-$ is not possible since the size of the contact zone is very small in all cases. Therefore, the first term of their asymptotic solutions becomes dominant at distances smaller than the smallest elements used at the crack tip. Nevertheless, the first term of the asymptotic solution of $\Delta u_x(\rho)^-$ is dominant up to $\rho \sim 10^{-6}a$ and the first term of the asymptotic solution of $\sigma_{xy}(\rho)^+$ is dominant up to $\rho \sim 10^{-8}a$.

BEM results obtained for the singularity order λ (using least square fit of the $\Delta u_x(\rho)^-$ results in the region $10^{-7} < \rho/a < 10^{-6}$, and of the $\sigma_{xy}(\rho)^+$ results in the region $10^{-9} < \rho/a < 10^{-8}$) are shown in Fig. 3(a), as a function of β for several μ values. Relative errors are shown in Fig. 3(b).

As can be seen, accuracy in the evaluation of relative sliding $\Delta u_x(\rho)^-$ is higher, the corresponding error in λ being below 1% in all cases. Although better results are obtained for the $\beta = 0.5$ case, in which the larger near-tip contact length is obtained, the decrease of accuracy in the rest of the cases is not significant, taking into account that the contact length is reduced several orders of magnitude, as can be seen in Fig 2(a).

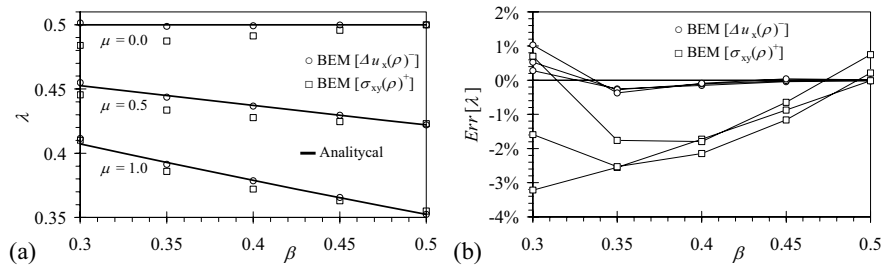


Figure 3: Singularity order: (a) λ evaluated from BEM results; (a) relative error.

Stress Intensity Factor. As the near-tip BEM solution of $\Delta u_x(\rho)^-$ is the most accurate, S.I.F. has been calculated from equation (8), averaging in the range $10^{-7} < \rho/a < 10^{-6}$. Results are shown in Fig. 4 as a function of β for several μ values. As can be seen, K_H increases with μ in all cases.

It has to be noticed that the values of K_{II} corresponding to different values of μ can not be directly compared, as the change in μ implies a change in λ and consequently in K_{II} units.

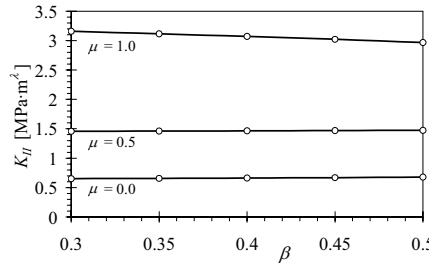


Figure 4: Stress Intensity Factor evaluated from BEM results.

Concluding remarks

The problem of a penny-shape interface crack at the interface of two dissimilar materials subjected to uniform far-field tensile loads has been analyzed, using an axi-symmetric formulation of the Boundary Element Method, considering the possibility of frictional contact between crack faces with a weak formulation of contact conditions.

The excellent accuracy of the numerical results has been checked evaluating the error obtained in the near-tip singularity order.

Numerical results show an increase of the near-tip contact length ρ_c and the Stress Intensity Factor K_{II} due to the friction between crack faces. Numerical results of ρ_c and K_{II} are presented for a wide range of values of the bi-material parameter β and the friction coefficient μ .

Acknowledgements

This work was supported by the Ministerio de Educación y Ciencia, Spain (Pr. TRA2005-06764 and TRA2006-08077) and the Junta de Andalucía, Spain (Pr. Excelencia TEP1207 and TEP2045).

References

- [1] E. Graciani, V. Mantič and F. París, in: *Boundary Element Techniques* edited by M.H. Aliabadi. Department of Engineering, Queen Mary and Westfield College, London (1999).
- [2] E. Graciani, V. Mantič, F. París and A. Blázquez: *Comput. Struct.* Vol. 83 (2005), p. 836–855.
- [3] M.K. Kassir and A.M. Bregman: *J. Appl. Mech.* Vol. 39 (1072), p. 308-310.
- [4] L.M. Keer, S.H. Chen and M. Comninou: *Int. J. Eng. Sci.* Vol. 16 (1978), p. 765-772.
- [5] M.L. Williams: *B. Seismol. Soc. Am.* Vol. 49 (1959), p. 199-204.
- [6] M. Comninou: *J. Appl. Mech.* Vol. 44 (1977), p. 631-636.
- [7] J.R. Rice: *J. Appl. Mech.* Vol. 55 (1988), p. 98-103.
- [8] M. Comninou: *J. Appl. Mech.* Vol. 44 (1977), p. 780-781.
- [9] F. París and J. Cañas: *Boundary Element Method. Fundamentals and Applications* (Oxford University Press, Oxford, 1997).
- [10] J. Balaš, J. Sládek and V. Sládek: *Stress Analysis by Boundary Element Method* (Elsevier, Amsterdam, 1989).
- [11] A. Blázquez, F. París V. Mantič: *Int. J. Solids Struct.* Vol. 35 (1998), p. 3259-3278.

BEM-FEM coupling in antiplane time-harmonic elastodynamics using localized Lagrange multipliers.

José M. Galán¹ and Ramón Abascal²

¹ Dpto. Ingeniería del Diseño. Escuela Técnica Superior de Ingenieros. Avda. de los Descubrimientos s/n, E-41092, Sevilla, Spain. Email: mffern@us.es

² Grupo de Estructuras. ETSI. Sevilla, Spain. Email: abascal@us.es

Keywords: FEM, BEM, coupling, localized Lagrange multipliers, time-harmonic elastodynamics.

Abstract. The method of localized Lagrange multipliers can be used to interconnect regions with nonmatching meshes [1,2]. This technique has been successfully applied to connect BEM and FEM regions in elastostatics and contact problems [3,4]. In this work, a BEM-FEM partitioned formulation based on localized Lagrange multipliers is developed for antiplane time-harmonic elastodynamics. A discrete surface or frame is placed between the subdomains to approximate the interface displacements. This frame is connected to each substructure by using localized Lagrange multipliers collocated at the interface nodes as shown in Fig 1.

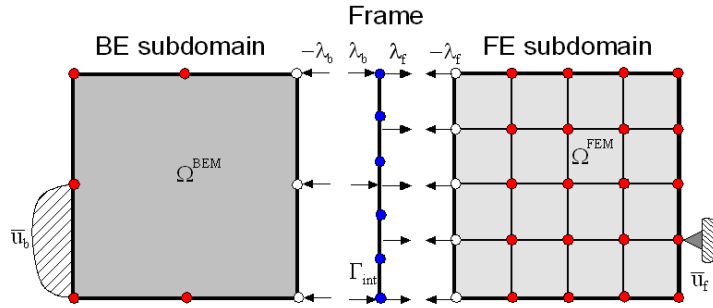


Fig 1. Sketch of nonmatching BE and FE subdomains connected by a frame through localized Lagrange multipliers. Blue: frame nodes. White: interface nodes (i.e. attached to a frame). Red: interior nodes.

The numerical implementation is firstly tested by solving a benchmark problem of known analytical solution, the plate under uniform traction. In addition, the formulation is used in an application from the field mechanical engineering: reflection of guided SH waves at the edge of a plate [5, 6].

Introduction

Let us assume two subdomains, Ω^{BEM} and Ω^{FEM} , connected by a common interface Γ_{int} . The first subdomain will be studied with BEM and the second with FEM, and let us assume nonmatching meshes at the interface, as illustrated in Fig 1. The method of localized Lagrange multipliers will be used. Instead of formulating the problem considering a direct interaction between those subdomains, we will introduce an auxiliary surface or *frame* between them and consider the coupling in terms of interaction of the two regions with this new surface.

Variational formulation of the coupled system

The virtual work variation of the total system, $\delta\Pi$ is composed by the energy of the FE substructure, $\delta\pi^{FEM}$, of the BEM structure, $\delta\pi^{BEM}$ and of the interface frame, $\delta\pi^{frame}$, and it can be written as [3]

$$\delta\Pi = \delta\pi^{FEM} + \delta\pi^{frame} + \delta\pi^{BEM} \quad (1)$$

The virtual work for the interface frame, $\delta\pi^{frame}$, enforces the displacement continuity between the subdomains and the frame at their interface Γ_{int} in a weak sense, with the following expression

$$\delta\pi^{frame} = \int_{\Gamma_{int}} \delta\{\lambda_{bi}(v_i - u_{bi})\} d\Gamma_{int} + \int_{\Gamma_{int}} \delta\{\lambda_{fi}(v_i - u_{fi})\} d\Gamma_{int} \quad (2)$$

where localized Lagrange multipliers and boundary displacements are introduced in the BE side, (λ_{bi}, u_{bi}) , and FE side, (λ_{fi}, u_{fi}) , respectively, and the frame displacements are denoted with v_i .

Discrete equations

BEM region. The displacement formulation of the direct BEM (DBEM) with time-harmonic full-space antiplane Green's function [7] is used. The starting point to obtain this formulation is Somigliana's identity

$$c_{ij}(\xi)u_{bj}(\xi, \omega) + \int_{\Gamma} T_{ij}(\mathbf{x}, \xi, \omega) \cdot u_{bj}(\mathbf{x}, \omega) d\Gamma(\mathbf{x}) = \int_{\Gamma} U_{ij}(\mathbf{x}, \xi, \omega) \cdot t_{bj}(\mathbf{x}, \omega) d\Gamma(\mathbf{x}) + \int_{\Gamma} U_{ij}(\mathbf{x}, \xi, \omega) \cdot \rho b_j d\Omega \quad (3)$$

where $U_{ij}(\mathbf{x}, \xi, \omega)$ and $T_{ij}(\mathbf{x}, \xi, \omega)$ are the displacements and tractions in the i -th direction at point \mathbf{x} when a unit time-harmonic antiplane load of frequency ω is applied in j -th direction at point ξ inside an infinite domain, t_{bj} are the components of the boundary tractions, u_{bj} are the components of the boundary displacements, b_j are the body loads, $c_{ij}(\xi)$ is the local tensor at point ξ , with $c_{ij}(\xi) = \delta_{ij}/2$ for smooth boundary points and $c_{ij}(\xi) = \delta_{ij}$ for internal points. Expressions for the fundamental solution can be found in [7].

The boundaries are discretized with continuous quadratic elements, which are used to interpolate the displacements and tractions at any boundary point from their corresponding nodal values with the following expressions

$$\{u_b\} = \mathbf{N}_b \mathbf{u}_b \quad ; \quad \{t_b\} = \mathbf{N}_b \mathbf{t}_b \quad (4)$$

where \mathbf{u}_b and \mathbf{t}_b are vectors containing the BE nodal displacements and tractions, respectively, and \mathbf{N}_b is the BE shape functions approximation matrix. By substituting these expressions in eq (3) and applying the boundary conditions, we obtain the following system of equations

$$\mathbf{H}(\omega)\mathbf{u}_b - \mathbf{G}(\omega)\mathbf{t}_b = \mathbf{b} \quad (5)$$

where $\mathbf{H}(\omega)$ and $\mathbf{G}(\omega)$ are the integrals over the boundary of the tractions and displacements of the fundamental solution, respectively, and vector \mathbf{b} contains the contributions of all boundary conditions.

A complementary virtual work for the BEM region can be defined as in [3], to enforce eq (5)

$$\delta\pi_{cvw}^{BEM} = \delta\mathbf{t}_b^T \{ \mathbf{H}(\omega)\mathbf{u}_b - \mathbf{G}(\omega)\mathbf{t}_b - \mathbf{b} \} \quad (6)$$

The BEM also contributes to the virtual work through the work done by BE tractions acting on the BE-frame interface when there is a virtual displacement. This additional term, $\delta\pi_{int}^{BEM}$, has the following expression

$$\delta\pi_{int}^{BEM} = \int_{\Gamma_{int}} \delta u_{bi} t_{bi} d\Gamma_{int} = \delta \mathbf{u}_b^T \left(\int_{\Gamma_{int}} \mathbf{N}_b^T \mathbf{N}_b d\Gamma_{int} \right) \mathbf{t}_b = \delta \mathbf{u}_b^T \mathbf{M}_b \mathbf{t}_b \quad (7)$$

where \mathbf{M}_b is a matrix that transforms boundary tractions into consistent nodal forces at the BE-frame interface [5]. Therefore,

$$\delta\pi^{BEM} = \delta\pi_{cvw}^{BEM} + \delta\pi_{int}^{BEM} \quad (8)$$

FEM region. The FEM region is discretized with isoparametric elements. The displacement field at any point is expressed in terms of the nodal values, \mathbf{u}_f , through the use of shape functions

$$\{u_f\} = \mathbf{N}_f \mathbf{u}_f \quad (9)$$

where \mathbf{u}_f is a vector containing the FE nodal displacements and \mathbf{N}_f is the FE shape functions approximation matrix and \mathbf{u}_f . Using this approximation, the virtual work of the FEM region in this time-harmonic case can be written in its usual form

$$\delta\pi^{FEM} = \delta\mathbf{u}_f^T \{(\mathbf{K} - \omega^2 \mathbf{M}) \mathbf{u}_f - \mathbf{f}_f\} \quad (10)$$

where \mathbf{K} and \mathbf{M} are the FE stiffness and mass matrices, respectively, both are symmetric, positive definite, and frequency independent, and \mathbf{f}_f is a nodal force vector.

Absorbing boundaries for guided waves in plates. An infinite plate can be discretized across the thickness with layer elements. A semi-analytical FE interpolation of the plate displacements can be written as

$$\{\mathbf{u}_p(x, y, t)\} = \mathbf{N}_p(y) \mathbf{u}_p \exp[i(kx + \omega t)] \quad (11)$$

where x is the propagation direction (parallel to the plate), y is the direction normal to the plate, \mathbf{N}_p is the finite element interpolation matrix in the y direction, \mathbf{u}_p is a vector containing the plate nodal displacements, k is the wavenumber in x direction. By application of the principle of virtual work and boundary conditions, the following quadratic eigensystem in k is obtained [5]

$$(k^2 \mathbf{A} + \mathbf{G} - \omega^2 \mathbf{M}) \mathbf{u}_a = \mathbf{f}_a \quad (12)$$

where \mathbf{A} , \mathbf{G} and \mathbf{M} are symmetric, positive definite, and frequency independent matrices. Its eigenvectors $\varphi^{(\alpha)}$ at any frequency are FE approximations to the SH guided modes in the plate. Once calculated, these modes can be used to express the scattered displacements in a semi-infinite plate as a normal mode expansion. This expansion, particularized at the edge of the plate, located at $x=0$, can be written as

$$\mathbf{u}_a - \mathbf{u}_a^I = \sum_{\alpha=1}^G \beta_\alpha \varphi^{(\alpha)} ; \quad \mathbf{f}_a - \mathbf{f}_a^I = \sum_{\alpha=1}^G \beta_\alpha (ik^{(\alpha)} \mathbf{A} \varphi^{(\alpha)}) \quad (13)$$

where β_α are mode participation factors, G is the total number of FE nodes, $k^{(\alpha)}$ is the α -th eigenvalue, \mathbf{u}_a^I and \mathbf{f}_a^I are the displacements and forces produced by an incident guided mode impinging from the far field onto the edge. By eliminating the mode participation factors in eq (13), we obtain the following

$$\mathbf{f}_a - \mathbf{f}_a^I = \mathbf{S}(\mathbf{u}_a - \mathbf{u}_a^I) \Rightarrow \mathbf{S}\mathbf{u}_a = \hat{\mathbf{f}}_a \quad (14)$$

where \mathbf{S} is the dynamic stiffness matrix of the semi-infinite plate, \mathbf{u}_a and \mathbf{f}_a are vectors with the nodal displacements and forces at the edge of the plate, \mathbf{u}_a^I and \mathbf{f}_a^I are the displacements and forces produced by an incident guided mode impinging from the far field onto the edge. The virtual work of this FE absorbing boundary conditions can be written as

$$\delta\pi^{absorb} = \delta\mathbf{u}_a^T \{\mathbf{S}\mathbf{u}_a - \hat{\mathbf{f}}_a\} \quad (15)$$

This expression is completely analogous to eq (10), by simply replacing $\mathbf{S} = (\mathbf{K} - \omega^2 \mathbf{M})$ and $\hat{\mathbf{f}}_a = \mathbf{f}_f$. Therefore, in the following we will include this term in $\delta\pi^{FEM}$ and its variables in \mathbf{u}_b , in order to simplify the notation. Hence, the FEM region will also include absorbing boundaries.

The frame. The displacements in any point of the frame are interpolated using isoparametric finite elements

$$\{v\} = \mathbf{N}_v \mathbf{v} \quad (16)$$

where \mathbf{N}_v is the frame interpolation matrix and \mathbf{v} is a vector containing the frame nodal displacements.

The localized multipliers are modeled as concentrated forces, that is, the interpolation functions for multipliers are Dirac's delta functions

$$\{\lambda(\xi)_f\} = \sum_i \delta(\xi - \xi_{fi}) \lambda_{fi}, \quad \{\lambda(\xi)_b\} = \sum_i \delta(\xi - \xi_{bi}) \lambda_{bi} \quad (17)$$

where ξ_{pi} , $p = f, b$ is the frame coordinate of the i -th interfacial node belonging to a substructure and the summations extend over all interfacial nodes. Substituting eq (17) in eq (2) gives

$$\delta\pi^{frame} = \delta\{\lambda_b^T (\mathbf{C}_b \mathbf{v} - \mathbf{u}_b)\} + \delta\{\lambda_f^T (\mathbf{C}_f \mathbf{v} - \mathbf{u}_f)\} \quad (18)$$

with the following definition

$$\mathbf{C}_p = \int_{\Gamma_{int}} \sum_i \delta(\xi - \xi_{pi}) \mathbf{N}_v d\Gamma_{int} = \sum_i \mathbf{N}_v(\xi_{pi}) \quad (19)$$

meaning that \mathbf{C}_p , with $p=f, b$, can be obtained by simple evaluation and summation of the frame shape functions at the interfacial node locations.

The coupled system. Substitution of eq (6), (7) (10) and (18) into eq (1), followed by the application of the chain rule in (18) and some reordering of terms, yields the following expression for the total energy variation

$$\begin{aligned} \delta\Pi = & \delta\mathbf{t}_b^T \{\mathbf{H}(\omega)\mathbf{u}_b - \mathbf{G}(\omega)\mathbf{t}_b - \mathbf{b}\} + \delta\mathbf{u}_b^T \{\mathbf{M}_b\mathbf{t}_b - \boldsymbol{\lambda}_b\} + \delta\boldsymbol{\lambda}_b^T (\mathbf{C}_b\mathbf{v} - \mathbf{u}_b) + \\ & + \delta\mathbf{u}_f^T \{(\mathbf{K} - \omega^2\mathbf{M})\mathbf{u}_f - \boldsymbol{\lambda}_f - \mathbf{f}_f\} + \delta\boldsymbol{\lambda}_f^T (\mathbf{C}_f\mathbf{v} - \mathbf{u}_f) + \delta\mathbf{v}^T \{\mathbf{C}_f^T\boldsymbol{\lambda}_f + \mathbf{C}_b^T\boldsymbol{\lambda}_b\} \end{aligned} \quad (20)$$

By enforcing that the virtual work must be zero for all possible virtual displacements, $\delta\Pi = 0$, we get the system of equations for the frame-coupled system

BEM equations →	$-\mathbf{G}(\omega) \quad \mathbf{H}(\omega) \quad \mathbf{0}$	$\mathbf{0}$	$\mathbf{0}$	$\mathbf{0}$	$\mathbf{0}$	[]
t _b -λ _b relation →	\mathbf{M}_b	$\mathbf{0}$	$-\mathbf{I}$	$\mathbf{0}$	$\mathbf{0}$		
BE-frame continuity →	$\mathbf{0}$	$-\mathbf{I}$	$\mathbf{0}$	$\mathbf{0}$	$\mathbf{0}$	[]
FEM equations →	$\mathbf{0}$	$\mathbf{0}$	$\mathbf{0}$	$(\mathbf{K} - \omega^2\mathbf{M})$	$-\mathbf{I}$		
FE-frame continuity →	$\mathbf{0}$	$\mathbf{0}$	$\mathbf{0}$	$-\mathbf{I}$	$\mathbf{0}$	[]
Frame equilibrium →	$\mathbf{0}$	$\mathbf{0}$	\mathbf{C}_b^T	$\mathbf{0}$	\mathbf{C}_f^T		

FEM equations →	$-\mathbf{G}(\omega) \quad \mathbf{H}(\omega) \quad \mathbf{0}$	$\mathbf{0}$	$\mathbf{0}$	$\mathbf{0}$	$\mathbf{0}$	[]
t _b -λ _b relation →	\mathbf{M}_b	$\mathbf{0}$	$-\mathbf{I}$	$\mathbf{0}$	$\mathbf{0}$		
BE-frame continuity →	$\mathbf{0}$	$-\mathbf{I}$	$\mathbf{0}$	$\mathbf{0}$	$\mathbf{0}$	[]
FEM equations →	$\mathbf{0}$	$\mathbf{0}$	$\mathbf{0}$	$(\mathbf{K} - \omega^2\mathbf{M})$	$-\mathbf{I}$		
FE-frame continuity →	$\mathbf{0}$	$\mathbf{0}$	$\mathbf{0}$	$-\mathbf{I}$	$\mathbf{0}$	[]
Frame equilibrium →	$\mathbf{0}$	$\mathbf{0}$	\mathbf{C}_b^T	$\mathbf{0}$	\mathbf{C}_f^T		

which is non-symmetrical due to the contribution of the BE substructure.

Numerical results

Layer under uniform antiplane shear. An infinite linearly elastic layer of constant thickness, h , fixed at its base and loaded with a uniform time-harmonic antiplane shear on its top surface, is considered. The analytical solution for this problem, assuming no damping is present, is the following

$$u_z(y) = \frac{p_z}{\mu} \frac{\sin(k_s y)}{k_s \cos(k_s h)}; k_s = \frac{\omega}{c_s}; c_s = \sqrt{\frac{\mu}{\rho}}; \omega_n = (2n-1) \frac{\pi c_s}{2h}, \text{ with } n \in \mathbb{N} \quad (22)$$

where c_s is the speed of shear waves in the material, μ is the shear modulus, ρ is the density, ω is the excitation frequency, k_s the wavenumber of shear waves at that frequency and ω_n the n th natural frequency.

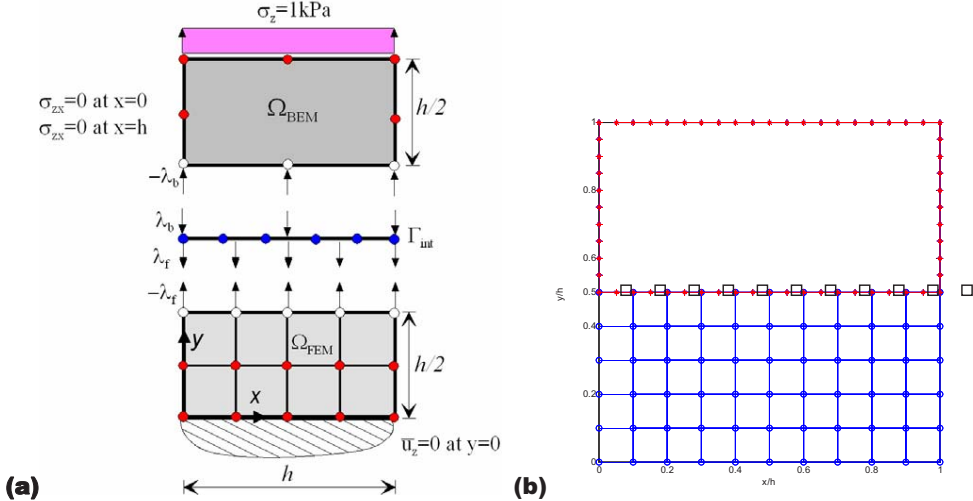


Fig 2. (a) Sketch of the layer problem and partitioned formulation used to solve it. (b) Plot of the actual meshes used. Circles: FE nodes. Stars: BE nodes. Squares: frame nodes.

A square domain with symmetry boundary conditions on its vertical sides ($x=0, x=h$) is used for the computations. Its upper half, $y/h \in [0.5, 1]$, is discretized with quadratic BEM elements of uniform length, $L_{BE}=h/10$. Its lower half, $y/h \in [0, 0.5]$, is discretized with linear quadrilateral FEM elements of the same shape and size (squares with side $L_{FE}=h/10$). The frame, located at $y=h/2$, is discretized with a uniform mesh of 1D linear elements, with an element size $L_{frame}=h/10$. The meshes are plotted in Fig 2. Notice that the BE and FE domains have different order of interpolation and nonmatching nodes. The numerical results obtained are plotted in Fig 3 for frequencies going well above the 2nd natural frequency, ω_2 . An excellent agreement with the exact solution is found. Although the results are plotted in a dimensionless manner, the following numerical parameters were used for the calculations: $h=1\text{m}$, $p_z=1\text{kPa}$, $\mu=1\text{kPa}$, $\rho=1\text{t/m}^3$, $c_s=1\text{m/s}$.

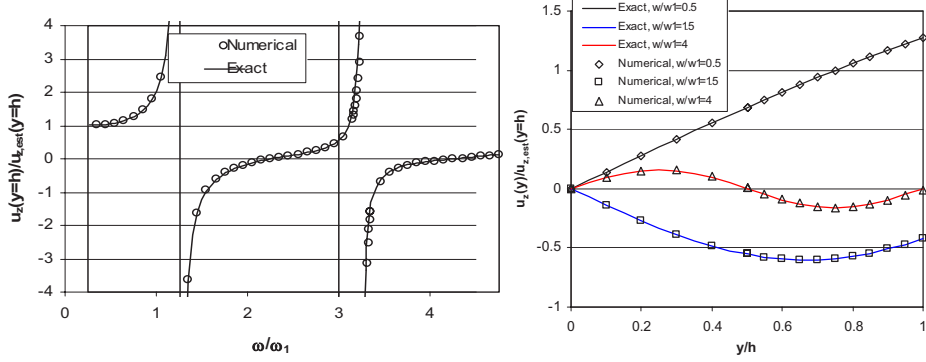


Fig 3. Comparison of the numerical results with the exact solution. Left: Displacement at the top surface of the layer, $u_z(y=h)$, normalized with its static value, $u_{z,est}(y=h) = p_z / \mu$, versus dimensionless frequency. Right: vibration pattern of the layer for three different values of the dimensionless frequency, $\omega/\omega_1 = 0.5, 1.5, 4$.

Reflection of guided SH waves at the edge of semi-infinite plates. A single guided SH mode impinges onto the free edge of a semi-infinite homogeneous plate of constant thickness $d=2h$. A portion of the plate near the edge will be discretized with BEM or FEM, and an FE absorbing boundary condition will be used to take into account the radiation of energy towards infinity through the plate. Dimensionless frequencies in the range $\Omega=\omega h/c_s < 2\pi$, where up to four propagating guided SH modes exist, are studied.

Four different solution strategies, depicted in Fig 4, half of which use localized Lagrangian multipliers, will be applied. Our goal is to determine if the frame introduces some artificial reflection or perturbation in the numerical results, in comparison to direct coupling techniques that were previously applied [5,6]. In order to allow comparisons at the same level of discretization error, meshes with matching nodes at the interfaces will be used in all cases. All regions will be discretized with uniform meshes: quadratic BE elements, $L_{BE}=h/5$; linear quadrilateral FE elements, $L_{FE}=h/10$ (side length of the square FE elements); linear frame elements, $L_{frame}=h/10$. In all the cases the FE absorbing boundary is derived with a quadratic FE discretization in the y direction, and it is directly coupled to a BE region.

When a single guided SH mode impinges onto the free edge of a semi-infinite homogeneous plate of constant thickness $d=2h$, it gets reflected back without any mode conversion [6]. All the numerical results show no mode conversion. In addition, the maximum error in the balance of energy flux (i.e. difference between the incident and scattered energy fluxes) is presented in Table 1, which can be used as a measure of the quality of the numerical results. By comparison between (a) and (b), and also between (c) and (d), it can be concluded that the frame does not introduce any additional errors, beyond those due to discretization.

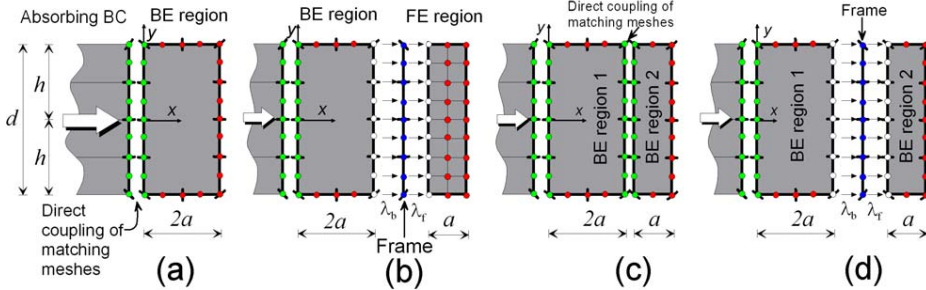


Fig 4. Sketch of the four solution strategies applied to solve the SH guided wave reflection problem. (a) FE absorbing boundary directly coupled to BEM region with $a=h/5$. (b) Same as (a), but with an additional FE region coupled with a frame. (c) Same as (a), but with an additional BEM region directly coupled to the first one. (d) Same as (c), but the 2nd BEM region is connected through a frame.

Incident mode	Error in energy flux balance: $\varepsilon = \left(\frac{E_{refl}}{E_{inc}} - 1 \right) \cdot 100$, in %.			
	BEM (a)	BEM-frame-FEM (b)	BEM-BEM (c)	BEM-frame-BEM (d)
SH0	0.029	0.029	0.022	0.022
SH1	0.049	0.049	0.052	0.052
SH2	0.102	0.102	0.194	0.194
SH3	0.680	0.680	1.293	1.293

Table 1. Reflection of guided SH waves at the free edge of a semi-infinite plate. Numerical results for several solution strategies.

Summary

A BEM-FEM coupling scheme for antiplane time-harmonic elastodynamics based on connecting substructures to an interface frame using localized Lagrange multipliers has been presented. This method has been successfully applied to solve a structural vibration problem and a guided wave scattering problem.

References

- [1] K.C. Park, C.A. Felippa *International Journal for Numerical Methods in Engineering*, **47**, 395-418. (2000).
- [2] K.C. Park, C.A. Felippa and G. Rebel *International Journal for Numerical Methods in Engineering*, **53**, 2117-2142. (2002).
- [3] J.A. González, K.C. Park and C.A. Felippa *International Journal for Numerical Methods in Engineering*, **69**, 2058-2074 (2007).
- [4] J.A. González, K.C. Park and C.A. Felippa *Communications In Numerical Methods In Engineering*, **22**, 319-333 (2006).
- [5] J.M. Galán and R. Abascal *International Journal for Numerical Methods in Engineering*, **53**, 1145-1173 (2002).
- [6] J.M. Galán and R. Abascal *Computers & Structures*, **83**, 740-757 (2005).
- [7] J. Domínguez *Boundary Elements in Dynamics*, CMP (1993).

BEM-FEM coupling in contact problems

José A. González¹, K. C. Park², Carlos A. Felippa² and Ramón Abascal³

¹Escuela Superior de Ingenieros, Universidad de Sevilla, Spain. japerez@us.es

²Department of Aerospace Engineering, University of Colorado, USA. kcpark@colorado.edu

³Escuela Superior de Ingenieros, Universidad de Sevilla, Spain. abascal@us.es

Keywords: Contact, BEM-FEM coupling.

Abstract. This work presents a unified formulation for the combination of the Finite Element Method (FEM) with the Boundary Element Method (BEM) in quasi-static 3D frictional contact problems. Resolution methods for the contact problem between non-matching meshes have traditionally been based on a direct coupling of the contacting solids, a strategy that generates strongly coupled systems that require a deep knowledge of the discretization characteristics at each side of the interface and complicates the process of mixing different numerical techniques. Our proposal is to approximate the interface variables in a new surface, or *contact frame*, inserted between the FEM and BEM meshes and connected to the contacting substructures using localized Lagrange multipliers (LLMs) collocated at the mesh-interface nodes. This methodology provides a partitioned formulation which preserves software modularity and facilitates the connection of non-matching FEM and BEM meshes.

Introduction; the contact frame

Let us consider two solids in contact and denote their domains Ω and $\bar{\Omega}$ with a common interface Γ_c . To formulate the contact problem, instead of considering the direct interaction between these two bodies during the contact process, we will insert a deforming non-physical surface called contact frame Λ with $\Gamma_c \subset \Lambda$ and reformulate the contact problem in terms of interaction of the solids with this auxiliary surface using LLMs collocated on each side of the frame.

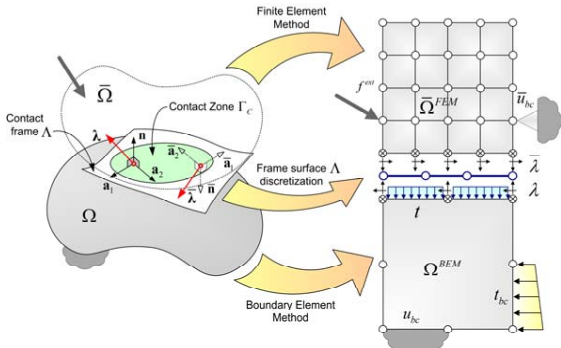


Figure 1. Abstract representation of two solids in contact with a frame and their discrete approximation using different numerical methods.

The contact forces acting on the frame are represented in the exploded view of Fig. (1) where the LLMs connecting the solid Ω with the frame are named using the vector quantity $\lambda = (\lambda_n, \lambda_{t_1}, \lambda_{t_2})'$ and the multipliers connecting solid $\bar{\Omega}$ are named $\bar{\lambda} = (\bar{\lambda}_n, \bar{\lambda}_{t_1}, \bar{\lambda}_{t_2})'$. These forces are expressed using two

locally orthonormal base systems attached to the frame; $\mathbf{B} = [\mathbf{n}, \mathbf{a}_1, \mathbf{a}_2]$ used to describe λ and $\bar{\mathbf{B}} = [\bar{\mathbf{n}}, \bar{\mathbf{a}}_1, \bar{\mathbf{a}}_2]$ used for $\bar{\lambda}$. These frame local systems are defined in the following way; \mathbf{a}_1 and \mathbf{a}_2 are the orthogonal vectors contained in the frame tangent plane at the considered point and vector \mathbf{n} points towards solid $\bar{\Omega}$. The barred base system $\bar{\mathbf{B}}$ at the same position will be defined in opposite direction to \mathbf{B} .

A key approach of the present localized formulation is to treat the non-matching contact interfaces by the method of LLMs using either the BEM or the FEM to model the contacting solids.

Variational formulation

The variational functional in the FEM-FEM contact case represents the total energy of the system and is composed by the energy of the two substructures plus the interface constraint functional associated with the contact phenomena

$$\delta\Pi = \delta\pi^{body1} + \delta\bar{\pi}^{body2} + \delta\pi^{int} \quad (1)$$

where the contact interface potential $\delta\pi^{int}$ groups contributions from both sides $\delta\pi^{int} = \delta\pi_i + \delta\bar{\pi}_i$ and will be derived in this section. To do that, let us decompose each one of the two interface functionals into two terms

$$\begin{aligned} \delta\pi_i &= \delta\pi_k + \delta\pi_c \\ \delta\bar{\pi}_i &= \delta\bar{\pi}_k + \delta\bar{\pi}_c \end{aligned} \quad (2)$$

the first one is related with the kinematic positioning of the frame, that is enforced in a weak sense using the variational form

$$\delta\pi_k = \iint_{\Gamma_c} (\delta\{\lambda \cdot [\mathbf{B}^t(\mathbf{x} - \mathbf{y}) - \mathbf{k}]\}) d\Gamma_c \quad (3)$$

and the second one represents the virtual work of the contact forces; a contribution to the weak form that can be expressed, using the frictional cone projection operator $\mathbf{P}_{\triangleleft}(\lambda)$ (see [2]), in the following way

$$\delta\pi_c = \iint_{\Gamma_c} (\mathbf{P}_{\triangleleft}(\lambda(r)) \cdot \delta\mathbf{k}) d\Gamma_c \quad (4)$$

equation that added to (3) and substituted back in (2) provides the expression for the total variation of the interface potential at the non barred side

$$\begin{aligned} \delta\pi_i &= \iint_{\Gamma_c} (\delta\lambda \cdot \langle \mathbf{B}^t(\mathbf{x} - \mathbf{y}) - \mathbf{k} \rangle + (\delta\mathbf{u} - \delta\mathbf{v}) \cdot \langle \mathbf{B}\lambda \rangle \\ &\quad + \delta\mathbf{v}_a \cdot \langle \mathbf{Q}^a \Phi_a(\mathbf{x} - \mathbf{y}) \rangle + \delta\mathbf{k} \cdot \langle -\lambda + \mathbf{P}_{\triangleleft}(\lambda(r)) \rangle) d\Gamma_c \end{aligned} \quad (5)$$

with $\Phi_a = \lambda_{ta} \mathbf{I} + \lambda_n e^{a\beta} (\mathbf{a}_\beta \times \mathbf{I})$.

Discrete equations

The discrete contact problem will be defined in terms of contact pairs, i.e. couples formed by a boundary node and its associated frame element. Those contact pairs are established before starting each time step, calculating for every potentially contacting boundary node its nearest frame element and projecting geometrically on it, see Fig. 2.

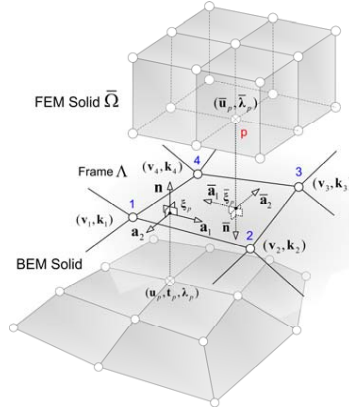


Figure 2. Each contact pair is constituted by a hitting boundary node p and its closest frame element.

The frame displacements $\mathbf{v}(\xi_1, \xi_2)$ and its average distance to the solids $\mathbf{k}(\xi_1, \xi_2)$ are interpolated using isoparametric finite elements in the following form

$$\mathbf{v}(\xi_1, \xi_2) = \mathbf{N}(\xi_1, \xi_2) \begin{bmatrix} v_1 \\ \vdots \\ v_{n_f} \end{bmatrix}, \quad \mathbf{k}(\xi_1, \xi_2) = \mathbf{N}(\xi_1, \xi_2) \begin{bmatrix} k_1 \\ \vdots \\ k_{n_f} \end{bmatrix} \quad (6)$$

where n_f is the number of nodes in the frame element, and \mathbf{N} is the shape functions approximation matrix.

The choice for multipliers discretization is to model them as concentrated forces, that is, support functions are Dirac's delta functions

$$\lambda(\xi_1, \xi_2) = \lambda_p \cdot \delta(\xi - \xi_p) \quad (7)$$

with $\xi = (\xi_1, \xi_2)$ and ξ_p the frame coordinates of the node projection, Fig. 2. This definition of the contact forces will reduce integrations over the contact zone to summations over the contact pairs, i.e.

$$\iint_{\Gamma_c} \lambda(\xi_1, \xi_2) \cdot \mathbf{f}(\xi_1, \xi_2) d\Gamma_c = \sum_{p=1}^{n_p} \lambda_p \cdot \mathbf{f}(\xi_p) \quad (8)$$

with n_p the total number of contact pairs. Eq. (8) is useful in order to maintain the contact interface generic, leading to modular coupling software since the frame needs to know very little information about the contacting solids.

To manage the discrete variables we have to introduce the substructural interface nodal indicator \mathcal{L} , the well known boolean finite element assembling operator defined in the following way

$$\begin{aligned} \mathbf{u}_p &= \mathcal{L}_{up} \mathbf{u}, \quad \lambda_p = \mathcal{L}_{\lambda p} \lambda \\ \mathbf{v}_p &= \mathcal{L}_{vp} \mathbf{v}, \quad \mathbf{k}_p = \mathcal{L}_{kp} \mathbf{k} \end{aligned} \quad (9)$$

where $\mathcal{L}_{\square p}$ is used to extract the variable associated with a boundary node p from the global vector of unknowns \square with $\square = u, v, k..$

BEM-FEM contact

Modularity of the preceding formulation becomes clear when it is extended to make possible a combination of contacting solids modeled using either the FEM or the BEM. For simplicity and without any loss of generality, we focus on the case where the elastic equations of the first solid in contact are obtained using the BEM and the second solid is modeled using the FEM. In a previous work by the authors [1] it was shown that in coupled elastostatic problems without contact conditions, the variational functional of a BE solid $\delta\pi^{\text{body}}$ to be combined with a variational form like (1) can be expressed by adding two terms: a complementary virtual work associated with the BE elastic equations $\delta\pi^{\text{BEM}}$ and an extra term to transform the boundary tractions into forces $\delta\pi^{\text{lump}}$, i.e. $\delta\pi^{\text{body}1} = \delta\pi^{\text{BEM}} + \delta\pi^{\text{lump}}$. The first term, associated with the BEM elastic equations, can be written

$$\delta\pi^{\text{BEM}} = \delta\mathbf{t}^t \cdot \{\mathbf{H}\mathbf{u} - \mathbf{G}\mathbf{t} - \mathbf{b}\} \quad (10)$$

where vectors \mathbf{t} and \mathbf{u} contain the solid boundary tractions and displacements respectively, \mathbf{H} and \mathbf{G} are the BEM system matrices obtained when assembling elemental contributions and vector \mathbf{b} is a known function of the boundary conditions. Those boundary tractions are in equilibrium with the Lagrange multipliers localized in the contact zone applying an energy equivalence principle that produces the following term

$$\delta\pi^{\text{lump}} = \delta\mathbf{u}^t \cdot \{\mathbf{M}\mathbf{t} + \mathbf{E}\lambda\} \quad (11)$$

with a lumping matrix used to transform tractions into equivalent forces given by

$$\mathbf{M} = \sum_{e=1}^{n_e} \mathcal{L}_{te}^t \mathbf{M}_e \mathcal{L}_{te} \quad (12)$$

where n_e is the number of boundary elements situated at the interface, \mathcal{L}_{te} is the boolean assembling operator used to extract the variables associated with a boundary element e from the global vector of unknowns and

$$\mathbf{M}_e = \int_{\Gamma_e} \mathbf{N}^T \mathbf{N} d\Gamma_e \quad (13)$$

is the elemental lumping matrix for an element e with boundary Γ_e . Finally and because not all the boundary nodes belong to the contact zone, a boolean matrix \mathbf{E} is used to associate the LLMs with their corresponding global nodes.

Substituting these two terms into the total variational equation, the functional variation is obtained for the BEM-FEM coupling case

$$\begin{aligned} \delta\Pi^{\text{BF}} = & \delta\mathbf{t}^t \cdot (\mathbf{H}\mathbf{u} - \mathbf{G}\mathbf{t} - \mathbf{b}) + \delta\mathbf{u}^t \cdot (\mathbf{M}\mathbf{t} + \mathbf{E}\lambda) + \delta\bar{\mathbf{u}}^t \cdot \bar{\mathbf{f}} + \\ & \delta\lambda^t \cdot \mathbf{g} + \delta\bar{\lambda}^t \cdot \bar{\mathbf{g}} - \delta\mathbf{v}^t \cdot (\mathbf{q} + \bar{\mathbf{q}}) + \delta\mathbf{k}^t \cdot (\mathbf{p} + \bar{\mathbf{p}}) \end{aligned} \quad (14)$$

where it should be noted that this new expression does not represent the variation of a potential energy functional.

The stationary of the BEM-FEM variational equation $\delta\Pi^{\text{BF}} = 0$ is obtained when solving for a new group of unknowns $\mathbf{z} = (\mathbf{u}, \bar{\mathbf{u}}, \mathbf{t}, \lambda, \bar{\lambda}, \mathbf{v}, \mathbf{k})$ the following B-differentiable system

$$\mathbf{F}^{\text{BF}}(\mathbf{z}) = \begin{bmatrix} \mathbf{h} \\ \bar{\mathbf{f}} \\ \mathbf{m} \\ \mathbf{g} \\ \bar{\mathbf{g}} \\ -\mathbf{q} - \bar{\mathbf{q}} \\ \mathbf{p} + \bar{\mathbf{p}} \end{bmatrix} = 0 \quad (15)$$

with definitions for the first and third equations given by

$$\mathbf{h} = \{\mathbf{H}\mathbf{u} - \mathbf{G}\mathbf{t} - \mathbf{b}\}, \mathbf{m} = \{\mathbf{M}\mathbf{t} + \mathbf{E}\lambda\} \quad (16)$$

where \mathbf{h} represents the BE elastic equations and \mathbf{m} the lumping procedure from tractions to forces. So carrying out the stationary conditions of eq. (15) we find the following equilibrium equation set

$$\begin{bmatrix} \mathbf{H} & \mathbf{0} & -\mathbf{G} & \mathbf{0} & \mathbf{0} & \mathbf{0} & \mathbf{0} \\ \mathbf{0} & \bar{\mathbf{K}} & \mathbf{0} & \mathbf{0} & \bar{\mathbf{B}} & -\bar{\mathbf{L}}_v & \mathbf{0} \\ \mathbf{0} & \mathbf{0} & \mathbf{M} & \mathbf{E} & \mathbf{0} & -\mathbf{L}_v & \mathbf{0} \\ \mathbf{B}^t & \mathbf{0} & \mathbf{0} & \mathbf{0} & \mathbf{0} & -\mathbf{L}_b & -\mathbf{N}_k \\ \mathbf{0} & \bar{\mathbf{B}}^t & \mathbf{0} & \mathbf{0} & \mathbf{0} & -\bar{\mathbf{L}}_b & -\bar{\mathbf{N}}_k \\ -\mathbf{L}_v^t & -\bar{\mathbf{L}}_v^t & \mathbf{0} & -\mathbf{L}_b^t & -\bar{\mathbf{L}}_b^t & -\mathbf{D}_v - \bar{\mathbf{D}}_v & \mathbf{0} \\ \mathbf{0} & \mathbf{0} & \mathbf{0} & \mathbf{P}_\lambda & \bar{\mathbf{P}}_\lambda & \mathbf{0} & \mathbf{P}_k + \bar{\mathbf{P}}_k \end{bmatrix} \begin{bmatrix} \Delta\mathbf{u} \\ \Delta\bar{\mathbf{u}} \\ \Delta\mathbf{t} \\ \Delta\lambda \\ \Delta\bar{\lambda} \\ \Delta\mathbf{v} \\ \Delta\mathbf{k} \end{bmatrix} = \begin{bmatrix} -\mathbf{h} \\ -\bar{\mathbf{f}} \\ -\mathbf{m} \\ -\mathbf{g} \\ -\bar{\mathbf{g}} \\ \mathbf{q} + \bar{\mathbf{q}} \\ -\mathbf{p} - \bar{\mathbf{p}} \end{bmatrix} \quad (17)$$

a non-symmetrical and strictly non-differentiable system representing the partitioned equations of motion for the frame-based BEM-FEM contact problem that is solved using the Generalized Newton Method with Line Search (GNMLS).

Note that the BEM-BEM contact formulation is straightforward using the same approach.

Application

In this example we study the case of a stopped tire connected to an infinitely rigid wheel that presents a controlled vertical displacement, imposed on its center axis, making the tire to interact with the ground surface. This problem is usually solved considering the road as an infinitely rigid surface, a good approximation when the stiffness ratio between the tire and the road is small and that liberates the analyst from the necessity of modeling a complete half space domain with its associated computational cost.

The analysis of the solids is taken under the hypotheses of small deformations and linear elastic behavior of the materials, with constitutive parameters for the tire $E_t=10$, $v_t=0.3$ and for the soil $E_s=1$, $v_s=0.3$. A comparable stiffness of the materials makes unacceptable substituting the soil by a rigid plane and this is the reason why the BE method is used to approximate the half space while the tire is modelled using the FEM. In the contact region a static friction coefficient of $\mu=0.25$ is supposed to simulate the frictional contact conditions.

Fig. 3 shows the displacement contours obtained in the boundary of the solids when a vertical displacement of 0.2 is imposed on the wheel. It is also represented the relative error of the solution obtained by the GNMLS algorithm with the iteration number, presenting a quadratical convergence rate to the solution and reaching a relative error $H(z_k)/H(z_1)$ of 10^{-9} after only six iterations of the GNMLS algorithm.

Conclusions

A unified formulation combining the BEM and FEM in 3D frictional contact problems using LLMs to connect different substructures to an adaptative contact frame is presented. The contact conditions are imposed mathematically using projection functions and the contact frame is allowed to move freely between the substructures maintaining the contact zone as an unknown. The GNMLS is applied to solve the non-smooth system of equations representing the equations of motion.

The algorithm and introduced formulations prove to be very robust and efficient when solving 3D non-matching contact problems even when presenting strong material heterogeneities and BEM-FEM transitions through the contact zone. Suggested methodology greatly simplifies the procedure to solve this

kind of problems, minimizing the geometrical knowledge of the contacting substructures needed to formulate the contact interface behavior.

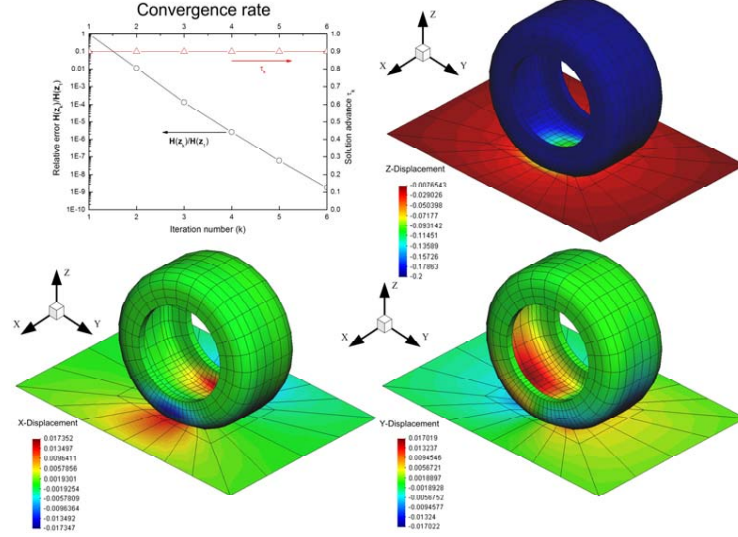


Figure 3. Displacement fields on the road and the tire when a vertical rigid body displacement is imposed on the wheel.

References

- [1] J. A. González, K. C. Park and Carlos A. Felippa, *FEM and BEM coupling in elastostatics using localized Lagrange multipliers*, *International Journal of Numerical Methods in Engineering*, **69**, 2058-2074 (2007).
- [2] J. A. González, K. C. Park and Carlos A. Felippa, *Partitioned formulation of frictional contact problems using localized Lagrange multipliers*, *Communications in Numerical Methods in Engineering*, **22**, 319-333 (2005).

BEM-FEM Coupling Model for the Analysis of Soil-Pile-Structure Interaction in the Frequency Domain

Luis A. Padrón, Juan J. Aznárez y Orlando Maeso

University Institute of Intelligent Systems and Numerical Applications in Engineering (SIANI)

University of Las Palmas de Gran Canaria, 35017, Spain

Email: {ipadron, jaznarez, omaeso}@iusiani.ulpgc.es

Keywords: Dynamic Soil-Structure Interaction (SSI), Structure-Soil-Structure Interaction, Boundary Elements, BEM-FEM Coupling, Piles, Pile Groups, Shear Buildings, Seismic Response.

Abstract. This communication presents a three-dimensional Boundary Element – Finite Element coupling model for the dynamic analysis of soil-pile-structure interaction in the frequency domain. The soil is modelled by the Boundary Element Method (BEM) and one-dimensional Finite Elements are used to model the piles as Bernoulli beams, whose heads can be linked by rigid pile caps. One or more superstructures can also be considered as piled shear building models, so that dynamic SSI problems can be addressed. Some structure-soil-structure interaction analyses are presented. It is shown that the presence of neighbouring structures with similar fundamental periods modifies the dynamic behaviour of buildings founded on soft to medium soils.

Introduction

The study of soil-structure interaction (SSI) has received considerable attention during the last decades [1, 2, 3, 4]. More recent [5] is the study of site-city interaction (SCI), focused on the influence of the presence of a densely urbanized area on the seismic response of zones placed inside or outside the city. SSI, site effects and structure-soil-structure interaction phenomena are the basic components of SCI. However, structure-soil-structure interaction, by itself, has received little attention, and even less work has been reported on the interaction between piled structures.

A three-dimensional BEM-FEM coupling model for the dynamic analysis of pile groups [6, 7] has been developed by the authors. The soil is modelled by the Boundary Element Method (BEM) [8] as a continuum, semi-infinite, isotropic, zoned homogeneous, linear, viscoelastic medium. The pile-soil interface tractions arising from the pile-soil interaction are regarded, from the integral equation point of view, as internal body forces. One-dimensional Finite Elements are used to model the piles as Bernoulli beams, whose heads can be linked by rigid pile caps. The code can take into account layered soils of generic stratigraphy and topography, including deposits and inclusions, and generic harmonic loads and incident seismic waves can be considered. Shear multi-storey piled structures can also be included in the model. Thus, the model can be used to obtain dynamic impedances and interaction factors of piled foundations and, under linear assumptions, the dynamic behaviour of complex soil-pile-structure systems can be studied rigorously with an affordable number of degrees of freedom.

This code has been used to study the structure-soil-structure interaction problem. Some results are presented here to show how the proximity of structures with similar fundamental periods modifies the dynamic behaviour of buildings and piles.

Problem Definition

All results presented herein correspond to one-storey shear buildings on a 3×3 fixed-head pile group embedded on a viscoelastic half-space. The geometric properties of building and piles are depicted in Fig. 1, where b = foundation halfwidth, L and d = length and sectional diameter of piles, s = centre-to-centre spacing between adjacent piles, h = structure effective height, m = structure effective mass, and m_o and I_o = cap mass and moment of inertia. The mechanical and geometrical properties of the piles and soil are defined by the following parameters: $s/d = 5$, pile/soil modulus ratio $E_p/E_s = 1000$, ratio between soil and pile densities $\rho_s/\rho_p = 0.7$, piles aspect ratio $L/d = 15$, soil damping coefficient $\beta_s = 0.05$ and Poisson ratio $\nu_s = 0.4$. The structure is defined by: aspect ratio $h/b = 2, 3$ and 4 ; structure/soil mass ratio $m/4\rho b^2 h = 0.20$; foundation/structure mass ratio $m_o/m = 0.25$; foundation mass moment of inertia $I_o = 20m$; structural damping $\zeta = 0.05$; and structure/soil stiffness ratio $h/T \cdot c_s = 0.3$, T being the fixed-base structure fundamental period and c_s the soil shear wave velocity. All figures are plotted against the dimensionless frequency $a_o = \omega d/c_s$, being ω the circular frequency.

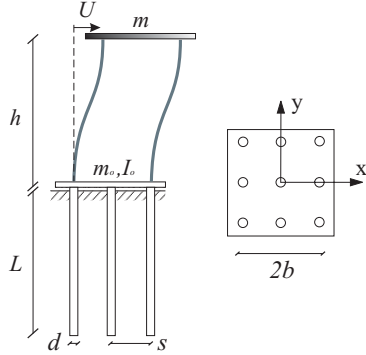


Fig. 1. Soil-pile-structure system.

Results

Fig. 2 presents the harmonic response spectra for structures of aspect ratio $h/b = 2$ and 4 subject to vertically-incident SH waves, considered alone or in groups of three as depicted in the figure, with the slenderest structure in the middle and two other structures symmetrically placed at both sides. Two different separations between middle points of adjacent structures have been considered, as well as two different alignments: one along the same direction of the free field shaking due to the SH incident wave (the y axis) and another one along its perpendicular. The results are presented in terms of the spectral horizontal deformation $\Omega^2 u / (\omega^2 u_{ff})$, where Ω is the fundamental frequency of the fixed-base structure, u is the amplitude of the horizontal displacement of the top mass along the y axis relative to the foundation displacement and excluding rotations (*i.e.* the structural horizontal deformation), and u_{ff} is the amplitude of the free-field motion at the ground surface. It is worth noting here how the SSI effect becomes apparent in these cases, as the fixed-base dimensionless fundamental frequency of $h/b = 2$ and 4 structures are 0.188 and 0.094 respectively, while the flexible-base fundamental frequencies are 0.155 and 0.074 . However, the interaction between structures of non-similar fundamental frequencies exists but is negligible.

Fig. 3 presents the harmonic response spectra for structures of aspect ratio $h/b = 2, 3$ and 4 subject to vertically-incident SH waves, considered alone or in groups of three *identical* structures with two different alignments as above, where it is shown that the interaction between structures of similar

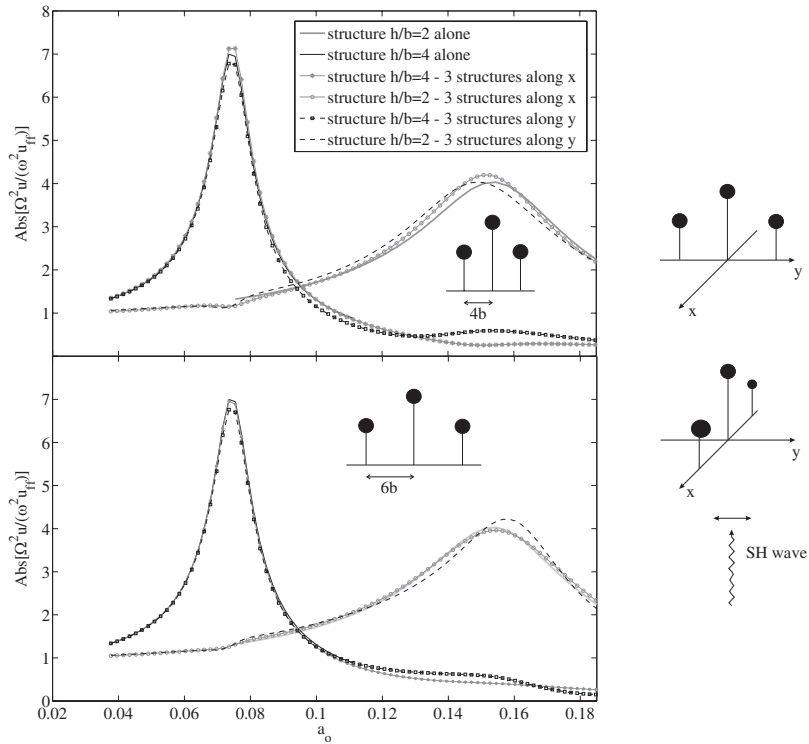


Fig. 2. Interaction between structures of non-similar fundamental frequencies in terms of their harmonic response spectra for different configurations.

fundamental frequencies highly modifies their dynamic response. In this case, the separation between adjacent structures is defined by the number of wave lengths between middle points of adjacent structures at the flexible-base structure fundamental frequency. Although problems with the same number of wave lengths between adjacent structures are not equivalent because the foundation is the same while the aspect ratio changes, it is shown that the same trend occurs in these cases. For instance, all plots on the left correspond to a distance of half a wave length for structures with different aspect ratios, and in all cases the response of the structures aligned according to the incident wave shaking direction is amplified while the response of structures aligned on the x axis decrease. When the distance corresponds to a quarter of wave length all responses decrease, but when it corresponds to three quarters, all responses increase. A different phenomenon that takes place when two or more similar structures interact is that a shifting in the flexible-base fundamental frequency of the system occurs, and it is different according to the distance, the structural characteristics and the direction of alignment.

The torsional motion of a symmetric structure alone (as that depicted in Fig. 1) to a vertically-incident SH wave acting along the y axis is null. However, the interaction between structures aligned along the x axis induces torsional motions. Fig. 4 presents the torsional motion of *two* structures of aspect ratios 2 and 4, and also, the torsional response of the lateral structure of the configuration of *three* different structures depicted in Fig. 2, with separations $4b$. The torsional

stiffness of the structures has been assumed to be very high, so that floor and cap present similar motions. It can be seen that the interaction exists and is even larger in the case of three buildings.

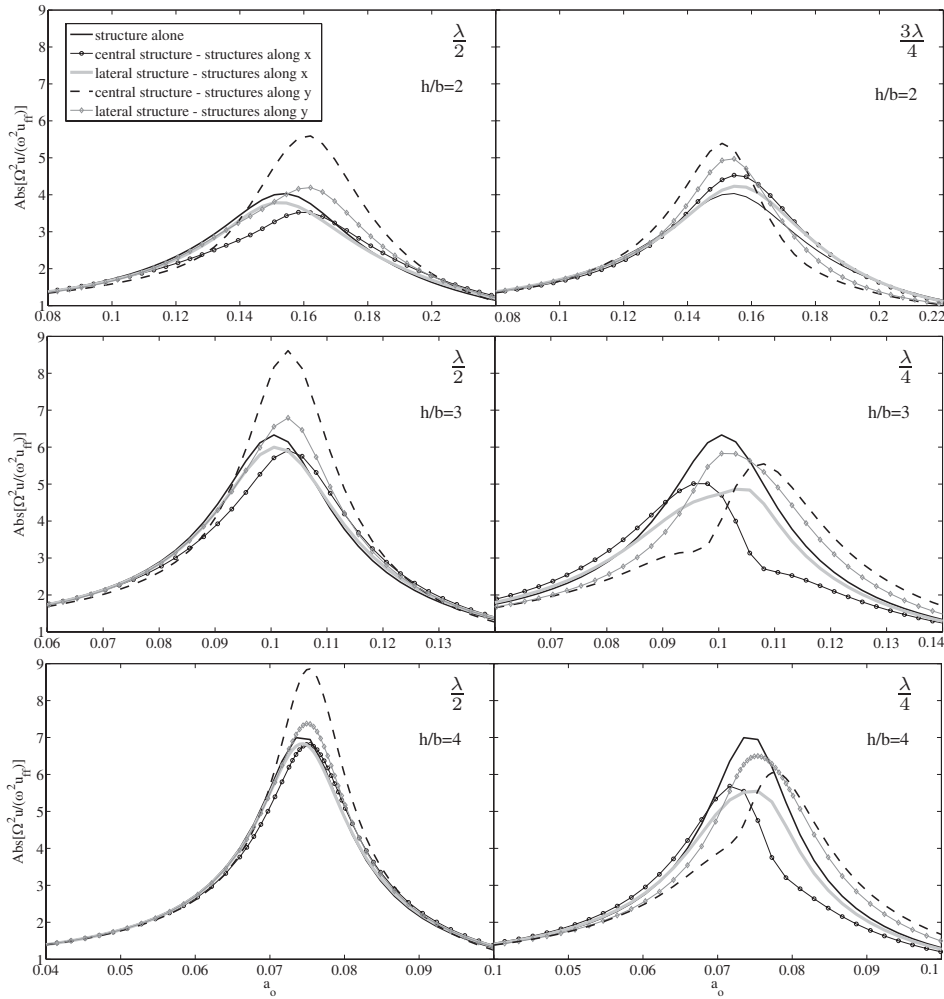


Fig. 3. Interaction between structures of identical fundamental frequencies in terms of their harmonic response spectra for different configurations.

Finally, the influence of the interaction between structures on the pile forces is illustrated in Fig. 5, where the shear forces on central and corner piles heads of the central structure foundation are shown for one $h/b = 4$ structure standing alone and *three* identical $h/b = 4$ structures separated $6b$. The shear forces are normalized by the static horizontal stiffness of a single pile. In this case, the importance of the interaction becomes apparent, as the amplitude of the shear forces increases up to 55% when the existence of other structures is taken into account.

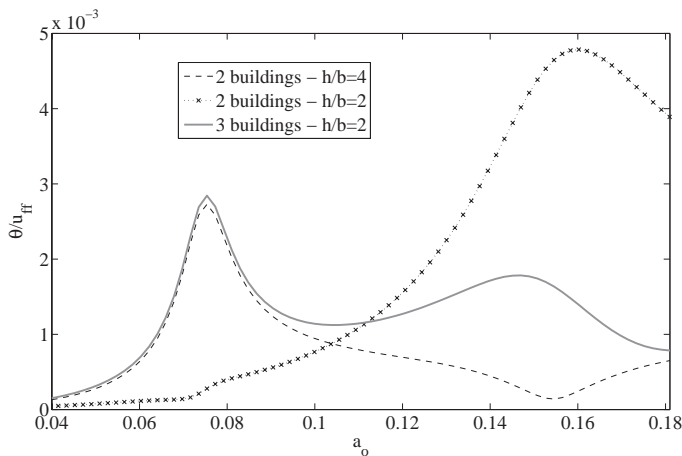
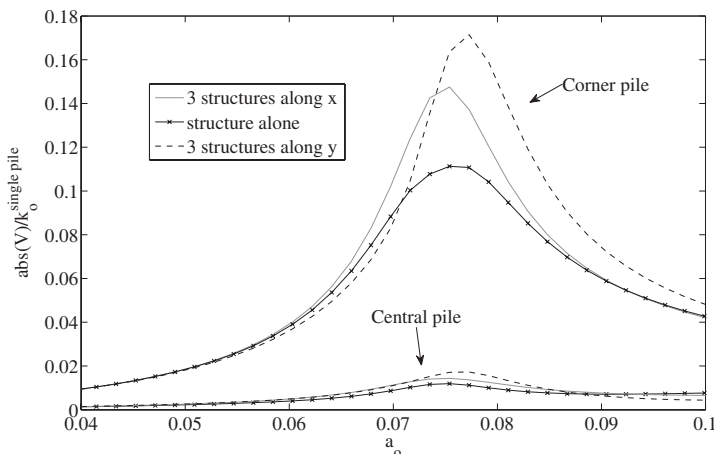


Fig. 4. Torsional motion due to interaction between adjacent structures.

Fig. 5. Influence of the interaction between structures on the pile heads shear forces. Three identical $h/b = 4$ structures separated $6b$.

Conclusions

A BEM-FEM coupling model for the dynamic analysis of pile groups have been used to study the influence of neighbouring structures on the dynamic response of one-storey piled shear buildings subject to vertically-incident SH waves, through a direct approach. The structures have been considered to be founded on a viscoelastic half-space and several parameters such as aspect ratio and distance between adjacent structures have been taken into account.

The interaction between structures with non-similar fundamental periods have been found to be negligible, except for the fact that it induces torsional motions that may be significant on the dynamic behaviour of buildings. On the contrary, the dynamic response of the structures is modified when other structures with similar fundamental frequencies exist in its vicinity, both in

amplitude and with respect to the system fundamental frequencies. However, the interaction is only significant at frequencies around resonance. Similar effects are observed in [5]. It is worth noting that the amplitude of the peak structural horizontal deformation can either increase or decrease in the presence of similar buildings, depending on the aspect ratios, the separation between adjacent buildings, the flexible-base fundamental frequency of the structures and the direction of alignment of the structures with respect to the seismic waves. Also, another variable of great importance from the engineering point of view, the maximum forces at the pile heads, has been shown to be highly influenced by the interaction between neighbouring structures.

These are just preliminary studies aimed at evaluating whether or not the dynamic response of a structure founded on soft to medium soils is modified by the presence of neighbouring structures. It has been found that the influence exists and can be of importance, so further studies will be made in order to investigate how parameters such as stratigraphy, foundation configuration, number and distribution of buildings, structural characteristics or type and angle of the incident waves modify the interaction phenomena. The response of the structures subject to recorded earthquake motions will also be investigating making use of the Fast Fourier Transform.

Acknowledgements

This work was supported by the Ministry of Education and Science of Spain through research project BIA2007-67612-C02-01 and co-financed by the European Fund of Regional Development. L.A. Padrón is recipient of the FPU fellowship AP-2004-4858 from the Ministry of Education and Science of Spain. The authors would like to thank for this support.

References

- [1] J. Bielak, *Dynamic behaviour of structures with embedded foundations*, Earthquake Eng Struct Dyn, **3**, 259-274 (1975)
- [2] J. Avilés and L.E. Pérez-Rocha, *Effects of foundation embedment during building-soil interaction*, Earthquake Eng Struct Dyn, **27**, 1523-1540 (1998)
- [3] J.P. Stewart, R.B. Seed and G.L. Fenves, *Seismic soil-structure interaction in buildings. I: Analytical methods*, J Geotech Eng, ASCE, **125** (1), 26-37 (1999)
- [4] J.P. Stewart, R.B. Seed and G.L. Fenves, *Seismic soil-structure interaction in buildings. II: Empirical results*, J Geotech Eng, ASCE, **125** (1), 38-48 (1999)
- [5] P.Y. Bard, P. Guéguen, J.L. Chazelas, M. Kham and J.F. Semblat, *Seismic hazard in urban environments: Can man modify the hazard?*, in Proc. of 3ed Congreso Nacional de Ingeniería Sísmica, Juan-Bautista Martínez-Guevara (Eds), CIMNE, Barcelona, 2007.
- [6] L.A. Padrón, J.J. Aznárez and O. Maeso, *BEM-FEM coupling model for the dynamic analysis of piles and pile groups*, Engineering Analysis Boundary Elements, **31**, 473-484, (2007)
- [7] L.A. Padrón, J.J. Aznárez and O. Maeso, *Dynamic analysis of piled foundation in stratified soils by a BEM-FEM model*, Soil Dynamics and Earthquake Engineering, *In Press*.
- [8] J. Domínguez, 'Boundary elements in dynamics', CMP and Elsevier Applied Science, Southampton-New York, (1993).

BEM-FEM coupling with non-conforming interfaces for static and dynamic problems

Thomas Rüberg^{1,a}, Martin Schanz^{2,b}, and Gernot Beer^{1,c}

¹Institute for Structural Analysis, Lessingstraße 25, 8010 Graz, Austria

²Institute for Applied Mechanics, Technikergasse 4, 8010 Graz, Austria

^arueberg@tugraz.at , ^bm.schanz@tugraz.at , ^cgernot.beer@tugraz.at

Keywords: BEM-FEM coupling, time domain BEM, non-conforming interfaces.

Abstract. The coupling of boundary and finite element methods allows for the optimal use of both methods. Especially in dynamics, the boundary element method represents well subdomains of infinite extent. Complex local phenomena, such as non-linearities, are handled easily by finite element methods. In addition, it is advantageous if the local mesh sizes can be chosen independently. On the one hand, this allows for a greater flexibility in the mesh generation, and, on the other hand, such non-conforming interface discretizations can be required in order to obey the stability criteria of the respective discretization methods.

In this work, a coupling strategy is presented which uses either finite or boundary element discretizations on the subdomain level for static or dynamic problems. Therefore, local Dirichlet-to-Neumann maps are realized by either method and for each time step which allow for a method-independent formulation. The interface conditions are then incorporated by means of Lagrange multipliers such that non-conforming interface discretizations can be handled. Results are given for examples from elastostatics and elastodynamics.

Basic equations

Elastodynamics and -statics. The dynamics of a linear elastic solid which occupies the domain Ω with boundary Γ are governed by the initial boundary value problem [1]

$$\begin{aligned} (\partial_t^2 \mathbf{u})(\mathbf{x}, t) - c_1^2 \nabla (\nabla \cdot \mathbf{u}(\mathbf{x}, t)) + c_2^2 \nabla \times (\nabla \times \mathbf{u}(\mathbf{x}, t)) &= \mathbf{0} & (\mathbf{x}, t) \in \Omega \times (0, \infty) \\ \mathbf{u}_\Gamma(\mathbf{y}, t) = \mathbf{g}_D(\mathbf{y}, t) & & (\mathbf{y}, t) \in \Gamma_D \times (0, \infty) \\ \mathbf{t}(\mathbf{y}, t) = \mathbf{g}_N(\mathbf{y}, t) & & (\mathbf{y}, t) \in \Gamma_N \times (0, \infty), \end{aligned} \quad (1)$$

where $\mathbf{u}(\mathbf{x}, t)$ denotes the displacement field depending on the position \mathbf{x} and the time t . Furthermore, \mathbf{u}_Γ and \mathbf{t} are the boundary displacements and tractions for which the Dirichlet and Neumann data, \mathbf{g}_D and \mathbf{g}_N , are prescribed on the boundary parts Γ_D and Γ_N , respectively. In Eq. (1), $c_1^2 = (\lambda + 2\mu)/\rho$ and $c_2^2 = \mu/\rho$ refer to the velocities of the pressure and shear waves, respectively, where λ and μ are the Lamé parameters of an isotropic linear elastic solid and ρ is the mass density. For simplicity, no body forces are considered and, furthermore, vanishing initial conditions are assumed, i.e., $\mathbf{u}(\mathbf{x}, 0) = \mathbf{0}$ and $(\partial_t \mathbf{u})(\mathbf{x}, 0) = \mathbf{0}$ for all $\mathbf{x} \in \Omega$.

The initial boundary value problem (1) is reduced to the elliptic boundary value problem of linear elastostatics by removing any dependence on the time variable t

$$\begin{aligned} -(\lambda + 2\mu) \nabla (\nabla \cdot \mathbf{u}(\mathbf{x})) + \mu \nabla \times (\nabla \times \mathbf{u}(\mathbf{x})) &= \mathbf{0} & \mathbf{x} \in \Omega \\ \mathbf{u}_\Gamma(\mathbf{y}) = \mathbf{g}_D(\mathbf{y}) & & \mathbf{y} \in \Gamma_D \\ \mathbf{t}(\mathbf{y}) = \mathbf{g}_N(\mathbf{y}) & & \mathbf{y} \in \Gamma_N. \end{aligned} \quad (2)$$

Variational principles. The introduced finite element method is based on the variational principle [3] which states that

$$\int_{\Omega} \rho \ddot{\mathbf{u}} \cdot \mathbf{v} \, d\mathbf{x} + \int_{\Omega} \boldsymbol{\sigma}(\mathbf{u}) : \boldsymbol{\varepsilon}(\mathbf{v}) \, d\mathbf{x} = \int_{\Gamma_N} \mathbf{g}_N \cdot \mathbf{v}_{\Gamma} \, ds \quad (3)$$

has to hold for a suitable set of test functions \mathbf{v} and for all times $0 < t < \infty$. Similarly, in the elastostatic case, one has to find \mathbf{u} such that

$$\int_{\Omega} \boldsymbol{\sigma}(\mathbf{u}) : \boldsymbol{\varepsilon}(\mathbf{v}) \, d\mathbf{x} = \int_{\Gamma_N} \mathbf{g}_N \cdot \mathbf{v}_{\Gamma} \, ds \quad (4)$$

for any admissible \mathbf{v} .

Boundary integral equations. The boundary integral equations of elastodynamics are derived from the dynamic representation formula [1]

$$\mathbf{u}(\tilde{\mathbf{x}}, t) = \int_0^t \int_{\Gamma} \mathbf{U}^*(\tilde{\mathbf{x}} - \mathbf{y}, t - \tau) \mathbf{t}(\mathbf{y}, \tau) \, ds_y \, d\tau - \int_0^t \int_{\Gamma} \mathbf{T}^*(\tilde{\mathbf{x}} - \mathbf{y}, t - \tau) \mathbf{u}_{\Gamma}(\mathbf{y}, \tau) \, ds_y \, d\tau, \quad (5)$$

where \mathbf{U}^* is the fundamental solution of the elastodynamic equation as in Eq. (1) and \mathbf{T}^* is the corresponding traction term. In Eq. (5), the point $\tilde{\mathbf{x}}$ is located strictly inside Ω . The limit $\Omega \ni \tilde{\mathbf{x}} \rightarrow \mathbf{x} \in \Omega$ yields the boundary integral equation in operator form [2]

$$(\mathcal{V}_t * \mathbf{t})(\mathbf{x}, t) = \mathcal{C}\mathbf{u}_{\Gamma}(\mathbf{x}, t) + (\mathcal{K}_t * \mathbf{u}_{\Gamma})(\mathbf{x}, t) \quad (\mathbf{x}, t) \in \Gamma \times (0, \infty), \quad (6)$$

where the asterisk denotes the temporal convolution $(g * h)(t) = \int_0^t g(t - \tau)h(\tau) \, d\tau$. In this expression, the following operators are used

$$\begin{aligned} (\mathcal{V}_t * \mathbf{t})(\mathbf{x}, t) &= \int_0^t \int_{\Gamma} \mathbf{U}^*(\mathbf{x} - \mathbf{y}, t - \tau) \mathbf{t}(\mathbf{y}, \tau) \, ds_y \, d\tau \\ (\mathcal{K}_t * \mathbf{u}_{\Gamma})(\mathbf{x}, t) &= \lim_{\varepsilon \rightarrow 0} \int_0^t \int_{\Gamma_{\varepsilon}} \mathbf{T}^*(\mathbf{x} - \mathbf{y}, t - \tau) \mathbf{u}_{\Gamma}(\mathbf{y}, \tau) \, ds_y \, d\tau \\ (\mathcal{C}\mathbf{u}_{\Gamma})(\mathbf{x}, t) &= \mathbf{u}_{\Gamma}(\mathbf{x}, t) + \lim_{\varepsilon \rightarrow 0} \int_{\gamma_{\varepsilon}} \mathbf{T}^*(\mathbf{x} - \mathbf{y}, 0) \mathbf{u}_{\Gamma}(\mathbf{y}, t) \, ds_y. \end{aligned} \quad (7)$$

In these definitions, the abbreviations $\Gamma_{\varepsilon} = \Gamma \setminus B_{\varepsilon}(\mathbf{x})$ and $\gamma_{\varepsilon} = \Omega \cap \partial B_{\varepsilon}(\mathbf{x})$ have been used, where $B_{\varepsilon}(\mathbf{x})$ is a ball of radius ε centered at \mathbf{x} and $\partial B_{\varepsilon}(\mathbf{x})$ its surface.

Similarly, the definition of the static boundary integral operators [9]

$$(\mathcal{V}\mathbf{t})(\mathbf{x}) = \int_{\Gamma} \mathbf{U}^*(\mathbf{x} - \mathbf{y}) \mathbf{t}(\mathbf{y}) \, ds_y \quad \text{and} \quad (\mathcal{K}\mathbf{u}_{\Gamma})(\mathbf{x}) = \lim_{\varepsilon \rightarrow 0} \int_{\Gamma_{\varepsilon}} \mathbf{T}^*(\mathbf{x} - \mathbf{y}) \mathbf{u}_{\Gamma}(\mathbf{y}) \, ds_y \quad (8)$$

with \mathcal{C} equivalently to Eq. (7) and the fundamental solution \mathbf{U}^* and its tractions kernel \mathbf{T}^* of the elastostatic equation yields the elastostatic boundary integral equation

$$(\mathcal{V}\mathbf{t})(\mathbf{x}) = \mathcal{C}\mathbf{u}_{\Gamma}(\mathbf{x}) + (\mathcal{K}\mathbf{u}_{\Gamma})(\mathbf{x}) \quad \mathbf{x} \in \Gamma. \quad (9)$$

Discretization methods

Finite element method. The finite element method considered here is simply a discretization of the variational principles (3) and (4) corresponding to the elastodynamic and elastostatic (initial) boundary value problems (1) and (2). Therefore, the domain Ω is approximated by Ω_h which is the union of simple geometric elements. These allow for the approximation of the displacement field

$$\mathbf{u}_h(\mathbf{x}, t) = \sum_{i=1}^I \mathbf{u}_i(t) \varphi_i(\mathbf{x}) \quad (10)$$

where the time dependence of the coefficients \mathbf{u}_i is removed in the static case. The system of linear equations for elastostatics reads [8]

$$\begin{pmatrix} \mathbf{A}_{II} & \mathbf{A}_{I\Gamma} \\ \mathbf{A}_{\Gamma I} & \mathbf{A}_{\Gamma\Gamma} \end{pmatrix} \begin{pmatrix} \mathbf{u}_I \\ \mathbf{u}_\Gamma \end{pmatrix} = \begin{pmatrix} \mathbf{f}_I \\ \mathbf{f}_\Gamma \end{pmatrix}. \quad (11)$$

This system has already been partitioned into degrees of freedom strictly belonging to the interior of Ω_h (index I) and degrees of freedom belonging to the boundary $\Gamma_h = \partial\Omega_h$ (index Γ). In dynamics, exactly the same system can be obtained by applying a time integration method, e.g. the Newmark method, the system of ordinary differential equations obtained from the spatial discretization of the corresponding variational principle. Now, a Dirichlet-to-Neumann map is formulated after elimination of interior degrees of freedom \mathbf{u}_I

$$\mathbf{S}_{fe}\mathbf{u}_\Gamma = \mathbf{g}_{fe}, \quad (12)$$

where $\mathbf{S}_{fe} = \mathbf{A}_{\Gamma\Gamma} - \mathbf{A}_{\Gamma I} \mathbf{A}_{II}^{-1} \mathbf{A}_{I\Gamma}$ is simply the Schur complement [8] of the matrix \mathbf{A} of Eq. (11). The fore term is computed by $\mathbf{g}_{fe} = \mathbf{f}_\Gamma - \mathbf{A}_{\Gamma I} \mathbf{A}_{II}^{-1} \mathbf{f}_I$. The extension to dynamics is then straightforward and has the same structure for every time point t_n .

Boundary element method. At first the boundary Γ is replaced by a geometry approximation Γ_h composed of simple surface elements upon which the shape functions φ_i and ψ_j are defined such that approximations for the boundary displacements \mathbf{u}_Γ and the surface tractions \mathbf{t} are formulated

$$\mathbf{u}_{\Gamma,h}(\mathbf{y}, t) = \sum_{i=1}^I \varphi_i(\mathbf{y}) \mathbf{u}_i(t) \quad \text{and} \quad \mathbf{t}_h(\mathbf{y}, t) = \sum_{j=1}^J \psi_j(\mathbf{y}) \mathbf{t}_j(t). \quad (13)$$

A system of convolution equations is obtained by inserting the approximation (13) into the time-dependent boundary integral equation (6) and evaluating the result at a certain set of collocation points $\mathbf{x}_k^* \in \Gamma$

$$(\mathcal{V}_t * \mathbf{t})(t) = \mathbf{C}\mathbf{u}(t) + (\mathcal{K}_t * \mathbf{u})(t). \quad (14)$$

Here, \mathcal{V}_t , \mathcal{K}_t , and \mathbf{C} are the spatial discretizations of the operators \mathcal{V}_t , \mathcal{K}_t , and \mathcal{C} as defined in Eq. (7). Using a temporal discretization scheme, the convolution (14) results in the equation for the time point $t_n = n\Delta t$

$$\sum_{\nu=1}^n \mathcal{V}_\nu \mathbf{t}_{n-\nu} = \mathbf{C}\mathbf{u}_n + \sum_{\nu=1}^n \mathcal{K}_\nu \mathbf{u}_{n-\nu}. \quad (15)$$

Here, the convolution quadrature method [5] is used but a classical time domain boundary element method is also feasible, see [6] for more details and comparisons of these approaches. In order to obtain a linear system of equations, the prescribed boundary conditions are employed. The given Dirichlet datum is assumed to be fulfilled directly, whereas the prescribed Neumann datum enters as a side condition. This yields the saddle point problem [7]

$$\begin{pmatrix} \mathbf{V}_0 & -\tilde{\mathbf{K}}_{N,0} \\ \mathbf{B} & \end{pmatrix} \begin{pmatrix} \mathbf{t}_n \\ \mathbf{u}_n \end{pmatrix} = \begin{pmatrix} \mathbf{f}_{D,n} \\ \mathbf{f}_{N,n} \end{pmatrix} - \sum_{\nu=1}^n \begin{pmatrix} \mathbf{V}_\nu & -\mathbf{K}_{N,\nu} \\ \mathbf{f}_{D,\nu} & \mathbf{f}_{N,\nu} \end{pmatrix} \begin{pmatrix} \mathbf{t}_{n-\nu} \\ \mathbf{u}_{n-\nu} \end{pmatrix}. \quad (16)$$

The matrix blocks \mathbf{V}_ν and $\mathbf{K}_{N,\nu}$ refer to the fully discretized operators \mathcal{V}_t and \mathcal{K}_t , where the latter is only applied to the unknown displacements on the Neumann boundary Γ_N . Furthermore, $\tilde{\mathbf{K}}_{N,0}$ contains the matrix \mathbf{C}_N , i.e., the discretization of the operator \mathcal{C} applied to the unknown displacements too. The mass matrix \mathbf{B} is simply the L_2 -product of the shape functions φ_i and ψ_j according to the approximation (13) and is responsible for the statement of the Neumann boundary condition in a weighted sense. The force terms $\mathbf{f}_{D,n}$ and $\mathbf{f}_{N,n}$ contain the prescribed boundary conditions \mathbf{g}_D and \mathbf{g}_N , respectively, for the time point t_n . Note that the sum on the right hand side of Eq. (16) contains the solution history of the boundary tractions and displacements up to the considered time point. The elastostatic counterpart is described by the system of equations

$$\begin{pmatrix} \mathbf{V} & -\tilde{\mathbf{K}}_N \\ \mathbf{B} & \end{pmatrix} \begin{pmatrix} \mathbf{t} \\ \mathbf{u} \end{pmatrix} = \begin{pmatrix} \mathbf{f}_D \\ \mathbf{f}_N \end{pmatrix}. \quad (17)$$

Both systems of linear equations (16) and (17) can be used to express Dirichlet-to-Neumann maps by solving the first equation for the unknown \mathbf{t}_n (or just \mathbf{t}) and inserting the result into the second equation

$$\mathbf{S}_{be} \mathbf{u}_n = \mathbf{g}_{be,n}. \quad (18)$$

Here, \mathbf{S}_{be} represents a boundary element discretization of the Steklov-Poincaré operator and is simply obtained by computing $\mathbf{S}_{be} = \mathbf{B} \mathbf{V}_0^{-1} \tilde{\mathbf{K}}_{N,0}$ and similarly in the static case. The right hand side term $\mathbf{g}_{be,n}$ represents a condensation of the given data and contains in the dynamic case the solution history.

Coupling algorithm

The domain Ω is partitioned into N non-overlapping subdomains, $\Omega = \cup_{r=1}^N \Omega^{(r)}$, each of which possibly having a Dirichlet and Neumann boundary part, $\Gamma_D^{(r)}$ and $\Gamma_N^{(r)}$. The interfaces of the partitions are denoted by $\Gamma^{(rp)}$ for boundary shared by $\Omega^{(r)}$ and $\Omega^{(p)}$ and the union of all interfaces is the skeleton Γ_s . On each subdomain $\Omega^{(r)}$ the (initial) boundary value problem (1) or (2) is stated locally and in addition the interface conditions

$$\mathbf{u}_\Gamma^{(r)} = \mathbf{u}_\Gamma^{(p)} \quad \text{and} \quad \mathbf{t}^{(r)} + \mathbf{t}^{(p)} = \mathbf{0} \quad \text{on } \Gamma^{(rp)}, \quad (19)$$

are posed for all interfaces $\Gamma^{(rp)}$ of connected subdomains. These pointwise conditions are introduced into the equations by means of a Lagrange multiplier field $\boldsymbol{\lambda}$ yielding the variational principle [8]

$$\begin{aligned} \int_{\Gamma^{(r)}} (\mathcal{S}^{(r)} \mathbf{u}_\Gamma^{(r)}) \cdot \mathbf{v}_\Gamma^{(r)} ds + \sum_p \int_{\Gamma^{(rp)}} \boldsymbol{\lambda} \cdot (\mathbf{v}_\Gamma^{(r)} - \mathbf{v}_\Gamma^{(p)}) ds &= \int_{\Gamma^{(r)}} \mathbf{g}^{(r)} \cdot \mathbf{v}_\Gamma^{(r)} ds \\ \sum_p \int_{\Gamma^{(rp)}} \boldsymbol{\mu} \cdot (\mathbf{u}_\Gamma^{(r)} - \mathbf{u}_\Gamma^{(p)}) ds &= 0. \end{aligned} \quad (20)$$

Here, \mathcal{S} denotes the Steklov-Poincaré operator for which discretizations are given in Eqs. (12) and (18). The term \mathbf{g} is the corresponding boundary force term. The sums in Eq. (20) are over all subdomains connected to the considered subdomain $\Omega^{(r)}$. The functions \mathbf{v}_Γ and $\boldsymbol{\mu}$ are the test functions corresponding to the boundary displacements \mathbf{u}_Γ and the Lagrange multiplier field $\boldsymbol{\lambda}$, respectively. The latter is now approximated by

$$\boldsymbol{\lambda}_h(\mathbf{y}, t) = \sum_{\ell=1}^L \boldsymbol{\lambda}_\ell(t) \chi_\ell(\mathbf{y}). \quad (21)$$

Using the discretized Dirichlet-to-Neumann maps (12) and (18) and the above approximation (21), the global system of equations obtained by discretization of the variational principle (20) has the form [4]

$$\begin{pmatrix} \mathcal{S}^{(1)} & & \mathcal{C}^{(1)\top} \\ \mathcal{S}^{(2)} & \ddots & \mathcal{C}^{(2)\top} \\ \vdots & & \vdots \\ \mathcal{C}^{(1)} & \mathcal{C}^{(2)} & \dots & \mathcal{C}^{(N)} \end{pmatrix} \begin{pmatrix} \mathbf{u}^{(1)} \\ \mathbf{u}^{(2)} \\ \vdots \\ \mathbf{u}^{(N)} \\ \lambda \end{pmatrix} = \begin{pmatrix} \mathbf{g}^{(1)} \\ \mathbf{g}^{(2)} \\ \vdots \\ \mathbf{g}^{(N)} \\ 0 \end{pmatrix}. \quad (22)$$

The matrices $\mathcal{C}^{(r)}$ in the system (22) are L_2 -products on the skeleton Γ_s of the shape functions φ_i (either boundary element or finite element shape functions) and the functions χ_ℓ . The system has exactly the same structure, if applied to a dynamic problem. Then, the left hand side stays the same throughout the computation (under the assumption of and equi-distant time grid) and the unknowns are the coefficients of the boundary displacements $\mathbf{u}_n^{(r)}$ for the time point t_n . Of course, in the dynamic calculation the right hand side changes throughout the calculation. The discretization of the Lagrange multiplier field λ refers only to one side of the interface. Therefore, the interface discretizations do not have to be matching in the sense of spatially coincident nodes or equal polynomial discretization orders. Confer [10] for the analysis of the mortar method and [8] for nonconforming coupling of finite and boundary element discretizations.

Numerical examples

Dynamic load on a rod. A benchmark for the dynamic analysis is an elastic rod which is fixed at one end and subjected to a unit step load in axial direction at the other end. The model of such a problem is given in Fig. 1(a). This model is represented by a three-dimensional body of dimensions $3\text{ m} \times 1\text{ m} \times 1\text{ m}$ which is subdivided into three unit cubes. The discretization of the model is shown in Fig. 1(b), where the first and third cube are discretized by 192 linear triangular boundary elements of size $h = 1/4\text{ m}$ and the middle cube is discretized by either 8 or 125 hexahedral trilinear finite elements of sizes $h = 1/2\text{ m}$ or $h = 1/5\text{ m}$, respectively. The different finite element discretizations are referred to as *fine* and *coarse* when considering the numerical outcome. The material has parameters $\lambda = 0$, $\mu = 1.06 \cdot 10^{11} \text{ N/m}^2$, and $\rho = 7850 \text{ kg/m}^3$. The time step of the temporal discretization is $\Delta t = 10^{-6}\text{ s}$ such that the ratio $(c_1 \Delta t)/h$ has approximately the value 0.2.

In Fig. 2, the results of the coupled solution of this problem are shown together with the analytical solution. The axial displacements are considered along the center line of the rod on the loaded surface (point A) and on the interfaces (points B and C). The surface tractions in

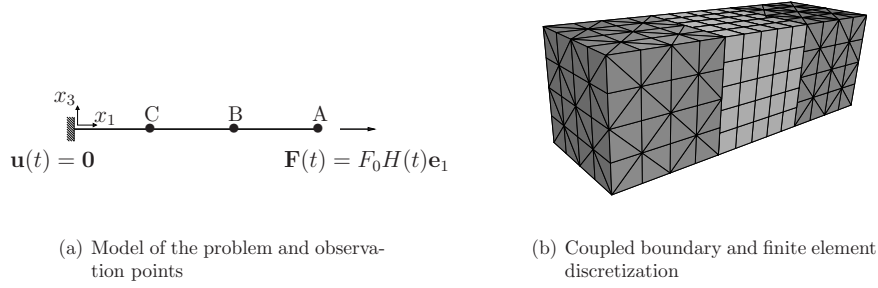


Figure 1: Model and discretization of an elastic rod subjected to a unit stop load.

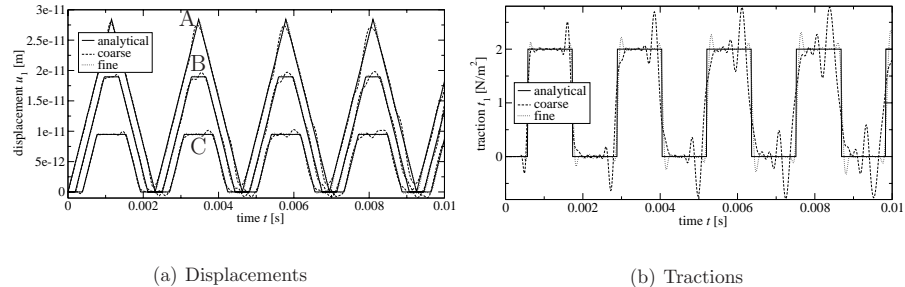


Figure 2: Coupled boundary and finite element solution for the three-dimensional rod — displacements at points A, B, and C and traction at point D against time.

axial direction are plotted for the fixed left surface. The displacement results are very close to the analytical solution for both finite element discretizations. The traction solution has the typical overshoots at the jumps of the piecewise constant analytical solution.

Soil-structure interaction. A typical example for the benefit of combining boundary and finite element discretizations is soil-structure interaction, where the unbounded soil is handled by a boundary element discretization and the finite-sized structure by a finite element method. Consider the foundation on a soil halfspace as shown in Fig. 3(a). The material parameters of the foundation are $\lambda = 9.72 \cdot 10^9 \text{ N/m}^2$, $\mu = 1.46 \cdot 10^{10} \text{ N/m}^2$, and $\rho = 2400 \text{ kg/m}^3$ and the soil has parameters $\lambda = \mu = 1.36 \text{ N/m}^2$ and $\rho = 1884 \text{ kg/m}^3$. The foundation is discretized by 216 trilinear hexahedral finite elements of length $h = 1/6 \text{ m}$ and the surface of the soil is discretized by 320 linear boundary elements of size $h = 1/4 \text{ m}$. Note that the chosen interface discretizations are nonconforming. The top of the foundation is subjected to a vertical load of magnitude 1 N/m^2 . In the dynamic case this load varies as a unit step function in time. The temporal discretization consists of 400 time steps of size $\Delta t = 1.5 \text{ s}$.

The results of the static and dynamic analyses are depicted in figure 3(b) for the vertical displacements of the top and the bottom of the foundation and a third point located on the surface of the soil at 4 m distance from the center of the interface. The disturbance due to the suddenly applied load travel through the foundation and the soil and reach the observation points at different times. Clearly, the dynamic responses quickly converge to the static solution due to the geometric damping of the unbounded elastic halfspace. Moreover, no spurious

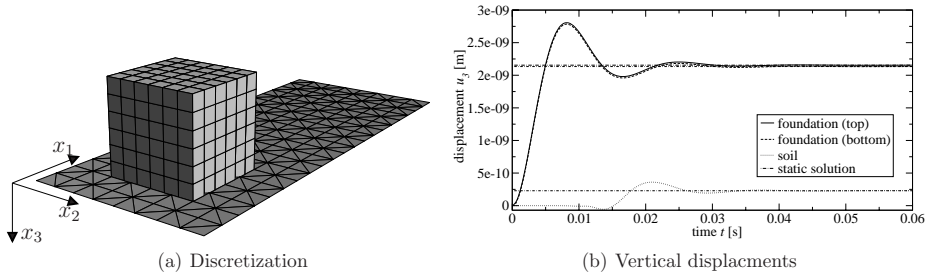


Figure 3: Dynamic and static analysis of individual footing on an elastic halfspace.

reflections of the waves occur as it would happen in the case of a standard finite element method.

References

- [1] J.D. Achenbach. *Wave propagation in elastic solids*. North-Holland, 2005.
- [2] M. Costabel. Time-dependent problems with the boundary integral equation method. In E. Stein, R. de Borst, and T.J.R. Hughes, editors, *Encyclopedia of Computational Mechanics*, volume 1, chapter 25, pages 703–721. John Wiley & Sons, Ltd., 2004.
- [3] T.J.R. Hughes. *The Finite Element Method: Linear Static and Dynamic Finite Element Analysis*. Dover Publications, New York, 2000.
- [4] U. Langer and O. Steinbach. Coupled finite and boundary element domain decomposition methods. In M. Schanz and O. Steinbach, editors, *Boundary Element Analysis — Mathematical Aspects and Applications*, volume 29 of *Lecture Notes in Applied and Computational Mechanics*, pages 61–95. Springer, 2007.
- [5] C. Lubich. Convolution quadrature and discretized operational calculus I & II. *Numerische Mathematik*, 52:129–145 & 413–425, 1988.
- [6] M. Schanz. *Wave propagation in Viscoelastic and Poroelastic Continua - A boundary element approach*. Springer, 2001.
- [7] O. Steinbach. Mixed approximations for boundary elements. *SIAM journal on Numerical Analysis*, 38:401–413, 2000.
- [8] O. Steinbach. *Stability Estimates for Hybrid Domain Decomposition Methods*. Springer, 2003.
- [9] O. Steinbach. *Numerical Approximation Methods for Elliptic Boundary Value Problems*. Springer, 2008.
- [10] B.I. Wohlmuth. *Discretization Methods and Iterative Solvers Based on Domain Decomposition*. Springer, 2001.

Cartesian transformation method for evaluation of regular and singular domain integrals in boundary element and other mesh reduction methods

M. R. Hematiyan^{1,a}, M. Mohammadi^{1,b}, R. Fazeli^{1,c} and A. Khosravifard^{1,d}

¹Department of Mechanical Engineering, Shiraz University, Shiraz, Iran

^amhemat@shirazu.ac.ir, ^bmohamadm@shirazu.ac.ir,

^cfazelirazieh@gmail.com, ^damirkhosravi@gmail.com

Keywords: Cartesian transformation method, domain integral, boundary integral.

Abstract. In this paper, an efficient method is presented for evaluation of domain integrals with boundary-only discretization. The method employs Green's theorem in Cartesian coordinate system to transform domain integrals into boundary integrals. Since the transformation is carried out in the Cartesian coordinate system, the method is called Cartesian Transformation Method (CTM). Here, emphasis is made on domain integrals with integrands that are defined by irregularly spaced data. The CTM seems to be the simplest method for evaluation of domain integrals with boundary-only discretization. Three examples including a 3D problem are presented to show the efficiency of the method.

Introduction

A regular domain integral in general form can be expressed as follows:

$$I = \int_{\Omega} g(\mathbf{x}) d\Omega \quad (1)$$

where \mathbf{x} is a point in the domain Ω . The function g may have an explicit mathematical expression or it may be defined by scattered data over a grid in a domain and on its boundary.

In formulations of boundary element method (BEM), domain integrals have a form like the following integral:

$$I_1 = \int_{\Omega - \Omega_{\epsilon}} f(\mathbf{x}) h^*(\xi, \mathbf{x}) d\Omega \quad (2)$$

where f , h^* , ξ and \mathbf{x} are respectively forcing function, singular kernel, source point, and field point. The singular kernel h^* has an explicit mathematical expression, but the function f in Eq. 2 may have an explicit mathematical expression or it may be defined by scattered data over a grid. The function h^* is singular at $\mathbf{x} = \xi$ and the order of its singularity is different in various problems. Ω in Eq. 2 represents the main domain of the problem and Ω_{ϵ} is an infinitesimal region (circle for 2D and sphere for 3D) around the singular point ξ .

A method for treatment of domain integrals in BEM, which is widely used by investigators, is Dual Reciprocity Method (DRM) [1]. In this method, the forcing function is approximated by a series of prescribed basis functions. Then the domain integral is transformed into boundary by employing particular solutions. Prescribed basis functions must be defined in a way that one can find corresponding particular solutions. This restriction may introduce some errors in the results especially for complicated problems.

Another method for the evaluation of domain integrals with boundary-only discretization is the Radial Integration Method (RIM) [2]. In this method the integrand is expressed in a radial form and the domain integral is transformed into a double integral consisting of a boundary integral and a radial integral.

If integrand of a domain integral has an analytical integral with respect to only one of Cartesian coordinates, the domain integral can be transformed exactly into a boundary integral. This rule has

been described in [3] and has been used for exact transformation of a wide variety of domain integrals into boundary in BEM formulation of potential and elastostatics problems. When the integrand of the domain integral has no analytical integral with respect to any direction, additional numerical integration must be carried out. Recently Hematiyan presented an adaptive meshless method for evaluation of very complicated domain integrals without domain discretization [4]. In the method presented in [4] it is supposed that the integrand of the domain integral has an explicit mathematical expression.

In the present paper, emphasis is made on domain integrals with integrands that are defined by irregularly spaced data over a grid. These kinds of integrands are generated in meshless methods such as element free Galerkin method [5] or in BEM formulation of nonlinear, transient or inhomogeneous problems. Moving least squares (MLS) method [6], is used for interpolation at internal points. A method similar to that, which has been used in [3, 4] is employed for transforming domain integrals into boundary. This general and robust method for evaluation of domain integrals with boundary-only discretization is called Cartesian Transformation Method (CTM).

The Cartesian Transformation Method (CTM)

Green's theorem has been previously used by many researchers for transformation of some domain integrals into boundary, but here it is employed for a more general use. The method to be presented here is robust and very simple. Since all manipulations and transformations are carried out in the global Cartesian coordinate system, it is called Cartesian transformation method.

The Green's theorem in general form for a 2D or 3D domain can be expressed as follows [7]:

$$\int_{\Omega} \frac{\partial u(\mathbf{x})}{\partial x_i} d\Omega = \int_{\Gamma} u(\mathbf{x}) n_i d\Gamma \quad (3)$$

where Ω and Γ are respectively, the domain and boundary of a simply or multiply connected 2D or 3D region and n_i are components of boundary unit normal vector.

Suppose that the following integral is to be computed:

$$I = \int_{\Omega} g(\mathbf{x}) d\Omega \quad (4)$$

The function G_i is defined as follows:

$$G_i(\mathbf{x}) = \int g(\mathbf{x}) dx_i \quad i=1, 2 \text{ or } 3 \quad (5)$$

Using Eq. 3 and the definition in Eq. 5, and since

$$\frac{\partial G_i}{\partial x_i} = g, \quad (\text{no sum on } i)$$

one can write:

$$I = \int_{\Gamma} G_i(\mathbf{x}) n_i d\Gamma, \quad i=1, 2 \text{ or } 3 \quad (\text{no sum on } i) \quad (6)$$

which is a boundary integral. As seen, if the integral of the integrand g (Eq. 5) with respect to only one of coordinates, i.e. x_i , can be found analytically, the domain integral in Eq. 4 is transformed exactly into a boundary integral. It has been shown that this is the case for a wide variety of domain integrals in BEM [3]. For cases where the integral in Eq. 5 cannot be found analytically, one can evaluate it numerically by the following relation.

$$G_i(\mathbf{x}) = \int_a^{x_i} g(\mathbf{x}) dx_i \quad i=1, 2 \text{ or } 3 \quad (7)$$

where a is an arbitrary constant. The method can be used efficiently for simply or multiply connected domains with very complicated boundaries. Suppose that the integral in Eq. 4 over the 2D domain shown in Fig. 1 is to be computed. It can be evaluated by the following relations:

$$I = \int_{\Gamma} G_1(\mathbf{x}) n_1 d\Gamma \quad (8)$$

$$G_1(\mathbf{x}) = \int_a^{x_1} g(\mathbf{x}) dx_1 \quad (9)$$

A point $\mathbf{x} = (X_1, X_2)$ on the boundary Γ is shown in the Fig. 1. The constant a is selected in a way that $x_1 = a$ locates in the left side of the domain. A horizontal ray (integration ray) is considered from $x_1 = a$ to point \mathbf{x} . The ray intersects with the boundaries of the domain t times and the ray is divided into t different parts, alternatively inside and outside the original domain. Considering the mentioned fact, one can write the integral in Eq. 9 as follows:

$$\begin{aligned} G_1(\mathbf{x}) &= \int_a^{x_1} g(x_1, X_2) dx_1 \\ &= \int_{a_1}^{a_2} g(x_1, X_2) dx_1 + \int_{a_2}^{a_3} g(x_1, X_2) dx_1 + \dots + \int_{a_{t-1}}^{a_t} g(x_1, X_2) dx_1 \end{aligned} \quad (10)$$

By this procedure, there is no need to evaluate the boundary integral in Eq. 8 over the internal boundaries of a multiply connected region.

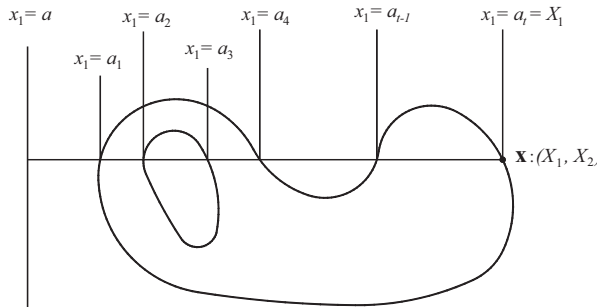


Figure 1: Intersection of an integration ray to boundary

Regular domain integrals with integrands that are defined by irregularly spaced data over a grid

Suppose that the integral in Eq. 4 is to be evaluated by CTM and the function g has been defined by a number of irregularly spaced data over a grid within the domain and on its boundary. These kinds of integrals appear in some meshless methods such as element free Galerkin method. To evaluate the domain integral by CTM it is required to compute the value of g in some internal points, which are not located at defined data. For this purpose, one must employ an interpolation method. Here the moving least squares (MLS) approximation is used.

In MLS, the function $g(\mathbf{x})$ is approximated by:

$$g^h(\mathbf{x}) = \sum_{i=1}^n \phi_i(\mathbf{x}) g_i \quad (11)$$

where g_i is nodal parameter of function $g(\mathbf{x})$ at node i and $\phi_i(\mathbf{x})$ is the shape function corresponding to node i and is obtained by:

$$\phi_i(\mathbf{x}) = \sum_{j=1}^m p_j(\mathbf{x}) (\mathbf{A}^{-1}(\mathbf{x}) \mathbf{B}(\mathbf{x}))_{ji} = \mathbf{P}^T(\mathbf{x}) (\mathbf{A}^{-1} \mathbf{B})_i \quad (12)$$

where $p_j(\mathbf{x})$ are monomials and m is the number of monomials used in construction of $\mathbf{P}(\mathbf{x})$.

In Eq. 12, $\mathbf{A}(\mathbf{x})$ and $\mathbf{B}(\mathbf{x})$ are expressed as follow:

$$\mathbf{A}(\mathbf{x}) = \sum_{i=1}^n w(\mathbf{x} - \mathbf{x}_i) \mathbf{P}^T(\mathbf{x}) \mathbf{P}(\mathbf{x}_i) \quad (13)$$

$$\mathbf{B}(\mathbf{x}) = [w(\mathbf{x} - \mathbf{x}_1) \mathbf{P}(\mathbf{x}_1), w(\mathbf{x} - \mathbf{x}_2) \mathbf{P}(\mathbf{x}_2), \dots, w(\mathbf{x} - \mathbf{x}_n) \mathbf{P}(\mathbf{x}_n)] \quad (14)$$

where n is total number of nodes in support domain of point \mathbf{x} and $w(\mathbf{x} - \mathbf{x}_i)$ is value of the weight function at point \mathbf{x} , associated with node i . One of the most common weight functions, used in EFG method is the quartic-spline function; it is given by:

$$w(\mathbf{x} - \mathbf{x}_i) = \begin{cases} 1 - 6r^2 + 8r^3 - 3r^4 & r \leq 1 \\ 0 & r > 1 \end{cases}, \quad (15)$$

where $r = d_i / d_{mi}$ with $d_i = \|\mathbf{x} - \mathbf{x}_i\|$. d_{mi} is the dimension of support domain of node i .

Singular domain integrals with forcing functions that are defined by irregularly spaced data over a grid

In some BEM formulations of nonlinear or transient problems, some singular domain integrals with forcing functions that are defined by irregularly spaced data appear. Also in problems with body forces, which are defined by scattered data, these kinds of integrals appear. These domain integrals can be expressed in the general form of Eq. 2, where the singular kernel h^* has a mathematical expression but the forcing function f , is defined by irregularly spaced data over a grid within domain and on boundary. For evaluation of the domain integral in Eq. 2 without internal discretization, first it is regularized as follows:

$$I = \int_{\Omega - \Omega_e} [f(\mathbf{x}) - f(\xi)] h^*(\xi, \mathbf{x}) d\Omega + f(\xi) \int_{\Omega - \Omega_e} h^*(\xi, \mathbf{x}) d\Omega \quad (16)$$

The first domain integral in Eq. 16 is evaluated by CTM without internal cells and the second integral is transformed exactly into a boundary integral by CTM. $f(\xi)$ and $f(\mathbf{x})$ are evaluated by MLS method. According to Eqs 8 and 9, the first integral in Eq. 16 can be expressed as follows:

$$I_1 = \int_{\Gamma} G_1(\mathbf{x}) n_1 d\Gamma - \int_{\Gamma_e} G_1(\mathbf{x}) n_1 d\Gamma \quad (17)$$

where,

$$G_1(\mathbf{x}) = \int_a^{x_1} [f(\mathbf{x}) - f(\xi)] h^*(\xi, \mathbf{x}) dx_1 \quad (18)$$

The above integral can be evaluated by a numerical method such as composite Gauss quadrature or Simpson method. The size of integration intervals may be selected with the same order of grid size. It can be shown that the second integral in Eq. 17 vanishes.

Similarly, the second integral in Eq. 16 can be written as follows

$$I_2 = \int_{\Omega - \Omega_e} h^*(\xi, \mathbf{x}) d\Omega = \int_{\Gamma} H_1(\mathbf{x}) n_1 d\Gamma - \int_{\Gamma_e} H_1(\mathbf{x}) n_1 d\Gamma \quad (19)$$

where,

$$H_1(\mathbf{x}) = \int_a^{x_1} h^*(\xi, \mathbf{x}) dx_1 \quad (20)$$

The integral in Eq. 20 can be evaluated analytically for a wide variety of problems [3]. The second integral in Eq. 19 vanishes for cases where function h^* is weakly singular and can be evaluated analytically for cases with higher order of singularity [3].

Examples

Several 2D and 3D examples are presented to show the accuracy and efficiency of the present method.

Example 1: Regular 3D domain integrals

In this example integrals of three different regular functions over one fourth of a cylinder with unit radius and unit height are computed by CTM. Functions are considered as follow:

$$g(\mathbf{x}) = x^2 + y^2 + z^2, \quad g(\mathbf{x}) = z \sin(\pi \sqrt{x^2 + y^2}), \quad g(\mathbf{x}) = \frac{1}{\sqrt{x^2 + y^2} + 0.1} \sin(\pi z)$$

Each function is discretized by coarse and fine grids and corresponding integrals are evaluated by CTM. The obtained results are compared with exact solutions. Discretization of domain with coarse and fine grids and boundary elements are shown in Figs 2 and 3. The obtained results in comparison with exact solutions are given in Table 1. As seen, the results are satisfactory.

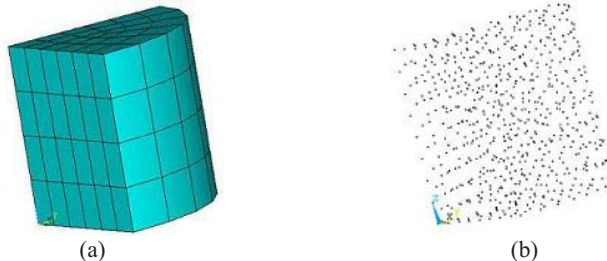


Figure 2: Coarse discretization, (a) discretization of boundary with 126 quadratic boundary elements, (b) discretization of integrand with 670 points

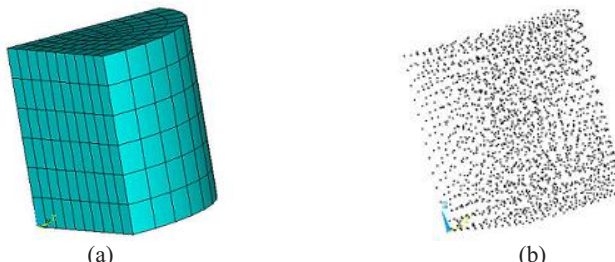


Figure 3: Fine discretization, (a) discretization of boundary with 320 quadratic boundary elements, (b) discretization of integrand with 2076 points

Table 1: Results of Example 1

Integrand $g(\mathbf{x})$	Discretization of $g(\mathbf{x})$	Value of integral, Present, (CTM)	Error	Value of integral, Exact
$g(\mathbf{x}) = x^2 + y^2 + z^2$	Coarse	0.6540	0.08%	0.6545
	Fine	0.6545	0.00%	
$g(\mathbf{x}) = z \sin(\pi \sqrt{x^2 + y^2})$	Coarse	0.2504	0.16%	0.2500
	Fine	0.2501	0.04%	
$g(\mathbf{x}) = \frac{1}{\sqrt{x^2 + y^2} + 0.1} \sin(\pi z)$	Coarse	0.7592	0.13%	0.7602
	Fine	0.7594	0.11%	

Example 2: Singular 2D domain integrals

In this example the integral

$$I = \int_{\Omega} f(\mathbf{x}) h^*(\mathbf{x}) d\Omega$$

for two different forcing functions f and singular kernels h^* is computed. Domain Ω is a 1×1 square with $(x, y) = (0, 0)$ at its lower left corner. The boundary of the domain is discretized by only 4 linear boundary elements. The following functions are considered as forcing functions:

$$f(\mathbf{x}) = \sin(6y) + y^5 x + x^2, \quad f(\mathbf{x}) = \cos(6y) + \exp(y)x + \frac{1}{y+0.1}x^2,$$

These forcing functions are used in discretized form over a coarse and a fine grid (Fig.4). The corresponding singular kernels are:

$$h^*(\mathbf{x}) = \ln\left(\frac{1}{r}\right), \quad h^*(\mathbf{x}) = \frac{r_1}{r^2}$$

where r is Euclidean distance from source point to field point and r_1 is the distance in the x -direction. Source point is located at $(0.25, 0.25)$.

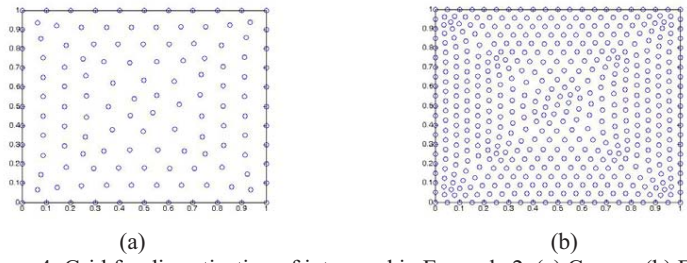


Figure 4: Grid for discretization of integrand in Example 2, (a) Coarse, (b) Fine

Obtained results are given in Table 2. The results are compared with accurate solutions, which are obtained using original forcing functions with no discretization [3]. As seen, the obtained results are in a good agreement with accurate solutions.

Table 2: Results of Example 2

Forcing function $f(\mathbf{x})$	Singular kernel $h(\mathbf{x})$	Discretization of $f(\mathbf{x})$	Present (CTM)	Error	Accurate solution [3]
$\sin(6y) + y^5 x + x^2$	$\ln\left(\frac{1}{r}\right)$	Coarse	0.48378	0.6%	0.48088
		Fine	0.48090	0.002%	
$\cos(6y) + \exp(y)x + \frac{1}{y+0.1}x^2$	$\frac{r_1}{r^2}$	Coarse	2.3712	0.6%	2.3578
		Fine	2.3585	0.03%	

Example 3: An element free Galerkin (EFG) method example

In this example, a linear elastic problem is analyzed by EFG method. The problem domain is shown in Fig 5. In this problem, a tapered cantilever beam is considered. A uniform pressure is applied at the upper edge of the beam. Domain integrals of the EFG method [5] are evaluated both by Gauss

quadrature method with background mesh (BM) and by CTM. In evaluation of the integrals, 4-point Gauss method is utilized. This problem is also analyzed by FEM with a fine mesh. The results of EFG and finite element analysis are compared.

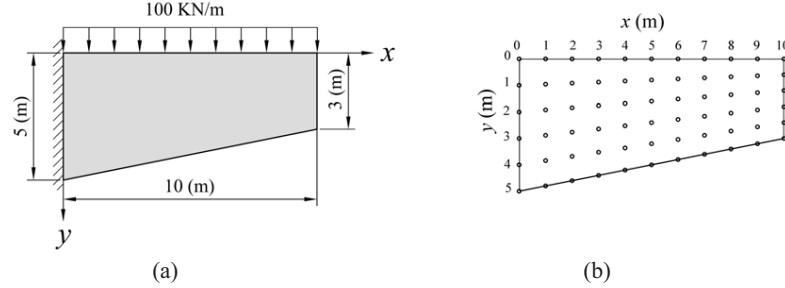


Figure 5: Domain of Example 3, (a) Geometry and boundary conditions, (b) Grid

The results of the analyses are shown in Fig. 6. The problem is analyzed by two different background meshes (4×2 and 8×4) and equivalent interval sizes of CTM. Horizontal and vertical displacements of the beam along its upper edge are illustrated in Fig. 6. As can be easily observed, the results of EFG by CTM in comparison with conventional EFG by background mesh are in better agreement with the results of accurate FEM solution. As the background mesh and intervals size of CTM are made fine, the results obtained by CTM and background mesh converge together. It should be noted that by CTM, integrals are evaluated faster and more accurately, meaning that with a coarse interval size of CTM, acceptable results can be obtained.

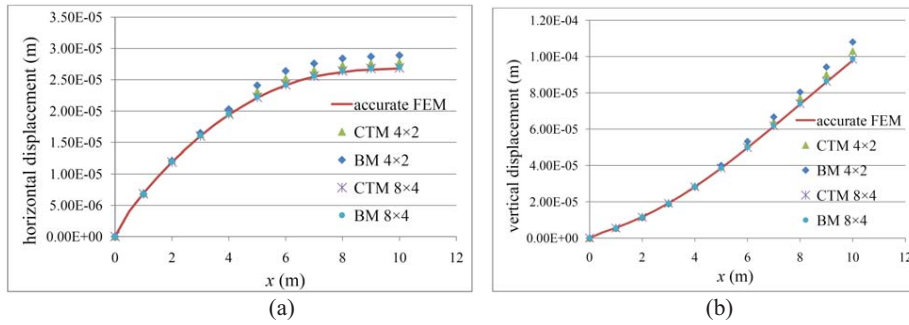


Figure 6: Comparison of results obtained by CTM and background mesh (BM), (a) Horizontal displacement of the beam, (b) Vertical displacement of the beam

In order to better understand the advantage of CTM in choosing integration points over the conventional Gauss quadrature method with background mesh, integration points of each method are depicted in Fig. 7. In Fig. 7-a, integration points of CTM are shown. Note that in CTM no integration point falls outside the domain. Fig. 7-b corresponds to background mesh; in this figure the dots represent the integration points that are located inside the domain and the cross signs represent the integration points which are located outside the domain. In this figure, the background mesh is also shown.

Using CTM for evaluation of domain integrals in EFG results in a truly element free Galerkin method.

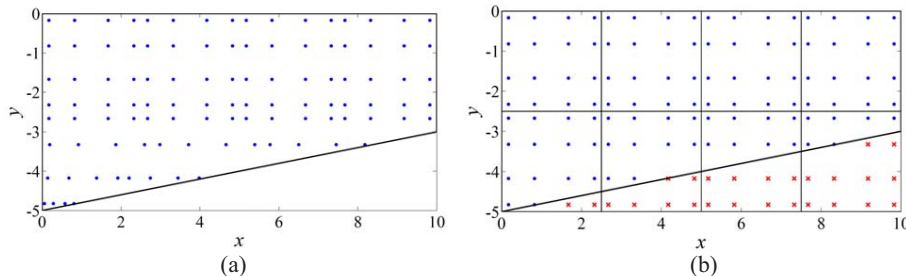


Figure 7: Integration points of background mesh and CTM, (a) Integration pints of CTM
(b) Integration points of background mesh

Conclusions

The Cartesian transformation method (CTM) for evaluation of regular and singular domain integrals with boundary-only discretization was presented. The method is useful for BEM and other mesh reduction methods such as EFG. Unlike DRM and RIM, which are organized in polar coordinate system, in CTM all computations are carried out simply in global Cartesian coordinate system. This characteristic makes CTM a very simple method. Similar to RIM there is no need for particular solutions in CTM. By CTM a wider range of domain integrals can be exactly transformed into boundary integrals. By presenting some examples, it was shown that the results obtained by CTM are in an excellent agreement with accurate solutions.

References

- [1] P.W. Partridge, C.A. Brebbia, L.C. Wrobel: The dual reciprocity boundary element method, Computational Mechanics Publications, (1992).
- [2] X.W. Gao: Engineering Analysis with Boundary Elements, 26, 905-916 (2002).
- [3] M.R. Hematiyan: Communication in numerical methods in engineering, Early View (2008).
- [4] M.R. Hematiyan: Computational mechanics, 39 (4), 509-520 (2007).
- [5] T. Belytschko, Y.Y. Lu and L. Gu: Int Journal for Numerical Methods in Engineering, 37, 229-256 (1994).
- [6] P. Lancaster and K. Salkauskas: Mathematics of Computation, 37, 141-158 (1981).
- [7] W.M. Lai, D. Rubin and E. Kremple: Introduction to continuum mechanics, Third Edition, Butterworth-Heinemann, (1999).

Design of Noise Barriers with Boundary Elements and Genetic Algorithms

Orlando Maeso^a, David Greiner^b, Juan José Aznárez^c, Gabriel Winter^d

Institute of Intelligent Systems and Numerical Applications in Engineering (IUSIANI), University of
Las Palmas de Gran Canaria, 35017, Spain

^aomaeso, ^bdgreiner, ^cjaznarez}@iusiani.ulpgc.es, ^dgabw@step.es

Keywords: noise barriers, shape optimization, genetic algorithms, boundary element method, multiobjective optimization, noise attenuation.

Abstract. Noise barriers are widely used for environmental protection, for example, close to high traffic roads near population nucleus in order to reduce the noise impact. In this paper, shape optimum design of noise barriers is carried out using BEM for modeling and genetic algorithms for optimization. The sound pressure level is calculated being known: the source position, the receptor position, the barrier shape, the acoustical admittances of the surfaces and the sound frequency. The model assumes an infinite, coherent line source of sound, parallel to an infinite noise barrier of uniform cross section and surface covering along its length. In these conditions the model is two-dimensional. The multiobjective optimum design is carried out in frequency domain. The first objective function to minimize is related with the insertion loss (IL, the difference between the sound level in the receptor with and without barrier, respectively) values differences at selected frequencies of the spectra between a reference IL and the searched design. The second objective function to minimize is the effective height of each barrier design. Geometric configurations for the barrier design are studied, including Y shaped barriers. In all cases, the proposed approach handled in this work leads to shape barrier solution designs, automatically generated without direct human intervention and with high noise attenuation quality corresponding to each effective height.

Introduction

Automatically generated optimum designs are possible by using coupled evolutionary computation with accurate numerical modeling. Many applications in the computational mechanics field, both with mono- and multi-objectives have been solved by the previous methodology [1, 2]. In this paper, a multiobjective optimum noise barrier shape design problem is solved. First, the sound pressure calculation using BEM is described. Then, the optimum design methodology handled is exposed, followed by the results and conclusions.

Sound pressure calculation using BEM

The integral equation for a boundary point i , to be solved numerically by BEM, can be written as:

$$c_i p_i = p_o^* - \int_{\Gamma_b} \left(\frac{\partial p^*}{\partial n} + ik \beta_b p^* \right) p d\Gamma \quad (1)$$

where:

p : acoustic pressure field on the barrier surface (Γ_b) of generic admittance β_b .

p^* : half-space fundamental solution. Acoustic pressure field due to a source at collocation point i over a plane with admittance β_g (ground surface). This fundamental solution only requires the discretization of the barrier boundary (Γ_b).

Without loss of generality, in this paper all the surfaces of the barrier and ground are assumed to be perfectly reflecting. ($\beta_b=0$ and $\beta_g=0$).

c_i : the local free term at collocation point i : $c_i = \theta / 2\pi$, where θ is the angle subtended by the tangents to the boundary at this point in radians. $c_i = 0.5$ for smooth boundaries.

p_o^* : half-space fundamental solution at the problem source due to collocation at point i .

$k = \omega/c$ is the wavenumber (c : sound wave velocity, ω : angular frequency) and i the imaginary unit. The numerical solution of Eq. 1 is possible after a discretization process. A system of equations is obtained from this process and lead to values of acoustic pressure over the barrier boundary. The BEM code in this paper uses quadratic elements with three nodal points. The acoustic pressure along this boundary element can be written in terms of their three nodal values as follows:

$$p^j = \phi_1 p_1^j + \phi_2 p_2^j + \phi_3 p_3^j \quad (2)$$

where the interpolation functions, in homogeneous coordinate ξ , are:

$$\phi_1 = \frac{1}{2} \xi (\xi - 1) \quad \phi_2 = (1 - \xi)(1 + \xi) \quad \phi_3 = \frac{1}{2} \xi (\xi + 1) \quad (3)$$

The integral representation (Eq. 2), after discretization of the barrier boundary into NE quadratic elements, can be written as:

$$c_i p_i = p_o^* - \sum_{j=1}^{NE} \sum_{k=1}^3 (h_k^{ij} + ik \beta_j g_k^{ij}) p_k^j \quad (4)$$

where:

$$h_k^{ij} = \int_{\Gamma_j} \frac{\partial p^*}{\partial n} \phi_k d\Gamma_j \quad ; \quad g_k^{ij} = \int_{\Gamma_j} p^* \phi_k d\Gamma_j \quad (5)$$

are the integrals along generic element j . These integrals can be calculated using a standard Gauss quadrature (see [3]). A system of equations in matrix form is obtained by applying the discretized equations at each node in the boundary successively, and follows:

$$(\mathbf{H} + ik \beta \mathbf{G}) \mathbf{P} = \mathbf{P}_o^* \quad (6)$$

where \mathbf{H} , \mathbf{G} are square matrixes ($N \times N$) and \mathbf{P} , \mathbf{P}_o^* are ($N \times 1$) vectors. The BEM computer code used in this work was validated by carrying out comparisons with the results obtained by other authors in the literature [4, 5, 6]. A detailed description is available in [7].

Figure 1 shows a two-dimensional configuration for scalar wave propagation problems in the frequency domain.

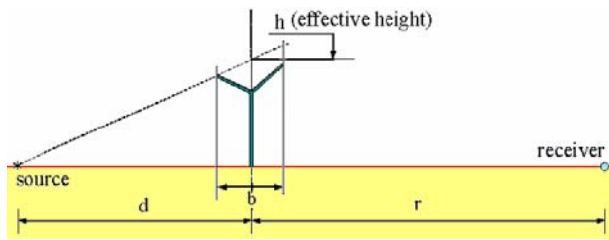


Fig. 1: Problem topology representation

Methodology

The simultaneous minimization of two conflicting objectives corresponding to a noise barrier design is performed in this paper. First, a fitness function related with the increase of the acoustic attenuation of the barrier. Concretely, the first fitness function which has to be minimized is:

$$FF1 = \sum_j^{N\text{Freq}} (IL_j - IL_j^R)^2 \quad (7)$$

where:

IL_j : insertion loss in the third octave band centre frequency for the Y-barrier profile evaluated

IL_j^R : insertion loss reference curve in the third octave band centre frequency .

The optimum monocrriteria design using this first fitness function was previously described in Greiner et al. [8]. It solves an inverse problem, where the objective IL curve at certain frequencies is known (IL^R) and it allows searching for the corresponding barrier design whose IL curve fits IL^R . In [8] was shown the capability to increase a certain percentage the acoustic efficiency of a certain Y-shape barrier taken as original design, where the shape designs corresponding to 15 and 30% improved IL values corresponding to five different frequencies (63, 125, 250, 500 and 1000 Hz) were obtained. The Y-barrier shape is modeled using the two extreme points of the arms and their join point. The x coordinate of the extreme points is supposed fixed in the extremes of the barrier (b in Fig. 1), where only y-coordinate varies. The join point has variable x- and y-coordinates. So, four variables are required to define each shape. Here $b = 1$ m, $d = 10$ m, $r = 50$ m and, in any case, $h \leq 3$ m. For more details, see [8]. The initial Y-shape reference is represented in Fig 4 (left), and their IL values with 30% improvement (here IL^R) are shown in Table 1. The best design obtained corresponds to Design 1 (Fig. 4 and Table 1).

The second fitness function to be minimized is the noise barrier design effective height. The higher its value, the better the noise attenuation capacity of the barrier, and therefore, the easier to fit the searched reference curve. On the contrary, the lower its value, the better environmental impact produced by the barrier.

Here, a multiobjective optimization noise barrier design with evolutionary algorithms is introduced. Concretely, the procedure searches for the barrier shape design which most fits IL^R for each effective height value.

With this geometry and for a given source position, the boundary element program calculates the acoustic pressure at the receiver position. Only the barrier surface is discretized, since the fundamental solution used satisfies the boundary conditions along the ground surface. A maximum element length not bigger than $\lambda / 4$ (being λ the wavelength) is necessary to obtain an appropriate accurate solution. With the acoustic pressure, the IL corresponding to each frequency is obtained.

Results

Sixteen independent runs of the evolutionary algorithm (NSGA-II [9]) were executed. A population size of 100 individuals and uniform crossover were used with Gray codification with two different mutation rates: 1.5% and 3% (half of the cases each). A total of 400 generations were run. All the final fronts of each run are represented in Fig. 2 (red points), where the best accumulated solution designs are highlighted with blue circles. Focusing the attention in the upper left corner of the figure, corresponding to the solutions which most fit IL^R , Fig 3. has been depicted. It contains the thirty best barrier designs which most fit IL^R for effective height values between 3m and 2.46 m. The detailed numerical values of both fitness functions as well as the IL values of the selected frequencies are shown in Table 1 (designs 1, 7, 8, 10, 15, 20, 25, 30). The shape designs are represented in the center and right parts of Fig. 4. From the acoustical point of view, those

automatically obtained designs belong to the same type (two long arms covering the total height of the design and being the right quasi-vertical), which adapt to its maximum effective height.

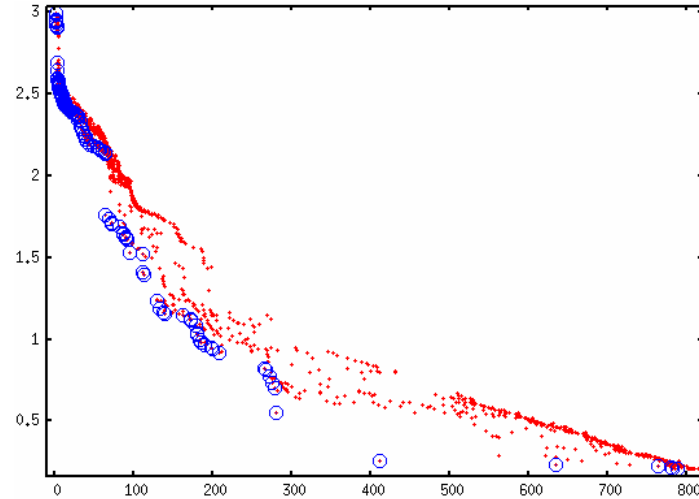


Fig. 2: Final designs corresponding to the sixteen independent runs (red points). The non-dominated points (blue circles) are the best accumulated designs.
(x-axis represents fitness function 1 and y-axis represents the effective height in meters)

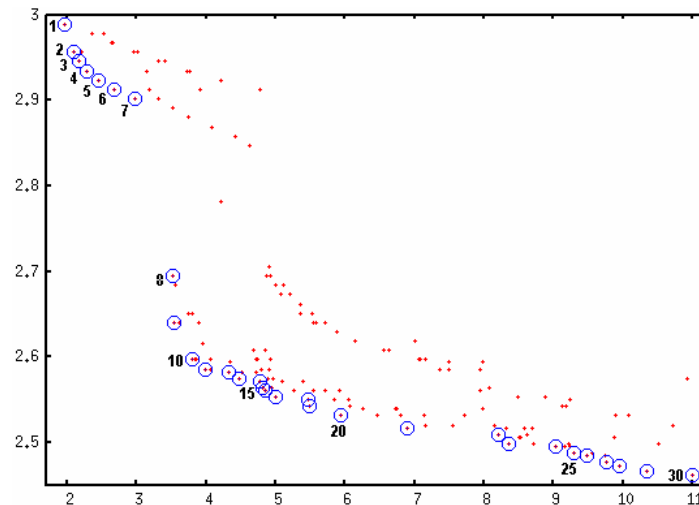


Fig. 3: Top left zoom of Fig. 1, where the engineering interest designs are located. They are numbered in the figure.
(x-axis represents fitness function 1 and y-axis represents the effective height in meters)

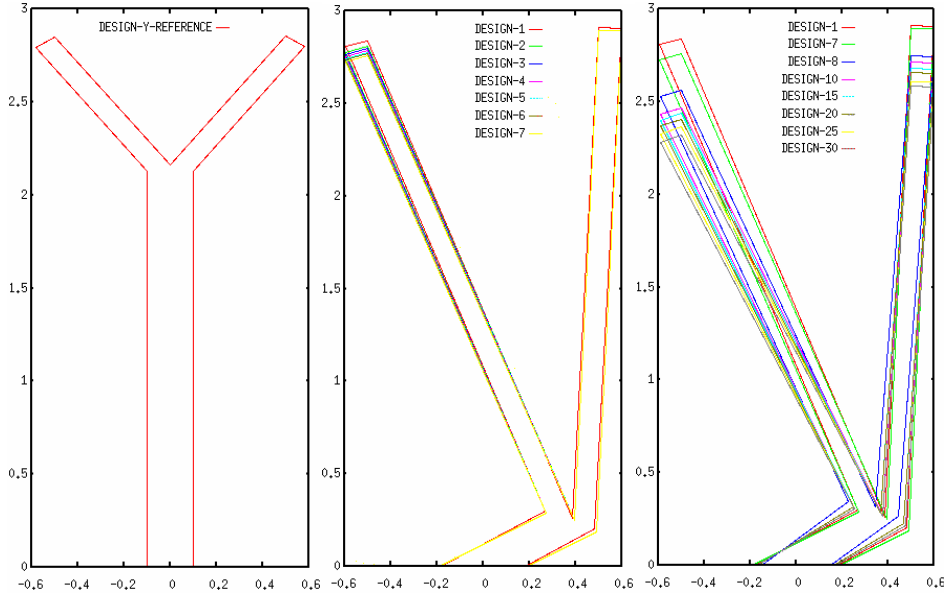


Fig. 4: Noise barrier shape designs: Reference shape (left figure); Designs 1 to 7 (center figure); Designs 1, 7, 8, 10, 15, 20, 25 and 30 (right figure)
(x-axis represents width and y-axis represents height, both in meters)

Frequenc y [Hz]	IL^R	Design 1	Design 7	Design 8	Design 10	Design 15	Design 20	Design 25	Design 30
63	-5.165	-5,459	-5,058	-5,811	-5,511	-5,82	-5,822	-5,552	-5,596
125	-9.078	-8,908	-8,911	-8,550	-8,39	-8,160	-7,971	-7,699	-7,3887
250	-11.609	-11,512	-11,731	-10,46	-10,54	-10,300	-10,150	-9,802	-9,657
500	-14.364	-13,109	-12,814	-13,155	-12,93	-13,014	-12,901	-12,654	-12,327
1000	-20.995	-20,490	-20,283	-21,197	-20,947	-20,994	-21,078	-22,017	-21,042
FF1-Value	---	1.955	2.9639	3.5137	3.7958	4.8118	5.9329	9.2855	10.9991
Effective Height [m]	---	2.9891	2.9019	2.6949	2.5968	2.5641	2.5314	2.4879	2.4622

Table 1: IL values corresponding to the frequencies considered in the optimization process of reference and several obtained designs

In order to deepen the acoustical analysis, the broadband IL corresponding to a standard road traffic noise spectrum (see [7]) has been evaluated for the obtained designs. The results of the first ten designs are represented in Fig 5.

Conclusions

The multiobjective optimum shape design of noise barriers has been successfully performed considering simultaneous minimization of the barrier effective height and the optimization of the noise attenuation in terms of IL considering an optimum IL^R curve at certain frequencies. The obtained designs are robust and acoustically speaking efficient. The exposed procedure

-evolutionary algorithm as optimizer and boundary element method as modeling- is useful and computationally affordable. As future work, other barrier shape topologies will be compared.

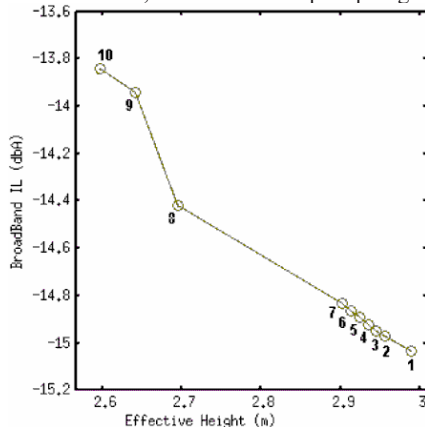


Fig 5: Standard road traffic noise spectrum IL values of several designs vs. their effective height

References

- [1] T. Burczynski, A. Osyczka (editors): IUTAM Symposium on Evolutionary Methods in Mechanics. *Solid Mechanics and its Applications n° 117*, Kluwer Academic Publishers (2004).
- [2] D. Greiner, J.M. Emperador, G. Winter: Single and Multiobjective Frame Optimization by Evolutionary Algorithms and the Auto-adaptive Rebirth Operator, *Computer Methods in Applied Mechanics and Engineering*, **193** 3711-3743 (2004).
- [3] J. Domínguez: *Boundary Elements in Dynamics*, CMP-Elsevier, (1993).
- [4] D.C. Hothersall, S.N. Chandler-Wilde, M.N. Hajmirzae: Efficiency of single noise barriers, *Journal of Sound and Vibration*, **146-2** 303-322 (1991).
- [5] D.C. Hothersall, D.H. Crombie, S.N. Chandler-Wilde: The performance of T-profile and associated noise barriers, *Applied Acoustics*, **32** 269-287 (1991).
- [6] D.H. Crombie, D.C. Hothersall: The performance of multiple noise barriers, *Journal of Sound and Vibration*, **176-4** 459-473 (1993).
- [7] O. Maeso, J.J. Aznárez: Strategies for reduction of acoustic impact near highways. An application of BEM, University of Las Palmas of GC, (2005).
http://contentdm.ulpgc.es/cdm4/item_viewer.php?CISOROOT=/DOCULPGC&CISOPTR=2389&CISOBOX=1&REC=2
- [8] D. Greiner, J.J. Aznárez, O. Maeso, G. Winter: Shape Design of Noise Barriers using Evolutionary Optimization and Boundary Elements, Proceedings of the Fifth International Conference on Engineering Computational Technology. Eds: Topping B, Montero G, Montenegro R, Civil-Comp Press, Las Palmas de Gran Canaria, (2006).
- [9] K. Deb, A. Pratap, S. Agrawal, T. Meyarivan: A fast and elitist multiobjective genetic algorithm: NSGA-II, *IEEE Transactions on Evolutionary Computation*, **6-2** 182-197 (2002).

Determination of the elastic response of materials with defects in three dimensional domains using BEM and Topological Derivative

Inas H. Faris¹ and Rafael Gallego²

¹ Dept. Structural Mechanics, University of Granada, Ed. Politécnico de Fuentenueva, 18071

Granada, Spain, inas@ugr.es

² Dept. Structural Mechanics, University of Granada, Ed. Politécnico de Fuentenueva, 18071

Granada, Spain, gallego@ugr.es

Keywords: Topological derivative

Abstract. The present work aims to analyze the elastic solid properties of three dimensional fields with random particle dispersions. In other words, its required to calculate the changes in the response (displacements and stresses) of a three dimensional domain due to the present of a small flaw (inclusion). To do this, the concept of the Topological Derivative (TD) is introduced, which is calculated using Boundary Integral Equations. This work determines the rank of applicability of the TD for this kind of problems, analyzing mainly the limit values of the size of the particles, as well as the density of these ones.

Also, in this investigation, a procedure for calculating the effect of the interaction among several defects is done. Then, a problem containing multiple cavities is replaced by a sequence of problems for a single cavity with boundary tractions adjusted iteratively to account for the cavity interactions.

Introduction

The idea of Topological Sensitivity was first introduced by Eschenauer et al. (1994) [1] (called *bubble method*), for compliance minimization in two dimensional elastostatic problems, and was later generalized and exploited for shape inverse problem by Sokolowski and coworkers [2](Sokolowski and Zochowski, 1998; Jackowska-Strumilo et al., 1999, Lewinski and Sokolowski, 1997) for circular and non-circular flaws. Garreau et al. (2001) [3] developed the idea for a general arbitrary-shaped flaw in the context of elastostatics, as well.

In the identification of defects important investigation works can be cited like the use of Boundary Integral Equations to calculate the *Topological Sensitivities* by Gallego and Rus [4] also works by M. Bonnet [5].

The Topological Derivative gives the sensitivity of a cost function defined in the domain of a boundary-value problem when a small hole is introduced in the domain [6]. More specifically, the idea is to make a perturbation on the domain Ω by subtracting a ball of radius ϵ , denoted by B_ϵ . In Sokolowski and Zochowski [7] a method to calculate the Topological Derivative via Shape Sensitivity Analysis was presented. Nevertheless, this method provides correct results only for homogeneous Neumann boundary conditions imposed on ∂B_ϵ . More recently, Novotny et al. [8] formally established the relationship between the Topological Derivative and Shape Sensitivity Analysis. This relationship provides an alternative way to compute the Topological Derivative using Shape Sensitivity Analysis results. Moreover, this new approach, which we will refer as the Topological-Shape Sensitivity Method, can be applied to any cost function and to any type of boundary condition on ∂B_ϵ . Therefore, this method is more general than others found in the literature .

Problem statement and solution method

The following equation [9] is the starting point of this work where its numerical treatment for three dimensional regions is presented.

$$c_{lk}^i u_k^i + \int_{\Gamma} p_{lk}^* u_k d\Gamma = \int_{\Gamma} u_{lk}^* p_k d\Gamma \quad (1)$$

in vector notation becomes

$$\mathbf{c}^i \mathbf{u}^i + \int_{\Gamma} \mathbf{p}^* \mathbf{u} d\Gamma = \int_{\Gamma} \mathbf{u}^* \mathbf{p} d\Gamma \quad (2)$$

The first step to solve the above equation is the discretization of the boundary Γ into elements, over which the displacement u and traction p are written in terms of their nodal values. Once the boundary has been discretized to NE elements, the respective values are substituted into eq (1) to obtain:

$$c^i u^i + \sum_{j=1}^{NE} \left\{ \int_{\Gamma_j} p^* \Phi d\Gamma \right\} u^j = \sum_{j=1}^{NE} \left\{ \int_{\Gamma_j} u^* \Phi d\Gamma \right\} p^j \quad (3)$$

where Γ_j indicates the surface of the j element. The above equation can be written as:

$$c^i u^i + \sum_{m=1}^N \hat{H}^{im} u^m = \sum_{j=1}^{NE} G^{ij} p^j \quad (4)$$

the matrices H and G are

$$G^{ij} = \int_{\Gamma_j} u^* \Phi d\Gamma \quad (5)$$

$$H^{ij} = \sum_t \int_{\Gamma_t} p^* \phi_k d\Gamma \quad (6)$$

The system of equations for all the i nodes on the boundary can be written in a matrix form as

$$\mathbf{H} \mathbf{U} = \mathbf{G} \mathbf{P} \quad (7)$$

There are $3N$ unknowns in the system (one per node and direction). Passing all the unknowns to the left-hand side by moving columns of H and G from one side to another, one obtains a $3N$ unknowns system,

$$\mathbf{A} \mathbf{X} = \mathbf{F} \quad (8)$$

where X is the vector of unknowns and F is obtained by multiplying columns of H or G by the known values of u_k or p_k .

Internal points

Once the system of equations is solved and all the values of u and p on the boundary are known, the value of u at any internal point i can be obtained from the following equation

$$u^i = \int_{\Gamma} u^* p d\Gamma - \int_{\Gamma} p^* u d\Gamma \quad (9)$$

with $c^i = I$, and the above equation can be written as follows:

$$u^i = \sum_{j=1}^{NE} G^{ij} p^j - \sum_{m=1}^N H^{im} u^m \quad (10)$$

The stresses at internal points can be computed by differentiation of the internal point displacement components:

$$u_l^i = \int_{\Gamma} u_{lk}^* p_k d\Gamma - \int_{\Gamma} p_{lk}^* u_k d\Gamma \quad (11)$$

and substitution of the displacement derivatives into the stress strain relations. Thus, the integral representation of the internal stresses is obtained from

$$\sigma_{mn}^i = \int_{\Gamma} D_{mn}^* p d\Gamma - \int_{\Gamma} S_{mn}^* u d\Gamma \quad (12)$$

where D^* and S^* are third order tensors obtained by differentiation of u_{lk}^* . The above equation can be discretized to yield [9]

$$\sigma_{mn}^i = \sum_{j=1}^{NE} D_{mn}^{ij} p^j - \sum_{m=1}^N S_{mn}^{ij} u^m \quad (13)$$

Where

$$D_{mn}^{ij} = \int_{\Gamma_j} D_{mn}^* \Phi d\Gamma \quad (14)$$

$$S_{mn}^{ij} = \int_{\Gamma_j} S_{mn}^* \Phi d\Gamma \quad (15)$$

The derivations to obtain the stresses at internal points where calculated and find to be as follows:

$$D_{kij} = \frac{1}{8\pi(1-v)r^2} [(1-2v)(\delta_{ik}r_{,j} + \delta_{jk}r_{,i} - \delta_{ij}r_{,k}) + 3r_{,i}r_{,j}r_{,k}] \quad (16)$$

$$S_{kij} = \frac{\mu}{4\pi(1-v)r^3} \left\{ 3 \frac{\partial r}{\partial n} [(1-2v)\delta_{ij}r_{,k} + v(\delta_{ik}r_{,j} + \delta_{jk}r_{,i}) - 5r_{,i}r_{,j}r_{,k}] + 3v(n_i r_{,j}r_{,k} + n_j r_{,i}r_{,k}) + (1-2v)(3n_k r_{,r}r_{,j} + n_j \delta_{ik} + n_i \delta_{jk}) - (1-4v)n_k \delta_{ij} \right\} \quad (17)$$

Topological Derivative

The presence of a stress free cavity centered at point \mathbf{z} whose boundary is Γ_z , which surrounds the domain Ω_z in a homogeneous domain Ω whose exterior boundary is Γ makes that the basic boundary eq (1) changes to : [4]

$$c_i^k(y) \tilde{u}_k(y) + \int_{\Gamma} [p_i^k(x; y) \tilde{u}_k(x) - u_k^i(x; y) \tilde{p}_k(x)] d\Gamma(x) + \int_{\Gamma_z} p_k^i(x; y) \tilde{u}_k(x) d\Gamma(x) = 0 \quad (18)$$

The tilde over the variables denotes that their values are modified due to the appearance of the infinitesimal flaw.

Considering $\tilde{p}_k(x) = 0$ along Γ_z , and that the displacements on the flaw's boundary can be split as $\tilde{u}_k(x) = u_k^0 + \delta \tilde{u}_k(x)$ that is equal to the rigid solid displacement (u_k^0) plus a movement relative to the center due to the local state of stresses ($\delta \tilde{u}_k(x)$). The integration along the boundary of the cavity Γ_z is transformed to

$$\int_{\Gamma_z} p_k^i(x; y) \tilde{u}_k(x) d\Gamma(x) = u_k^0 \int_{\Gamma_z} p_k^i(x; y) d\Gamma(x) + \int_{\Gamma_z} \delta \tilde{u}_k(x) p_k^i(x; y) d\Gamma(x) \quad (19)$$

and since the fundamental solution stresses along a close path are self equilibrated

$$\int_{\Gamma_z} p_k^i(x; y) \tilde{u}_k(x) d\Gamma(x) = \int_{\Gamma_z} \delta \tilde{u}_k(x) p_k^i(x; y) d\Gamma(x) \quad (20)$$

The first order stresses at any point inside Ω/Ω_z far from the flaw location are equal to those from the primary state $\sigma_{ij}(x)$ and therefore the displacement $\delta\bar{u}_k(x)$ along the vanishing flaw are equal to those due to a uniform remote stress field in an infinite plate. Then:

$$\delta\bar{u}_k(x) = \delta\tilde{u}_k^\infty(x) + h.o.t. \quad (21)$$

Where h.o.t stands for *higher order terms*, and $\delta\tilde{u}_k^\infty(x)$ represents the solution of the infinitesimal flaw problem due to the stresses $\sigma_{ij}(z)$, the integral along the flaw boundary turns therefore to:

$$\int_{\Gamma_z} p_k^i(x; y) \tilde{u}_k(x) d\Gamma(x) = \sigma_{jk}^i(z; y) \int_{\Gamma_z} n_j \delta u_k^\infty(x) d\Gamma(x) + h.o.t \quad (22)$$

Subtracting the BIE of the damage state from the non damage state BIE one reaches to the following

$$\begin{aligned} & c_i^k(y) \delta u_k(y) + \int_{\Gamma} [p_i^k(x; y) \delta u_k(x) - u_k^i(x; y) \delta p_k(x)] d\Gamma(x) \\ &= -\sigma_{jk}^i(z; y) \int_{\Gamma_z} n_j(x) \delta u_k^\infty(x) d\Gamma(x) \end{aligned} \quad (23)$$

where $\delta u_k(y)$ and $\delta q_k(y)$ are the topological sensitivities of the displacements and tractions on the boundary, due to the appearance of an infinitesimal arbitrarily shape flaw at \mathbf{z} . The above equation is called the *Topological Sensitivity Boundary Integral Equation*.

The term $\int_{\Gamma_z} n_j(x) \delta u_k^\infty d\Gamma(x)$ was approximated by Guzina and Bonnet [10] and Lure [11].

Simplifying one can reach to the following:

$$I_{jk} = -\frac{4\pi a^3}{3\mu} [CA \sigma_{kj}^{\infty(z)} - CB \sigma_{ii}^\infty \delta_{jk}] \quad (24)$$

Where the value of CA and CB depend only upon the Poisson's ratio

$$CA = \frac{15}{2} \left[\frac{(1-\nu)}{(7-5\nu)} \right], \quad CB = \frac{3}{4} \left[\frac{(1-\nu)(1+5\nu)}{(7-5\nu)(1+\nu)} \right] \quad (25)$$

Numerical Results

Example I : Cube under prescribed uniform traction with a central cavity:

A 6m x 6m x 6m cubic domain is subjected to a uniform traction $p = 100 \text{ N/m}^2$ on the upper face. The lower face has a prescribed potential $u = 0$ and the lateral faces a prescribed flux of $q = 0$. The domain has the following material properties having shear modulus $\mu = 10^6 \text{ N/m}^2$, density $\rho = 100 \text{ kg/m}^3$ and Poisson's ratio $\nu = 0.25$. The boundary mesh of the problem, consist of 216 quadratic elements ((866) nodes). Its required to obtain the response of this cubic domain when a cavity is placed at its center $x = 3m; y = 3m; z = 3m$. The problem was solved using both of the direct formulation '*total problem*' and using the DTOP program. Comparisons of the results obtained from both formulations are done for different values of the cavity's radius, the values selected are $r = 0.1, 0.2, 0.3, 0.5$ and 0.9 . Fig.1 shows the computed value of the displacement at the mid-point of the upper face ($x = 3; y = 3; z = 6$) versus the volume of the sphere for the radius above mentioned. Results are of the total problem and using the DTOP.

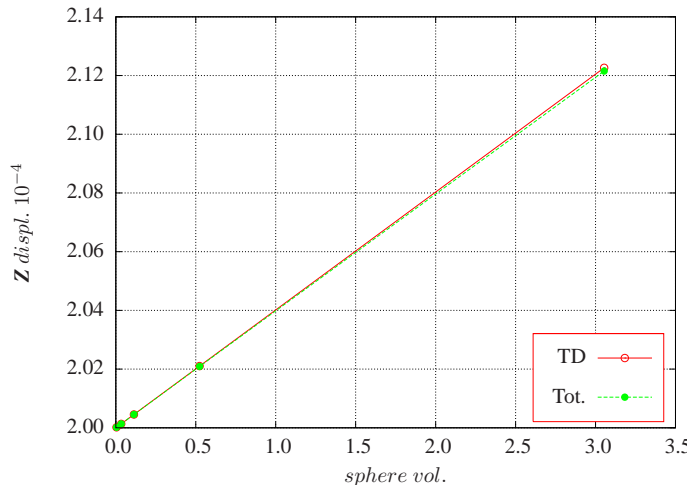


Figure 1: Displ. of TOTAL and DTOP of the upper mid-face node

Example II: Cube under uniform traction applied to three faces having a cavity at (4., 5., 4.5)

The same cubic geometry and boundary conditions of Example I are used, also the material properties and discretizations are identic. The applied loads are as follow: a uniform traction $p = 100 \text{ N/m}^2$ on the upper face, a uniform traction of $p = -10 \text{ N/m}^2$ on the right face (parallel to the y direction) and a uniform traction of $p = 30 \text{ N/m}^2$ on the front face of the cube (parallel to the x direction). Fig.2 shows a comparison of the value of stresses at a critical node ($x = 3.; y = 4.; z = 0.$) on the lower face of the example II cube, for different values of cavity radius, using the TD and resolving the total problem. The next result shown in Fig.3 shows

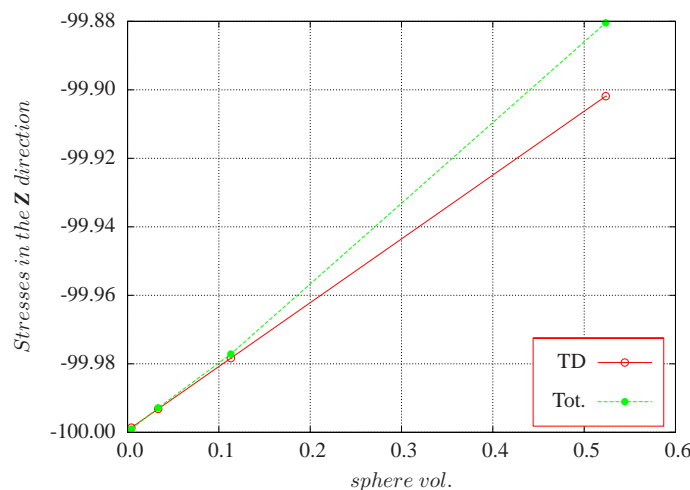


Figure 2: Stresses of TOTAL and DTOP for a lower face node (3., 4., 0.)

a comparison of the value of stresses at the node ($x = 0.; y = 2.; z = 4.$), a back face node, also for the mentioned values of cavity radius, using the TD and resolving the total problem

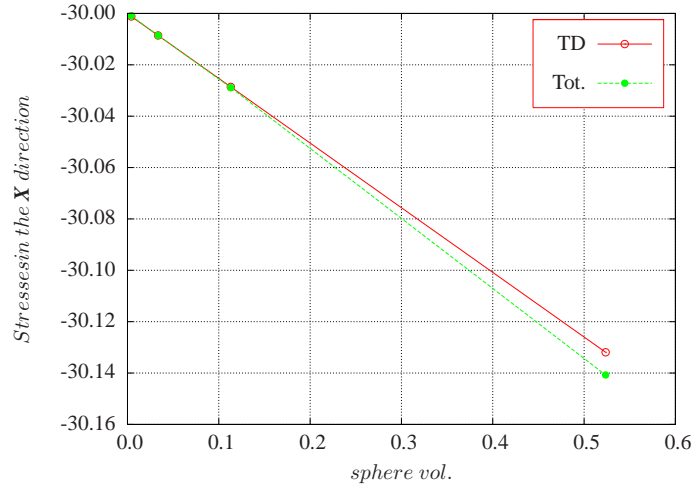


Figure 3: Stresses of *TOTAL* and *DTOP* for a back side node (0., 2., 4.)

References

- [1] H. A. Eschenauer, V. V. Kobelev, and A. Schumacher 1994. *Bubble method for topology and shape optimization of structures*. Structural Optimization, vol. 8, pp42-51.
- [2] T. Lewiński and J. Sokołowski 1997. *Topological derivative for nucleation of non-circular voids*. Rapport de Recherche, Inria,3398.
- [3] S. Garreau , P. Duillaume and M. Massamoudi 2001. *The topological asymptotic for the PDE systems: the elasticity case*. SIAM Journal on Control and Optimization, vol. 39, no.6, pp1756-1778.
- [4] R. Gallego and G. Rus 2004. *Identification of cracks and cavities using the topological sensitivity boundary integral equation*. Computational Mechanics 33.
- [5] M. Bonnet 1992. *A numerical approach for shape identification problems using BIE and shape differentiation*. Ed. C. A. Brebbia, J. Dominguez y F. París. Computational Mechanics Publications, Southampton, pp.541-53
- [6] G. Rus 2001. *Métodos numéricos para la detección no destructiva de defectos* PhD thesis, Grupo de Mecánica de Sólidos y Estructuras, Univ. Granada.
- [7] J. Sokołowski and A. Żochowski 1997. *On topological derivative in shape optimization*. Rapport de Recherche, Inria,3170.
- [8] A. A. Novotny, R. A. Feijoo et al. 2005. *Topological Derivative for Linear Elastic Plate Bending Problems*. Control and Cybernetics, Vol 34, Part 1, pp 339-362.
- [9] C. A. Brebbia and J. Dominguez 1992. *Boundary Elements: An Introductory Course* McGraw Hill Book Company.
- [10] B. Guzina and M. Bonnet 2004. *Topological derivative for the inverse scattering of elastic waves*. Mechanical Application Math, 57 pp.161-179.
- [11] A. I. Lure 1964. *Three dimensional problems of the theory of elasticity*. John Wiley and Sons.

Dual Boundary Elements for Analysis of Non-Shear Reinforced Concrete Beams

Sonia Parvanova and Gospodin Gospodinov

Department of Civil Engineering, University of Architecture Civil Engineering and Geodesy
1 Hristo Smirnenski blv, 1046 Sofia, Bulgaria, slp_fce@uacg.bg, gospgosp_frf@uacg.bg

Keywords: Dual boundary elements, R/C beams, Non-linear fracture mechanics

Abstract In this paper the two-dimensional dual boundary element method (DBEM) for the static analysis of non-shear reinforced concrete beams is applied. The concrete model is built upon the cohesive crack approach along with a nonlinear non-iterative technique called “event-to-event” technique. The present variant of the nonlinear numerical procedure put some restrictions on the model development, such as continuity of process of discrete crack growth and necessity of converting the constitutive law curves in a multi-linear form. In this respect a suitable modification of the dual boundary integral equations is developed and implemented in the computer code. The longitudinal steel-concrete interaction is taken into account by employing a simple modification of a bond slip model, known from the literature. A number of numerical examples are solved, analyzed and compared with known results from experimental studies in order to reveal the specific features of the theory and to evaluate the potential of the numerical method, nonlinear technique and constitutive modeling employed.

Introduction The mechanical behaviour of lightly reinforced concrete (R/C) structural components is very much affected by the formation of tensile cracks during loading [1-4]. It is observed in the experiments that in some cases the ultimate loading capacity of these components is determined by a fracture mechanism, induced by the formation and propagation of a single crack. Therefore, in order to handle adequately the post-critical behaviour of R/C member it is important to develop a reliable numerical method capable to describe the crack development in the plain concrete matrix with the steel reinforcement embedded in it [5- 8]. The problem becomes quite challenging as far as concrete members with minimum reinforcement are considered [4, 5]. In this paper R/C members are defined as “lightly” reinforced when the reinforcement ratio ρ is between 0 - 0.5 %, opposite to “normally” or “strongly” reinforced, as commented in book [2]. The main point is that the lightly reinforced beams are brittle structures and they are considered to be fracture sensitive, susceptible to theoretical analysis by means of the nonlinear fracture mechanics [4].

A dual boundary element method employing linear boundary elements is applied for analysis of reinforced concrete beams [4]. A single vertical tensile crack is assumed to develop at the middle cross section of a symmetrical 3 point bending beam. The cohesive crack approach due to Hillerborg [9] is implemented in order to account for the concrete nonlinearity in the tensile zone. The steel force is smeared over an appropriate number of boundary elements as tractions at the corresponding nodes. The nonlinear solution algorithm, accounting for the physical nonlinearity of the material is called “event-to-event” nonlinear algorithm and it is presented and described in detail by Parvanova [4]. The bond slip constitutive model is taken from paper [8] and implemented in the software code with a suitable modification. Some limitations concerning the shape of the used constitutive relationships are commented in the following sections.

A number of experimental test reported in the literature are reproduced in the paper in order to illustrate the feasibility of the developed methodology.

1. The dual boundary element method

The development of the DBEM using a discontinuous double-node linear boundary element is given in [4] and [10], so due to space limitation the details will be omitted. According to the fictitious crack model the fracture zone is replaced by cohesive forces which depend on the crack opening displacement. In fact, both the displacements and tractions of the nodes in the fracture zone are unknown parameters and their discrete values cannot be found via the boundary conditions. A relationship between tractions t and crack opening displacements Δu^{cr} is presented in a general form by the equation $t = k \cdot \Delta u^{cr}$, where k is a constant (usually

it is a known stiffness coefficient) and could be either positive or negative. A new modification of the dual boundary integral equations then follows – details are given in reference [4].

2. The constitutive modelling

In this paragraph we shall briefly describe the constitutive models for concrete, steel, bond slip interaction model and finally - the combined (steel plus concrete) model for the crack points belonging to both materials. We emphasize on the common feature of the all constitutive models: they all have multi-linear shape which is a strong requirement of the developed analytical and numerical methodology [4].

Concrete modeling: The fracture process zone of concrete is represented by means of the cohesive (or fictitious) crack model [9]. The cohesive crack opens when the normal stress reaches the tensile strength f_t of the concrete and descending branch of the constitutive relationship follows. With that end in view three different softening laws are adopted: single, double and three straight lines approximation – see details in [4];

Reinforcement steel modeling: A simple bilinear approximation is accepted for the steel stress-strain law - elastic-perfectly plastic with yield stress σ_y . Plasticity in the reinforcement bar is taken into account during the process of deformation;

Bond slip modeling: The idea of present bond slip model is taken from paper [8] which is built upon the results from the experimental work presented in [7]. As a basis the elastic-perfectly plastic steel relationship is employed, however when the bond slip model is added a final multi-linear (with four lines) constitutive law is obtained – see [4] for details;

Combined model: The combined constitutive model concerns the boundary nodal points on the crack faces which are common for both materials - steel and concrete. It is shown in Fig. 1(a) where the three cases are indicated: concrete, reinforcement and the combine relationship. The later is simply received as a sum of concrete (linear) and reinforcement (four lines) approximations. The concrete contribution is clearly seen over the steel hardening multi-linear stress-elongation relationship.

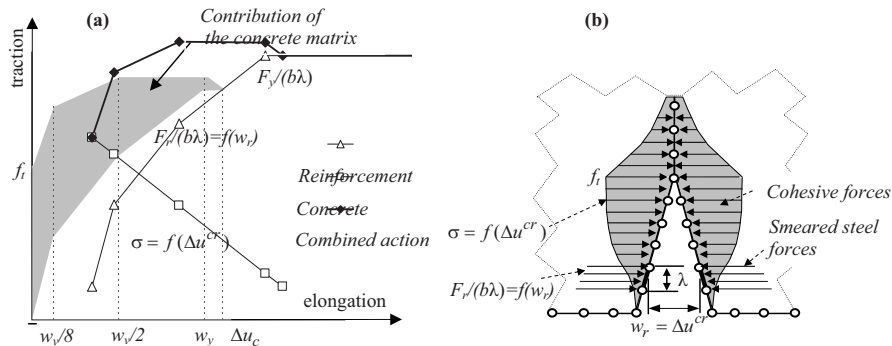


Fig. 1 (a) Concrete plus steel combined constitutive model; (b) Mixed modelling on the crack faces.

Fig. 1(b) presents the corresponding picture of the boundary nodes on both crack faces. The distribution of cohesive forces is shown for few nodal points of the crack having different status. In the same figure the following notations are used: Δu^{cr} is the crack opening displacement which in this model is assumed to be equal to steel elongation w_r ; λ is the length of the boundary element over which the steel stress resultant F_r is distributed as equivalent traction; b is the beam thickness.

3. The non-iterative “event-to-event” technique

A graphical presentation of the nonlinear “event-to-event” approach is given in Fig. 2(a). For simplicity a bilinear constitutive model is chosen, so the shown points should be considered as “state” points where the current incremental solution begins or stops. In the context of the suggested name an “event” is happening when a particular “state” point reaches a corner point of the constitutive model – that is the point where the slope k gets another value. It should be pointed out that the movement of the state points is always from left to right, which implies the assumption that the crack always grows. The crack begins to propagate (to open) when the normal stress at the mathematical crack tip exceeds the maximum tensile strength of the material.

The crack propagation can be controlled incrementally by increasing the crack length as a monotonic increasing function. In such a case it is arrived to the somehow reverse problem - the global unknowns of the problem are the load for the given new crack length increment and the calculated traction at the nodal points.

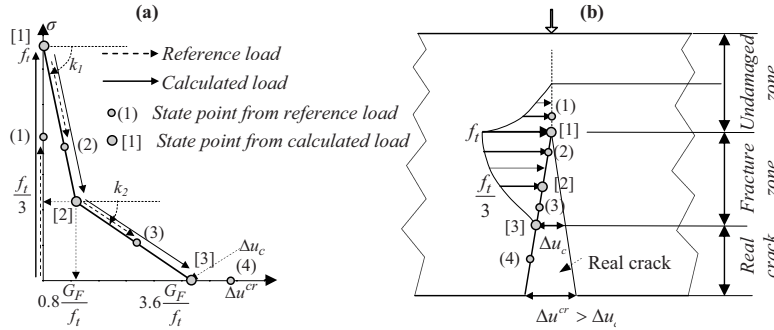


Fig. 2 Graphical representation of the nonlinear “event-to-event” solution algorithm with “reference” and “calculated” state points: (a) $\sigma - \Delta u^{cr}$ bi-linear model; (b) Fictitious crack model and respective state points.

The present incremental procedure works like that: at the beginning there is no loading, the state point is in the undamaged zone and the traction is zero. In the first sub-step of the first step a reference load with unit value is applied and the system behaves linear elastic. As a result the traction becomes smaller or larger than the tensile strength f_t , see the state point (1) in Fig. 2. Having this solution available, using a simple linear approximation, we can obtain the necessary increment of load (called calculated load) in order to get traction equal to the tensile strength. Then in the second sub-step of the first step the calculated load is applied and the state point gets into position [1] of Fig. 2. The first “event” is happening and the current results are saved. After that the considered state point falls into the fracture zone, so the relationship between traction and opening displacement is already $t^i = -k_i \Delta u^i$ - note that the slope value is $(-k_i)$. In the first sub-step of the second step the reference unit load is applied again and the new state point is (2), as shown in Fig. 2. The necessary load increment can be obtained so that the considered state point reaches the new corner position [2]. As the state point position [2] is again in the fracture zone, for the next step the stress-displacement law is $t^i = -k_2 \Delta u^i$, using the new slope $(-k_2)$. The obtained results are added to these from the first step and saved again. The above procedure is repeated and the state point is consecutively in the position (3) and [3] respectively. The results are accumulated and saved at the end of each step. Finally the point into consideration falls in the real crack zone (position (4)) and it is traction free.

Practically, many nodal points from the boundary elements located to the crack faces, are in the undamaged or fracture zones, so the above checking procedure must be performed for every single point. The smallest calculated load is taken as authoritative. Therefore, this load is applied at the end of each step and only one state point is located at a corner point of the constitutive graphics. The crack growing procedure continues until the whole crack path, obtained by the user in advance, becomes traction free or alternatively until the steel yielding capacity is reached.

4. Numerical results and comparisons

The aim of numerical simulations is to validate the present nonlinear DBEM solution and implemented constitutive models against some experimental results given in [7]. The R/C beam geometry, loading and boundary conditions, concrete and steel wires mechanical properties are identical for all numerical simulations - they are given in Fig. 3 with the respective tables. The only parameter to be varied is the beam height D , which shall be given for each different case.

It is worth analyzing a typical load-deflection curve for a beam height $D=300\text{ mm}$. The section OA in Fig. 4(a) is linear and it corresponds to elastic behavior of both materials: concrete and steel. Then it is followed by a nonlinear zone AB which is due to crack opening development. The peak point B is considered to be the load carrying capacity of the R/C beam. It is reached when a critical combination of few parameters is formed. After the peak B a softening branch BC is coming next due to growing of the fracture zone. The crack growth is in general sewed up by the reinforcement, on the other hand a softening process is happening owe to steel pullout and slip included in the model. It is presumed that at point C the concrete contribution is

spent and from this moment on an eventual hardening is happening because of the ascending branches of the steel constitutive model. The hardening ends at point D at which the reinforcement yields. The shape of BCD curve considerably depends on the value of the bond shear strength τ_c . Load-Crack Mouth Opening Displacement (CMOD) relationship is plotted in Fig. 4(b).

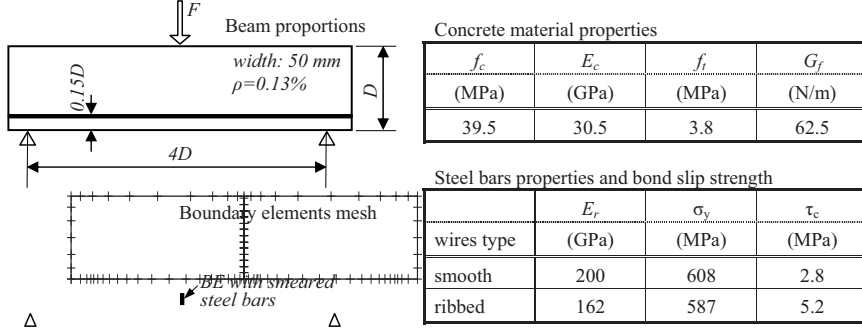


Fig. 3 Reinforced concrete beam proportions, material properties, boundary element mesh

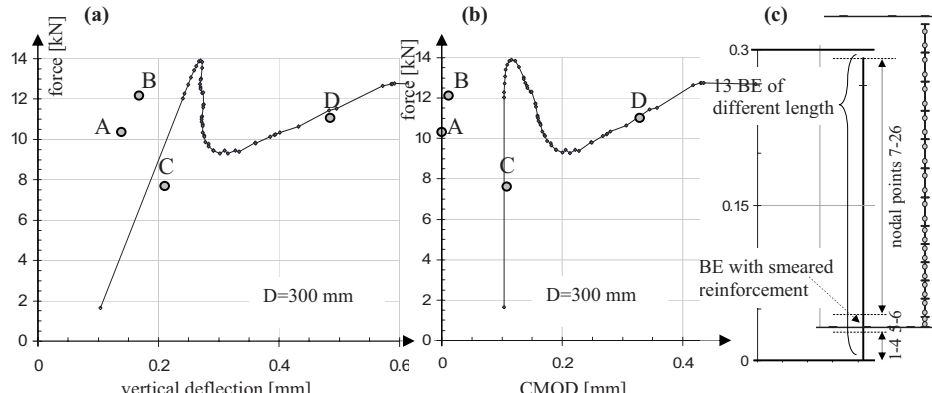


Fig. 4 (a) Typical load-deflection relationship; (b) Load-crack mouth opening displacement curve;
(c) The boundary elements layout on the crack faces

The respective variation of the stress profile in the central cross-section for the representative points A , B , C and D is given in Fig. 5. It is interesting to analyze the evolution of the steel stresses during the development of the nonlinear process. In the second picture the tractions of the nodal points at the reinforcement level reach the tensile strength of the concrete. From this moment on the bond slip model is activated and the combined constitutive law is into action. It is also instructive to observe the “movement” of the nodal crack points (see Fig. 4(c)) over the constitutive graphics for certain representative states, which are plotted in Fig. 6. In the final state D the crack is almost traction free and the steel yields.

The results for the second example are given in Figs. 7 and 8. The beam height in this case is $D=150\text{ mm}$ and the left graphic of Fig. 7 corresponds to R/C beams with ribbed steel bars, whereas the right one draws the results for smooth reinforcement. Obviously the curves get within the envelope of experimental data from the multiply tests [8], especially as far as the peak load is concerned.

The aim of the numerical simulation presented in Fig. 8 is to check whether the method is capable to handle the “snap-back” phenomena reported in some experiments. For this purpose the value of the fracture energy has been changed from $G_f=62.5\text{ N/mm}$ for upper case to $G_f=42.5\text{ N/mm}$. Again the load-deflection (Fig. 8(a)) and load-CMOD (Fig. 8(b)) curves are plotted along with a larger picture (Fig. 8(c)) reproducing

the snap-back. It is clear from the figure that the driving parameter (crack extension respectively CMOD) always grows.

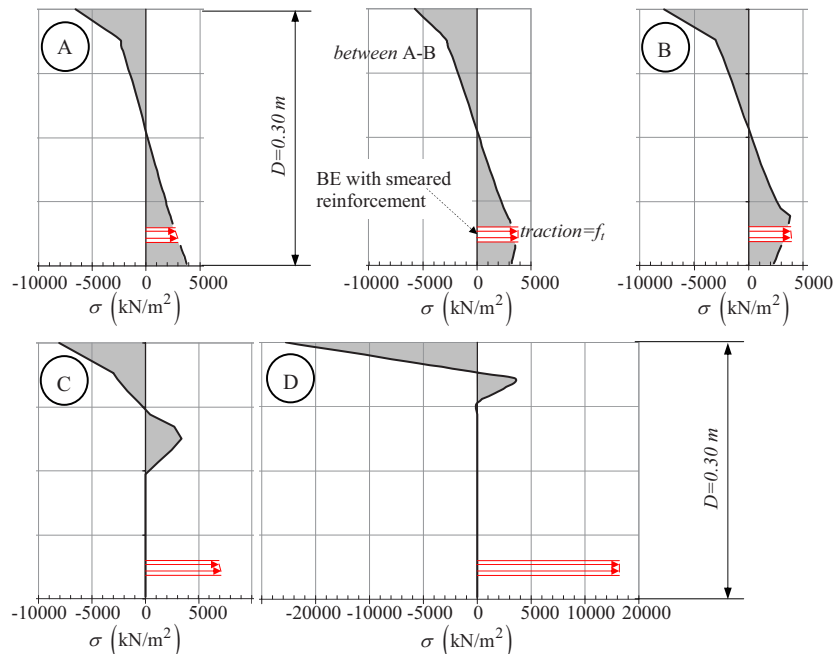


Fig. 5 Variation of the stress profile in the central cross-section for the representative points A, B, C and D from Fig. 4

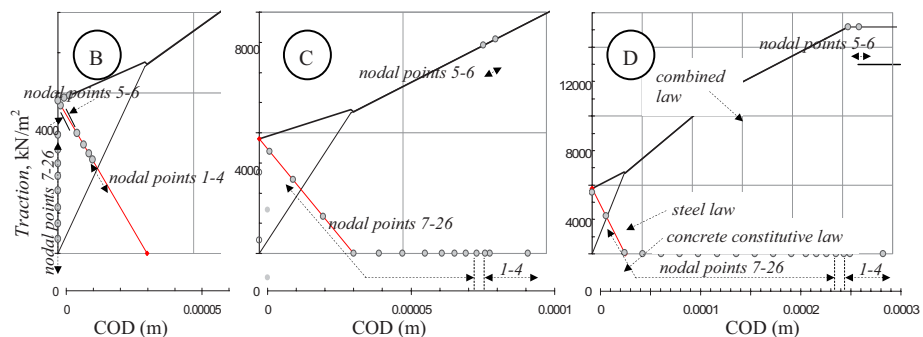


Fig. 6 Location of the nodal crack points upon constitutive graphics for the representative points B, C and D

A static analysis of the nonlinear behaviour of lightly reinforced concrete beams is the subject of this paper. The bond slip model, proposed in [8], was modified and implemented in a software code based on the two-dimensional dual boundary element method. A nonlinear numerical procedure was developed without iterations which requires multi-linear constitutive diagrams for the boundary crack points. By means of such a multi-linear diagram any real nonlinear law could be satisfactorily approximated.

Based on the above numerical simulations, analysis and the experimental validation a conclusion could be drawn that this variant the dual boundary element method, the non-iterative nonlinear procedure and the developed constitutive modelling constitute a good, accurate and reliable numerical tool for analysis of reinforced concrete beams with non-shear reinforcement.

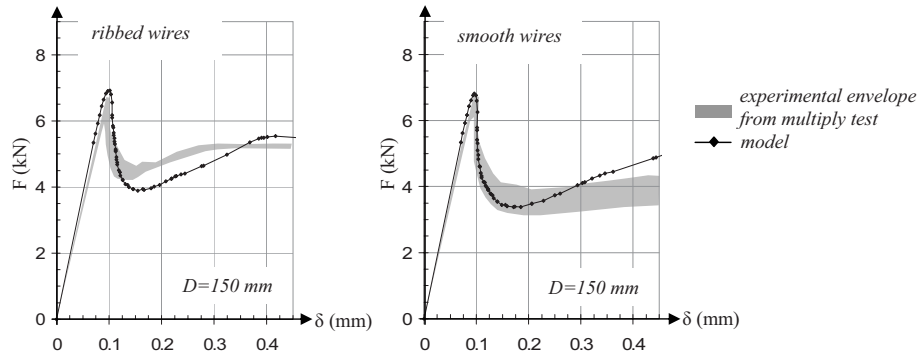


Fig. 7 Experimental verifications of load-displacement curves for different type of reinforcement wires

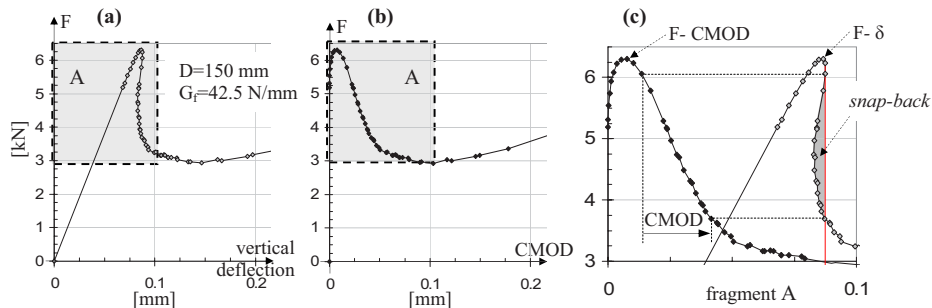


Fig. 8 Numerical simulation with value of $G_f=42.5 \text{ N/mm}$; (a) Load-deflection curve; (b) Load-CMOD curve; (c) Snap-back phenomena – fragment taken from (a) and (b)

References

- [1] M. Aliabadi and D. Rooke. *Numerical fracture mechanics*. Kluwer Academic Publishers, (1991).
- [2] Z. Bazant, J. Planas. *Fracture and size effect in concrete and other quasibrittle materials*. CRC Press, LLC, (1998).
- [3] A. L. Saleh. *Crack growth in concrete using boundary elements*. CMP, Volume 30, Southampton, (1997).
- [4] S. Parvanova. *Dual boundary element method applied to linear and nonlinear fracture mechanics*. (In Bulgarian). PhD thesis, UACEG Sofia, July, (2008).
- [5] C. Bosco and A. Carpinteri. *Fracture mechanics evaluation of minimum reinforcement in concrete structures*. In Application of Fracture Mechanics to R/C. Carpinteri, A., ed., London, (1992).
- [6] A. Carpinteri. *A fracture mechanics model for reinforced concrete collapse*. In Proceedings of IABSE Colloquium on Advanced Mechanics of Reinforced Concrete, (1981).
- [7] G. Ruiz, M. Elices and J. Planas. *Experimental study of fracture of lightly reinforced concrete beams*. Materials and Structures 31, (1998).
- [8] G. Ruiz. *Propagation of a cohesive crack crossing a reinforcement layer*. Int. J. of Fracture 111, (2001).
- [9] A. Hillerborg, M. Modeer and P. Petersson. *Analysis of crack formation and crack growth in concrete by means of fracture mechanics and finite elements*. Cement and Concrete Research 6, (1976).
- [10] S. Parvanova and G. Gospodinov, *Dual Boundary Elements for Crack Propagation by Means of Linear Fracture Mechanics*, Proceedings of Beteq 2007, Naples, Italy, (2007).

Evaluation of Green's Functions for 3D Anisotropic Elastic Solids

Y.C. Shiah¹, C.L. Tan^{2*}, V.G. Lee³ and Y.H. Chen⁴

- 1. Department of Aerospace Engineering and Systems Engineering
Feng Chia University, Taichung, Taiwan, R.O.C.
- 2. Department of Mechanical & Aerospace Engineering,
Carleton University, Ottawa, Canada K1S 5B6
* Corresponding author; Email: *ctan@mae.carleton.ca*
- 3. Department of Civil Engineering, National Chi Nan University,
Nantou 545, Taiwan, R.O.C.
- 4. Department of Computer Science and Information Management
Providence University, Taichung, Taiwan, R.O.C.

Keywords: 3D Anisotropic Green's displacements

Abstract. The numerical evaluation of the Green's functions (fundamental solutions) in BEM stress analysis of 3D anisotropic elastic solids has been a subject of much discussion over the years because of the relatively large amount of computations required if they are in their basic form in terms of a contour integral. The ability to reduce and express them as explicitly as possible will offer significant cost savings computationally. In this paper, a formulation for the explicit solution of Green's displacements is investigated. An attractive feature of this solution is that it has the final form of an algebraic expression in terms of the Stroh eigenvalues and remains valid for the degenerate cases of when there are repeated roots. The computation for Green's strains/stresses is carried out using a simple Lagrange interpolation scheme. The formulation and numerical algorithm for obtaining the Green's displacements and its derivatives have been implemented into a FORTRAN code. Two examples, one involving a degenerate case of transversely isotropy, and another involving general material anisotropy, are presented to illustrate the veracity of the approach.

Introduction

A necessary item in the formulation of the direct boundary element method (BEM) is the availability of the fundamental solution (Green's function) to the governing differential equation for the physical problem. An efficient scheme to evaluate this Green function and its derivatives is important for the development of a robust and successful BEM formulation for the stress analysis of 3D, generally anisotropic elastic solids. In isotropic elasticity, the fundamental solution and its derivatives can be expressed in relatively simple explicit forms which can be efficiently evaluated numerically. This is also true for 2D anisotropic elasticity. However, the same cannot be said for 3D anisotropic elasticity.

The Green's function for the displacement field in a 3D generally anisotropic elastic medium due to a unit point load was derived by Lifschitz and Rozentsweig [1]. It was expressed as a line integral around a unit circle with the integrand containing the Christoffel matrix defined in terms of the elastic material constants. The evaluation of this integral into simpler explicit analytical forms, as well as the development of efficient algorithms for its accurate and stable numerical evaluation have eluded researchers for several decades, see, e.g., [2]-[4], although simplifications to special cases of anisotropy have been met with some success. Employing the Radon transform and the calculus of residues, Wang [5] derived an explicit algebraic expression for the displacement Green's function in three-dimensional general anisotropy and presented a strategy for determining its derivatives. No numerical results were obtained by Wang [5], however; instead his work was implemented by Tonon, *et al* [6] in a BEM formulation. It is assumed in these works that the roots of the sextic equation (Stroh's eigenvalues) are distinct.

An alternative explicit solution of the Green's function for the displacements in a 3D anisotropic body has also been derived by Ting and Lee [7] using the Fourier transform. It is simpler in form to that obtained by Wang [5] and is expressed primarily in terms of Stroh's eigenvalues and remains valid even in the degenerate cases of equal eigenvalues. The issues involved with the numerical evaluation of this Green's function solution and its derivatives, to the authors' knowledge, have not been reported in the literature, and are the focus of the present paper. In this paper, the Green's displacements are computed using the formulations proposed by Ting and Lee [7], and their derivatives are obtained by simple Lagrange interpolation which leads to a central difference scheme. Comparison of the results obtained using these procedures with other numerical solutions for two example cases are then presented.

Green's function for general anisotropic materials

The boundary integral equation (BIE), which relates the nodal displacements u_i and tractions t_j at the boundary S of the homogeneous elastic domain, is written in indicial notation as

$$C_{ij}(P) u_i(P) + \int_S u_i(Q) T_{ij}(P, Q) dS = \int_S t_i(Q) U_{ij}(P, Q) dS \quad (1)$$

where the value of $C_{ij}(P)$ depends upon the local geometry of S at the source point P ; $U_{ij}(P, Q) \equiv U(\mathbf{x})$, and $T_{ij}(P, Q)$ represent the fundamental solutions of displacements and tractions, respectively, in the x_i -direction at the field point Q due to a unit load in the x_j -direction at P in a homogeneous infinite plane. The focus of this paper is to numerically evaluate the Green's functions - $U_{ij}(P, Q)$ and its derivatives, $U_{ij,l}(P, Q)$, since $T_{ij}(P, Q)$ can be directly calculated from the strain components; the comma index denotes partial differentiation. A brief review of the derivation of the explicit forms of the Green's displacements proposed by Ting and Lee [7] is first given here.

In 3D, the Green's displacements for the infinite space can be expressed as

$$\mathbf{U}(\mathbf{x}) = \frac{1}{8\pi^2 r} \int \mathbf{Q}^{-1}(\mathbf{n}^*) dS, \quad (2)$$

where r is the radial distance between the source point at the origin and the field point at $\mathbf{x} = (x_1, x_2, x_3)$. In Eq. (2), the integral is taken around the unit circle $|\mathbf{n}^*| = 1$ on the oblique plane normal to \mathbf{x} ; the components of \mathbf{Q} , Q_{ik} , are expressed in terms of the stiffness matrix C_{jks} as

$$Q_{ik}(\mathbf{n}^*) = C_{jks} n_j^* n_s^* \quad (3)$$

where the unit vector \mathbf{n}^* on the oblique plane can be represented in terms of an arbitrary parameter ψ by

$$\mathbf{n}^* = \mathbf{n} \cos \psi + \mathbf{m} \sin \psi, \quad (4)$$

In Eq. (4), the vectors $[\mathbf{n}, \mathbf{m}, \mathbf{x}/r]$ form a right-handed triad. As shown schematically in Fig. 1, the general form of \mathbf{n} and \mathbf{m} can be expressed as

$$\begin{aligned} \mathbf{n} &= (\cos \phi \cos \theta, \cos \phi \sin \theta, -\sin \phi), \\ \mathbf{m} &= (-\sin \theta, \cos \theta, 0). \end{aligned} \quad (5)$$

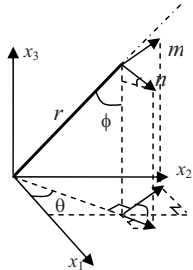


Fig. 1: Definition of the unit vectors \mathbf{n} , \mathbf{m}

By letting $\mathbf{V} = \mathbf{R} + \mathbf{R}^T$, equation (9) may also be rewritten as

$$\Gamma(p) = \mathbf{Q} + p\mathbf{V} + p^2\mathbf{T}. \quad (10)$$

The vanishing of the determinant, $|\Gamma(p)|$, would lead to a sextic equation in p . By defining a matrix, $\mathbf{H}[\mathbf{x}]$, which depends only on the direction of \mathbf{x} , as

$$\mathbf{H}[\mathbf{x}] = \frac{1}{\pi} \int_{\pi/2}^{\pi/2} \mathbf{Q}^{-1}(\psi) d\psi, \quad (11)$$

the Green's displacements can be expressed as

$$\mathbf{U}(\mathbf{x}) = \frac{1}{4\pi r} \mathbf{H}[\mathbf{x}]. \quad (12)$$

The six roots of the sextic equation are the Stroh eigenvalues; they must be complex to yield positive strain energy [7] and they appear as three pairs of complex conjugates. It has been proved [8] that the sextic equation is not tractable analytically. The computational effort to find these roots numerically is, however, not heavy as compared with the numerical burden of performing the integration of Eq. (9).

For an oblique plane, $\mathbf{H}[\mathbf{x}]$ remains symmetric and positive definite and so is the Green's function $\mathbf{U}(\mathbf{x})$. BY writing the complex roots as

$$p_v = \alpha_v + i\beta_v, \quad \beta_v > 0, \quad (v=1, 2, 3), \quad (13)$$

where both α_v are real, $\mathbf{H}[\mathbf{x}]$ can be expressed as

$$\mathbf{H}[\mathbf{x}] = \frac{1}{|\mathbf{T}|} \sum_{t=1}^3 \frac{\hat{\Gamma}(p_t)}{\beta_t(p_t - p_{t+1})(p_t - \bar{p}_{t+1})(p_t - p_{t+2})(p_t - \bar{p}_{t+2})}, \quad (14)$$

in which the subscript t follows the cyclic rule $t=(t-3)$ if $t>3$, and $\hat{\Gamma}$ is the adjoint of Γ , being a polynomial in p of degree four. Equation (14) provides an explicit expression of the Barnett-Lothe tensor $\mathbf{H}[\mathbf{x}]$, and hence the Green's function $\mathbf{U}(\mathbf{x})$, in terms of the Stroh eigenvalues p_v for general anisotropic elastic materials. It is evident that the expression for $\mathbf{H}[\mathbf{x}]$ as in Eq. (14) cannot be valid for the degenerate cases when there are repeated roots, i.e. when $p_t=p_{t+1}$ or $p_t=p_{t+2}$. Ting and Lee [7] resolved this problem by rewriting $\mathbf{H}[\mathbf{x}]$ as

$$\mathbf{H}[\mathbf{x}] = \frac{1}{|\mathbf{T}|} \sum_{n=0}^4 q_n \hat{\Gamma}^{(n)}, \quad (15)$$

where q_n is given by

$$q_n = \begin{cases} \frac{-1}{2\beta_1\beta_2\beta_3} \left[\operatorname{Re} \left\{ \sum_{t=1}^3 \frac{p_t^n}{(p_t - \bar{p}_{t+1})(p_t - \bar{p}_{t+2})} \right\} - \delta_{n2} \right] & \text{for } n=0,1,2, \\ \frac{1}{2\beta_1\beta_2\beta_3} \left[\operatorname{Re} \left\{ \sum_{t=1}^3 \frac{p_t^{n-2} \bar{p}_{t+1} \bar{p}_{t+2}}{(p_t - \bar{p}_{t+1})(p_t - \bar{p}_{t+2})} \right\} - \delta_{n2} \right] & \text{for } n=3,4, \end{cases} \quad (16)$$

In Eq. (16), $\operatorname{Re}\{\cdot\}$ represents the operation of taking real part, and δ is the Kronecker delta defined as usual. By basic algebraic arrangements, $\hat{\Gamma}_{ij}^{(n)}$, components of $\hat{\Gamma}^{(n)}$, may be expressed as

$$\hat{\Gamma}_{ij}^{(n)} = \tilde{\Gamma}_{(i+1)(j+1)(i+2)(j+2)}^{(n)} - \tilde{\Gamma}_{(i+1)(j+2)(i+2)(j+1)}^{(n)}, \quad (i,j=1,2,3), \quad (17)$$

where the subscript follows the cyclic rule as described before, and the 4th-order tensor $\tilde{\Gamma}^{(n)}$ is given by

$$\begin{aligned} \tilde{\Gamma}_{pqrs}^{(4)} &= T_{pq} T_{rs}, \\ \tilde{\Gamma}_{pqrs}^{(3)} &= V_{pq} T_{rs} + T_{pq} V_{rs}, \\ \tilde{\Gamma}_{pqrs}^{(2)} &= T_{pq} Q_{rs} + T_{rs} Q_{pq} + V_{pq} V_{rs}, \\ \tilde{\Gamma}_{pqrs}^{(1)} &= V_{pq} Q_{rs} + V_{rs} Q_{pq}, \\ \tilde{\Gamma}_{pqrs}^{(0)} &= Q_{pq} Q_{rs}. \end{aligned} \quad (18)$$

The computations involved in Eqs. (15)-(18) are relatively straightforward and easy to be programmed in a computer code.

In BEM formulations, it is necessary to compute the corresponding stresses σ_{ij} when the unit load is applied in the direction of x_i . This is carried out using

$$\boldsymbol{\sigma}_i = \mathbf{C} \boldsymbol{\epsilon}_i, \quad (19a)$$

where

$$\boldsymbol{\sigma}_i = (\sigma_{11}, \sigma_{22}, \sigma_{33}, \sigma_{23}, \sigma_{13}, \sigma_{12})_i^T, \quad (19b)$$

$$\boldsymbol{\varepsilon}_l = (\varepsilon_{11}, \varepsilon_{22}, \varepsilon_{33}, 2\varepsilon_{23}, 2\varepsilon_{13}, 2\varepsilon_{12})_l^T, \quad (19c)$$

$$(\varepsilon_y)_l = (U_{ilj} + U_{jli})/2. \quad (19d)$$

A relatively simple way to obtain $U_{ij,l}$ is by a simple Lagrange interpolation scheme which results in a finite difference equation as [6] :

$$U_{ij,l}(\mathbf{x}) \approx \frac{U_{ij}(\mathbf{x} + \Delta_l) - U_{ij}(\mathbf{x} - \Delta_l)}{2h}, \quad (l=1, 2, 3), \quad (20)$$

where Δ_l represents an increment of h in the abscissas direction of x_l . In the present work, the step size as recommended in [6], $h = r \times 10^{-6}$, is employed. This interpolation is capable of yielding accurate results for the derivatives with an error order $O(h^2)$. To illustrate the validity and accuracy of the above formulation and algorithm, two numerical examples are presented next.

Numerical examples

The first example involves the degenerate case of transverse isotropy as has been treated in [6], for which analytical solutions are available for the Green's displacements and stresses [9]. Consider a transversely isotropic, linearly elastic solid with its isotropic plane parallel to the x_1-x_2 plane and having the these material properties:

$$\begin{aligned} E &= 20 \times 10^7 \text{ (N/m}^2\text{)}, \quad E' = 4 \times 10^7 \text{ (N/m}^2\text{)}, \\ \nu &= 0.25, \quad \nu' = 0.25, \quad G' = 1.6 \times 10^7 \text{ (N/m}^2\text{)}, \end{aligned} \quad (21)$$

where

E and E' : represent the Young's moduli in the plane of transverse isotropy and in the direction normal to it, respectively.

ν and ν' : represent the Poisson's ratios characterizing the later strain response in the plane of transverse isotropy to a stress acting parallel and normal to it, respectively.

G' : represents the shear modulus in planes normal to the plane of symmetry.

Accordingly, the stiffness matrix \mathbf{C} is [6]

$$\mathbf{C} = \begin{pmatrix} 88 & 72 & 40 & 0 & 0 & 0 \\ 72 & 88 & 40 & 0 & 0 & 0 \\ 40 & 40 & 88 & 0 & 0 & 0 \\ 0 & 0 & 0 & 24 & 0 & 0 \\ 0 & 0 & 0 & 0 & 16 & 0 \\ 0 & 0 & 0 & 0 & 0 & 16 \\ \text{sym.} & & & & 0 & 8 \end{pmatrix} \times 10^7 \text{ (N/m}^2\text{)}. \quad (22)$$

The source point, where a unit load (1 N) is applied, is placed at the origin and a field point located at $\mathbf{x} = (-1, 0.8, 1.5)$ (m) is considered. The Green's displacements computed using the above formulation and the closed-form solution of [9] are listed in Table 1; the corresponding computed Green's stresses are shown in Table 2.

Table 1: Comparison of the Green's displacements- Example 1

(i,j)	G_{ij} (present algorithm) $\times 10^{-10}$ (m)	G_{ij} (closed-form solution [9]) $\times 10^{-10}$ (m)	$ Error \%) $
(1,1)	2.8127404834	2.8127406201	4.87E-6
(1,2)	-0.5897686915	-0.5897686584	5.61E-6
(1,3)	-0.8915142618	-0.8915142588	3.37E-7
(2,2)	2.5473447532	2.5473447238	1.15E-6
(2,3)	0.7132113160	0.7132114071	1.28E-5
(3,3)	4.1965508792	4.1965510002	2.88E-6

Table 2: Comparison of the Green's stresses- Example 1

(i,j)	σ_l (present algorithm) $\times 10^{-2}$ (N/m 2)	σ_l (closed-form solution [9]) $\times 10^{-2}$ (N/m 2)	Error %
$(l=1)$	(1,1) 0.1406003504	0.1406140034	9.71E-3
	(1,2) -0.6061582393	-0.6061594080	1.87E-4
	(1,3) -0.7182432535	-0.7182406182	3.65E-4
	(2,2) -0.2048588290	-0.2048501374	4.24E-3
	(2,3) 1.0538501210	1.0538525268	2.26E-4
	(3,3) 0.5309695195	0.5309746490	9.65E-4
$(l=2)$	(1,1) -0.0415743069	-0.0415717811	6.08E-3
	(1,2) 0.5008838349	0.5008843960	1.19E-4
	(1,3) 1.0538493011	1.0538525263	3.05E-4
	(2,2) 0.0929606921	0.0929606880	0.08E-4
	(2,3) -0.2440074880	-0.2440069803	2.08E-4
	(3,3) -0.4247797192	-0.4247797192	2.88E-4
$(l=3)$	(1,1) 1.1122945491	1.1122950360	0.43E-4
	(1,2) -0.2094440111	-0.2094421788	8.75E-4
	(1,3) 0.6679945057	0.6679991466	6.96E-4
	(2,2) 1.0180457709	1.0180460556	0.23E-4
	(2,3) -0.5343965016	-0.5343993173	5.24E-4
	(3,3) -1.0020006486	-1.0019987199	2.02E-4

For the second example, consider the same material constants as in the first example but with rotations of the material axes. As a result of successive rotations of the x_2 -axis and x_3 -axis respectively by 45° and 150° counterclockwise, the elastic matrix is shown below; it has the features of general anisotropy:

$$\mathbf{C} = \begin{pmatrix} 71.5 & 54.5 & 38.0 & -11.0 & -12.124355653 & -6.0621778265 \\ & 83.5 & 50.0 & -5.0 & -15.588457268 & -4.3301270189 \\ & & 64.0 & -8.0 & -13.856406461 & -10.3923048454 \\ & \text{sym.} & & 11.0 & -1.7320508076 & 1.7320508076 \\ & & & & 9.0 & -1.0 \\ & & & & & 10.5 \end{pmatrix} \times 10^7 \text{ (N/m}^2\text{)}. \quad (23)$$

In the rotated coordinate system, the source point has new coordinates (1.9309310892, 0.1910631535, 0.3535533906). The analytical solution for this generally anisotropic case can now be obtained by coordinate transformation of the closed-form solution of [9]. The Green's displacements and stresses computed by the present algorithm and the closed-form solutions are tabulated in Table 3 and Table 4, respectively. From these tables, it can be seen that the numerical solutions obtained by the present algorithm are indeed in excellent agreement with the closed-form solutions [9].

Table 3: Comparison of the Green's displacements- Example 2

(i,j)	G_{ij} (present algorithm) $\times 10^{-10}$ (m)	G_{ij} (closed-form solution [9]) $\times 10^{-10}$ (m)	Error %
(1,1)	4.7318653092	4.7318653090	3.42E-9
(1,2)	0.3398875079	0.3398875079	2.17E-8
(1,3)	0.6428510739	0.6428510739	1.98E-9
(2,2)	2.2116394839	2.2116394837	7.82E-9
(2,3)	0.2703596584	0.2703596583	1.42E-8
(3,3)	2.6131315514	2.6131315513	2.85E-9

Table 4: Comparison of the Green's stresses- Example 2

(I,j)		σ_I (present algorithm) $\times 10^{-2}$ (N/m ²)	σ_I (closed-form solution [9]) $\times 10^{-2}$ (N/m ²)	Error %
$(l=1)$	(1,1)	-2.0218036487	-2.0218036624	6.77E-7
	(1,2)	-0.5036077370	-0.5036077299	1.41E-6
	(1,3)	-0.9596786167	-0.9596786151	1.64E-7
	(2,2)	1.1528828009	1.1528827897	9.73E-7
	(2,3)	-0.0631731680	-0.0631731651	4.52E-6
	(3,3)	1.0873734471	1.0873734317	1.41E-6
$(l=2)$	(1,1)	0.4471925715	0.4471925984	6.01E-6
	(1,2)	0.0951357949	0.0951357928	2.17E-6
	(1,3)	-0.4673364944	-0.4673365035	1.96E-6
	(2,2)	0.4299261505	0.4299261891	8.98E-6
	(2,3)	0.2557893240	0.2557893218	8.67E-7
	(3,3)	-0.3198405997	-0.3198405717	8.75E-6
$(l=3)$	(1,1)	0.9558228971	0.9558228968	3.48E-8
	(1,2)	-0.4476686361	-0.4476686348	2.86E-7
	(1,3)	-0.6018816517	-0.6018816532	2.48E-7
	(2,2)	-0.0688423846	-0.0688423816	4.30E-6
	(2,3)	-0.1765151922	-0.1765151891	1.74E-6
	(3,3)	0.2409119981	0.2409119964	7.05E-7

Conclusions

In this paper, an explicit formulation for the 3D anisotropic Green's displacements is investigated. Except for the numerical procedure to determine the Stroh's eigenvalues, the formulations to obtain the displacement components are very straightforward indeed. It has the added advantage that it remains valid for the degenerate cases of repeated eigenvalues. To compute the Green's stresses, a simple interpolation scheme is employed. The algorithm to compute the Green's functions has been built into a FORTRAN computer code. The veracity of this formulation and the numerical algorithm has been demonstrated by two numerical examples with closed form solutions, showing excellent accuracy. Work is currently under way to implement this in a BEM code.

Acknowledgement

The first two authors, YCS and CLT, gratefully acknowledge the financial support of the National Science Council of Taiwan, Republic of China, (Grant Number: 96-2221-E-035-011), and the National Science and Engineering Research Council (NSERC) of Canada, respectively.

References

- [1] I.M. Lifshitz and L.N. Rozenzweig, *Zh. Eksp. Teor. Fiz.*, **17**, 783-791 (1947)
- [2] R.B. Wilson and T.A. Cruse, *Int. J. Numer. Meth. Engng.*, **12**, 1383-1397 (1978)
- [3] M.A. Sales and L.J. Gray, *Comp. & Struct.*, **69**, 247-254 (1998)
- [4] A.V. Phan, L.J. Gray and T. Kaplan, *Comm. Numeric. Meth. Engng.*, **20**, 335-341 (2004)
- [5] C.Y. Wang, *J. Engng. Math.*, **32**, 41-52 (1997)
- [6] F. Tonon, E. Pian and B. Amadei, *Comp. & Struct.*, **79**, 469-482 (2001)
- [7] T.C.T. Ting and V.G. Lee, *Q. J. Mech. Appl. Math.*, **50**, 407-426 (1997).
- [8] Thomas R. Hagedorn, *Journal of Algebra* **233**, 704-757 (2000).
- [9] Y.C. Pan and Chou, T.W., *J. Appl Mech* **29**, 225-236 (1976).

Experimental Measurement Error in the Inverse Identification Problem in a Viscoelastic Layer

Alejandro E. Martínez-Castro¹ and Rafael Gallego²

¹ Dept. Structural Mechanics, University of Granada, Ed. Politécnico de Fuentenueva, 18071

Granada, Spain, amcastro@ugr.es

² Dept. Structural Mechanics, University of Granada, Ed. Politécnico de Fuentenueva, 18071

Granada, Spain, gallego@ugr.es

Keywords: Waveguide, Green's function, Adjoint Variable Method, Inverse Problem, Measurement Error

Abstract. In this communication, the inverse identification problem of a single ellipsoid cavity is considered. The identification of the 3D parametrized cavity (center coordinates and diameters) is done by solving an optimization problem. The cost function consists on two terms: i) the misfit between the experimental measurements for the 'real' cavity and the measurements taken for the 'trial' cavity; ii) a-priori information in terms of the cavity volume. The gradient computations are done via the Adjoint Variable Method.

The experimental data are generated through the same forward problem solver. The effect of noise on such numerical solution is considered by a random perturbation given to the nodal numerical displacements, given as 'experimental' data. This approach is usual in the inverse problem literature, and it is a first step in order to check the convergence properties of the problem (although the 'inverse crime' is considered also). The noise level is tested, in order to check the noise percentage admissible for this inverse identification problem. Through numerical tests, the noise levels and convergence properties are discussed, comparing the conclusions with other existing results published in the literature.

Introduction

The identification of defects (in this context, ellipsoid cavities) inner in a 3D viscoelastic solid is mathematically treated as an optimization problem. The solid in this case is a single layer, a three-dimensional solid limited by two parallel planes. The identification of a parametrized cavity requires a cost function. Such function is built, for a trial position of the cavity, through the misfit between the experimental data measurements at selected points, and the one obtained solving the forward problem for the trial position of the cavity. The Boundary Element Method (BEM) is a good method to solve each forward problem. At each optimization step, only the position of an inner boundary should be re-meshed. The re-meshing cost is low in BEM. Also, choosing the adequate Green function, mesh is necessary only in selected surfaces. In the context of this work, the Green function for the layer domain in time-harmonics dynamics has been chosen: thus, only cavity mesh is required, because no other surfaces (patches or supports) are considered.

One of the most important stages in the optimization process is the computation of the gradients of the cost function respect to parameters. The computing of such gradient might be done analytic (2D works by Gallego and Rus [1–3]). The analytic computation of gradients shows advantages, in terms of precision and direct differentiation of any parameter required, but some problems are presented: first, for each parameter derived it is required to solve one problem; second, a Green function must be derived, but in some cases, like the one presented here (layer solution) it is a difficult task. An alternative semi-analytical technique is the gradient computation via the Adjoint Variable Approach (AVA) [4–6, 8]. The gradient computation of the cost function respect to any set of parameters is solved by a convolution integral over the defect surface. Only one problem has to be solved, the one called 'The Adjoint Problem'. Due to the particular Green's function used in this work, this second technique has been used.

Experimental data are subjected to random noise. Testing random noise sensitivity is an important task to check the convergence of the inversion method. In this paper, the experimental data are simulated by solving

the forward problem for the 'real' cavity position. The noise generation is based on such measurements, and it is defined through a Normal distribution. The use of the AVM to solve the gradients and the experimental errors are discussed in this paper.

Formulation

Figure 1 shows the 3D layer domain Ω , thickness h . A 6 degrees of freedom's cavity is considered (3 center coordinates and 3 radii). Let Γ be the cavity boundary. In reference to the cartesian basis $\{O; x_1, x_2, x_3\}$, it is defined the region $\Omega = \{(x_1, x_2, x_3) | 0 \leq x_3 \leq h\}$. At certain points \mathbf{x}^f corresponding to the upper layer, a set of time-harmonics sources are considered.

$$\mathbf{f}(\mathbf{x}) = \sum_{m=1}^{NS} P_m e^{i\omega t} \delta(\mathbf{x} - \mathbf{x}^f) \quad (1)$$

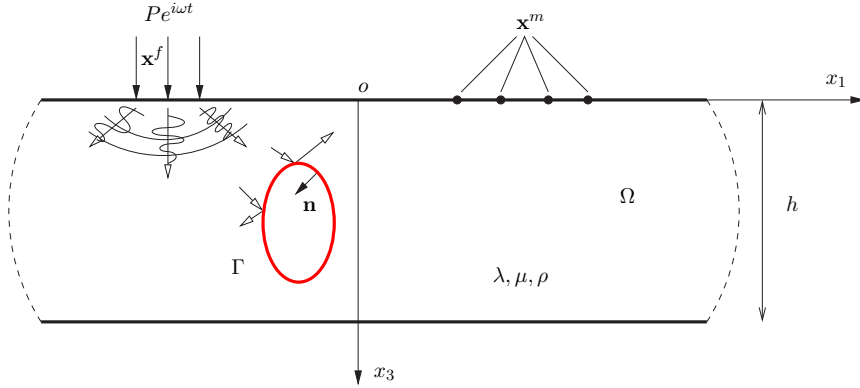


Figure 1: Ellipsoid cavity in a single layer domain. Sources and measurement points

The material is elastic, isotropic (λ, μ) and density ρ . The time-harmonic response includes damping, through the damping rates ξ_α y ξ_β and the complex-valued material modules $\lambda = \lambda^*$ y $\mu = \mu^*$, *corresponding principle* [7].

$$\begin{aligned} \lambda^* + 2\mu^* &= (\lambda + 2\mu)[1 + 2i\xi_\alpha(\omega)], \quad \xi_\alpha \geq 0 \\ \mu^* &= \mu[1 + 2i\xi_\beta(\omega)], \quad \xi_\beta \geq 0 \end{aligned}$$

The boundary conditions for the upper and lower surfaces of Ω are $t = 0$ (traction-free). The layer is infinite in directions x_1, x_2 ; thus, the radiation boundary condition is applied at these directions. At the cavity surface Γ traction-free condition is imposed ($t = 0$). See at figure (1) the outward normal \mathbf{n} in Γ .

Direct Problem

The forward problem is the computation of displacements \mathbf{u} at Γ . This problem is numerically solved by the Boundary Element Method, including an specific Green function for the layer [9]. The only domain to mesh is the ellipsoid's surface. The solution of the forward problem produces vector \mathbf{U} ; in matrix form,

$$\mathbf{H}\mathbf{U} = \mathbf{F} \quad (2)$$

Inverse Problem

Once the forward problem is solved, it is possible to compute the displacements \mathbf{u}^m at the measurement points \mathbf{x}^m , for a fixed ellipsoid position. For the 'true' cavity (real position), the experimental measurements are \mathbf{u}^e . Considering the measurement differences, and includig the a-priori information (volume cavity V^{ref}) it is build the object function $\mathcal{J}(\Gamma)$.

$$\mathcal{J}(\Gamma) = \frac{Q}{2} \sum_{n=1}^{NEP} (\overline{\mathbf{u}^m - \mathbf{u}^e}) \cdot (\mathbf{u}^m - \mathbf{u}^e) + \frac{G}{2} (V - V^{ref})^2 \quad (3)$$

with NEP the number of experimental points in \mathbf{x}^m where response is measured. Parameters Q and G are coeficients used to weight the a-priori data, and the global cost function.

The position and shape of Γ depends on d design parameters; thus, a parameter vector $\mathbf{p} = (p_1, p_2, \dots, p_d)$ is defined. After the computation of $\mathcal{J}(\Gamma)$, an optimization algorithm is defined in order to find the position and shape of Γ which minimizes $\mathcal{J}(\Gamma)$. The minimization algorithm is based on a Quasi-Newton method. It requires the computation of the first derivative of the cost function respect to design parameters. In order to compute $\partial\mathcal{J}/\partial p_d$ the direct differentiation is a tool useful for specific Green's functions. In the context of the present work, the semi-analitical integration done by the Adjoint Variable Method has been choosen, because of the complexities of the Green's function for the layer, in terms of an inverse Hankel Transform.

The Adjoint Variable Method for gradient computations

The Adjoint Variable Method is used to compute the gradient of the cost function. The first step of the method consists on the adjoint problem definition, once the forward problem is solved. The structure of the adjoint problem is analogous to the direct problem, but:

- The original excitation sources are cancelled. Instead of that, a set of point sources $\tilde{\mathbf{f}}$ are defined at the measurement points \mathbf{x}^m . The intensity of each source is equal to the difference between the measured and computed displacements (the conjugate complex number). Thus,

$$\tilde{\mathbf{f}}(\mathbf{x}) = Q \sum_{m=1}^{NEP} (\overline{\mathbf{u}^m - \mathbf{u}^e}) \delta(\mathbf{x} - \mathbf{x}^e) \quad (4)$$

- The boundary conditions of the adjoint problem have the same type than the forward problem, but they are homogeneous. For this case $\mathbf{t} = 0$ in Γ .

The adjoint problem is solved by the BEM. A matrix system is obtained,

$$\mathbf{H}\tilde{\mathbf{U}} = \tilde{\mathbf{F}} \quad (5)$$

In this sistem, \mathbf{H} is the same matrix used in the forward problem; the only computation required is vector $\tilde{\mathbf{F}}$. The solution of the adjoint problem is a displacement field $\tilde{\mathbf{u}}$. The gradient of the functional \mathcal{J} is computed via the following integral in Γ ,

$$\begin{aligned} \frac{\partial \mathcal{J}}{\partial p_d} &= \operatorname{Re} \left\{ \int_{\Gamma} [\rho \omega^2 \mathbf{u} \cdot \tilde{\mathbf{u}} - \frac{2\lambda\mu}{\lambda+2\mu} \operatorname{div}_S \mathbf{u} \operatorname{div}_S \tilde{\mathbf{u}} - \mu (\nabla_S \mathbf{u} + \nabla_S^T \mathbf{u}) : \nabla_S^T \tilde{\mathbf{u}} \right. \\ &\quad \left. + \mu (\nabla_S \mathbf{u} \cdot \mathbf{n}) \cdot (\nabla_S^T \tilde{\mathbf{u}} \cdot \mathbf{n})] \theta_n^d d\Gamma \right\} + G (V - V^{dato}) \frac{\partial V}{\partial p_d} \end{aligned} \quad (6)$$

with θ_n^d the normal transformation velocity, for parameter d .

The design parameter vector for cavity Γ is $\mathbf{p} = (c_1, c_2, c_3, a, b, c)$. The volume V can be computed fom axis, as

$$V = \frac{4}{3} \pi a b c$$

Thus, the volume variations respecto to parameters are obtained as a closed-form formula, for each step. The transformation velocity vector in the normal direction is $\theta_n^d \equiv \mathbf{n} \cdot \bar{\theta}^d$ ($d = 1, \dots, 6$); it has the following representation,

$$\theta_n^d = \left(n_1, n_2, n_3, \frac{x_1 - c_1}{a}, \frac{x_2 - c_2}{b}, \frac{x_3 - c_3}{c} \right) \quad (7)$$

To compute the gradient of the object function, in a boundary element mesh, the integral shown in Eq (6) is done. For an isoparametric BEM formulation, it is required the computation of the surface gradients of shape functions. In ref [8] the most relevant practical aspects of the implementation are shown, which have been followed in the present work.

Experimental measurement noise

In order to check the convergence properties of the inverse algorithm, it is required to check the sensitivity of the algorithm respect to noise in experimental measurement. One common technique consists on applying a random noise to the 'true' experimental observed measurements, at each component, as follows

$$u_i^{e,noise} = u_i^e (1 + \varphi) \quad (8)$$

where φ is a random variable uniformly distributed over the interval $[-\eta, \eta]$. Values of η tested in this study cover range from $\eta=0.03$ to $\eta=0.40$. A set of numerical benchmarks, varying several aspects (numbers of experimental points, sources, a-priori data) gives an interesting result for this layer domain. Noise levels up to 40 % gives convergence. Convergence is better when a-priori information is considered, and when more measurement points are considered. This particular layer problem seems to be better for convergence due to the layer configuration (reflection waves at the lower layer).

Numerical results

A numerical example has been chosen in order to show the three main aspects of this research: i) the gradient computation based on the Adjoint Variable Method; ii) the use of the layer Green's function; iii) the noise effects on measurements. A layer thickness $h = 6$ has been considered. $\mu = 1 + 0.2i$ (damping is considered), $\nu = 0.3$. The angular frequency is $\omega = 1$. An spherical cavity has been considered, centered at $(0, 0, 3)$, and diameter $d = 2.2$. A 2-parameter inverse identification problem is solved. Parameters are: x_1 central coordinate (c_1), and the cavity diameter d (thus, $a=b=c=d$).

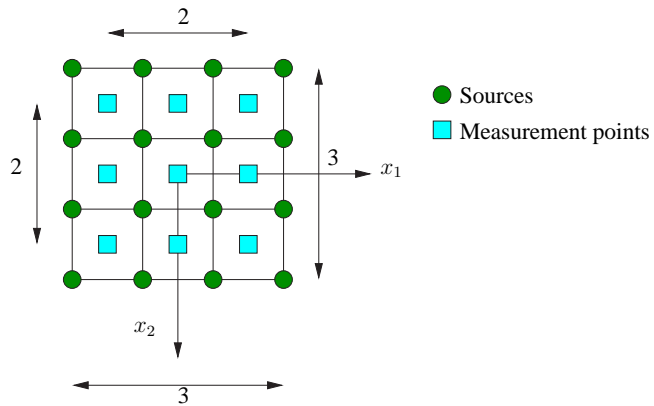


Figure 2: Sources and receivers, at $x_3 = 0$

Figure 2 shows the arrays of sources and experimental points. Sources are located at $x_3 = 0$, in a 3x3 array, centered at $x_1 = 0$, $x_2 = 0$, a total of 16 points (4x4 array). Each source is a point-load pointing to the x_3 direction, with time-harmonic excitation frequency $\omega = 1$. Receivers take displacement measurements \mathbf{u}^m at points \mathbf{x}^m , distributed in a 2x2 array, centered at $x_1 = 0$, $x_2 = 0$, 9 receivers.

A first step consists on defining the experimental data, and the polluted random-noised data from this first measurement vector. The forward problem is solved, considering the true cavity position, and \mathbf{u}^e is obtained by post-processing. Other $\mathbf{u}^{e,noise}$ are generated from this one, considering different noise levels.

The solution of the Inverse Problem requires a first guess point; in this case, $(c_1, d) = (-1, 1.8)$; close parameters to the true cavity, $(c_1 = 0, d = 2.2)$. The inverse computation has been solved with MATLAB Optimization Toolbox. The BFGS Quasi-Newton algorithm has been chosen. In order to take into account the tolerances based on absolute values, an specific cost function has been defined,

$$\mathcal{J} = \frac{W}{u_{rms}} \sum_{n=1}^{NPE} (\bar{\mathbf{u}}^m - \bar{\mathbf{u}}^e) \cdot (\mathbf{u}^m - \mathbf{u}^e) \quad (9)$$

with u_{rms} the RMS value for displacements obtained at the first mesh and W a weight coefficient, in this case $W = 1E8$. The experimental data (volume information) is introduced in a second stage.

Table 1 shows the evolution of parameters when no a-priori nor random noise are considered. A fast convergence is observed. The final solution $(-0.0004, 2.1992)$ is close to the real one $(0, 2.2)$,

Iteration number	c_1	d	\mathcal{J}
0	-1.0E0	1.8000	5.88E6
1	0.0E0	2.2606	1.79E3
2	-4.0E-4	2.2551	1.51E3
3	5.7E-3	2.1822	3.84E2
4	1.3E-3	2.2079	4.69E1
5	4.0E-4	2.2018	2.96E0
6	-4.0E-4	2.1992	1.30E0

Table 1: Numerical values of parameters and cost function

From this solution, convergence is tested when: i) Noise is considered, up to 40 %; ii) A-priori information is considered. In this test, as in other tests, convergence properties are similar to the one tested in [8], but in general, better convergence is obtained, maybe due to the reflection waves given by the lower layer and some love-waves. More tests are performed in order to check the sensitivity respect to the frequency considered.

References

- [1] G. Rus and R. Gallego. Boundary integral equation for inclusion and cavity shape sensitivity in harmonic elastodynamics. *Engineering Analysis with Boundary Elements*, **29**, 77–91 (2005)
- [2] G. Rus and R. Gallego. Solution of identification inverse problems in elastodynamics using semi-analytical sensitivity computation. *Engineering Analysis with Boundary Elements*, **31**, 343–360 (2007).
- [3] G. Rus and R. Gallego. Optimization algorithms for identification inverse problems with the boundary element method. *Engineering Analysis with Boundary Elements*, **26**, 315–327 (2002).
- [4] T. Burczyński, J. H. Kane and C. Balakrishna. Shape design sensitivity analysis via material derivative–adjoint variable technique for 3-D and 2-D curved boundary elements. *International Journal for Numerical Methods in Engineering*. **38**, 2839–2866, (1995)

- [5] M. Bonnet, T. Burczyński and M. Nowakowski, Sensitivity analysis for shape perturbation of cavity or internal crack using BIE and adjoint variable approach. *International Journal of Solids and Structures*, **39**, 2365–2385 (2002).
- [6] M. Bonnet. BIE and material differentiation applied to the formulation of obstacle inverse problems. *Eng. Anal. with Bound. Elem.*, **15**, 121–136 (1995)
- [7] R. M. Christensen, *Theory of viscoelasticity*, Academic Press, New York (1971).
- [8] S. Nintcheu Fata, B. B. Guzina y M. Bonnet. Computational framework for the BIE solution to inverse scattering problems in elastodynamics. *Computational Mechanics*, **32**, 370–380, (2003).
- [9] A. Martínez-Castro y R. Gallego. Three-dimensional Green's function for time-harmonic dynamics in a viscoelastic layer. *International Journal of Solids and Structures*, **44**, 4541–4558 (2007)

Computation of stresses on the boundary of laminate composites plates by the boundary element method

A. R. Gouvêa¹, E. L. Albuquerque¹, L. Palermo Jr.², and P. Sollero¹

1: Faculty of Mechanical Engineering, State University of Campinas
13083-970, Campinas, Brazil, [adriana,ederlima,sollero]@fem.unicamp.br

2: Faculty of Civil Engineering, State University of Campinas
13083-852, Campinas, Brazil, leandro@fec.unicamp.br

Keywords: Laminate composites, stress analysis, Kirchhoff plates, anisotropic material.

Abstract. This paper presents a procedure to compute stresses on the boundary of laminated composite plates using the boundary element method (BEM). Kirchhoff hypothesis for thin plates are assumed. Stresses are computed by a procedure that uses integral equations, derivatives of shape functions, and constitutive relations. The accuracy of the proposed procedure is assessed by an example that shows good agreement with numerical results available in literature.

Introduction

The attempt of developing analytical models for the representation of the behavior of plates come since middle of 1800 with works developed by Sophie Germain, Lagrange, and Poisson as stated by [1].

Since 1978, when the first BEM direct formulation based on the Kirchhoff's hypothesis appeared, the method has had a large growth, being nowadays applied to several practical engineering problems. The first works discussing the use of boundary element direct formulation, in conjunction with the Kirchhoff's theory, were by [2], [3], and [4].

The fundamental solution is an essential of the boundary element method. Bending analysis of plates by the BEM requires the use of two fundamental solutions: the displacement field due to a transverse point load, and the displacement field due to a point moment. Fundamental solutions for anisotropic plates utilize complex variable theory following [5].

In 1988, [6] presented a boundary element analysis of plate bending problems using fundamental solutions proposed by [7] based on Kirchhoff plate bending assumptions. [8] proposed a formulation where the singularities were avoided by placing source points outside the domain. [9] presented an analytical treatment for singular and hypersingular integrals for the formulation presented in [6]. [10] presented a method to transform domain integrals into boundary integrals in the formulation presented in [6]. Later, in [11], this formulation was extended for dynamic problems. Shear deformable plates have been analyzed using the boundary element method by [12] and [13] with the analytical fundamental solution proposed by [14]. [15] presented a boundary element formulation for orthotropic shear deformable plates. Recently, [16] presented a displacement discontinuity formulation for modeling cracks in orthotropic Reissner plates. Fundamental solutions for displacement discontinuity were derived for the first time using a Fourier transform method.

Kirchhoff plate theory

Stresses in a lamina k of a laminate composite plate is given by:

$$\begin{Bmatrix} \sigma_x \\ \sigma_y \\ \tau_{xy} \end{Bmatrix} = \begin{Bmatrix} \bar{Q}_{11} & \bar{Q}_{12} & \bar{Q}_{16} \\ \bar{Q}_{12} & \bar{Q}_{22} & \bar{Q}_{26} \\ \bar{Q}_{16} & \bar{Q}_{26} & \bar{Q}_{66} \end{Bmatrix}_k \begin{Bmatrix} \epsilon_x \\ \epsilon_y \\ \gamma_{xy} \end{Bmatrix}, \quad (1)$$

where $\begin{Bmatrix} \bar{Q} \end{Bmatrix}_k$ is the stiffness matrix of the lamina k , and k does not imply summation. Strains, are given by:

$$\begin{aligned} \epsilon_x &= -z \frac{\partial^2 w}{\partial x^2}, \\ \epsilon_y &= -z \frac{\partial^2 w}{\partial y^2}, \\ \gamma_{xy} &= -2z \frac{\partial^2 w}{\partial x \partial y}, \end{aligned} \quad (2)$$

where z is a coordinate in the transversal direction of the laminate and w is the transversal displacement.

So, in order to compute stresses on boundary nodes it is necessary to compute the second derivatives $\frac{\partial^2 w}{\partial x^2}$, $\frac{\partial^2 w}{\partial y^2}$, and $\frac{\partial^2 w}{\partial x \partial y}$.

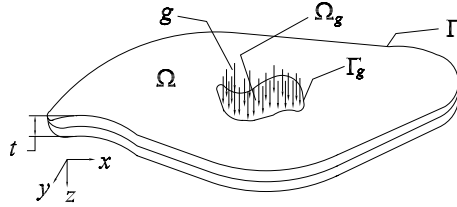


Figure 1: Thin plate.

The boundary integral equation for the transversal displacement w is given by:

$$\begin{aligned} \frac{1}{2}w(Q) + \int_{\Gamma} \left[V_n^*(Q, P)w(P) - m_n^*(Q, P)\frac{\partial w(P)}{\partial n} \right] d\Gamma(P) + \sum_{i=1}^{N_c} R_{ci}^*(Q, P)w_{ci}(P) - \\ \int_{\Gamma} \left[V_n(P)w^*(Q, P) - m_n(P)\frac{\partial w^*}{\partial n}(Q, P) \right] d\Gamma(P) + \sum_{i=1}^{N_c} R_{ci}(P)w_{ci}^*(Q, P) + \\ \int_{\Omega} g(P)w^*(Q, P)d\Omega, \end{aligned} \quad (3)$$

where $\frac{\partial}{\partial n}$ is the derivative in the direction of the outward vector n that is normal to the boundary Γ ; m_n and V_n are, respectively, the normal bending moment and the Kirchhoff equivalent shear force on the boundary Γ ; R_c is the thin-plate reaction of corners; w_c is the transverse displacement at corners points N_c ; P is the field point; Q is the source point; and an asterisk denotes a fundamental solution.

Fundamental solutions required at equation (3) are given by [17].

The directional derivative of equation (3) at the source point in the boundary normal direction (m) is given by:

$$\begin{aligned} \frac{1}{2} \frac{\partial w}{\partial m} + \int_{\Gamma} \left(\frac{\partial V_n^*}{\partial m} w - \frac{\partial M_n^*}{\partial m} \frac{\partial w}{\partial n} d\Gamma \right) + \sum \frac{\partial R_{ci}^*}{\partial m} w_{ci} = \\ \int_{\Gamma} \left(V_n \frac{\partial w^*}{\partial m} - M_n \frac{\partial^2 w^*}{\partial n \partial m} \right) d\Gamma + \sum R_{ci} \frac{\partial w_{ci}^*}{\partial m} + \int_{\Omega} g \frac{\partial w^*}{\partial m} d\Omega. \end{aligned} \quad (4)$$

Similarly, the directional derivative of equation (3) at the source point in the boundary tangential direction (t) is given by:

$$\begin{aligned} \frac{1}{2} \frac{\partial w}{\partial t} + \int_{\Gamma} \left(\frac{\partial V_n^*}{\partial t} w - \frac{\partial M_n^*}{\partial t} \frac{\partial w}{\partial n} d\Gamma \right) + \sum \frac{\partial R_{ci}^*}{\partial t} w_{ci} = \\ \int_{\Gamma} \left(V_n \frac{\partial w^*}{\partial t} - M_n \frac{\partial^2 w^*}{\partial n \partial t} \right) d\Gamma + \sum R_{ci} \frac{\partial w_{ci}^*}{\partial t} + \int_{\Omega} g \frac{\partial w^*}{\partial t} d\Omega. \end{aligned} \quad (5)$$

Considering quadratic discontinuous elements, $\frac{\partial w}{\partial t}$ is interpolated inside an element by:

$$\frac{dw}{dt} = N_1 \frac{\partial w_1}{\partial t} + N_2 \frac{\partial w_2}{\partial t} + N_3 \frac{\partial w_3}{\partial t}, \quad (6)$$

where N_i are quadratic discontinuous shape functions and $\frac{\partial w_i}{\partial t}$ are the nodal values of $\frac{\partial w}{\partial t}$.

Following a similar procedure to $\frac{d^2 w}{dm dt}$, it is possible to obtain:

$$\frac{d^2 w}{dm dt} = \left(\frac{dN_1}{d\xi} \frac{\partial w_1}{\partial m} + \frac{dN_2}{d\xi} \frac{\partial w_2}{\partial m} + \frac{dN_3}{d\xi} \frac{\partial w_3}{\partial m} \right) \left(1/d\xi \right), \quad (7)$$

where ξ is the local coordinate through the boundary.

In the same way,

$$\frac{d^2 w}{dt^2} = \left(\frac{dN_1}{d\xi} \frac{\partial w_1}{\partial t} + \frac{dN_2}{d\xi} \frac{\partial w_2}{\partial t} + \frac{dN_3}{d\xi} \frac{\partial w_3}{\partial t} \right) \left(1/d\xi \right). \quad (8)$$

It was not possible to calculate $\frac{d^2 w}{dm^2}$ in the same way of $\frac{d^2 w}{dt^2}$ and $\frac{d^2 w}{dm dt}$ because we do not have $\frac{dm}{d\xi}$. The alternative is to write the equations of the moments in system (mt) instead of (xy):

$$\begin{aligned} M_m &= - \left(D'_{11} \frac{\partial^2 w}{\partial m^2} + D'_{12} \frac{\partial^2 w}{\partial t^2} + 2D'_{16} \frac{\partial^2 w}{\partial m \partial t} \right), \\ M_t &= - \left(D'_{12} \frac{\partial^2 w}{\partial m^2} + D'_{22} \frac{\partial^2 w}{\partial t^2} + 2D'_{26} \frac{\partial^2 w}{\partial m \partial t} \right), \\ M_{mt} &= - \left(D'_{16} \frac{\partial^2 w}{\partial m^2} + D'_{26} \frac{\partial^2 w}{\partial t^2} + 2D'_{66} \frac{\partial^2 w}{\partial m \partial t} \right), \end{aligned} \quad (9)$$

where $D'_{ij} = (i, j = 1, 2, 6)$ are the flexural rigidities in system mt , that are given by:

$$\mathbf{D}' = \mathbf{T}^{-1} [\mathbf{D}] (\mathbf{T}^{-1})^t, \quad (10)$$

where D_{ij} are the flexural rigidities in system xy .

In this system, the known variables are: M_m , $\frac{\partial^2 w}{\partial t^2}$ and $\frac{\partial^2 w}{\partial m \partial t}$, and the unknown variables are: M_t , M_{mt} , and $\frac{\partial^2 w}{\partial m^2}$.

Writting equations (9) in a matrix form, we have:

$$\begin{Bmatrix} M_m \\ M_t \\ M_{mt} \end{Bmatrix} = \begin{bmatrix} D'_{11} & D'_{12} & D'_{16} \\ D'_{12} & D'_{22} & D'_{26} \\ D'_{16} & D'_{26} & D'_{66} \end{bmatrix} \begin{Bmatrix} \frac{\partial^2 w}{\partial m^2} \\ \frac{\partial^2 w}{\partial t^2} \\ 2 \frac{\partial^2 w}{\partial m \partial t} \end{Bmatrix}, \quad (11)$$

Equation (11) can be written as:

$$\begin{Bmatrix} \frac{\partial^2 w}{\partial m^2} \\ \frac{\partial^2 w}{\partial t^2} \\ 2 \frac{\partial^2 w}{\partial m \partial t} \end{Bmatrix} = \begin{bmatrix} S_{11} & S_{12} & S_{16} \\ S_{12} & S_{22} & S_{26} \\ S_{16} & S_{26} & S_{66} \end{bmatrix} \begin{Bmatrix} M_m \\ M_t \\ M_{mt} \end{Bmatrix}, \quad (12)$$

where $\mathbf{S} = [\mathbf{D}']^{-1}$.

Thus,

$$\begin{aligned} \frac{\partial^2 w}{\partial m^2} &= S_{11}M_m + S_{12}M_t + S_{16}M_{mt}, \\ \frac{\partial^2 w}{\partial t^2} &= S_{12}M_m + S_{22}M_t + S_{26}M_{mt}, \\ 2 \frac{\partial^2 w}{\partial m \partial t} &= S_{16}M_m + S_{26}M_t + S_{66}M_{mt}. \end{aligned} \quad (13)$$

Isolating the unknown variables, we have:

$$\begin{aligned} -\frac{\partial^2 w}{\partial m^2} + S_{12}M_t + S_{16}M_{mt} &= -S_{11}M_m, \\ S_{22}M_t + S_{26}M_{mt} &= \frac{\partial^2 w}{\partial t^2} - S_{12}M_m, \\ S_{26}M_t + S_{66}M_{mt} &= 2 \frac{\partial^2 w}{\partial m \partial t} - S_{16}M_m, \end{aligned} \quad (14)$$

that can be written in the matrix form:

$$\begin{bmatrix} -1 & S_{12} & S_{16} \\ 0 & S_{22} & S_{26} \\ 0 & S_{26} & S_{66} \end{bmatrix} \begin{Bmatrix} \frac{\partial^2 w}{\partial m^2} \\ M_t \\ M_{mt} \end{Bmatrix} = \begin{Bmatrix} -S_{11}M_m \\ \frac{\partial^2 w}{\partial t^2} - S_{12}M_m \\ 2 \frac{\partial^2 w}{\partial m \partial t} - S_{16}M_m \end{Bmatrix}. \quad (15)$$

and the unknowns can be computed by solving the resulting linear system:

$$\mathbf{Ay} = \mathbf{x}. \quad (16)$$

Numerical results

Consider a cross-ply laminated graphite/epoxy composite square plate with clamped edges under uniformly distributed load of intensity q and with edge length $a = 1$ m. The results presented here are for the nine layered symmetrical laminate with [0/90/0/90/0/90/0/90/0] lay-up. All layers have the same thickness. The total thickness is equal to $h = 0.001$ m and material properties are: $E_L = 207$ GPa, $E_T = 5.2$ GPa, $G_{LT} = 3.1$ GPa, and $\nu_{LT} = 0.25$. The plate was discretized using 28 quadratic discontinuous boundary elements, as shown in Figure 2. Displacement at point A and moment at point B , shown in Figure 2, are compared with finite element results obtained by [18]. As it can be seen in Table 1, the agreement between the boundary element thin plate and the finite element shear deformable plate is very good for the displacement. However, the same agreement is not obtained for moments. This was already expected provided that the ratio E_L/G_{LT} is 66.7. This becomes the effect of the shear deformation considerably important even for very thin plates.

Figure 3 shows the distribution of the stress σ_x at point B along the thickness of the plate, from the mid-surface to the top surface. It can be seen that, as the stiffness of the material is higher in the direction of the fibers, the stress is higher in the lamina with fibers oriented parallel to the axis x ($\theta = 0^\circ$).

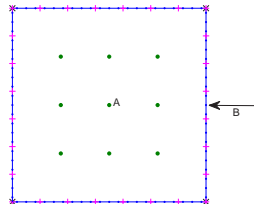


Figure 2: Discretization square plate using 7 elements per side.

Node		Nume- rical	ref.: [18]
A	$wETh^3/qa^4 \times 10^3$	0.9512	0.9494
B	$M_{xx}/qa^2 \times 10^2$	-7.0708	-6.6019

Table 1: Displacements and moments in a square plate with clamped edges.

Conclusions

This paper presented a boundary integral formulation for the computation of stresses in boundary points of anisotropic thin plates. In the proposed approach, in order to avoid a singularities higher than hypersingular, second derivatives of transversal displacement were computed using constitutive equations and shape functions derivatives. The results show that the method is accurate.

Acknowledgment

The authors would like to thank the State of São Paulo Research Foundation (FAPESP) and the National Council for Scientific and Technological Development (CNPq) for financial support for this work .

References

- [1] W.D. Pilkey and W. Wunderlich, *Mechanics of structures: variational and computational methods*, CRC Press, Inc Boca Raton, Florida, USA, (1994).
- [2] G.P. Bezine. Boundary integral formulation for plate flexure with arbitrary boundary conditions, *Mech. Res. Comm.*, Vol. **5**, pp. 197–206, (1978).
- [3] M.A. Stern. A general boundary integral formulation for the numerical solution of plate bending problems, *Int. J. Solids Struct.*, Vol. **15**, pp. 769–782, (1979).
- [4] H. Tottenham, *The boundary element method for plates and shells* , P.K. Banerjee and R. Butterfield (Editors), Vol. I, (1979).
- [5] S.G. Lekhnitskii, *Anisotropic plates*, Gordon and Breach, New York, (1968).

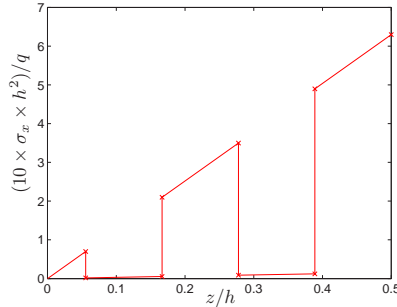


Figure 3: Stress distribution (σ_x) along the thickness for $\theta = 0^\circ/90^\circ$ at the center point of the plate.

- [6] G. Shi and G. Bezine. A general boundary integral formulation for the anisotropic plate bending problems, *J. Composite Materials*, Vol. **22**, pp. 694–716, (1988).
- [7] B.C. Wu and N.J. Altiero. A new numerical method for the analysis of anisotropic thin plate bending problems, *Computer Meth.in Appl.Mech. and Eng.*, Vol. **25**, pp. 343–353, (1981).
- [8] C. Rajamohan and J. Raamachandran. Bending of anisotropic plates charge simulation method, *Advances in Eng. Software*, Vol. **30**, pp. 369–373, (1999).
- [9] W.P. Paiva, P. Sollero and E.L. Albuquerque. Treatment of hypersingularities in boundary element anisotropic plate bending problems, *Latin American J. of Solids and Struc.*, Vol. **1**, pp. 49–73, (2003).
- [10] E.L. Albuquerque, P. Sollero, W. Venturini and M.H. Aliabadi. Boundary element analysis of anisotropic Kirchhoff plates, *Int. J. of Solids and Struc.*, Vol. **43**, pp. 4029–4046, (2006).
- [11] E.L. Albuquerque, P. Sollero, W.P. Paiva. The radial integration method applied to dynamic problems of anisotropic plates, *Communicat. in Num. Methods in Eng.*, (2007). Early view.
- [12] J. Wang and K. Schweizerhof. Study on free vibration of moderately thick orthotropic laminated shallow shells by boundary-domain elements, *Appl. Math. Modelling*, Vol. **20**, pp. 579–584, (1996).
- [13] J. Wang and K. Schweizerhof. Free vibration of laminated anisotropic shallow shells including transverse shear deformation by the boundary-domain element method, *Computers and Structures*, Vol. **62**, pp. 151–156, (1997).
- [14] J. Wang and K. Schweizerhof. The fundamental solution of moderately thick laminated anisotropic shallow shells, *Int. J. Eng. Sci.*, Vol. **33**, pp. 995–1004, (1995).
- [15] J. Wang and M. Huang. Boundary element method for orthotropic thick plates, *Acta Mech. Sin.*, Vol. **7 (3)**, pp. 258–266, (1991).
- [16] P.H. Wen and M.H. Aliabadi. Displacement discontinuity formulation for modeling cracks in orthotropic shear deformable plates, *Int. J. Fract.*, Vol. **142**, pp. 69–79, (2006).
- [17] E. L. Albuquerque, P. Sollero, W. S. Venturini and M. H. Aliabadi, Boundary element analysis of anisotropic kirchhoff plates. *International Journal of Solids and Structures*, 43:4029-4046, (2006).
- [18] H. V. Lakshminarayana and S. S. Murthy. A shear-flexible triangular finite element model for laminated composite plates. *International Journal for Numerical Methods in Engineering*, 20: 591–623, (1984).

General 3-D Dynamic Fracture Mechanics Problems in Transversely Isotropic Solids

P. Ruiz, M.P. Ariza, J. Domínguez

Departamento de Mecánica de los Medios Continuos, Escuela Técnica Superior de Ingenieros,
Universidad de Sevilla, Camino de los descubrimientos s/n, 41092 Sevilla, SPAIN
mpariza@us.es, jose@us.es

Keywords: Boundary Element Method, Fracture Mechanics, Three-Dimensional Cracks, Transversely Isotropic Materials.

Abstract. The development of new materials has made the study of fracture mechanics problems in transversely isotropic and general anisotropic solids an important and attractive issue for many researchers. The use of both traction and displacement integral representations lead to a mixed formulation of the BEM where the discretization effort for crack problems is much smaller than in the classical formulation. In this work a mixed formulation is used, in combination with three-dimensional quadratic and quarter-point elements, to obtain accurate results for practical dynamic crack problems. Cracks in boundless and finite domains are studied. Since the number of problems of this kind that have been studied is very small, we have mostly compared our results with those we have obtained in previous works for the same geometry but isotropic materials.

Introduction

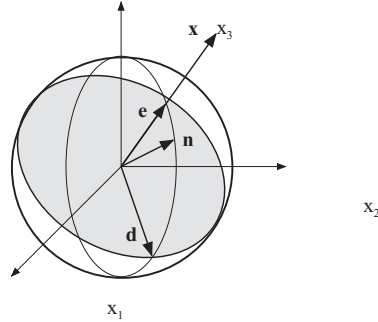
The basic concepts for cracks in transversely isotropic solids were set by Kassir and Sih [1] forty years ago. They showed that the stress singularity near the front of 3-D cracks was of the same order as in the isotropic case. The magnitude of the local stresses may be described in terms of Stress Intensity Factors (SIFs). The Boundary Element Method (BEM), which has revealed as a very well suited tool for static and dynamic fracture mechanics analysis in isotropic solids, should also be adequate for anisotropic cases. Nevertheless, due to formulation and implementation difficulties, a small number of boundary element (BE) papers has been dedicated to the analysis of fracture mechanics problems in non-isotropic materials. Among these papers, the early work of Snyder and Cruse [2] and the more recent one of Chan and Cruse [3] should be mentioned. The first 3-D BE formulation for fracture mechanics in non-isotropic materials was presented by Ishikawa [4]. This author studied crack problems in 3-D transversely isotropic and fully anisotropic bodies. The approach is based on the subdomain technique and the use of quarter-point elements and transition elements placed next to them. No singularity is introduced to represent the tractions at the crack front.

Loakimidis [5] and Sladek and Sladek [6] presented the first traction integral equation formulations for 3-D crack problems in isotropic and anisotropic solids, respectively, twenty five years ago. Ten years later, Mi and Aliabadi [7] formulated the so called Dual BEM for the general solution of 3-D crack problems in isotropic solids, and obtained numerical solutions for several problems. Another mixed (or dual) BE approach for 3-D fracture problems in isotropic domains was presented by Dominguez et al. [8, 9]. Only very recently Pan and Yuang [10] and Ariza and Dominguez [11] have presented BE approaches for anisotropic crack problems based on the combined use of displacement and traction integral representation for external boundaries and crack surface, respectively.

In this article we are going to analyze 3-D finite crack problems in transversely isotropic solids under transient loading conditions including viscoelastic properties for the material.

Traction integral equation

The classical displacement integral equation representation for an integral point \mathbf{y} of an isotropic or anisotropic elastic body Ω bounded by a regular surface Γ with unit outward normal $\mathbf{n}(\mathbf{x})$ under time

Figure 1: Geometry of unit sphere and \mathbf{e} , \mathbf{x} , \mathbf{n} and \mathbf{d} vectors.

harmonic loading and zero body forces conditions can be written as

$$u_l(\mathbf{y}, \omega) + \int_{\Gamma} p_{lk}^*(\mathbf{x}, \mathbf{y}, \omega) u_k(\mathbf{x}, \omega) d\Gamma - \int_{\Gamma} u_{lk}^*(\mathbf{x}, \mathbf{y}, \omega) p_k(\mathbf{x}, \omega) d\Gamma = 0 \quad (1)$$

for $l, k = 1, 2, 3$, where u_k and p_k stand for the k component of displacement and traction vectors, respectively, ω is the frequency, and u_{lk}^* , p_{lk}^* are the 3-D elastic time harmonic fundamental solution displacement and traction tensors respectively.

Internal stresses can be obtained by differentiation of displacement at point \mathbf{y} and substitution into the stress-strain relationship. The traction vector component at \mathbf{y} over a surface with unit outward normal \mathbf{N} is:

$$p_l(\mathbf{y}, \omega) = \sigma_{lm}(\mathbf{y}, \omega) N_m(\mathbf{y}) \quad (2)$$

and the integral representation for the traction components

$$p_l(\mathbf{y}, \omega) + \int_{\Gamma} s_{lmk}^*(\mathbf{x}, \mathbf{y}, \omega) N_m(\mathbf{y}) u_k(\mathbf{x}, \omega) d\Gamma - \int_{\Gamma} d_{lmk}^*(\mathbf{x}, \mathbf{y}, \omega) N_m(\mathbf{y}) p_k(\mathbf{x}, \omega) d\Gamma = 0 \quad (3)$$

where d_{lmk}^* and s_{lmk}^* are linear combinations of derivatives of u_{lk}^* y p_{lk}^* , respectively. The four fundamental solution kernels in Equations 1 and 3 can be written as

$$\begin{aligned} u_{lk}^*(\mathbf{x}, \mathbf{y}, \omega) &= u_{lk}^R(\mathbf{x}, \mathbf{y}, \omega) + u_{lk}^S(\mathbf{x}, \mathbf{y}) \\ p_{lk}^*(\mathbf{x}, \mathbf{y}, \omega) &= p_{lk}^R(\mathbf{x}, \mathbf{y}, \omega) + p_{lk}^S(\mathbf{x}, \mathbf{y}) \\ d_{lmk}^*(\mathbf{x}, \mathbf{y}, \omega) &= d_{lmk}^R(\mathbf{x}, \mathbf{y}, \omega) + d_{lmk}^S(\mathbf{x}, \mathbf{y}) \\ s_{lmk}^*(\mathbf{x}, \mathbf{y}, \omega) &= s_{lmk}^R(\mathbf{x}, \mathbf{y}, \omega) + s_{lmk}^S(\mathbf{x}, \mathbf{y}) \end{aligned} \quad (4)$$

where $u_{lk}^R(\mathbf{x}, \mathbf{y}, \omega)$, $p_{lk}^R(\mathbf{x}, \mathbf{y}, \omega)$, $d_{lmk}^R(\mathbf{x}, \mathbf{y}, \omega)$ and $s_{lmk}^R(\mathbf{x}, \mathbf{y}, \omega)$ are regular functions of r which tend to zero as ω does, and $u_{lk}^S(\mathbf{x}, \mathbf{y})$, $p_{lk}^S(\mathbf{x}, \mathbf{y})$, $d_{lmk}^S(\mathbf{x}, \mathbf{y})$ and $s_{lmk}^S(\mathbf{x}, \mathbf{y})$, correspond to the static counterpart of u_{lk}^* , p_{lk}^* , d_{lmk}^* and s_{lmk}^* , respectively. The four static terms present singularities of the type r^{-1} , r^{-2} , r^{-2} and r^{-3} , respectively, when $r \rightarrow 0$.

Explicit expressions of $u_{lk}^S(\mathbf{x}, \mathbf{y})$ and the corresponding stress tensor $\sigma_{lmk}^S(\mathbf{x}, \mathbf{y})$ for three-dimensional transversely isotropic materials can be found in Pan and Chou [13]. Tractions p_{lk}^S are obtained by projection of the stress tensor over the surface defined by its normal.

$$p_{lk}^{*S}(\mathbf{x}, \mathbf{y}) = \sigma_{lmk}^S(\mathbf{x}, \mathbf{y}) n_m(\mathbf{x}) \quad (5)$$

It can be seen from the tractions definition in Equation (2) that d_{lmk}^{*S} is obtained as a stress tensor at collocation point. Therefore, d_{lmk}^{*S} coincide, except for a change of sign due to the different location of the r derivatives, with the stress tensor components in Equation 5. The terms $s_{lmk}^{*S}(\mathbf{x}, \mathbf{y})$ are linear

combinations of first derivatives of $p_{lk}^{*S}(\mathbf{x}, \mathbf{y})$ and consequently, linear combinations of u_{lk}^{*S} second derivatives. Explicit expressions for these kernels for 3-D transversely isotropic materials can be found in Ariza and Dominguez [11].

The time harmonic fundamental solution for general anisotropic solids $u_{lk}^*(\mathbf{x}, \mathbf{y}, \omega)$ was obtained by Wang and Achenbach [14]. They used the Radon transform to reduce the 3-D system of coupled partial differential equations to a 1-D system of coupled ordinary differential equations. This system is uncoupled by means of its eigenvalues and eigenvectors. The subsequent application of the inverse Radon transform yields the displacement fundamental solution in terms of an integral over the surface of a unit sphere. By subtracting the static fundamental solution displacement from the time harmonic one derived by Wang and Achenbach [14], one obtains the frequency dependent regular part as an integral over the surface of a unit radius sphere at the collocation point (Figure 1)

$$u_{lk}^R(\mathbf{x}, \mathbf{y}, \omega) = \frac{i}{16\pi^2} \int_{|\mathbf{n}|=1} \sum_{m=1}^3 A_{lk}^m(\mathbf{n}, \omega) e^{ik_m |\mathbf{n} \cdot \mathbf{x}|} dS(\mathbf{n}) \quad (6)$$

where \mathbf{n} is the external unit normal to the sphere, $k_m = \omega/c_m$ is the number associated to the c_m phase velocity in direction \mathbf{n} , and \mathbf{x} is the position vector from the collocation point. The displacement space first derivatives are

$$u_{lk,q}^{*R} = \frac{i}{16\pi^2} \int_{|\mathbf{n}|=1} \sum_{m=1}^3 ik_m n_q \text{sign}(\mathbf{n} \cdot \mathbf{x}) A_{lk}^m(\mathbf{n}, \omega) e^{ik_m |\mathbf{n} \cdot \mathbf{x}|} dS(\mathbf{n}) \quad (7)$$

and their second derivatives

$$\begin{aligned} u_{lk,pq}^{*R} &= -\frac{i}{16\pi^2} \int_{|\mathbf{n}|=1} \sum_{m=1}^3 A_{lk}^m(\mathbf{n}, \omega) k_m^2 n_p n_q e^{ik_m |\mathbf{n} \cdot \mathbf{x}|} dS(\mathbf{n}) - \\ &\quad \frac{i}{16\pi^2} \int_{|\mathbf{n}|=1} \sum_{m=1}^3 2A_{lk}^m(\mathbf{n}, \omega) k_m n_p n_q e^{ik_m |\mathbf{n} \cdot \mathbf{x}|} \delta(\mathbf{n} \cdot \mathbf{x}) dS(\mathbf{n}) \end{aligned} \quad (8)$$

Details related to functions $A_{lk}^m(\mathbf{n}, \omega)$ and its coefficients for a transversely isotropic material with axis of symmetry x_3 can be found in Ariza and Dominguez [15].

Taking into account the fundamental solution kernels decomposition in Equation (4) and after some algebra, the traction integral representation for a boundary point become

$$\begin{aligned} \frac{1}{2} p_l(\mathbf{y}, \omega) + \int_{\Gamma} \{ s_{lmk}^S N_m [u_k(\mathbf{x}, \omega) - u_k(\mathbf{y}, \omega) - u_{k,h}(\mathbf{y}, \omega)(x_h - y_h)] - \\ d_{lmk}^S N_m [p_k(\mathbf{x}, \omega) - p_k(\mathbf{y}, \omega)] \} d\Gamma + \\ [u_k(\mathbf{y}, \omega) I_{lk} + u_{k,h}(\mathbf{y}, \omega) J_{lhk} + p_k(\mathbf{y}, \omega) K_{lk}] + \\ \int_{\Gamma} \{ s_{lmk}^R N_m u_k(\mathbf{x}, \omega) - d_{lmk}^R N_m p_k(\mathbf{x}, \omega) \} d\Gamma = 0 \end{aligned} \quad (9)$$

The regularization details and explicit expressions for the terms I_{lk} , J_{lhk} and K_{lk} containing only regular or weakly singular integrals can be seen in Ariza and Dominguez [11] and in Dominguez et al. [8] for transversely isotropic and isotropic materials, respectively.

Dynamic stress intensity factors

According to the work of Kassir and Sih [1] there is an asymptotic relation between the COD near the crack front and the SIFs, for cracked transversely isotropic media. Using the leading terms of those relations, the SIFs can be evaluated from the three components of the COD at a distance r from the crack front. Assuming that z is the material axis of symmetry perpendicular to the crack plane and the t -axis is tangent to the crack front line at the point where a node is located (Figure 2), the SIF components at this point can be written in terms of the cracks opening displacements at the quarter-point node as:

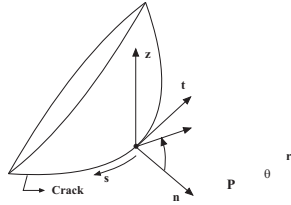


Figure 2: Local coordinates at crack boundary point P.

$$\begin{aligned}
 K_I &= \sqrt{\frac{\pi}{2L}} \Delta u_z \frac{\beta_1}{\frac{m_1}{1+m_1} - \frac{m_2}{1+m_2}} \\
 K_{II} &= \sqrt{\frac{\pi}{2L}} \Delta u_n \frac{C_{44} (\sqrt{n_2} - \sqrt{n_1}) (1+m_1)(1+m_2)}{(m_2 - m_1) \sqrt{n_1 n_2}} \\
 K_{III} &= \sqrt{\frac{\pi}{2L}} \Delta u_t \frac{C_{44}}{\sqrt{n_3}}
 \end{aligned} \tag{10}$$

where L is the quarter-point element width, n_1 and n_2 are the two solutions of the quadratic equation of the material properties

$$C_{11} C_{44} n^2 + [C_{13}(C_{13} + 2C_{44}) - C_{11} C_{33}]n + C_{33} C_{44} = 0 \tag{11}$$

$$n_3 = \frac{2C_{44}}{C_{11} - C_{12}} \tag{12}$$

$$m_j = \frac{(C_{13} + C_{44})n_j}{C_{33} - C_{44}n_j}, \quad j = 1, 2 \tag{13}$$

and

$$\beta_1 = C_{44} (\sqrt{n_1} - \sqrt{n_2}) \tag{14}$$

Numerical results

A homogeneous elastic material is transversely isotropic when it has symmetric properties in all planes perpendicular to a given direction. In this case, only five materials constant of the general Hooke's law are independent. We are also going to consider damping properties for the material following the viscoelastic model defined by Melo and Radford [16].

A square cross-section prismatic bar with a central penny-shaped crack loaded by a uniform traction at both ends is studied. The geometry of the problem is shown in Figure 3. The radius of the crack is a with $a/w=w/h=0.5$. The 3-D viscoelastic properties of the material (PEEK/IM7) are defined in [16]. Results for $\beta=0$ and $\beta=0.01$ were obtained. The two ends uniform load is first considered to have a harmonic variation with time. The magnitude of mode-I SIF is normalized with respect to the static infinite domain solution. The obtained results are shown versus frequency in Fig. 12. To the author's knowledge, there are not frequency domain results for this problem in the literature. The present results show the resonance peaks for the undamped bar and the effects of internal damping in the response to time harmonic loading. The amplitude of the first peak decreases with internal damping. Other peaks are damped in a great extent remaining the first peak as the only clear resonance for $\beta=0.01$.

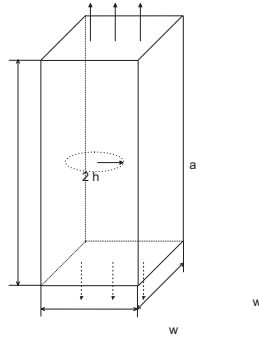


Figure 3: Penny-shaped central crack in prismatic bar.

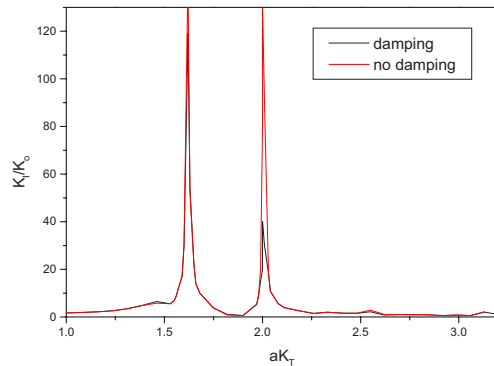


Figure 4: Amplitude of mode-I SIF for time harmonic uniform traction.

Summary and conclusions

A BE formulation for the dynamic analysis of fracture problems in 3-D transversely isotropic finite domains has been presented. Time harmonic loading conditions are considered. The hypersingular or strongly singular kernels are regularized following the approach presented in [11]. Stress intensity factors have been obtained in an accurate and direct way from nodal values of quarter-point elements. Transient loading conditions are studied using a Fourier transform.

Acknowledgments

This work was support by the *Consejería de Innovación Ciencia y Empresa de la Junta de Andalucía*, Spain, research project P06-TEP-01514, and by the *Ministerio de Educación y Ciencia* of Spain, research project DPI2006-05045. The financial support is gratefully acknowledged.

References

- [1] MK. Kassir and GC. Sih. Three-dimensional stresses around elliptical cracks in transversely isotropic solids. *Engng. Fract. Mech.*, 1:327–345, 1968.
- [2] MD. Snyder and TA. Cruse. Boundary integral equation analysis of cracked anisotropic plates. *Int. J. Fract.*, 11:315–328, 1975.
- [3] KS. Chan and TA. Cruse. Stress intensity factors for anisotropic compact-tension specimens with inclined cracks. *Engng. Fract. Mech.*, 23:863–874, 1986.
- [4] H. Ishikawa. Application of the boundary element method to anisotropic crack problems. *in: MH. Aliabadi, CA. Brebbia, eds., Advances in boundary element methods for fracture mechanics, Computational Mechanics Publications, Southampton*, pages 269–292, 1990.
- [5] NI. Iokimidis. Application of finite-part integrals to the singular integral equations of crack problems in plane and three-dimensional elasticity. *Acta Mechanica*, 45:31–47, 1982.
- [6] V. Sladek and J. Sladek. Three dimensional crack analysis for an anisotropic body. *Applied Mathematical Modelling*, 6:374–382, 1982.
- [7] Y. Mi and MH. Aliabadi. Dual boundary element method for three-dimensional fracture mechanics analysis. *Engng. Anal. Boundary Elem.*, 10:161–171, 1992.
- [8] MP. Ariza J. Dominguez and R. Gallego. Flux and traction boundary elements without hypersingular or strongly-singular integrals. *Int. J. Numer. Meth. Engng.*, 48:111–135, 2000.
- [9] J. Dominguez and MP. Ariza. A direct traction bie approach for three-dimensional crack problems. *Engng. Anal. Boundary Elem.*, 24:727–738, 2000.
- [10] E. Pan and FG. Yuan. Boundary element analysis of three-dimensional cracks in anisotropic solids. *Int. J. Numer. Meth. Engng.*, 48:211–237, 2000.
- [11] MP. Ariza and J. Dominguez. Boundary element formulation for 3-d transversely isotropic cracked bodies. *Int. J. Numer. Meth. Engng.*, 60:719–753, 2004.
- [12] MH. Aliabadi. Boundary element formulations in fracture mechanics. *Appl. Mech. Review ASME*, 50:83–96, 1997.
- [13] YC. Pan and TW. Chou. Point force solution for an infinite transversely isotropic solid. *J. Appl. Mech.*, 43:608–612, 1976.
- [14] CY. Wang and JD. Achenbach. 3-d time-harmonic elastodynamic green's functions for anisotropic solids. *Proc. Roy. Soc. London*, A449:441–458, 1995.
- [15] MP. Ariza and J. Dominguez. Dynamic be analysis of 3-d cracks in transversely isotropic solids. *Comput. Methods Appl. Mech. Engrg.*, 193:765–779, 2004.
- [16] J.D.D. Melo D.W. Radford. Viscoelastic charaterization of transversely isotropic composite laminae. *Journal of Composite Materials*, 37(2):129–145, 2003.

Identification of Blood Perfusion Parameters Using an Inverse DRBEM/Genetic Algorithm

P W Partridge¹ and L C Wrobel²

¹ Dept. Eng. Civil e Ambiental, Universidade de Brasília, 70910-900 Brasília DF, Brazil.

Email: paulp@unb.br

² School of Engineering and Design, Brunel University, Uxbridge UB8 3PH, UK.

Email: luiz.wrobel@brunel.ac.uk

Keywords Dual Reciprocity, Boundary Elements, Genetic Algorithm, Blood Perfusion, Inverse Analysis, Thermal Analysis, Tumour.

Abstract. The temperature distribution in biological bodies is described by the Pennes' bioheat equation, which is non-linear if blood perfusion is considered to be variable. Here, the Dual Reciprocity Boundary Element Method is coupled to a Genetic Algorithm in an inverse procedure through which the coefficients describing the non-linear thermal properties of blood perfusion may be identified. This allows accurate, direct solutions for quantitative diagnostics on the physiological conditions of biological bodies and for optimisation of hypothermia for cancer therapy.

1 Introduction

It is well known that the body surface temperature is controlled by blood circulation, local metabolism and heat transfer between the skin and the environment [1]. It is also known that several types of tumours, *e.g.* skin or breast, can lead to an increase in local blood flow, and thus to an increase in the local temperature [2]. On the other hand, thrombosis or vascular sclerosis decreases the blood flowing to the skin, resulting in lower skin temperatures [2].

The Pennes bioheat equation can be used for the quantitative diagnostics of physiological conditions on biological bodies, *e.g.* for simulations of regional hyperthermia for cancer therapy [3-4]. The parameters in Pennes' equation are usually assumed to be constant except for the blood perfusion, which varies with temperature [2-4]. Herein, a numerical technique for identification of the temperature-dependent blood perfusion parameters in Pennes' equation is proposed based on the Dual Reciprocity Method (DRM), which has already been used for the direct solution of the bioheat equation [1,2,5,6]. It is assumed that the size and location of the tumour are known from previous diagnostics; in the DRM, the tumour is treated as a sub-region and, in addition to the nodes used to model the boundary of the tumour, no other internal points are required.

Previous work on inverse analysis of biological bodies was carried out by Ren *et al.* [7], who applied the Boundary Element Method (BEM) to identify heat sources in biological bodies based on the simultaneous measurement of temperature and heat flux at the skin surface, by Majchrzak and Paruch [8], who estimated the (constant) thermophysical parameters of a tumour using a least-squares algorithm based on sensitivity coefficients, and by Partridge and Wrobel [9], who presented a BEM inverse analysis based on a Genetic Algorithm (GA) [10,11] to identify the position and size of shallow tumours using skin temperature measurements.

This paper extends the algorithm developed in [9] for the identification of the coefficients of blood perfusion. A simple GA, as described in the literature [12], is adequate for the problem. A cubic radial basis function is employed as the approximation function for the DRM, with linear augmentation.

The DRM formulation for the bioheat equation is considered in the next section. This is followed by some results of direct analyses, which illustrate the use of the DRM and the relationship between the parameters adopted to model blood perfusion and the temperature distribution on the skin surface. Then, the parameter identification problem is described and the results of some inverse analyses are presented, considering linear expansions for the blood perfusion rate. The advantages and limitations of the proposed technique are also discussed.

2 Dual Reciprocity Method for the bioheat equation

The Pennes bioheat equation can be written in the following form [1-5],

$$\nabla^2 T = -\frac{\omega_b \rho_b c_b}{k} (T_a - T) - \frac{Q}{k} = b \quad (1)$$

where k denotes the thermal conductivity of tissue, ρ_b , c_b are density and specific heat of blood, ω_b is the blood perfusion rate, T_a is the arterial blood temperature and Q is metabolic heating. Eq (1) is subject to the usual boundary conditions for thermal problems, (i) prescribed temperature $T = \bar{T}$; (ii) prescribed heat flux, $q = \bar{q}$. Eq (1) is a Poisson-type equation with two inhomogeneous terms, the first of which is dependent on the problem variable T , the other term being a function of space but not of the problem variable. Herein, this equation is solved using the DRM [13] in which the fundamental solution to the Laplace equation is employed to treat the term on the left-hand side of eq (1) and the inhomogeneous terms are taken to the boundary using the standard DRM [13], leading to the system of equations:

$$HT - Gq = (H\hat{U} - G\hat{Q})F^{-1}b \quad (2)$$

where the F matrix is calculated from the definition of the approximating functions [13]. Replacing $S = (H\hat{U} - G\hat{Q})F^{-1}$ in eq (2), one obtains

$$HT - Gq = Sb \quad (3)$$

In the linear case (used here for the healthy tissue), it is possible to define $c_1 = \omega_b \rho_b c_b / k$ and $c_2 = -(\omega_b \rho_b c_b T_a + Q) / k$, and eq (3) can be written in the form:

$$HT - Gq = c_1 ST + c_2 S \quad (4)$$

or

$$(H - c_1 S)T - Gq = c_2 S \quad (5)$$

For a direct, well-posed problem, boundary conditions (temperature or heat flux) are applied to eq (5) in the usual way to produce

$$Ax = y + d \quad (6)$$

Eq (6) may finally be solved for the unknown boundary values contained in vector x .

Considering the temperature-dependence of the tumour's perfusion, ω_b , the parameters c_1 and c_2 are redefined as follows:

$$\begin{aligned} c_1 &= c_3 \omega_b \\ c_2 &= -(c_4 \omega_b + \frac{Q}{k}) \end{aligned} \quad (7)$$

where $c_3 = \rho_b c_b / k$ and $c_4 = \rho_b c_b T_a / k$. When considering a linear variation for ω_b ,

$$\omega_b = (\alpha + \beta T) \quad (8)$$

parameters c_1 and c_2 assume the form

$$\begin{aligned} c_1 &= c_3(\alpha + \beta T) \\ c_2 &= -c_4(\alpha + \beta T) - \frac{Q}{k} \end{aligned} \quad (9)$$

Defining a diagonal matrix R with the non-zero terms given by $R_i = (\alpha + \beta \bar{T}_i)$, where \bar{T}_i are known values of T_i taken from a previous iteration and i is the column and row number of the main diagonal, eq (9) can be rewritten as

$$\begin{aligned} c_1 &= c_3 R \\ c_2 &= -(c_4 R + \frac{Q}{k}) \end{aligned} \quad (10)$$

Replacing the above expressions into eq (5) finally gives

$$HT - Gq = -(c_4 R + \frac{Q}{k})S + c_3 RST \quad (11)$$

Taking the term with the unknown value of T to the left-hand side in the usual way produces the final equation:

$$(H - c_3 RS)T - Gq = -(C_4 R + \frac{Q}{k})S \quad (12)$$

The above equation is solved by iterating on the values of \bar{T}_i in matrix R .

A cubic radial basis function, r^3 , is used in the DRM approximation, with linear augmentation terms 1, x and y . The above choice is justified by the results of the tests carried out in [9] with several radial basis functions, including the ‘classical’ function r and the thin plate spline $r^2 \log r$, with and without augmentation. Results obtained using each of these functions were found to differ little. The tests in [9] also showed that no internal points appear to be necessary in the DRM formulation for this type of problem.

3. Direct results for different values of the blood perfusion parameters

Considering Figure 1, the external boundary, ABCD or Γ_2 , is a vertical section through the skin tissue, the part AD being at the skin surface while the opposite boundary BC is an internal boundary maintained at body temperature, $T = 37^\circ\text{C}$. The boundaries AB and CD are truncation boundaries, due to considering a section; at these boundaries, the boundary condition is $q = 0 \text{ W/m}^2$. If the boundary AD is assumed to have a zero flux boundary condition, this is equivalent to thermal isolation on that boundary, for instance a bandage. The internal boundary or Γ_1 in Figure 1 divides the domain into two parts, Ω_2 the external part and Ω_1 which is a sub-region. On the boundary Γ_1 the usual compatibility and equilibrium conditions apply, *i.e.* $T_1 = T_2$ and $q_1 = -q_2$. The thickness of the skin is 0.03m and a section of length 0.08m is considered. In what follows, the parameters c_1 and c_2 given in eq (5) are constant on Ω_2 , and taken to be the values for healthy tissue. However, in the sub-region Ω_1 , a non-linear model is assumed and different parameters are used for the blood perfusion, considering this sub-region to be a tumour.

With the boundary condition at the skin surface AD taken to be $q = 0 \text{ W/m}^2$, values of the parameters necessary to calculate c_1 and c_2 for the healthy tissue are [2]: $\rho_b = 1000 \text{ kg/m}^3$, $c_b = 4000 \text{ J/(kg }^\circ\text{C)}$, $k = 0.5 \text{ W/(m }^\circ\text{C)}$, $\omega_b = 0.0005 \text{ ml}/\text{ml/s}$ and $Q = 420 \text{ J/(m}^3\text{s)}$. For the tumour, the same values of ρ_b , c_b and k are taken, with $Q = 4200 \text{ J/(m}^3\text{s)}$. The unit employed for the perfusion coefficient ω_b is such that $\rho_b \omega_b$ represents mass flow rate of blood per unit volume of tissue.

A first-order expansion for the perfusion is considered, $\omega_b = (\alpha + \beta T)$. Following [5], possible variations which the coefficients α and β might take are as follows: (i) $\omega_b = 0.0005 + 0.0001T$, (ii) $\omega_b = 0.005 + 0.0001T$ and (iii) $\omega_b = 0.005 + 0.0003T$. According to eq (7), the parameter ω_b always appears multiplied by $\rho_b c_b / k$. Using the above numerical values gives the following expressions: (i) $c_1 = 800 \times (5 + 1T)$, (ii) $c_1 = 800 \times (50 + 1T)$ and (iii) $c_1 = 800 \times (50 + 3T)$. Similar considerations are valid for the parameter c_2 .

The discretisation adopted involved 16 linear elements along the internal boundary Γ_1 and 56 linear elements along Γ_2 . Sensitivity tests were performed with different discretisations; for instance, using half the above number, *i.e.* 8 linear elements along Γ_1 and 28 linear elements along Γ_2 , produces results which are virtually the same as those in Table 1.

Results for different first-order variations for the tumour perfusion are given in Table 1. The table shows temperature values at the skin surface, boundary AD in Figure 1. It can be seen that the temperature variation in all cases is very small. The results for curves B, C and D are flat or nearly so and the curvature changes for curves E and F, in the sense that the temperatures at the centre points are lower than at the end points.

Since the temperature is almost constant in all cases, around 37°C, the average value of the tumour perfusion for the linear variations considered are $\omega_b = 0.00195 \text{ ml}_b/\text{ml}_t/\text{s}$ for curve A, $\omega_b = 0.0042 \text{ ml}_b/\text{ml}_t/\text{s}$ for curve B, $\omega_b = 0.00655 \text{ ml}_b/\text{ml}_t/\text{s}$ for curve C, $\omega_b = 0.094 \text{ ml}_b/\text{ml}_t/\text{s}$ for curve D, $\omega_b = 0.0141 \text{ ml}_b/\text{ml}_t/\text{s}$ for curve E and $\omega_b = 0.0161 \text{ ml}_b/\text{ml}_t/\text{s}$ for curve F. The values for curves D, E and F are high compared to average tumour perfusion values of $\omega_b = 0.002 \text{ ml}_b/\text{ml}_t/\text{s}$ quoted in the literature [2], explaining the unexpected results obtained with these curves.

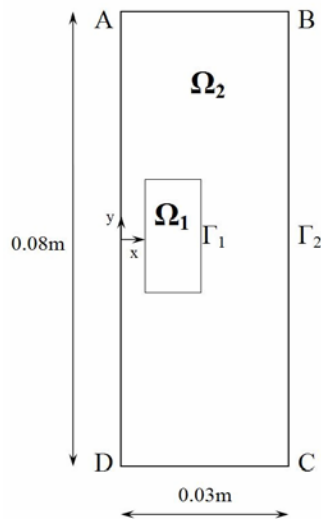


Figure 1. Tumour within a matrix of healthy tissue

4. Procedure for identification of blood perfusion parameters

GAs are ideally suited to the inverse problem of identifying the parameters used in the temperature-dependence expansions for blood perfusion [7,8]. The method is of an evolutionary type, based on the process of natural selection, requiring no initial guess for the values of the parameters. It is necessary to know only the range of values that these might take in order to choose the number of bits to allocate in each chromosome. No calculations of derivatives, sensitivities or directions in which to search are required.

In this work, a simple GA detailed in [12] has been implemented. The geometry of each tumour is initially considered to be rectangular, of size 0.01 by 0.02m, with its centre at position (0.01, 0.0) as shown in Figure 1. The size of the initial population of chromosomes is defined considering the range of values which the parameters used to calculate c_i in Table 1 might take.

Table 1: Temperature variations ($^{\circ}\text{C}$) at the skin surface considering first-order tumour perfusion

y at skin surface	$c_1 = 800 \times (1 + 0.5T)$ Curve A	$c_1 = 800 \times (5 + 1.0T)$ Curve B	$c_1 = 800 \times (10 + 1.5T)$ Curve C	$c_1 = 800 \times (20 + 2.0T)$ Curve D	$c_1 = 800 \times (30 + 3.0T)$ Curve E	$c_1 = 800 \times (50 + 3.0T)$ Curve F
0.03	37.18	37.15	37.15	37.14	37.13	37.13
0.02	37.21	37.15	37.15	37.14	37.12	37.12
0.01	37.27	37.16	37.15	37.13	37.10	37.09
0.0	37.30	37.17	37.15	37.12	37.09	37.08
-0.01	37.27	37.16	37.15	37.13	37.10	37.09
-0.02	37.21	37.15	37.15	37.14	37.12	37.12
-0.03	37.18	37.15	37.15	37.14	37.13	37.13

The highest expansion, curve F, has $c_1 = 800 \times (50 + 3.0T)$. If this is written as $c_1 = 800 \times (p_1 + p_2T)$, then p_1 will take positive integer values up to 50 and the largest value of p_2 is 3, with an interval of 0.1 considered between successive values. Thus, the chromosome has two alleles; for p_1 and p_2 the first allele has 6 bits, $2^6 - 1 = 63 > 50$, while the second has 5 bits, in such a way that the largest number which can be represented is 3.1 for the interval of 0.1. Thus, the chromosome is of size 11. The parameter p_1 is calculated directly by converting the binary value of the allele to decimal; for p_2 , the decimal value of the allele is divided by 10. The population size was fixed at 20.

After establishing an initial population, the values of p_1 and p_2 for each chromosome are obtained as considered above, and results for the temperature distribution at the skin surface, (nodes along the part AD of the Γ_2 boundary in Figure 1) are calculated using the DRM. The objective of the algorithm is to minimize the value of the sum of the squares of the differences between the temperatures calculated at the surface nodes and the predetermined values corresponding to given values of p_1 and p_2 . The chromosomes are ordered according to the value of the sum of the squares, with the smallest value first, the position in this new order being considered the fitness. Individuals are selected for crossover using the roulette wheel method described by Goldberg [10], the fitter individuals having the greater probability of selection. The probability of crossover is 80%. Two point crossover and mutation with a probability of 1% is carried out, following the results in [11]. A process of elitism is employed by which the best individual from one generation passes automatically to the next, in order to ensure that the best solution is not lost. A maximum of 100 generations is permitted; if the process has not converged after this, iterations are halted. The stopping criterion considered is that 80% of the individuals in the fitness table must have converged to the same value.

5. Some results for the identification of perfusion parameters using the GA

Considering the geometry shown in Figure 1, in which a 0.08m section of tissue of thickness 0.03m is selected with the tumour in the position shown, the temperature values for part AD of the boundary Γ_2 for the inverse analysis are fixed using the values given in Table 1. These values are compared with those calculated for each tentative set of perfusion parameters indicated by the chromosomes in the GA, and the sum of the squares of the differences minimised. Similar to the direct simulations, Γ_2 is discretised with 56 linear boundary elements and Γ_1 with 16. It is considered that c_1 in eq (11) is given by $c_1 = 800 \times (p_1 + p_2T)$ and the parameters p_1 and p_2 are identified. The temperature values used as input on the skin surface are taken from Table 1.

Case 1. In this case, the data for the measured temperatures on the skin surface are taken from curve A. The results produced by the GA were $p_1 = 1$ and $p_2 = 0.6$, and converged in 31 generations. The data used to

generate the values at the skin surface are $p_1 = 1$ and $p_2 = 0.5$. No convergence was obtained for curves B to D as these curves are flat or nearly flat, and the resulting surface temperatures constant or nearly constant.

Case 2. In this case, the data for the measured temperatures on the skin surface are taken from curve E. Although the results are physically unrealistic since the tumour perfusion is too high, it is possible to identify the perfusion parameters due to the surface temperature variations. The results produced by the GA were $p_1 = 31$ and $p_2 = 2.9$, and converged in 21 generations. The data used to generate the values at the skin surface are $p_1 = 30$ and $p_2 = 3$.

Case 3. In this case, the data for the measured temperatures on the skin surface are taken from curve F. The results produced by the GA were $p_1 = 56$ and $p_2 = 2.9$, and converged in 21 generations. The data used to generate the values at the skin surface are $p_1 = 50$ and $p_2 = 3$.

6. Conclusions

In this paper, the DRBEM was coupled to a GA in an inverse procedure for identifying parameters of a temperature-dependent approximation for the tumour perfusion, considering temperature data on the skin surface. The procedure has the advantage of not requiring the calculation of derivatives or sensitivities, or an initial estimate of these values. The DRBEM formulation requires no internal discretisation, and in this case no internal nodes either, apart from those defining the interface tissue/tumour. The technique can be directly extended to more realistic three-dimensional inverse analysis estimations, at an increased computational cost.

It is seen that the skin temperature variation changes as the blood perfusion increases, and in certain cases flat or nearly flat curves are produced. The proposed algorithm has difficulty to identify the perfusion parameters in these cases, although a more advanced GA may provide improved results.

Acknowledgement

The first author gratefully acknowledges the support of the Brazilian agency CAPES in funding this work.

References

- [1] Z-S. Deng and J. Liu *Computers in Biology and Medicine*, **34**, 495-521 (2004)
- [2] J. Liu, J. and L.S. Xu *Int. Journal of Heat and Mass Transfer*, **43**, 2827-2839 (2000)
- [3] D.T. Tompkins, R. Vanderby, S.A. Klein, W.A. Beckman, R.A. Steeves, D.M. Frye and B.R. Paliwal *Int. Journal of Hyperthermia*, **10**, 517-536 (1994)
- [4] B. Erdmann, J. Lang, and M. Seebass *Annals of the New York Academy of Sciences*, **858**, 36-46 (1998)
- [5] Z-S. Deng and J. Liu *Medical Engineering & Physics*, **22**, 693-702 (2000)
- [6] W-Q. Lu, J. Liu and Y. Zeng *Eng. Analysis with Boundary Elements*, **22**, 167-174 (1998)
- [7] Z.P. Ren, J. Liu and C.C. Wang *J. of Thermal Sciences*, **4**, 117-124 (1995)
- [8] E. Majchrzak and M. Paruch Proceedings ECCOMAS 2004, Eds P. Neittaanmaki *et al.*, 1-14 (2004)
- [9] P.W. Partridge and L.C. Wrobel *Eng. Analysis with Boundary Elements*, **31**, 803-811 (2007)
- [10] D.E. Goldberg *Genetic Algorithms in Search, Optimization and Machine Learning*, Addison-Wesley, Boston (1989)
- [11] D.E. Goldberg, K. Zakrewsky, B. Sutton, R. Gadiant, C. Chong, P. Galego, B. Miller and E. Cantu-Paz Technical Report 97011, University of Illinois at Urbana-Champaign (1997)
- [12] L.C. Castro and P.W. Partridge *Latin American J. of Solids and Structures*, **3**, 107-123 (2006)
- [13] P.W. Partridge, C.A. Brebbia and L.C. Wrobel *The Dual Reciprocity Boundary Element Method*, Elsevier, London (1992)

Improved solution algorithm for the BEM analysis of multiple semipermeable piezoelectric cracks in 2-D

M. Denda

Mechanical and Aerospace Engineering Department, Rutgers University
98 Brett Road, Piscataway, NJ 08854-8058, USA
denda@jove.rutgers.edu

Keywords: Piezoelectricity, Electrically Semipermeable Crack, Solution Algorithm for Multiple Cracks, Boundary Element Method, Numerical Green's Function

Abstract. The solution of the semipermeable crack is a nonlinear process that requires an iteration since both the electric potential jump and the electric induction over the crack surface, which must satisfy the semipermeable boundary condition, are unknown. An iteration process proposed earlier by the author [1] converges to the semipermeable solution stably and accurately for the single crack, but not so for multiple cracks. An improved solution algorithm, with a refined iteration process, that gives the accurate semipermeable solution stably for multiple straight center cracks is proposed.

The core of the analysis consists of a boundary element method (BEM) using the numerical Green's function approach for simple and accurate crack modeling for the impermeable and permeable cracks. The continuous distribution of extended dislocation dipoles, which represents the extended crack opening displacement (COD) of the straight crack, with the built-in \sqrt{r} COD behavior at each crack tip is integrated analytically to give the whole crack singular element (WCSE) equipped with the \sqrt{r} COD and the $1/\sqrt{r}$ crack tip extended stress singularity. A refined iterative procedure is proposed to reach the semipermeable solution stably using the combination of the impermeable and permeable linear BEM solvers. The convergence study is performed for multiple cracks with numerical results for the extended stress intensity factors (SIFs) and other variables.

Introduction

The boundary condition of the piezoelectric solids can be described by the extended displacement and traction vectors. The extended displacement vector has three displacement and one electric potential components and the extended traction vector has three traction and one electric induction components. Similarly, the stress, strain and material constants can be extended from the anisotropic elastic to piezoelectric quantities by appending the electric quantities to the elastic ones. On the surface of an opened piezoelectric crack, located horizontally along the x_1 -axis, we observe the normal displacement u_2 , electric potential Φ and the normal electric induction D_2 . This paper is concerned with the crack with the semipermeable boundary condition (BC),

$$D_2^+ = D_2^-; \quad D_2^+(u_2^+ - u_2^-) = -\varepsilon^C(\Phi^+ - \Phi^-), \quad (1)$$

proposed by Hao and Shen [2], which gives the consistent BC for opened cracks, where \pm signs indicate the quantities for the upper (+) and the lower (-) surfaces, respectively, and ε^C is the permittivity of the cracked medium. Two other electric boundary conditions on the piezoelectric crack surface come in different degrees of shielding the electric induction defined by the electric permittivity. The permeable crack along the x_1 -axis given by the BC,

$$D_2^+ = D_2^-; \quad \Phi^+ - \Phi^- = 0, \quad (2)$$

does not shield the electric induction at all. The impermeable crack with the BC,

$$D_2^+ = D_2^- = 0, \quad (3)$$

shields the electric induction completely. The permeable BC is correct for the closed crack and the impermeable BC is correct if the permittivity ε^C of the crack medium is zero. However, there is no medium with zero permittivity (the vacuum has the least permittivity $\varepsilon^{air} = 8.854 \times 10^{-12} C/Vm$) and the two boundary conditions are not correct for opened cracks. Notice that the semipermeable BC becomes the impermeable BC when $\varepsilon^C = 0$ and the permeable BC when $u_2^+ - u_2^- = 0$ and that these two BCs set the bounds for the semipermeable BC. Works on the impermeable and permeable BCs are abundant compared to the semipermeable BC (see references in [3]).

The solution procedure of the semipermeable crack is nonlinear that requires iteration process since the distribution of the electric induction on the crack surface, which is needed to determine the crack opening displacement and the electric potential jump across the crack, are unknown. The solution algorithm proposed earlier by Denda [1] works well for the single crack but not for multiple cracks. We propose an improved iteration scheme to achieve the semipermeable BC for multiple straight center cracks using the linear solution procedure by the boundary element method (BEM) developed for permeable and impermeable cracks. The convergence of the iteration is studied for various multiple crack configurations and the extended stress intensity factor results are reported.

Piezoelectric BEM in 2-D for Crack Modeling

As the basis of the direct formulation of the boundary element method for piezoelectricity, we use the physical interpretation of the extended Somigliana's identity [3], according to which the extended displacement field in a domain A can be represented by continuous distributions of the extended line forces (T_I) and dislocation dipoles (U_I) along the contour ∂A in an infinite body that coincides with the boundary of the domain, where T_I and U_I are the magnitudes of the extended traction and displacement on the boundary, respectively. The extended Lekhnitskii formalism developed by Denda and Mansukh [3] for the general piezoelectric solids in 2-D serves as the theoretical basis for the BEM providing, above all, means to derive the fundamental solutions necessary for the BEM formulation. We follow the standard implementation of the BEM straight boundary elements and the quadratic interpolation functions for the extended displacement and traction. The boundary integrals are evaluated analytically with the results given in [3].

The crack modeling in this paper is also based on the physical interpretation of the extended Somigliana's identity in which the crack is represented by the continuous distribution of the extended dislocation dipoles along a line. To embed the \sqrt{r} crack tip opening displacement behavior we interpolate the extended dislocation dipole distribution by the formula

$$\delta_K(\eta) = \sqrt{1 - \eta^2} \sum_{m=1}^M \delta_K^{(m)} U_{m-1}(\eta), \quad (4)$$

where η is the normalized local coordinate along the crack $-1 \leq \eta \leq +1$ and $U_{m-1}(\eta)$ is Chebyshev polynomial of the second kind. This distribution is integrated analytically to give the whole crack singular element (WCSE) [3] which is the basis of the numerical Green's function. The numerical Green's function has the built in \sqrt{r} extended COD and the $1/\sqrt{r}$ extended stress singularity at the crack tip and is given in terms of the unknown extended COD coefficients $\delta_K^{(m)}$ defined in (4). These coefficients are determined by satisfying the extended

traction boundary condition on the crack surface, which is zero for the impermeable crack and nonzero for the permeable and semipermeable cracks. Further, the extended stress intensity factors (SIFs) are determined in terms of $\delta_K^{(m)}$ in the main-processing.

This WCSE can readily be extended to multiple cracks in the finite domain with the introduction of the boundary elements. For the impermeable crack the crack surface electric induction is zero (i.e., $D_2^c = 0$), but this is nonzero for the permeable and semipermeable cracks. The solution strategies for the impermeable and permeable cracks are summarized as follows. (1) For the impermeable crack set all four traction components zero ($T_I^c = 0; I = 1, 2, 3, 4$) and solve for four components ($\delta_I; I = 1, 2, 3, 4$) of the extended COD. (2) For the permeable crack set the three traction components and the electric potential jump to zero ($T_I^c = 0; I = 1, 2, 3$ and $\delta_4 = 0$) and solve for the three components of the COD and the electric induction ($\delta_I; I = 1, 3$ and T_4^c). Notice that Both (1) and (2) are linear procedures with four equations for four unknowns at each crack surface point that can be solved by the BEM. However, the semipermeable crack has five unknowns ($\delta_I; I = 1, 2, 3, 4$ and T_4^c) that require a nonlinear iterative solution procedure introduced later. Numerical results for the extended stress intensity factors for multiple permeable and impermeable crack configurations are reported in [3].

Numerical Solution Procedure for Semipermeable Cracks

Consider N straight cracks $n = 1, \dots, N$. For the impermeable crack $\delta_4^{n(m)} \neq 0$ and $T_4^{Cn(m)} = 0$, while for the permeable crack $\delta_4^{n(m)} = 0$ and $T_4^{Cn(m)} \neq 0$, where the superscripts n and (m) indicate n -th crack and m -th coefficient in the interpolation (4), respectively. Notice that there are NM terms for each of the coefficients $\delta_4^{n(m)}$ and $T_4^{Cn(m)}$ to deal with, where M is the number of terms in the interpolation (4). Knowing that the semipermeable crack solution is somewhere in between the impermeable and permeable crack solutions, we suggest the following iteration procedure for the semipermeable multiple cracks. First, apply the preliminary iteration as follows.

1. Get the impermeable solution $\delta_4^{n(m)[0]}$ using the impermeable BEM solver. Here the superscript $[0]$ indicates the initial value. In the following, the superscript $[k]$ is attached to indicate the k -th iteration values of variables.
2. (a) Set $\delta_4^{n(m)[1]} = p^{[1]} * \delta_4^{n(m)[0]}$ for a slightly reduced value of $\delta_4^{n(m)[1]}$ given by a control parameter $p = p^{[1]} < 1.0$,
- (b) Calculate, using the permeable BEM solver, the crack opening coefficients $\delta_2^{n(m)[1]}$ and the electric induction coefficients $D_2^{Cn(m)[1]} = -T_4^{Cn(m)[1]}$ based on the set value $\delta_4^{n(m)[1]}$ of the electric potential.
- (c) Use (1) to calculate

$$\varepsilon^{Cn[1]}(\zeta_i) = -D_2^{Cn[1]}(\zeta_i) \frac{\delta_2^{n[1]}(\zeta_i)}{\delta_4^{n[1]}(\zeta_i)} \quad (5)$$

at M sample points ζ_i ($i = 1, \dots, M$) on each crack n ($n = 1, \dots, N$), where $D_2^{Cn[1]}(\zeta_i)$, $\delta_2^{n[1]}(\zeta_i)$ and $\delta_4^{n[1]}(\zeta_i)$ are given by

$$\begin{aligned} D_2^{Cn[1]}(\zeta_i) &= \sum_{m=1}^M U_{m-1}(\zeta_i) D_2^{Cn(m)[1]}, \\ \delta_2^{n[1]}(\zeta_i) &= \sum_{m=1}^M U_{m-1}(\zeta_i) \delta_2^{n(m)[1]}, \quad \delta_4^{n[1]}(\zeta_i) = \sum_{m=1}^M U_{m-1}(\zeta_i) \delta_4^{n(m)[1]}. \end{aligned} \quad (6)$$

Notice that $\sqrt{1 - \zeta^2}$ term for $\delta_2^{n[1]}(\zeta_i)$ and $\delta_4^{n[1]}(\zeta_i)$ are omitted since they cancel each other. For the sample points ζ_i we have used the Gaussian quadrature points.

- (d) Calculate the average

$$\hat{\varepsilon}^{Cn[1]} = \frac{\sum_{i=1}^M \varepsilon^{Cn[1]}(\zeta_i)}{M} \quad (7)$$

for each crack.

- 3. Repeat STEP 2 R times for progressively reduced values of $\delta_4^{n(m)[k]} = p^{[k]} * \delta_4^{n(m)[0]}$ for the control parameter $p = p^{[k]}$ ($k = 2, 3, 4, \dots, R$) to plot $p^{[k]} - \hat{\varepsilon}^{Cn[k]}$ curve for each crack.
- 4. Intersection of the $p^{[k]} - \hat{\varepsilon}^{Cn[k]}$ curve obtained in STEP 3 and the horizontal line $\varepsilon^C = \varepsilon^{air}$ gives the best fit parameter value $p^{n[best]}$ for each crack. Use

$$\delta_4^{n(m)[best]} = p^{n[best]} * \delta_4^{n(m)[0]} \quad (m = 1, \dots, M; \text{ no sum on } n), \quad (8)$$

for each crack $n = 1, \dots, N$ and calculate $\delta_2^{n(m)[best]}$ and the electric induction coefficients $D_2^{Cn(m)[best]} = -T_4^{Cn(m)}$.

Notice that in each iteration step the mode (i.e., the ratio among the coefficients) of $\delta_4^{n(m)[k]} = p^{[k]} * \delta_4^{n(m)[0]}$ remains identical with that of $\delta_4^{n(m)[0]}$ and only the amplitude $p^{[k]}$ is reduced. Since the mode of $\delta_4^{n(m)[semipermeable]}$ usually differs from that of $\delta_4^{n(m)[0]} = \delta_4^{n(m)[impermeable]}$, the solution obtained by $\delta_4^{n(m)[best]}$ given by (8) does not satisfy the semipermeable condition (1). The only exception is the single crack for which the number M of the polynomial terms in the interpolation (4) is one. For multiple cracks, further iteration is necessary to improve the accuracy of the solution. The refined iteration process starts with the solution given by (8).

- 5. Let $\delta_4^{n(m)[0]} = \delta_4^{n(m)[best]}$, $\delta_2^{n(m)[0]} = \delta_2^{n(m)[best]}$ and $D_2^{Cn(m)[0]} = D_2^{Cn(m)[best]}$. Notice that the notation $\delta_4^{n(m)[0]}$ for the starting value of the iteration is reused here with a different definition.
- 6. Calculate

$$\delta_4^{n[prj]}(\eta_i) = -\frac{D_2^{Cn[0]}(\eta_i) * \delta_2^{n[0]}(\eta_i)}{\varepsilon^C} \quad (9)$$

at M collocation points η_i ($-1 \leq \eta_i \leq +1; i = 1, \dots, M$) used for the extended traction calculation, where

$$D_2^{Cn[0]}(\eta_i) = \sum_{m=1}^M U_{m-1}(\eta_i) D_2^{Cn(m)[0]}, \quad \delta_2^{n[0]}(\eta_i) = \sum_{m=1}^M U_{m-1}(\eta_i) \delta_2^{n(m)[0]}.$$

Solve the system of equations

$$\sum_{m=1}^M U_{m-1}(\eta_i) \delta_4^{n(m)[prj]} = \delta_4^{n[prj]}(\eta_i),$$

for M projected coefficients $\delta_4^{n(m)[prj]}$ for each crack n ($n = 1, \dots, N$). Here for the first time the efforts are made to alter the mode of $\delta_4^{n(m)}$.

- 7. Divide the interval $\|\delta_4^{n(m)}\| = \delta_4^{n(m)[prj]} - \delta_4^{n(m)[0]}$ by L equal sub-intervals of magnitude $\Delta\delta_4^{n(m)} = \|\delta_4^{n(m)}\|/L$. For L values of $\delta_4^{n(m)[k]}$ given by $\delta_4^{n(m)[k]} = \delta_4^{n(m)[0]} + k * \Delta\delta_4^{n(m)}$ ($k = 1, \dots, L$), run the permeable BEM solver to calculate the crack opening coefficients $\delta_2^{n(m)[k]}$ and the electric induction coefficients $D_2^{Cn(m)[k]} = -T_4^{Cn(m)[k]}$.

8. Follow the STEP 2 (c)-(d) of the preliminary iteration to calculate the average $\hat{\varepsilon}^{Cn[k]}$ for each crack according to (7).
9. Following the step similar to STEP 4 in the preliminary iteration, obtain the best fit $\delta_4^{n(m)[best]}$ for each crack and calculate $\delta_2^{n(m)[best]}$ and the electric induction coefficients $D_2^{Cn(m)[best]} = -T_4^{Cn(m)[best]}$.
10. Repeat STEP 5-9 total of S times if necessary.

For the single crack in the infinite body the extended crack opening displacement is given exactly by one term of the interpolation (i.e., $M = 1$) in (4). Thus the ratio of δ_2/δ_4 , used in the iteration by equation (5), is constant $\delta_2^{(1)}/\delta_4^{(1)}$ over the entire crack surface. This feature guarantees that the electric induction on the crack surface is also constant over the surface. During the iteration it is sufficient to sample them at a single point on the crack, typically at the center. In contrast to this, the interpolation of the extended crack opening displacement for multiple cracks requires multiple polynomial terms $U_{m-1}(\eta)$ as in (4). Consequently the ratio δ_2/δ_4 is not constant over the crack surface. In calculating the ϵ^C , we suggest to evaluate it at M discrete points on each crack and take the average. In the preliminary iteration process, the amplitude of the electric potential jump is varied gradually from the impermeable to the permeable condition, while its mode is fixed. However, in the refined iteration process, the mode is also varied. The final converged results indicate that the mode of the semipermeable solution is indeed different from the original impermeable solution. We have found out that the preliminary iteration stage is necessary to go to the approximate solution close enough to the semipermeable solution. The omission of this stage did not give us the convergent solution.

Numerical Results

The stress, strain, electric induction and electric field are of the order of $\sigma_0 = 10^8$ (N/m^2), $\epsilon_0 = 10^{-3}$, $D_0 = 10^{-2}$ (C/m^2), and $E_0 = 10^7$ (V/m), respectively, and the elastic stiffness, piezoelectric stress and dielectric permittivity constants have the order of $c_0 = 10^{11}$ (N/m^2), $e_0 = 10^1$ (C/m^2) and $\varepsilon_0 = 10^{-9}$ ($C/(mV)$), respectively. The potential truncation error, caused by the wide variation in the order of magnitudes for the piezoelectric variables and coefficients, should be avoided by their normalization. In general, the normalization of a dimensional quantity q can be given by $\bar{q} = q/q_0$ in terms of the its reference quantity q_0 . The numerical calculations are all performed in terms of these normalized quantities. Piezoelectric solids considered here is Barium Sodium Niobate (BSN: $Ba_2NaNb_5O_{15}$, Orthogonal 2mm) whose material constants are given in [3]. It has the electrical/out-of-plane mechanical coupling with no in-plane/out-of-plane mechanical and electrical/in-plane mechanical couplings.

Results for the single crack in the infinite body is reported by Denda [1]. Details of the normalization, with reference values used, of the quantities appearing below can be found in [3]. Under a combined remote loading $\bar{\sigma}_{22}^\infty = 1$ (tension) and $\bar{D}_2^\infty = 1$ (electric induction), only the preliminary iteration (STEP 1-4) was applied $R = 1000$ times. The semipermeable solution is given by $\bar{K}_{IV}^{(smp)} = p^{(smp)} \bar{K}_{IV}^{(imp)}$ and $\bar{D}_2^{(smp)} = (1 - p^{(smp)}) \bar{D}_2^{c(per)}$, where $p^{(smp)} = 0.189292$, $\bar{K}_{IV}^{(imp)} = \sqrt{\pi}$ and $\bar{D}_2^{c(per)} = 1$. The value of $\bar{D}_2^{c(smp)} = 0.810708$ agrees perfectly with the theoretical value $\bar{D}_2^{c(smp)} = 0.810709$ [3]. The quantities \bar{K}_{IV} , \bar{D}_2^c and \bar{K}_{II} (very small value) vary linearly between the impermeable and permeable conditions, while \bar{K}_I and $\bar{\delta}_2$ remain constant throughout the iteration and \bar{K}_{II} is zero.

Although, the single crack in the infinite body does not require the refined iteration, the preliminary iteration is not enough for the single crack in the finite domain and for multiple cracks in any domain. Consider a crack ($\bar{a} = 1$) in a finite BSN body ($\bar{H} = \bar{W} = 4$) under the unit

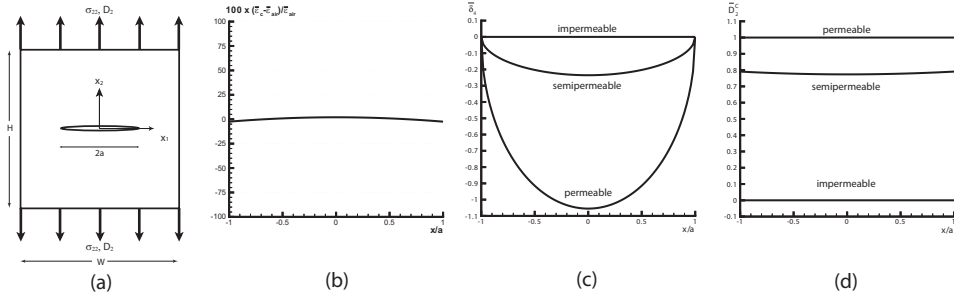


Figure 1: (a) A center crack in a finite body under uniaxial tension and electric induction. (b) Relative error in $\bar{\epsilon}_C$ over the semipermeable crack surface for a crack in a finite body under uniaxial tension and electric induction in the preliminary iteration. Variation of (c) $\bar{\delta}_4$ and (d) \bar{D}_2^C over impermeable, semipermeable and permeable conditions for a crack in a finite body under uniaxial tension and electric induction obtained using the refined iteration.

normalized tension and electric induction, $\bar{\sigma}_{22} = 1$ (tension) and $\bar{D}_2 = 1$ (electric induction), as shown in Fig. 1 (a). The iteration has been applied to this crack using $M = 7$ terms in the interpolation (4) and the average value of the permittivity was calculated. Fig. 1 (b) shows the relative error in the permittivity over the crack surface for the semipermeable solution, which confirms that the ratio δ_2/δ_4 is indeed not constant over the crack. The maximum error in the permittivity obtained by the preliminary iteration is 2 % from the required constant value $\bar{\epsilon}^{air}$. The refined iteration stage using $S = 10$ iteration in STEP 5-9 (with $L = 20$ in STEP 7) was applied following the preliminary (with $R = 10$) iteration. The average value of the permittivity has agreed with $\bar{\epsilon}^{air}$ up to four significant digits for the entire crack length. The extended stress intensity factors are given by $\bar{K}_I^{(smp)} = 2.36716$, $\bar{K}_II^{(smp)} = 0.0$, $\bar{K}_III^{(smp)} = -0.802325 \times 10^{-4}$ and $\bar{K}_IV^{(smp)} = 0.437143$. The electric intensity factors of the impermeable and permeable cracks are given by $\bar{K}_IV^{(imp)} = 2.00409$ and $\bar{K}_IV^{(per)} = 0.0$, respectively. Other stress intensity factors (\bar{K}_I , \bar{K}_{II} and \bar{K}_{III}) remain the same for three crack BCs. The electric potential jump and electric induction field over the crack are shown in Figs. 1 (c) and (d). Notice that the \bar{D}_2 for the semipermeable crack is not constant along the crack in comparison to the constant values for the impermeable and permeable cracks. The crack opening $\bar{\delta}_2$ is the same for all three crack surface electric BCs.

Concluding Remarks

We have developed a boundary element method (BEM) for the analysis of multiple semipermeable cracks using the numerical Green's function approach. An improved iterative procedure to reach the semipermeable solution using the linear BEM impermeable and permeable solvers is proposed. More results on multiple cracks will be presented at the BETEQ 2008 conference.

References

- [1] M. Denda: Key Engng. Mater. (2008), in press.
- [2] T.H. Hao and Z.Y. Shen: Eng. Frac. Mech. Vol. 47(1994), p. 793
- [3] M. Denda and M. Mansukh: Engng. Anal. with Boundary Elements Vol. 29 (2005), p. 533

BEM model for the free-molecule flow in MEMS

Attilio Frangi

Dept. Structural Engng., Politecnico di Milano, P.zza L. da Vinci 32, Milano, 20133, Italy

attilio.frangi@polimi.it

Keywords: BEM, MEMS, free-molecule flow.

Abstract. We present and discuss a numerical approach based on integral equations apt to provide an estimate of the dissipation in MEMS in the free-molecule regime. Two different techniques are compared: a classical Test Particle Monte Carlo method and the Boundary Integral Equation method proposed. The latter proves to be robust, fast and very competitive for the class of applications at hand.

Introduction

Polysilicon inertial MEMS typically are an assembly of fixed parts and vibrating shuttles separated by gaps which are few microns wide. Resonating frequencies are in the order of few kHz and the shuttle velocity appears always small with respect to the mean molecular velocity. These devices are used in a wide variety of applications in environments which exhibit very different pressures, from standard conditions down to almost vacuum. Gas-structure interaction becomes the dominant source of dissipation and intrinsic, solid dissipation can be neglected above a threshold typically occurs between 10^{-5} and 10^{-4} bar. This dissipation strongly affects the quality factor Q which is a key factor in quantifying the performance of the MEMS in industrial environments.

At the length scales of interest rarefaction effects in the flow are always a key factor. These are conventionally quantified by means of the Knudsen number, defined as $\text{Kn} = \lambda/L$, where L is a characteristic length of the flow and λ the mean free path of gas molecules.

Based on the Knudsen number, gas flows can be qualitatively classified as continuum ($\text{Kn} < 0.01$), slip ($0.01 < \text{Kn} < 0.1$), transition ($0.1 < \text{Kn} < 10$), and free-molecule ($\text{Kn} > 10$) [2–4]. Reliable tools exist for the prediction of gas damping in the first two regimes (see e.g. [1,5–8]) but the situation is less defined at lower pressures. Even though numerical techniques of deterministic and statistical nature have been developed in the transition regime, their application to realistic 3D low-speed MEMS is still under investigation. On the contrary, the collisionless or free-molecule flow lends itself to the development of simpler numerical models. Based on the formal classification given above, the free-molecule flow represents the limiting case where the Knudsen number tends to infinity. In inertial MEMS this applies typically at pressures in the range of few mbars and below.

The numerical technique typically employed for estimating the quality factor of MEMS at low pressure is the Test Particle Monte Carlo (TPMC). However, this approach is stochastic in nature which is a major drawback for the extremely low-speed applications at hand, often implying long runs in order to obtain reliable averages, while in the design and optimization phase of MEMS fast and agile tools are preferred.

A different technique based on a Boundary Integral Equation (BIE) approach is very competitive with respect to the TPMC for the typical working conditions of inertial MEMS since it is fast, robust, of relatively simple implementation and does not suffer from the issue of statistical noise.

In the last Section, the formulations analysed are benchmarked against data available for a real inertial MEMS.

Numerical analysis: theoretical basis

It is assumed that the velocity of moving surfaces \mathbf{v}_w is small with respect to the average thermal molecular speed, hence it is $|\tilde{\mathbf{v}}_w| = |\mathbf{v}_w| / \sqrt{2RT} \ll 1$. This assumption is generally acceptable for the class of inertial MEMS here considered. For a periodic motion with amplitude $q(t) = A \sin \omega_0 t$, this condition can be written as $c_L \ll 1$, where $c_L = \omega_0 A / \sqrt{2RT}$.

Thanks to the absence of molecular collisions, the flow impinging on a shuttle surface can be decomposed in the contribution of molecules coming from the far field region with a given distribution function and a contribution from molecules reflected by other solid surfaces. The former can indeed be evaluated analytically. As far as the latter is concerned, if L denotes a typical distance between visible surfaces, and if the average time required by a molecule to bounce back to the shuttle is small with respect to the duration of one oscillation, i.e. $c_Q := \omega_0 L / \sqrt{\rho RT}$, the properties of the flow can be computed assuming quasi-static conditions.

Clearly the two conditions $c_L \ll 1$, $c_Q \ll 1$ need to be accurately checked in the applications. However, for the class of inertial resonators of interest herein, they are generally largely met. As an example, in the case of the rotational accelerometer presented in the last Section, $c_Q \approx 6 \cdot 10^{-4}$, $c_L \approx 10^{-5}$.

Although not strictly necessary, in the sequel it will also be assumed that the displacement $\mathbf{s}(\mathbf{x}, t)$ of movable parts in a MEMS can be expressed as $\mathbf{s}(\mathbf{x}, t) = \psi(\mathbf{x}) q(t)$ where $\psi(\mathbf{x})$ is a function of position \mathbf{x} to be specified and corresponds to a modal shape of shuttle and springs. This implies a sort of decoupling between the structural response and the fluid action, the latter never affecting the shape of the displacement field but only the time dependent weight $q(t)$. The rather frequent case in which the global MEMS movement is the linear combination of several similar terms requires only a straightforward extension of the techniques analysed herein and will not be addressed.

If $c_L \ll 1$ and $c_Q \ll 1$ the force exerted on the shuttle by the gas flow admits the form $\mathbf{p}(\mathbf{x}, t) = \mathbf{t}(\mathbf{x}) q(t)$, where $\mathbf{t}(\mathbf{x})$ is a real vector function and the global analysis can be reduced to the 1D model $M\ddot{q}(t) + B\dot{q}(t) + Kq(t) = F(t)$ where, if S_{SH} denotes the surface of the shuttle, the damping coefficient B is:

$$B = - \int_{S_{SH}} \psi(\mathbf{x}) \mathbf{t}(\mathbf{x}) dS \quad (1)$$

This model predicts the quality factor $Q = (2/\pi) E/D = \omega_0 M/B$ where E is the maximum elastic energy stored in the system $\frac{1}{2} K A^2$ and D is the dissipation per unit-cycle $D = \pi B A^2 \omega_0$.

According to the kinetic theory of gases [2–4], all the macroscopic quantities of interest, like mean velocity \mathbf{v} , density ρ , temperature T can be expressed as moments of the distribution function $f(\mathbf{x}, \xi)$ in the velocity space:

$$\rho(\mathbf{x}) = \int_{R^3} f(\mathbf{x}, \xi) d\xi, \quad \rho(\mathbf{x}) \mathbf{v}(\mathbf{x}) = \int_{R^3} f(\mathbf{x}, \xi) \xi d\xi, \quad T(\mathbf{x}) = \frac{1}{3R\rho(\mathbf{x})} \int_{R^3} f(\mathbf{x}, \xi) |\xi - \mathbf{v}|^2 d\xi$$

where R is the universal gas constant divided by the molar mass.

The gas interacts with both fixed and movable surfaces of the MEMS. As a matter of fact, silicon surfaces originating from etching procedures are very rough so that, as a first approximation, diffuse reflection from the solid surface will be assumed in the sequel. If $\mathbf{n}(\mathbf{x})$ denotes the unit normal

vector to the solid surface pointing inside the fluid domain, diffuse reflection [3] means that molecules are re-emitted from a given solid surface S_R according to the distribution function

$$f(\mathbf{x}, \xi) = \frac{\rho_w(\mathbf{x})}{(2\pi RT_w)^{3/2}} \exp\left(-\frac{|\xi - \mathbf{v}_w|^2}{2RT_w}\right) \quad \text{for } (\xi - \mathbf{v}_w) \cdot \mathbf{n} > 0 \quad (2)$$

where T_w is the wall temperature and \mathbf{v}_w is the wall velocity. The function ρ_w is proportional to the flux of incoming molecules:

$$\rho_w(\mathbf{x}) = \left(\frac{2\pi}{RT_w(\mathbf{x})} \right)^{1/2} \int_{R^3, (\xi - \mathbf{v}_w) \cdot \mathbf{n} < 0} f(\mathbf{x}, \xi) (|\xi - \mathbf{v}| \cdot \mathbf{n}) d\xi \quad (3)$$

and is defined in such a way that the global net flux of incoming and outgoing molecules vanishes. Moreover it will be assumed that the flow is nearly isothermal, with far field temperature T_0 and wall temperature $T_w = T_0$ (see e.g.[12] for a discussion on this point).

If the analysis domain extends to infinity in some direction, the distribution function for incoming molecules is $f = f_0$, where f_0 is the far-field equilibrium Maxwellian defined by temperature T_0 , density ρ_0 and zero average velocity:

$$f(\mathbf{x}, \xi) = f_0 = \frac{\rho_0}{(2\pi RT_0)^{3/2}} \exp\left(-\frac{\xi^2}{2RT_0}\right) \quad (4)$$

Boundary Integral Equation approach

Since intermolecular collisions are neglected, the total (material) derivative of f along the molecular trajectories vanishes:

$$\frac{\partial f}{\partial t} + \xi \cdot \nabla f = 0 \quad (5)$$

The condition $c_L \ll 1$ discussed in the previous section implies that the deviation from the equilibrium state of the gas is small and f can be expressed as

$$f(\mathbf{x}, \xi) = f_0(\xi) (1 + f_1(\mathbf{x}, \xi)) ,$$

where f_1 is a perturbation of the equilibrium distribution f_0 eqn. (4) and all the governing equations can be linearized with respect to f_1 . Boundary conditions simply to:

$$f_1(\mathbf{x}, \xi) = \rho_{w1}(\mathbf{x}) + 2\tilde{\xi} \cdot \tilde{\mathbf{v}}_w(\mathbf{x}) \quad \text{for } (\xi - \mathbf{v}_w) \cdot \mathbf{n} > 0 \quad (6)$$

with $\tilde{\xi} = \xi / \sqrt{2RT}$ and

$$\rho_{wl}(\mathbf{x}) = \sqrt{\pi} \tilde{\mathbf{v}}_w(\mathbf{x}) \cdot \mathbf{n}(\mathbf{x}) - \frac{2}{\pi} \int_{\mathbb{R}^3, \xi < 0} (\xi \cdot \mathbf{n}) \exp\left(-|\tilde{\xi}|^2\right) f_l(\mathbf{x}, \xi) d\tilde{\xi} \quad (7)$$

on solid surfaces. In eqn. (7) ρ_{wl} is the linear term in the expansion of ρ_w eqn. (3).

Finally, for the flow of molecules impinging on the structures and coming from infinity, $f_l(\mathbf{x}, \xi) = 0$.

The stresses exerted the solid surfaces can be linearized as well yielding:

$$\begin{aligned} \boldsymbol{\sigma}(\mathbf{x}) &= \int_{\mathbb{R}^3} f(\mathbf{x}, \xi) (\xi - \mathbf{v}) \otimes (\xi - \mathbf{v}) d\xi \equiv \\ &= \int_{\mathbb{R}^3} f_0 \xi \otimes \xi d\xi + \int_{\mathbb{R}^3} f_0 f_1 \xi \otimes \xi d\xi = \\ &= \rho_0 RT \left[\mathfrak{I} + \frac{2}{\pi^{3/2}} \int_{\mathbb{R}^3} \exp\left(-|\tilde{\xi}|^2\right) f_1 \xi \otimes \xi d\tilde{\xi} \right] \end{aligned} \quad (8)$$

Typically, the output of interest from the analysis is the global viscous force exerted on the shuttle surfaces, which can be obtained through integration over the surfaces of the tractions $\mathbf{p} = \boldsymbol{\sigma} \cdot \mathbf{n}$.

The quasi-static condition $c_Q \ll 1$ implies that the time derivative in eqn. (5) can be dropped and the velocity of the shuttle can be simply enforced as a stationary boundary condition. As a consequence, for any \mathbf{y} in the analysis domain, the probability $f_l(\mathbf{x}, \xi)$ remains always constant along the line $\mathbf{y} + \lambda \xi$, with $\lambda > 0$ (i.e. along the trajectories of molecules emitted from \mathbf{y}). Thus, for any bounded and simply connected region of fluid, for given $\mathbf{x} \in S$ and ξ , there exist one and only one $\mathbf{y} \in S$ such that:

$$f_l(\mathbf{x}, \xi) = f_l(\mathbf{y}, \xi), \quad \mathbf{x} = \mathbf{y} + \lambda \xi, \quad \lambda > 0 \quad (9)$$

and \mathbf{x} is visible from \mathbf{y} . Let us denote $\rho(\mathbf{x}, \xi)$ the vector such that $\mathbf{y} = \mathbf{x} + \mathbf{r}$ and \mathbf{x} and \mathbf{y} are associated in the sense defined above. Hence we have:

$$\xi = -\xi \frac{\mathbf{r}}{r} \quad (10)$$

where r is the length of \mathbf{r} and ξ is the velocity module.

An idea frequently exploited in similar applications [3] is to transform the integration over the molecular velocity space into an integration over the surface S^+ visible from \mathbf{x} .

Indeed, $d\xi = \xi^2 d\xi dS_1$, where ξ is the velocity module and S_1 is the surface of the unit sphere, and

$$dS_1 = -\frac{1}{r^3} \mathbf{r}(\mathbf{x}, \xi) \cdot \mathbf{n}(\mathbf{y}) dS(\mathbf{y}). \quad (11)$$

The final integral equation writes:

$$\begin{aligned}\rho_{wl}(\mathbf{x}) = & \sqrt{\pi} \tilde{\mathbf{v}}_w(\mathbf{x}) \cdot \mathbf{n}(\mathbf{x}) \\ & - \frac{1}{\pi} \int_{S^+} \rho_{wl}(\mathbf{y}) (\mathbf{r} \cdot \mathbf{n}(\mathbf{x})) (\mathbf{r} \cdot \mathbf{n}(\mathbf{y})) \frac{1}{r^4} dS \\ & - \frac{3}{2} \frac{1}{\sqrt{\pi}} \int_{S^+} (\mathbf{r} \cdot \tilde{\mathbf{v}}_w(\mathbf{y})) (\mathbf{r} \cdot \mathbf{n}(\mathbf{x})) (\mathbf{r} \cdot \mathbf{n}(\mathbf{y})) \frac{1}{r^5} dS\end{aligned}\quad (12)$$

It is worth stressing that eqn. (12) is the extension to moving boundaries of a classical integral identity in the kinetic theory of rarefied gases [3].

The numerical implementation of the scalar equation eqn. (12) is straightforward and advantage is taken of the techniques developed in the last decade for the evaluation of boundary integral equations with high order singularities. In the implementation employed in this work the surface is discretized with three-node triangles and ρ_w is assumed to be constant over each triangle. These choices permit to adopt simple and fast integration strategies which suit well into the iterative solver employed.

Testing the visibility condition, as required by the occurrence of S^+ in eqn. (12), could be potentially a major issue but this is eventually mitigated for MEMS thanks to the very regular layout of the structures to analyse.

A similar procedure applied to eqn. (8) leads to an integral identity for the tractions $\mathbf{p} = \boldsymbol{\sigma} \cdot \mathbf{n}$ on the MEMS surfaces:

$$\begin{aligned}\frac{\pi^{3/2}}{\rho_0 2RT} \mathbf{p}(\mathbf{x}) = & \left(1 + \frac{1}{2} \rho_{wl}\right) \frac{\pi^{3/2}}{2} \mathbf{n} + \pi \tilde{\mathbf{v}}_{wn} \mathbf{n} + \frac{\pi}{2} \tilde{\mathbf{v}}_{wt} \\ & - \frac{3\sqrt{\pi}}{8} \int_{S^+} \mathbf{r} (\mathbf{r} \cdot \mathbf{n}(\mathbf{x})) (\mathbf{r} \cdot \mathbf{n}(\mathbf{y})) \frac{1}{r^5} \rho_{wl}(\mathbf{y}) dS \\ & + 2 \int_{S^+} \mathbf{r} (\mathbf{r} \cdot \tilde{\mathbf{v}}_{wl}(\mathbf{y})) (\mathbf{r} \cdot \mathbf{n}(\mathbf{x})) (\mathbf{r} \cdot \mathbf{n}(\mathbf{y})) \frac{1}{r^6} dS\end{aligned}\quad (13)$$

Indeed, if the index t denotes tangential components, using the decompositions $\tilde{\xi} = \xi_n \mathbf{n} + \tilde{\xi}_t$ and $\tilde{\mathbf{v}}_w(\mathbf{x}) = \tilde{\mathbf{v}}_{wn}(\mathbf{x}) \mathbf{n}(\mathbf{x}) + \tilde{\mathbf{v}}_{wt}(\mathbf{x})$, it can be shown that:

$$\int_{R^2, \tilde{\xi}_n > 0} \exp(-|\tilde{\xi}|^2) f_1 \tilde{\xi} \otimes \tilde{\xi} d\tilde{\xi} = \rho_{wl} \frac{\pi^{3/2}}{4} \mathbf{n} + \pi \tilde{\mathbf{v}}_{wn} \mathbf{n} + \frac{\pi}{2} \tilde{\mathbf{v}}_{wt} \quad (14)$$

Application

Let us now consider the out-of-plane rotational resonator presented in Figure 1 and produced by STMicroelectronics.

It is basically a plane structure (plane $\mathbf{e}_1-\mathbf{e}_2$) with uniform out-of-plane (along \mathbf{e}_3) thickness $t = 15 \mu\text{m}$. The gap with the substrate is $g = 1.8 \mu\text{m}$. The highly perforated central mass is attached to the substrate via a set of four flexible beams connect to the solid circle in the middle and it (almost) rigidly vibrates around the in plane axis \mathbf{e}_2 so that the whole structure can be approximated with a

one degree-of-freedom model in terms of the rotation angle θ , with $s = x_1 \theta(t) \mathbf{e}_3$. Hence, according to the notation introduced, $q(t) = \theta(t)$ and $\psi(\mathbf{x}) = x_1 \mathbf{e}_3$. The first resonating frequency of the MEMS is $f \approx 4000$ Hz.

As can be appreciated from the enlargement in Figure 1, all the holes are squares of constant size and are aligned along circles so as to have almost constant spacing all over the MEMS. Dissipation occurring in the comb-finger capacitors can be reasonably neglected. According to the assumptions of previous Sections, gas dissipation is proportional to $\dot{\theta}$ through $\mathbf{t}(\mathbf{x})$ and the governing equation is:

$$\rho t \ddot{\theta}(t) \int_S x_1^2 dS + \dot{\theta}(t) \int_{\partial V} x_1^2 t_3(\mathbf{x}) dS + K\theta(t) = T(t) \quad (15)$$

where S is the in-plane distribution of masses in the MEMS, $T(t)$ accounts for the sinusoidal electrostatic forcing and K for the elastic stiffness of the four central springs.

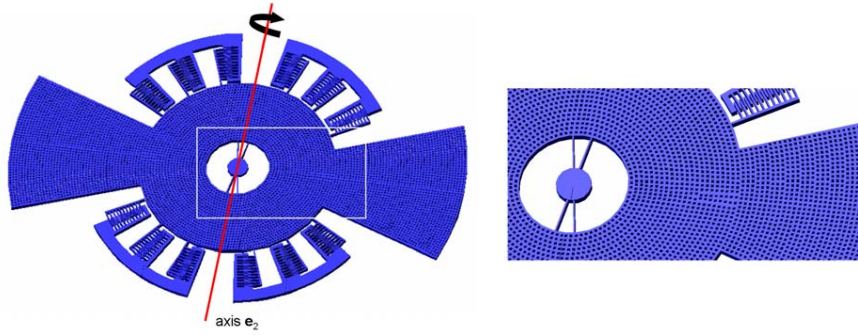


Figure 1: Out-of-plane rotational resonator: global layout and detail of the perforated mass.

If we make the realistic assumption that the MEMS is made by the assemblage of N identical units containing one hole each and having infinitesimal dimensions and that the cells near the axis \mathbf{e}_2 contribute negligibly to the damping forces, the integrals in eqn. (15) can be simplified with good accuracy as:

$$\rho t \int_S x_1^2 dS \cong M \left(\sum_i X_i^2 \right) := Mb \int_{\partial V} x_1^2 t_3(\mathbf{x}) dS \cong \int_{\partial V} t_3(\mathbf{x}) dS \left(\sum_i X_i^2 \right) = Cb$$

where M is the mass of the typical unit, ∂V the surface of the unit, X_i is the x_1 coordinate of its centre of mass, \mathbf{t}_3 is the out-of-plane damping force exerted on the surface of the unit due to a uniform unit velocity in the \mathbf{e}_3 direction and $b = \sum_i X_i^2$. The coefficient C represents the damping force exerted

by the fluid on the typical cell subject to symmetry conditions for the flow and to a unit velocity along \mathbf{e}_3 . Finally:

$$\ddot{\theta}(t) + 2\nu\omega_0 \dot{\theta}(t) + \omega_0^2 \theta(t) = \frac{T(t)}{Mb} \quad \text{with: } \omega_0 = \sqrt{\frac{K}{Mb}} \quad \frac{C}{M} = 2\nu\omega_0$$

The integral equation approach has been employed to compute C with a mesh of ~6000 elements and introducing small modifications in order to account for symmetry conditions. Once again the method converges in few seconds of CPU time.

Also in this case a comparison with the TPMC method has been performed, adopting the oscillation amplitude $A=0.2 \mu\text{m}$. The two approaches eventually converge to the same results, provided that the frequency adopted in the TPMC method is small enough so as to respect the most stringent quasi-static assumption $c_Q \ll 1$.

For this calculation the coefficients c_Q have been computed, rather arbitrarily, with a characteristic length $L=10 \mu\text{m}$. It is worth stressing that using the resonating frequency of the actual device one has $c_Q \approx 6 \cdot 10^{-4}$, $c_L \approx 10^{-5}$ so that both the quasi-static and the small perturbation assumptions are fully respected. However, applying the TPMC method with these conditions generates very high statistical noise and hence the results obtained with $c_Q=0.01$ are considered as a reliable estimate for the response in quasi-static conditions.

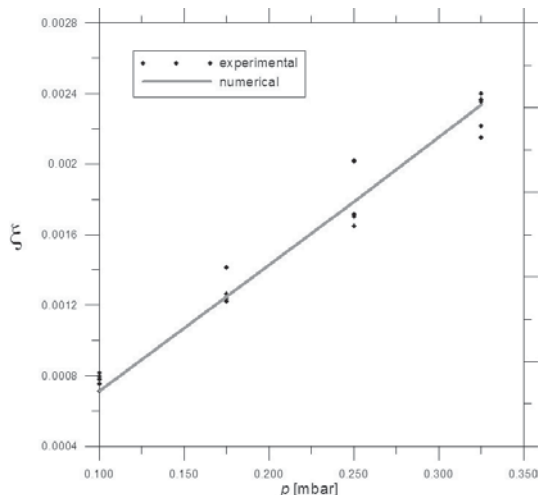


Figure 2: Damping coefficients: comparison of experiments and simulations.

Nevertheless, even in this case the CPU time required is at least 2 orders of magnitude larger than with the integral approach. Experimental tests were conducted by ST Microelectronics on several different resonators and the results are collected in Figure 2 showing surprisingly good agreement.

Acknowledgments

Financial support from MIUR and Fondazione Cariplo is gratefully acknowledged. The authors express their gratitude to Prof. Aldo Frezzotti for the invaluable suggestions and discussions. ST Microelectronics MEMS BU in Cornaredo (Italy) furnished the experimental data.

References

- [1] Frangi, A. *et al.* “On the evaluation of damping in MEMS in the slip-flow regime”, *Int. J. Num. Meth. Engng.*, 68, 1031–1051, 2006.
- [2] Chapman, S., Cowling, T.G., “The mathematical theory of non-uniform gases”, Cambridge University Press, 1960.
- [3] Cercignani, C., “The Boltzmann equation and its applications”, Springer, 1988
- [4] Bird, G.A., “Molecular gas dynamics and the direct simulation of gas flows”, Clarendon Press, 1994.
- [5] Ye, W., Wang, *et al.*, “Air damping in lateral oscillating micro-resonators: a numerical and experimental study”, *Journal of MEMS*, 12, 557–566, 2003.
- [6] Frangi, A., Di Gioia, A., “Multipole BEM for the evaluation of damping forces on MEMS”, *Computational Mechanics*, 37, 24–31, 2005.
- [7] Frangi, A., Tausch, J., “A qualocation enhanced approach for the Dirichlet problem of exterior Stokes flow”, *Engng. Analysis with Boundary Elem.*, 29, 886–893, 2005.
- [8] Frangi, A., “A fast multipole implementation of the qualocation mixed-velocity-traction approach for exterior Stokes flows”, *Engng. Analysis with Boundary Elem.*, 29, 1039–1046, 2005.
- [9] Yuhong, S., *et al.*, “Inverted velocity profiles in rarefied cylindrical Couette gas flow and the impact of the accommodation coefficient”, *Physics of Fluids*, 17, 047102–7, 2006.
- [10] Liu, Y.J., Shen, L., “A dual BIE approach for large-scale modelling of 3-D electrostatic problems with the fast multipole boundary element method”, *Int. J. Num. Meth. Engng.*, 71, 837–855, 2007.
- [11] Emerson, D.R., *et al.*, “Nonplanar oscillatory shear flow: from the continuum to the free-molecular regime”, *Physics of Fluids*, 19, 107–105, 2007.
- [12] Frangi, A., *et al.*, “On the application of the BGK kinetic model to the analysis of gas-structure interactions in MEMS”, *Computers & Structures*, 85, 810–817, 2007.
- [13] Bao, M., *et al.*, “Energy transfer model for squeeze-film air damping in low vacuum”, *J. Micromech. Microeng.*, 12, 341–346, 2002.
- [14] Hutcherson, S., Ye, W., “On the squeeze-film damping of micro-resonators in the free-molecule regime”, *J. Micromech. Microeng.*, 14, 1726–1733, 2004.

Laplace Domain Two Dimensional Fundamental Solutions to Dynamic Unsaturated Poroelasticity

Iman Ashayeri¹, Mohsen Kamalian², Mohammad Kazem Jafari³

¹Ph.D. Student, International Institute of Earthquake Engineering and Seismology (IIEES), Tehran, Iran,
P.O.Box: 19537-14453; i.ashayeri@iiees.ac.ir

²Ph.D., Assistant Professor, IIEES, Tehran, Iran, P.O.Box: 19537-14453; kamalian@iiees.ac.ir

³Ph.D., Professor, IIEES, Tehran, Iran, P.O.Box: 19537-14453; jafari@iiees.ac.ir

Keywords: Poroelastodynamics, Unsaturated Porous Media, Boundary Element Method, Fundamental Solutions.

Abstract. Governing differential equations of unsaturated porous media is provided by applying a macro mechanical approach in terms of solid displacement and fluids pressures in Laplace transform domain. In order to solve the problem of elastic wave propagation in unsaturated porous media by BEM, the Laplace transformed fundamental solutions are provided and are verified by obtaining well known solutions provided for classical elastodynamics and saturated poroelastodynamics by vanishing the appropriate coefficients.

Introduction

Dynamics of saturated poroelastic media have received attentions of several investigators from the mid twentieth century, but problems concerning unsaturated soils necessitate the theoretical developments for mechanics of unsaturated media. Unsaturated Poromechanics expresses the unsaturated porous medium as the superposition of different continuum phases in time and space. In this approach, all constituents are considered continuous media, which are overlapped in a macroscopic volume, known as Representative Elementary Volume (REV), and the continua are porous skeleton and at least two immiscible fluids, saturating the pore space.

On the other hand, one of the most common problems in Geotechnical earthquake engineering is the problem of seismic wave propagation from the seismic source to the structure's foundation, and soil-structure interaction (SSI). The well known boundary element method (BEM) is a very effective boundary type numerical method for dynamic analysis of linear elastic bounded and unbounded media. The BEM encompasses the governing boundary integral equation and the corresponding fundamental solutions. Several investigators presented fundamental solutions to dynamic poroelastic problems of saturated media in transformed and time domains. Bonnet [1] presented fundamental solutions in frequency domain for the set of unknowns of solid particle displacement and fluid pressure. He mentioned the analogy between poroelasticity and thermoelasticity for $u-p$ formulation in frequency domain. However, there is some confusing regarding the sign of the time variation assumed for harmonic variables in Bonnet's paper that is corrected and represented by Dominguez [2,3]. For the set of unknowns of solid and fluid particles displacements Manolis and Beskos [4,5] presented fundamental solutions in Laplace transformed domain. Laplace domain fundamental solutions of full dynamic saturated poroelasticity were provided about fifteen years ago by Chen [6,7]. He also provided closed form approximate time domain fundamental solutions that are in good agreement with the result of numerical inversion of Laplace domain solutions. Afterward, Gatmiri and Kamalian [8] pointed out the time domain fundamental solutions presented by Chen are too complex to be applied in BEM. They suggested simplified set of governing equations by omitting fluid acceleration terms and presented Laplace domain as well as time domain fundamental solutions. Based on the same governing equations, more simplified fundamental solutions presented by Gatmiri and Nguyen [9] by considering incompressibility of constituents. Schanz and Pryl [10] also simplified Chen's fundamental solutions and presented Laplace domain solutions with incompressible constituents.

However, recently the fundamental solutions of quasi static unsaturated poroelastic media with incompressible constituents were presented by Gatmiri and Jabbari [11,12] in Laplace and time domains, the fundamental solutions for dynamic unsaturated poroelasticity have not been presented yet in transformed or time domains. The aim of this paper is to provide two dimensional fundamental solutions of dynamic unsaturated poroelasticity based on the poromechanics theory in Laplace transformed domain. In this work the skeleton is defined by incompressible solid matrix and the pore space. The compressible fluids are assumed chemically inert liquid and gas like water and air in soil. The governing differential equations and constitutive relations of the media are derived by the assumption of isothermal infinitesimal evolution considering the second thermodynamics' law [13,14]. Full dynamic Laplace transformed domain governing

equations are well established in terms of four variables in 2D (five in 3D) of skeleton displacement field and the liquid and gas pressures.

Governing Differential Equations and Constitutive Relations

Governing differential equations consist of mass balance of liquid and gaseous phases, momentum balance of whole mixture and mass conduction laws for liquid and gaseous phases. Due to the assumptions of infinitesimal transformation and incompressibility of solid matrix the mass balance equations yield:

Liquid mass balance

$$\frac{(1+\varepsilon)\phi^{lq}}{D^{lq}} \dot{p}^{lq} + (1+\varepsilon)\dot{\phi}^{lq} + \phi^{lq}\dot{u}_{i,i} + q_{i,i}^{lq} = \gamma^{lq} \quad (1)$$

Gas mass balance

$$\frac{(1+\varepsilon)(\phi^g)}{D^g} \dot{p}^g - (1+\varepsilon)\dot{\phi}^g + (1-\phi^{lq})\dot{u}_{i,i} + q_{i,i}^g = \gamma^g \quad (2)$$

where $\phi_{\alpha=lq,g}^\alpha$ is the fluid phase volume fraction; ε is the skeleton volume dilatation or volumetric strain that is constant in the time step; $p_{\alpha=lq,g}^\alpha$ is the liquid or gas pressure; $D_{\alpha=lq,g}^\alpha$ is the bulk modulus of the fluid phase; u_i is the displacement vector of the skeleton particle; $q_{\alpha=lq,g}^\alpha$ is the liquid or gas flux vector and $\gamma_{\alpha=lq,g}^\alpha$ is the rate of liquid or gas injection to the medium.

The momentum balance for the whole mixture reads

$$\sigma_{ij,j} + f_i - \rho \ddot{u}_i - \rho^{lq} \phi^{lq} \ddot{v}_i - \rho^g \phi^g \ddot{w}_i = 0 \quad (3)$$

where $\rho = \rho^m(1-\phi) + (\rho^\alpha \phi^\alpha)_{\alpha=lq,g}$ is the apparent mass density of the whole medium; $\rho_{\alpha=m,lq,g}^\alpha$ is the intrinsic mass density of the solid matrix, liquid or gas; $\phi = \sum_{\alpha=lq,g} \phi^\alpha$ is the total porosity; f_i is the body force

density per volume unit; v_i, w_i are the relative displacement vectors of the liquid and gas particles with respect to the skeleton particle.

The mass conduction laws or generalized Darcy laws for liquid and gaseous phases yield;

$$q^{lq} = \phi^{lq} \dot{v}_i = k^{lq} (-p_j^{lq} - \rho^{lq} \ddot{u}_i - \rho^{lq} \ddot{v}_i) \quad (4)$$

$$q^g = \phi^g \dot{w}_i = k^g (-p_j^g - \rho^g \ddot{u}_i - \rho^g \ddot{w}_i) \quad (5)$$

where $k_{\alpha=lq,g}^\alpha$ is the isotropic permeability coefficient of the liquid or gaseous phase.

Two constitutive relations are required to express the skeleton deformation and liquid phase volume change in an unsaturated porous media that is formed by compressible fluids and incompressible solid matrix. Assumption of isotropic linear elastic behaviour for the skeleton yields

$$\sigma_{ij} + p^g \delta_{ij} = \lambda \varepsilon_{kk} \delta_{ij} + 2\mu \varepsilon_{ij} + b^{lq} p_c \delta_{ij} \quad (6)$$

where λ, μ are drained Lame coefficients; $p_c = p^g - p^{lq}$ is the capillary pressure and; δ_{ij} is the Kronecker delta and b^{lq} is the Biot's coefficient for liquid phase.

The next relation is the capillary pressure constitutive relation as follows:

$$c^{lq} \dot{p}_c + (b^{lq} - \phi^{lq}) \dot{u}_{i,i} = (1+\varepsilon) \dot{\phi}^{lq} \quad (7)$$

where $c^{lq} = (1+\varepsilon) \phi^{lq} / D^{lq} - N$ is material properties coefficient, with N being the modulus linking liquid pressure change to the liquid mass content of the element.

Substituting eq(7) into eq(1) and eq(2) results the final relations for liquid and gas mass balance as follows:

$$c^{lq} \dot{p}^g + N \dot{p}^{lq} + b^{lq} \dot{u}_{i,i} + \phi^{lq} \dot{v}_{i,i} = \gamma^{lq} \quad (8)$$

$$(c^g - c^{lq}) \dot{p}^g + c^{lq} \dot{p}^{lq} + (1 - b^{lq}) \dot{u}_{i,i} + \phi^g \dot{w}_{i,i} = \gamma^g \quad (9)$$

with $c^g = (1+\varepsilon) \phi^g / D^g$. Equations (3), (4), (5), (8) and (9) are the five governing equations of the medium.

Laplace Domain Governing Equations

The Laplace transformation usually is used to solve mixed partial differential equations. Therefore, the Laplace transforms of eqs (3), (4), (5), (8) and (9), with the assumption of zero initial condition, yield:

momentum balance

$$\tilde{\sigma}_{ij,j} + \tilde{f}_i - \rho s^2 \tilde{u}_i - \rho^{lq} \phi^{lq} s^2 \tilde{v}_i - \rho^g \phi^g s^2 \tilde{w}_i = 0 \quad (10)$$

mass conduction (Darcy's law) of liquid and gaseous phases

$$\tilde{v}_i = (-\tilde{p}_j^{lq} - \rho^{lq} s^2 \tilde{u}_i) \eta^{lq} / s \quad (11)$$

$$\tilde{w}_i = (-\tilde{p}_j^g - \rho^g s^2 \tilde{u}_i) \eta^g / s \quad (12)$$

introducing the coefficients $\eta^{lq/l} = \phi^{lq} / k^{lq} + \rho^{lq} s$ and $\eta^{g/l} = \phi^g / k^g + \rho^g s$;

mass balance (liquid and gas)

$$c^{lq} s \tilde{p}^g + N s \tilde{p}^{lq} + b^{lq} s \tilde{u}_{i,i} + \phi^{lq} s \tilde{v}_{i,i} = \tilde{\gamma}^{lq} \quad (13)$$

$$(c^g - c^{lq}) s \tilde{p}^g + c^{lq} s \tilde{p}^{lq} + (1 - b^{lq}) s \tilde{u}_{i,i} + \phi^g s \tilde{w}_{i,i} = \tilde{\gamma}^g \quad (14)$$

where the tilde bar indicates the Laplace transformed quantity. The divergence can now be taken from mass conduction, eqs (11) and (12) and substituted into mass balance eqs (13) and (14), respectively. Hence:

$$\phi^{lq} \eta^{lq} \tilde{p}_{ii}^{lq} - c^{lq} s \tilde{p}^g - N s \tilde{p}^{lq} - (b^{lq} - \rho^{lq} \phi^{lq} \eta^{lq} s) s \tilde{u}_{i,i} + \tilde{\gamma}^{lq} = 0 \quad (15)$$

$$\phi^g \eta^g \tilde{p}_{ii}^g - (c^g - c^{lq}) s \tilde{p}^g - c^{lq} s \tilde{p}^{lq} - (1 - b^{lq} - \rho^g \phi^g \eta^g s) s \tilde{u}_{i,i} + \tilde{\gamma}^g = 0 \quad (16)$$

Also, \tilde{v}, \tilde{w} can be eliminated from eqs (10), (11) and (12), resulting in:

$$\tilde{\sigma}_{ij,j} - (\rho - \rho^{lq} \rho_{lq} \eta^{lq} s - \rho^g \rho_g \eta^g s) s^2 \tilde{u}_i + \rho_{lq} \eta^{lq} s \tilde{p}_j^{lq} + \rho_g \eta^g s \tilde{p}_j^g + \tilde{f}_i = 0 \quad (17)$$

where $\rho_\alpha = \rho^\alpha \phi^\alpha$ is the apparent mass density of fluid phase α . Substituting Laplace transform of constitutive relation eq (6) into eq (17) final set of governing equations in transformed domain yields

$$(\lambda + \mu) \tilde{u}_{j,ji} + \mu \tilde{u}_{i,ji} - \bar{\rho} s^2 \tilde{u}_i - \bar{b}^{lq} \tilde{p}_i^{lq} - \bar{b}^g \tilde{p}_i^g + \tilde{f}_i = 0 \quad (18)$$

$$\bar{\eta}^{lq} \tilde{p}_{ii}^{lq} - N s \tilde{p}^{lq} - c^{lq} s \tilde{p}^g - \bar{b}^{lq} s \tilde{u}_{i,i} + \tilde{\gamma}^{lq} = 0 \quad (19)$$

$$\bar{\eta}^g \tilde{p}_{ii}^g - c^{lq} s \tilde{p}^{lq} - \bar{c}^g s \tilde{p}^g - \bar{b}^g s \tilde{u}_{i,i} + \tilde{\gamma}^g = 0 \quad (20)$$

where

$$\bar{\rho} = \rho - \rho^{lq} \rho_{lq} \eta^{lq} s - \rho^g \rho_g \eta^g s, \bar{b}^{lq} = b^{lq} - \rho_{lq} \eta^{lq} s, \bar{b}^g = 1 - b^{lq} - \rho_g \eta^g s, \bar{\eta}^{lq} = \phi^{lq} \eta^{lq}, \bar{\eta}^g = \phi^g \eta^g,$$

$$\bar{c}^g = c^g - c^{lq}$$

Using these substitutions, eqs (18) to (20) provide governing equations in transformed domain which are expressed by only five (four in 2D) unknowns. These unknowns are the three u_i components (two in 2D), p^{lq} and p^g .

Laplace Domain Fundamental Solutions

Set of eqs (18) to (20) are arranged into matrix product form as follows:

$$B \tilde{U} + \tilde{F} = 0 \quad (21)$$

where $B(\partial x, s) = B_{mn}(\partial x, s)|_{4x4}$ is the differential operator matrix for two dimensional problem $i, j = 1, 2$ and \tilde{U} and \tilde{F} are defined as

$$\tilde{U} = \begin{bmatrix} \tilde{u}_i \\ \tilde{p}^{lq} \\ \tilde{p}^g \end{bmatrix}_{4x1}, \tilde{F} = \begin{bmatrix} \tilde{f}_i \\ \tilde{\gamma}^{lq} \\ \tilde{\gamma}^g \end{bmatrix}_{4x1} \quad (22)$$

Fundamental solutions are the response of the medium to point excitations which is a Dirac delta function in space i.e. $\delta(x_i)$, and either a Dirac delta function or a Heaviside step function in time i.e. $H(t)$. However, regarding its future applications in BEM, the solutions which results from Heaviside step function is considered. Therefore, for a continuous line force in i -th direction suddenly applied at origin i.e. $f_i(x, t) = \delta(x)H(t)$, and a unit rate of liquid line injection at the origin i.e. $\gamma^{lq}(x, t) = \delta(x)H(t)$, and a unit rate of gas line injection at the origin i.e. $\gamma^g(x, t) = \delta(x)H(t)$, the Laplace transform of which is $1/s\delta(x)$. Then the problem is to find the fundamental solution matrix $\tilde{G}|_{4x4}$, which satisfies

$$B\tilde{G} + I\delta(x)/s = 0 \quad (23)$$

where I is the unit matrix. Following the Hormander's method [15] or Kupradze method [16] the solution of eq (23) is found through the calculating cofactor matrix of B that is \bar{B} as follows

$$B\bar{B}^T = \det(B)I \quad (24)$$

Now consider φ is the scalar function which satisfies

$$[\det(B)I]\varphi + \frac{1}{s}I\delta(x) = 0 \quad (25)$$

Substituting eq (25) into eq (26) gives

$$B\bar{B}^T\varphi + \frac{1}{s}I\delta(x) = 0 \quad (26)$$

Comparing eq (27) with eq (23) yields

$$\tilde{G} = \bar{B}^T\varphi \quad (27)$$

Equation (27) enables us to determine the sixteen components of $\tilde{G}_{mn}|_{4x4}$ by applying the transpose of cofactor of differential operator matrix to the single unknown function φ . Computing the determinant of differential operator matrix yields

$$\det(B) = \mu(\lambda + 2\mu)\bar{\eta}^{lq}\bar{\eta}^g(\nabla^2 - \hat{\lambda}_4^2)(\nabla^2 - \hat{\lambda}_3^2)(\nabla^2 - \hat{\lambda}_2^2)(\nabla^2 - \hat{\lambda}_1^2) \quad (28)$$

Equation (28) is a polynomial of order four of ∇^2 , which one of its roots is the $\hat{\lambda}_4^2 = \bar{\rho}s^2/\mu$ that is related to the shear wave velocity propagating through the medium. The remaining part of eq (28) is a polynomial of order three of ∇^2 , which have three roots as $\hat{\lambda}_1^2, \hat{\lambda}_2^2, \hat{\lambda}_3^2$. Substituting eq (28) into eq (25) yields

$$\mu(\lambda + 2\mu)\bar{\eta}^{lq}\bar{\eta}^g(\nabla^2 - \hat{\lambda}_4^2)(\nabla^2 - \hat{\lambda}_3^2)(\nabla^2 - \hat{\lambda}_2^2)(\nabla^2 - \hat{\lambda}_1^2)s\varphi + \delta(x) = 0 \quad (29)$$

Following Kupradze method, define the function $\Phi = \mu(\lambda + 2\mu)\bar{\eta}^{lq}\bar{\eta}^g s\varphi$ and rewrite eq (29)

$$(\nabla^2 - \hat{\lambda}_4^2)(\nabla^2 - \hat{\lambda}_3^2)(\nabla^2 - \hat{\lambda}_2^2)(\nabla^2 - \hat{\lambda}_1^2)\Phi + \delta(x) = 0 \quad (31)$$

Now to solve eq (31), we assume

$$\varphi_1 = (\nabla^2 - \hat{\lambda}_4^2)(\nabla^2 - \hat{\lambda}_3^2)(\nabla^2 - \hat{\lambda}_2^2)\Phi \quad (32-1)$$

$$\varphi_2 = (\nabla^2 - \hat{\lambda}_4^2)(\nabla^2 - \hat{\lambda}_3^2)(\nabla^2 - \hat{\lambda}_1^2)\Phi \quad (32-2)$$

$$\varphi_3 = (\nabla^2 - \hat{\lambda}_4^2)(\nabla^2 - \hat{\lambda}_2^2)(\nabla^2 - \hat{\lambda}_1^2)\Phi \quad (32-3)$$

$$\varphi_4 = (\nabla^2 - \hat{\lambda}_3^2)(\nabla^2 - \hat{\lambda}_2^2)(\nabla^2 - \hat{\lambda}_1^2)\Phi \quad (32-4)$$

Substituting eqs (32-1 to 4) into eq (31) yields

$$(\nabla^2 - \hat{\lambda}_i^2)\varphi_i = -\delta(x)|_{i=1,2,3,4} \quad (33)$$

Equation (33) is the Helmholtz equation, which its solutions in two dimensions are expressed by modified Bessel function of zero order.

$$\varphi_i = \frac{1}{2\pi} K_0(\lambda_i r) \quad (34)$$

where $r = x_i x_i$. After some algebra one can find

$$\varphi = \frac{1}{2\pi\mu(\lambda + 2\mu)\bar{\eta}^{lq}\bar{\eta}^g s(\hat{\lambda}_3^2 - \hat{\lambda}_4^2)(\hat{\lambda}_2^2 - \hat{\lambda}_1^2)} \left\{ \frac{\varphi_3 - \varphi_2}{(\hat{\lambda}_3^2 - \hat{\lambda}_2^2)} - \frac{\varphi_3 - \varphi_1}{(\hat{\lambda}_3^2 - \hat{\lambda}_1^2)} + \frac{\varphi_4 - \varphi_1}{(\hat{\lambda}_4^2 - \hat{\lambda}_1^2)} - \frac{\varphi_4 - \varphi_2}{(\hat{\lambda}_4^2 - \hat{\lambda}_2^2)} \right\} \quad (35)$$

According to eq (27) applying the differential operator \bar{B}^T to $\varphi(r, s)$ the fundamental solution matrix in two dimensional case results as

$$\begin{aligned} \tilde{G}_{44} &= \frac{1}{2\pi(\hat{\lambda}_3^2 - \hat{\lambda}_2^2)(\hat{\lambda}_3^2 - \hat{\lambda}_1^2)s\bar{\eta}^g} \{(\hat{\lambda}_3^2 - \Pi_{lq}^2)(\hat{\lambda}_3^2 - A^2) - \frac{\bar{b}^{lq^2}s\hat{\lambda}_3^2}{(\lambda + 2\mu)\bar{\eta}^{lq}}\}K_0(\hat{\lambda}_3 r) - \\ &\quad \frac{1}{2\pi(\hat{\lambda}_2^2 - \hat{\lambda}_1^2)(\hat{\lambda}_3^2 - \hat{\lambda}_2^2)s\bar{\eta}^g} \{(\hat{\lambda}_2^2 - \Pi_{lq}^2)(\hat{\lambda}_2^2 - A^2) - \frac{\bar{b}^{lq^2}s\hat{\lambda}_2^2}{(\lambda + 2\mu)\bar{\eta}^{lq}}\}K_0(\hat{\lambda}_2 r) + \\ &\quad \frac{1}{2\pi(\hat{\lambda}_2^2 - \hat{\lambda}_1^2)(\hat{\lambda}_3^2 - \hat{\lambda}_1^2)s\bar{\eta}^g} \{(\hat{\lambda}_1^2 - \Pi_{lq}^2)(\hat{\lambda}_1^2 - A^2) - \frac{\bar{b}^{lq^2}s\hat{\lambda}_1^2}{(\lambda + 2\mu)\bar{\eta}^{lq}}\}K_0(\hat{\lambda}_1 r) \end{aligned} \quad (36-1)$$

$$\begin{aligned} \tilde{G}_{33} = & \frac{1}{2\pi(\hat{\lambda}_3^2 - \hat{\lambda}_2^2)(\hat{\lambda}_3^2 - \hat{\lambda}_1^2)s\bar{\eta}^q} \{(\hat{\lambda}_3^2 - \Pi_g^2)(\hat{\lambda}_3^2 - \Lambda^2) - \frac{\bar{b}^{g^2}s\hat{\lambda}_3^2}{(\lambda + 2\mu)\bar{\eta}^g}\} K_0(\hat{\lambda}_3 r) - \\ & \frac{1}{2\pi(\hat{\lambda}_2^2 - \hat{\lambda}_1^2)(\hat{\lambda}_3^2 - \hat{\lambda}_1^2)s\bar{\eta}^q} \{(\hat{\lambda}_2^2 - \Pi_g^2)(\hat{\lambda}_2^2 - \Lambda^2) - \frac{\bar{b}^{g^2}s\hat{\lambda}_2^2}{(\lambda + 2\mu)\bar{\eta}^g}\} K_0(\hat{\lambda}_2 r) + \end{aligned} \quad (36-2)$$

$$\begin{aligned} \tilde{G}_{43} = \tilde{G}_{34} = & \frac{1}{2\pi(\lambda + 2\mu)\bar{\eta}^q\bar{\eta}^g s} \left[\frac{((\lambda + 2\mu)c^{lq} + \bar{b}^{lq}\bar{b}^g)s\hat{\lambda}_3^2 - c^{lq}\bar{\rho}s^3}{(\hat{\lambda}_3^2 - \hat{\lambda}_1^2)(\hat{\lambda}_3^2 - \hat{\lambda}_1^2)} K_0(\hat{\lambda}_3 r) \right. \\ & \left. - \frac{((\lambda + 2\mu)c^{lq} + \bar{b}^{lq}\bar{b}^g)s\hat{\lambda}_2^2 - c^{lq}\bar{\rho}s^3}{(\hat{\lambda}_2^2 - \hat{\lambda}_1^2)(\hat{\lambda}_3^2 - \hat{\lambda}_1^2)} K_0(\hat{\lambda}_2 r) + \frac{((\lambda + 2\mu)c^{lq} + \bar{b}^{lq}\bar{b}^g)s\hat{\lambda}_1^2 - c^{lq}\bar{\rho}s^3}{(\hat{\lambda}_3^2 - \hat{\lambda}_1^2)(\hat{\lambda}_2^2 - \hat{\lambda}_1^2)} K_0(\hat{\lambda}_1 r) \right] \end{aligned} \quad (36-3)$$

$$\begin{aligned} \tilde{G}_{4i|j=i,2} = & \frac{1}{2\pi(\lambda + 2\mu)\bar{\eta}^g} \left[\frac{-1}{(\hat{\lambda}_3^2 - \hat{\lambda}_2^2)(\hat{\lambda}_3^2 - \hat{\lambda}_1^2)} (\hat{\lambda}_3^2 - \frac{(\bar{b}^g N - \bar{b}^{lq}c^{lq})s}{\bar{b}^g\bar{\eta}^{lq}}) \frac{\hat{\lambda}_3 x_i}{r} K_i(\hat{\lambda}_3 r) + \right. \\ & \left. \frac{1}{(\hat{\lambda}_2^2 - \hat{\lambda}_1^2)(\hat{\lambda}_3^2 - \hat{\lambda}_1^2)} (\hat{\lambda}_2^2 - \frac{(\bar{b}^g N - \bar{b}^{lq}c^{lq})s}{\bar{b}^g\bar{\eta}^{lq}}) \frac{\hat{\lambda}_2 x_i}{r} K_i(\hat{\lambda}_2 r) + \right. \\ & \left. \frac{-1}{(\hat{\lambda}_2^2 - \hat{\lambda}_1^2)(\hat{\lambda}_3^2 - \hat{\lambda}_1^2)} (\hat{\lambda}_1^2 - \frac{(\bar{b}^g N - \bar{b}^{lq}c^{lq})s}{\bar{b}^g\bar{\eta}^{lq}}) \frac{\hat{\lambda}_1 x_i}{r} K_i(\hat{\lambda}_1 r) \right] \end{aligned} \quad (36-4)$$

$$\begin{aligned} \tilde{G}_{3i|j=i,2} = & \frac{1}{2\pi(\lambda + 2\mu)\bar{\eta}^{lq}} \left[\frac{-1}{(\hat{\lambda}_3^2 - \hat{\lambda}_2^2)(\hat{\lambda}_3^2 - \hat{\lambda}_1^2)} (\hat{\lambda}_3^2 - \frac{(\bar{b}^{lq}\bar{c}^g - \bar{b}^g c^{lq})s}{\bar{b}^{lq}\bar{\eta}^g}) \frac{\hat{\lambda}_3 x_i}{r} K_i(\hat{\lambda}_3 r) + \right. \\ & \left. \frac{1}{(\hat{\lambda}_2^2 - \hat{\lambda}_1^2)(\hat{\lambda}_3^2 - \hat{\lambda}_1^2)} (\hat{\lambda}_2^2 - \frac{(\bar{b}^{lq}\bar{c}^g - \bar{b}^g c^{lq})s}{\bar{b}^{lq}\bar{\eta}^g}) \frac{\hat{\lambda}_2 x_i}{r} K_i(\hat{\lambda}_2 r) + \right. \\ & \left. \frac{-1}{(\hat{\lambda}_2^2 - \hat{\lambda}_1^2)(\hat{\lambda}_3^2 - \hat{\lambda}_1^2)} (\hat{\lambda}_1^2 - \frac{(\bar{b}^{lq}\bar{c}^g - \bar{b}^g c^{lq})s}{\bar{b}^{lq}\bar{\eta}^g}) \frac{\hat{\lambda}_1 x_i}{r} K_i(\hat{\lambda}_1 r) \right] \end{aligned} \quad (36-5)$$

$$\begin{aligned} \tilde{G}_{j4|j=i,2} = & \frac{1}{s} \tilde{G}_{4i|j=i,2}, \quad \tilde{G}_{j3|j=i,2} = \frac{1}{s} \tilde{G}_{3i|j=i,2} \end{aligned} \quad (36-6)$$

$$\begin{aligned} \tilde{G}_{ij} = & \frac{1}{2\pi\mu s} \left[\frac{-1}{(\hat{\lambda}_3^2 - \hat{\lambda}_2^2)(\hat{\lambda}_4^2 - \hat{\lambda}_1^2)(\hat{\lambda}_4^2 - \hat{\lambda}_2^2)} \right. \\ & \left\{ \left(\frac{c^{lq^2}s^2}{\bar{\eta}^{lq}\bar{\eta}^g} - (\hat{\lambda}_4^2 - \Pi_g^2)(\hat{\lambda}_4^2 - \Pi_{lq}^2) \right) \left[\left(\frac{(\lambda + \mu)\Lambda^2}{\bar{\rho}s^2} \right) (\hat{\lambda}_4 A_{ij} K_i(\hat{\lambda}_4 r) + \hat{\lambda}_4^2 B_{ij} K_0(\hat{\lambda}_4 r)) + \delta_{ij}(\Lambda^2 - \hat{\lambda}_4^2) K_0(\hat{\lambda}_4 r) \right] \right. \\ & + \frac{(\bar{\eta}^g \bar{b}^{lq^2} + 2c^{lq}\bar{b}^{lq}\bar{b}^g + \bar{\eta}^{lq}\bar{b}^{k^2})s\hat{\lambda}_4^2 - (\bar{b}^{lq^2}\bar{c}^g + \bar{b}^{k^2}N)s^2}{(\lambda + 2\mu)\bar{\eta}^{lq}\bar{\eta}^g} \{ \hat{\lambda}_4 A_{ij} K_i(\hat{\lambda}_4 r) + \hat{\lambda}_4^2 B_{ij} K_0(\hat{\lambda}_4 r) - \delta_{ij}\hat{\lambda}_4^2 K_0(\hat{\lambda}_4 r) \} \\ & + \frac{1}{(\hat{\lambda}_4^2 - \hat{\lambda}_2^2)(\hat{\lambda}_3^2 - \hat{\lambda}_2^2)(\hat{\lambda}_4^2 - \hat{\lambda}_1^2)} \\ & \left\{ \left(\frac{c^{lq^2}s^2}{\bar{\eta}^{lq}\bar{\eta}^g} - (\hat{\lambda}_3^2 - \Pi_g^2)(\hat{\lambda}_3^2 - \Pi_{lq}^2) \right) \left[\left(\frac{(\lambda + \mu)\Lambda^2}{\bar{\rho}s^2} \right) (\hat{\lambda}_3 A_{ij} K_i(\hat{\lambda}_3 r) + \hat{\lambda}_3^2 B_{ij} K_0(\hat{\lambda}_3 r)) + \delta_{ij}(\Lambda^2 - \hat{\lambda}_3^2) K_0(\hat{\lambda}_3 r) \right] \right. \\ & + \frac{(\bar{\eta}^g \bar{b}^{lq^2} + 2c^{lq}\bar{b}^{lq}\bar{b}^g + \bar{\eta}^{lq}\bar{b}^{k^2})s\hat{\lambda}_3^2 - (\bar{b}^{lq^2}\bar{c}^g + \bar{b}^{k^2}N)s^2}{(\lambda + 2\mu)\bar{\eta}^{lq}\bar{\eta}^g} \{ \hat{\lambda}_3 A_{ij} K_i(\hat{\lambda}_3 r) + \hat{\lambda}_3^2 B_{ij} K_0(\hat{\lambda}_3 r) - \delta_{ij}\hat{\lambda}_3^2 K_0(\hat{\lambda}_3 r) \} \\ & + \frac{1}{(\hat{\lambda}_2^2 - \hat{\lambda}_1^2)(\hat{\lambda}_3^2 - \hat{\lambda}_1^2)(\hat{\lambda}_4^2 - \hat{\lambda}_1^2)} \\ & \left\{ \left(\frac{c^{lq^2}s^2}{\bar{\eta}^{lq}\bar{\eta}^g} - (\hat{\lambda}_2^2 - \Pi_g^2)(\hat{\lambda}_2^2 - \Pi_{lq}^2) \right) \left[\left(\frac{(\lambda + \mu)\Lambda^2}{\bar{\rho}s^2} \right) (\hat{\lambda}_2 A_{ij} K_i(\hat{\lambda}_2 r) + \hat{\lambda}_2^2 B_{ij} K_0(\hat{\lambda}_2 r)) + \delta_{ij}(\Lambda^2 - \hat{\lambda}_2^2) K_0(\hat{\lambda}_2 r) \right] \right. \\ & + \frac{(\bar{\eta}^g \bar{b}^{lq^2} + 2c^{lq}\bar{b}^{lq}\bar{b}^g + \bar{\eta}^{lq}\bar{b}^{k^2})s\hat{\lambda}_2^2 - (\bar{b}^{lq^2}\bar{c}^g + \bar{b}^{k^2}N)s^2}{(\lambda + 2\mu)\bar{\eta}^{lq}\bar{\eta}^g} \{ \hat{\lambda}_2 A_{ij} K_i(\hat{\lambda}_2 r) + \hat{\lambda}_2^2 B_{ij} K_0(\hat{\lambda}_2 r) - \delta_{ij}\hat{\lambda}_2^2 K_0(\hat{\lambda}_2 r) \} \\ & + \frac{-1}{(\hat{\lambda}_2^2 - \hat{\lambda}_1^2)(\hat{\lambda}_3^2 - \hat{\lambda}_1^2)(\hat{\lambda}_4^2 - \hat{\lambda}_1^2)} \\ & \left\{ \left(\frac{c^{lq^2}s^2}{\bar{\eta}^{lq}\bar{\eta}^g} - (\hat{\lambda}_1^2 - \Pi_g^2)(\hat{\lambda}_1^2 - \Pi_{lq}^2) \right) \left[\left(\frac{(\lambda + \mu)\Lambda^2}{\bar{\rho}s^2} \right) (\hat{\lambda}_1 A_{ij} K_i(\hat{\lambda}_1 r) + \hat{\lambda}_1^2 B_{ij} K_0(\hat{\lambda}_1 r)) + \delta_{ij}(\Lambda^2 - \hat{\lambda}_1^2) K_0(\hat{\lambda}_1 r) \right] \right. \\ & + \frac{(\bar{\eta}^g \bar{b}^{lq^2} + 2c^{lq}\bar{b}^{lq}\bar{b}^g + \bar{\eta}^{lq}\bar{b}^{k^2})s\hat{\lambda}_1^2 - (\bar{b}^{lq^2}\bar{c}^g + \bar{b}^{k^2}N)s^2}{(\lambda + 2\mu)\bar{\eta}^{lq}\bar{\eta}^g} \{ \hat{\lambda}_1 A_{ij} K_i(\hat{\lambda}_1 r) + \hat{\lambda}_1^2 B_{ij} K_0(\hat{\lambda}_1 r) - \delta_{ij}\hat{\lambda}_1^2 K_0(\hat{\lambda}_1 r) \} \end{aligned} \quad (36-7)$$

$$\text{where } A_{ij} = \frac{2x_i x_j}{r^3} - \frac{\delta_{ij}}{r}, B_{ij} = \frac{x_i x_j}{r^2}, \Pi_{lq}^2 = \frac{Ns}{\bar{\eta}^{lq}}, \Pi_g^2 = \frac{\bar{c}^g s}{\bar{\eta}^g}$$

Thus, fundamental solutions are presented through eqs (36-1) to (36-7) respect to roots of eq (28).

Verification of the Solutions

In order to verify the validity of the solutions, two limiting cases are presented here. First, the case of elastodynamics is investigated by letting $k_{\alpha=lq,g}^\alpha$ approach infinity and the fluids intrinsic densities $\rho_{\alpha=lq,g}^\alpha$ approaches to zero. Then the solutions of saturated poroelastodynamics as proposed by [6,7] are investigated.

Limiting Case 1: Elastodynamics. Letting permeability coefficients $k_{\alpha=lq,g}^\alpha$ approach infinity and the fluids intrinsic densities $\rho_{\alpha=lq,g}^\alpha$ approach to zero equations (36) should approaches to the elastodynamics line load solution. Hence,

$$\frac{1}{\bar{\eta}^\alpha} = \bar{b}^\alpha \Big|_{\alpha=lq,g} = 0, \bar{\rho} = \rho = \rho^m(1-\phi), \mathcal{A}_i^2 = \Lambda^2 = \frac{\rho s^2}{(\lambda + 2\mu)}, \mathcal{A}_2^2 = \mathcal{A}_3^2 = 0, \mathcal{A}_4^2 = \frac{\rho s^2}{\mu} \quad (37)$$

Then using $K_0(\mathcal{A}_i r) + 2K_1(\mathcal{A}_i r)/(\mathcal{A}_i r) = K_2(\mathcal{A}_i r)$ the two dimensional solutions yield

$$\tilde{G}_{ij} = \frac{1}{2\pi\mu s} \left[\frac{x_i x_j}{r^2} d + \delta_{ij} c \right] \quad (38)$$

$$c = \frac{1}{\mathcal{A}_4 r} K_1(\mathcal{A}_4 r) + K_0(\mathcal{A}_4 r) - \frac{\mathcal{A}_4^2}{\mathcal{A}_4^2 - \mathcal{A}_i^2} \frac{1}{\mathcal{A}_i r} K_1(\mathcal{A}_i r), d = \left(\frac{\mathcal{A}_i^2}{\mathcal{A}_4^2} K_2(\mathcal{A}_i r) - K_2(\mathcal{A}_4 r) \right)$$

$$\tilde{G}_{i3} = \tilde{G}_{i4} = \tilde{G}_{3\beta} = \tilde{G}_{4\beta} \Big|_{i=1,2, \beta=1,2,3,4} = 0 \quad (39)$$

Limiting Case 2: Saturated Poroelastodynamics. Letting the permeability coefficient of gaseous phase approaches infinity and intrinsic density and volume fraction of this phase approach zero. Thus

$$\bar{\eta}^{g^{-1}} = 0, \bar{b}^g = 0, \bar{b}^{lq} = 1 - \rho_{lq} \eta^{lq} s, \bar{\rho} = \rho - \rho^{lq} \rho_{lq} \eta^{lq} s, \Lambda^2 = \rho s^2 / (\lambda + 2\mu) \quad (40)$$

$$\mathcal{A}_i^2 + \mathcal{A}_2^2 = \Lambda^2 + \Pi_{lq}^2 + \frac{\bar{b}^{lq} s}{(\lambda + 2\mu) \bar{\eta}^g}, \mathcal{A}_i^2 \mathcal{A}_2^2 = \Lambda^2 \Pi_{lq}^2, \mathcal{A}_3^2 = 0, \mathcal{A}_4^2 = \rho s^2 / \mu \quad (41)$$

$$\tilde{G}_{ij} = \frac{1}{2\pi\mu s} \left[\frac{1}{-\mathcal{A}_4^2} (\mathcal{A}_4 A_{ij} K_1(\mathcal{A}_4 r) + \mathcal{A}_4 B_{ij} K_0(\mathcal{A}_4 r)) + K_0(\mathcal{A}_4 r) \delta_{ij} \right] \quad (42-1)$$

$$+ \frac{\Lambda^2 - \mathcal{A}_2^2}{\mathcal{A}_4^2 (\mathcal{A}_2^2 - \mathcal{A}_i^2)} (\mathcal{A}_2 A_{ij} K_1(\mathcal{A}_2 r) + \mathcal{A}_2 B_{ij} K_0(\mathcal{A}_2 r)) - \frac{\Lambda^2 - \mathcal{A}_i^2}{\mathcal{A}_i^2 (\mathcal{A}_2^2 - \mathcal{A}_i^2)} (\mathcal{A}_i A_{ij} K_1(\mathcal{A}_i r) + \mathcal{A}_i B_{ij} K_0(\mathcal{A}_i r))$$

$$\tilde{G}_{3i} \Big|_{i=1,2} = \frac{\bar{b}^{lq}}{2\pi(\lambda + 2\mu) \bar{\eta}^{lq}} \left[\frac{-1}{(\mathcal{A}_2^2 - \mathcal{A}_i^2)} \frac{\mathcal{A}_2 x_i}{r} K_1(\mathcal{A}_2 r) + \frac{1}{(\mathcal{A}_2^2 - \mathcal{A}_i^2)} \frac{\mathcal{A}_i x_i}{r} K_1(\mathcal{A}_i r) \right] \quad (42-2)$$

$$\tilde{G}_{33} = \frac{1}{2\pi(\mathcal{A}_2^2 - \mathcal{A}_i^2) s \bar{\eta}^{lq}} \{ (\mathcal{A}_i^2 - \Lambda^2) K_0(\mathcal{A}_i r) - (\mathcal{A}_2^2 - \Lambda^2) K_0(\mathcal{A}_2 r) \} \quad (42-3)$$

$$\tilde{G}_{4i} = \tilde{G}_{i4} = \tilde{G}_{34} = \tilde{G}_{43} = \tilde{G}_{44} = 0 \quad (42-4)$$

Which are the solutions of poroelastodynamics due to line load presented by Chen [6,7]. The only difference is the definition of $\bar{b}^{lq} = 1 - \rho_{lq} \eta^{lq} s$ which is due to the assumption of incompressible solid matrix in the present work.

Summary

One of the most important problems in geotechnical earthquake engineering is the elastic wave propagation through the soil layers to the structure's foundation. In other word the response analysis of structures is closely related to the accuracy and correctness of the site response analysis. Definitely, such problem can be solved by the aid of newly developed numerical methods correctly and more accurately. The domain type numerical methods have been developed for saturated and unsaturated media like finite element method. The advantage of domain type methods is the ability of modeling nonlinear or plastic behaviour of materials. On the other hand they have difficulties in modeling semi infinite or unbounded media. The boundary type

method like boundary element method fulfills this problem and intrinsically models the outgoing waves to the infinite domain. Besides, in this method discretization is applied on boundaries, which reduces the set of equations to be solved. BEM encompasses of boundary integral equations and corresponding fundamental solutions. The authors have presented boundary integral equation of unsaturated poroelastodynamic media [15]. The fundamental solutions to unsaturated poroelastodynamics have not been provided before. This paper presents the Laplace domain two dimensional fundamental solutions of full dynamic unsaturated porous medium that is composed of incompressible solid matrix. The solutions are verified by expressing two limiting cases of elastodynamics and saturated poroelastodynamics. It was shown that let the appropriate coefficients vanish will reduce the present solutions to the solutions for two limiting cases.

References

- [1] G. Bonnet, *Basic singular solutions for a poroelastic medium in the dynamic range*, J. Acoust. Soc. Am., **82**: 1758-1762, (1987).
- [2] J. Dominguez, *An integral formulation for dynamic poroelasticity*, J. Appl. Mech., **58**, 588-591, (1991).
- [3] J. Dominguez, *Boundary element approach for dynamic poroelastic problems*, Int. J. Numer. Meth. Engng. **35**, 307-324 (1992).
- [4] G. Manolis and D. Beskos, *Integral formulation and fundamental solutions of dynamic poroelasticity and thermoelasticity* Acta Mechanica, **76**: 89-104 (1989).
- [5] G. Manolis and D. Beskos, *Corrections and assitions to the paper Integral formulation and fundamental solutions of dynamic poroelasticity and thermoelasticity* Acta Mechanica, **83**: 223-226 (1990).
- [6] J. Chen, *Time domain fundamental solution to Biot's Complete equations of dynamic poroelasticity. Part I. Two dimensional solution* Int. J. Solids Structures., **31** (10): 1447-1490 (1994a).
- [7] J. Chen, *Time domain fundamental solution to Biot's Complete equations of dynamic poroelasticity. Part I. Three dimensional solution* Int. J. Solids Structures., **31** (2): 169-202 (1994b).
- [8] B. Gatmiri, and M. Kamalian, *On the Fundamental Solution of Dynamic Poroelastic Boundary Integral Equations in the Time Domain* Int. J. Geomech. ASCE, **2**, pp. 381-398 (2002).
- [9] B. Gatmiri and K.V. Nguyen, *Time 2D fundamental solutions for saturated porous media with incompressible fluid* Commun. Numer. Meth. Engng., **21** (3): 119-132 (2004).
- [10] M. Schanz, and D. Prial, *Dynamic fundamental solutions for compressible and incompressible modeled poroelastic continua* Int. J. Solids and Structures, **41**, pp.4047-4073 (2004).
- [11] B. Gatmiri and E. Jabbari, *Time-domain functions for unsaturated soils. Part I: Two dimensional solution* Int. J. Solids and Structures, **42**, pp. 5971-5990 (2005a).
- [12] B. Gatmiri and E. Jabbari *Time-domain functions for unsaturated soils. Part II: Three dimensional solution* Int. J. Solids and Structures, **42**, pp. 5991-6002 (2005b).
- [13] O. Coussy, *Mechanics of Porous Continua*, John Wiley & Sons, Ltd (1995).
- [14] O. Coussy, *Poromechanics*, John Wiley & Sons, Ltd (2004).
- [15] I. Ashayeri, M. Kamalian, and M.K. Jafari *Transient Boundary Integral Equation of Dynamic Unsaturated Poroelastic Media* Proceeding of 4th Geotech. Earth. Eng. & Soil Dynamics, ASCE, GeoInstitute, May 18-22, 2008, Sacramento, CA.

